

# Medium Voltage Impedance and Admittance Measurement and System Identification Techniques

Présentée le 27 août 2021

Faculté des sciences et techniques de l'ingénieur  
Laboratoire d'électronique de puissance  
Programme doctoral en énergie

pour l'obtention du grade de Docteur ès Sciences

par

**Marko PETKOVIC**

Acceptée sur proposition du jury

Dr S.-R. Cherkaoui, président du jury  
Prof. D. Dujic, directeur de thèse  
Dr S. Srdic, rapporteur  
Prof. P. Mattavelli, rapporteur  
Prof. A. Karimi, rapporteur





*Dedicated to all of those who helped make this work happen.*

*It ain't much but it's honest work.*

David Brandt

# Abstract

The recent trend of an increasing share of renewable energy sources in modern power systems, as well as the integration of power electronics equipment, is shaping the requirements for stable grid infrastructure. These requirements mainly come from the stability-related phenomena arising from different subsystem interactions. Namely, medium voltage systems require special attention due to the lack of equipment and solutions intended for their impedance measurement. Hence, this thesis provides the perception of the problem of medium voltage impedance measurement and system identification from the point of view of perturbation injection converters. A cascaded H-bridge the converter supplied from a medium-voltage multi-winding phase-shifting transformer is proposed in this thesis. Moreover, in combination with wideband injection signal, it imposes itself as a viable solution to this problem.

The thesis commences with an overview of readily available converter topologies and injection signals. The converter topologies are discussed, their downsides are pointed out and it is outlined how these issues can be addressed by using the cascaded H-bridge topology. Additionally, the lack of flexibility of the state-of-the-art solutions is highlighted.

Furthermore, the modelling approach of the single power electronics building block of the cascaded H-bridge converter is presented. Initially, the open-loop control model in the dq-frame is presented. The dq-frame modelling approach is adopted for both the three-phase active front end and for the single-phase H-bridge inverter. An estimation of the source-load affected dynamics is provided on the basis of the closed-loop control modelling. This question needed to be answered out of the concern for the interaction between the active front end and the H-bridge inverter. For efficient perturbation injection, the active front end should not limit the output dynamics of the H-bridge inverter. Real-time simulations in combination with additional single-phase dq-frame measurement and identification methods revealed that there is in fact very little to no influence between two sub-converters. Moreover, the terminal characteristics of the active front end, i.e. its input admittance and output impedance are measured in an experimental setup, providing the first result in the full experimental verification of the notions proposed.

The hardware and control designs of the active front end are subsequently verified through the power circulation tests in a setup including two active front ends and the medium voltage multi-winding transformer. On one side, the verification is made possible due to the transformer primary side synchronization method, effectively alleviating the need for the filter part of the active front end. Namely, the transformer leakage inductances are used as the filter inductors. On the other side, the control verification is performed on the basis of an industrial control system required owing to the size and complexity of the full-scale converter.

The flexibility issue of the medium voltage perturbation injection converters is addressed through the hardware and control reconfiguration of the cascaded H-bridge. The ac converter is reconfigured for dc operation with three different modes of operation possible, depending on the desired voltage level. The ideas behind the converter flexibility are demonstrated through the simulations covering the measurement of the terminal characteristics of the modular multilevel converter.

**Keywords** *medium voltage, high-power, impedance measurement, system identification, cascaded H-bridge*



# Résumé

La tendance récente de l'augmentation de la part des sources d'énergie renouvelables dans le système électrique moderne, ainsi que l'intégration des équipements électroniques de puissance, élaborent les exigences d'une infrastructure de réseau stable. Ces exigences proviennent principalement des phénomènes liés à la stabilité résultant de différentes interactions de sous-systèmes électrique. Les systèmes de moyenne tension nécessitent une attention particulière en raison du manque d'équipements et de solutions destinés au mesure de leur impédance. Ainsi, cette thèse fournit une perception du problème de la mesure d'impédance moyenne tension et de l'identification du système du point de vue des convertisseurs d'injection de perturbation. Un convertisseur en pont en H en cascade alimenté par un transformateur déphaseur multi-enroulements moyenne tension est proposé dans cette thèse. De plus, en combinaison avec un signal d'injection large bande, il s'impose comme une solution viable à ce problème.

La thèse commence par un aperçu des topologies de convertisseur et des signaux d'injection facilement disponibles. Les topologies des convertisseurs sont discutées, leurs inconvénients sont signalés et il est décrit comment ces problèmes peuvent être résolus en utilisant la topologie en H-bridge en cascade. De plus, le manque de flexibilité des solutions de pointe est mis en évidence.

En outre, l'approche de modélisation du bloc de construction électronique de puissance du convertisseur à pont en H en cascade est présentée. Au départ, le modèle de contrôle en boucle ouverte dans le repère  $dq$  est présenté. L'approche de modélisation dans le repère  $dq$  est adoptée à la fois pour le redresseur actif triphasé et pour l'onduleur à pont en H monophasé. Une estimation de la dynamique du onduleur à pont en H, affectée par la source active, i.e. le redresseur actif triphasé, est fournie sur la base de la modélisation de contrôle en boucle fermée. Il fallait répondre à ces questions par souci d'interaction entre le redresseur actif triphasé et l'onduleur en pont en H. Pour une injection de perturbation efficace, le redresseur actif ne doit pas limiter la dynamique de sortie de l'onduleur à pont en H. Des simulations en temps réel combinées avec des méthodes supplémentaires de mesure et d'identification dans le repère  $dq$  monophasées ont révélé qu'il y a en fait très peu ou pas d'influence entre deux sous-convertisseurs. De plus, les caractéristiques terminales du redresseur actif triphasé, c'est-à-dire son admittance d'entrée et son impédance de sortie sont mesurées dans un montage expérimental, fournissant un premier résultat dans la vérification expérimentale complète des notions proposées.

Les conceptions de matériel et de commande du redresseur actif triphasé sont ensuite vérifiées par les tests de circulation de puissance dans une configuration comprenant deux redresseurs et le transformateur déphaseur multi-enroulements. D'un côté, la vérification est rendue possible grâce à la méthode de synchronisation côté primaire du transformateur, ce qui réduit efficacement le besoin de la partie filtre du redresseur actif triphasé. A savoir, les inductances de fuite du transformateur sont utilisées comme inductances de filtre. De l'autre côté, la vérification du contrôle est effectuée sur la base d'un système de contrôle industriel nécessaire en raison de la taille et de la complexité du convertisseur pleine échelle.

Le problème de flexibilité des convertisseurs d'injection de perturbation moyenne tension est résolu par la reconfiguration matérielle et de commande du pont en H en cascade. Le convertisseur en courant alternatif est reconfiguré pour un fonctionnement en courant continu avec trois modes de fonctionnement différents possibles, en fonction du niveau de tension souhaité. Les idées qui

sous-tendent la flexibilité du convertisseur sont démontrées à travers les simulations couvrant la mesure des caractéristiques des bornes du convertisseur modulaire multiniveau.

**Mots-clés** *moyenne tension, haute-puissance, mesure d'impédance, identification de système, pont en H en cascade*

# Acknowledgments

*"No one who achieves success does so without acknowledging the help of others."*

Alfred North Whitehead

A bit more than four years ago, on my first day as a fresh graduate and a trainee in the Power Electronics Laboratory (PEL), I was offered to start a PhD at the end of my traineeship. Hesitant at first and after some discussions with Prof. Dražen Dujić, I have accepted the offer. And what a mistake it would have been if I had not listened to him. Thus, I would like to express my immense gratitude to Prof. Dražen Dujić, my thesis advisor. Prof. Dujić provided me with invaluable advice and support, which pushed me through the PhD years and through the last meters of a bike ride to Col du Marchairuz, and finally brought me to their respective ends.

I am also grateful to the members of the jury, Prof. Rachid Cherkaoui from the DESL at EPFL, Dr. Srđan Srdić of EGSTON Power Electronics in Eggenburg, Austria, Prof. Paolo Matavelli of the Power Electronics Group at the University of Padova and finally to Prof. Alireza Karimi from the Automatic Laboratory at EPFL, for accepting to evaluate this work. I hope they didn't only read this thesis when they couldn't fall asleep.

These words certainly wouldn't have been written without the help of my friends and colleagues, especially those belonging to PEL. They have also played a great part in my decision to start and finish this PhD. Their professional input has been extremely valuable. However, maybe even more important than that, our Satellite outings and coffee breaks have made me a very *spiritually* rich person today. I hope that other PhD students have felt and will feel the same once they leave PEL. It would be unfair to single someone out, you were all great!

My Serbian and non-Serbian friends have definitely played a big role in my life in Lausanne over the course of the last 10 years. It has been a tremendous hike full of ups and downs. Thank you all for being there and for all the moments of laughter, joy and happiness.

Finally before finally, I have to acknowledge the role of my parents and my brother providing me with their love and support, and for being there for me whenever I needed it.

And really finally, my biggest gratitude goes to the love of my life, Marguerite! Without her « *Hey, Viking guy!* » moment, nothing would have been the same. Je t'aime plus que tout, ma chérie!

Lausanne, April 25, 2021  
Marko Petković





# List of Abbreviations

3L-NPC	3-level neutral point clamped
ac	alternate current
AFE	active front end
CHB	cascaded H-bridge
CPSD	cross-power spectral density
CSU	command and supervisory unit
dc	direct current
DFE	diode front end
DFT	discrete Fourier transform
DUT	device under test
DVC	dc-link voltage control
FFT	fast Fourier transform
FlexCHB	flexible cascaded H-bridge
GaN	gallium-nitride
GDU	gate driver unit
HB	H-bridge
HIL	hardware-in-the-loop
HVdc	high voltage dc
I/O	input and output
ICC	input current control
INU	inverter unit
KCL	Kirchhoff's current law
KVL	Kirchhoff's voltage law
LV	low voltage
LVdc	low voltage dc

MLBS	maximum-length binary sequence
MMC	modular multilevel converter
MV	medium voltage
MVac	medium voltage ac
MVdc	medium voltage dc
MWT	multi-winding transformer
NPC	neutral point clamped
OCC	output current control
PEBB	power electronics building block
PEC-GDU	PEC gate driver unit
PEC-MI	PEC measurement interface
PI	proportional integral
PIC	perturbation injection converter
PLL	phase-locked loop
PR	proportional resonant
PRBS	pseudo-random binary sequence
PS-PWM	phase-shifted PWM
QSG	quadrature signal generator
RES	renewable energy sources
Si	silicon
SiC	silicon-carbide
SM	submodule
SOGI	second-order generalized integrator
SRF	synchronous reference frame
STATCOM	static synchronous compensator
SUT	system under test
UPS	uninterruptible power supply
VSC	voltage-source converter





# Table of Contents

<b>Abstract</b>	<b>i</b>
<b>Résumé</b>	<b>iii</b>
<b>Acknowledgments</b>	<b>v</b>
<b>List of Abbreviations</b>	<b>vii</b>
<b>1 Introduction</b>	<b>1</b>
1.1 Towards a Power Electronics Dominated Power Systems	1
1.2 Stability Issues Related to Power Electronics in Power Systems	2
1.3 Impedance-Based Stability and Overview of Stability Criteria	3
1.4 Impedance Measurement Methods for Ac and Dc Systems	6
1.5 Perturbation Injection and Impedance Measurement Devices	7
1.6 CHB Converter Potential in the MV Impedance Measurement and System Identification	10
1.7 Objectives and Contributions of the Thesis	11
1.8 Outline of the Thesis	12
1.9 List of Publications	13
<b>2 Technology Overview for Medium Voltage Impedance and Admittance Identification</b>	<b>15</b>
2.1 Industry-Based Perturbation Injection Converters	15
2.2 Academia-Based Perturbation Injection Converters	17
2.3 Perturbation Signals Overview	19
2.3.1 Single Tone Sinusoidal Signal	19
2.3.2 Chirp Signal	19
2.3.3 Multi-Tone Signal	20
2.3.4 Pseudo-Random Binary Sequence Signal	21
2.3.5 CHB Converter Considerations for Medium Voltage Perturbation Injection and Impedance Measurement	22
2.4 Summary	24
<b>3 Power Electronics Building Block Open Loop Modelling</b>	<b>25</b>
3.1 Cascaded H-Bridge Converter Power Electronics Building Block	25
3.2 Active Front End Modelling	26
3.2.1 Active Front End State-Space Model and Open-Loop Dynamics	30
3.2.2 Open-Loop Model Verification	38
3.3 H-Bridge Inverter Modelling	40
3.3.1 H-Bridge State-Space Model and Open-Loop Dynamics	43
3.3.2 Open-Loop Model Verification	49
3.4 Summary	50
<b>4 Closed-Loop Control Modelling</b>	<b>51</b>
4.1 Active-Front-End Closed-Loop Control and Synchronization Design	51
	xi

4.1.1	Synchronous Reference Frame Phase-Locked-Loop	51
4.1.2	Grid Current Control	53
4.1.3	Dc-link Voltage Control	54
4.1.4	Closed-loop Control Model Verification of the AFE	56
4.2	H-Bridge Control	57
4.2.1	Inductor Current Control	57
4.2.2	Output Voltage Control	59
4.2.3	Second Order Generalised Integrator in the $dq$ -Frame	60
4.3	Summary	62
<b>5</b>	<b>Load and Source Affected Dynamics</b>	<b>63</b>
5.1	Source-Affected Dynamics Characterization	63
5.2	Single-Phase Measurements in the $dq$ -Frame	65
5.2.1	Single-Phase Output Impedance Measurement in $dq$ -Frame	65
5.2.2	Single-Phase Control-to-Output Characteristics Measurement in $dq$ -Frame	66
5.3	Summary	71
<b>6</b>	<b>Power Electronics Building Block Testing and Power Circulation Test</b>	<b>73</b>
6.1	Multi-Winding Phase-Shifting Transformer Measurements	73
6.2	Primary-Based Source Synchronization	77
6.3	Cascaded H-Bridge Converter Power Electronics Building Block	79
6.3.1	Back-to-Back Setup for Active Front End Testing	80
6.4	Control Parameter Tuning	82
6.4.1	Control Performance	86
6.5	Power Electronics Building Block Thermal System Design	88
6.6	Power Circulation Testing	91
6.6.1	Cooling System Performance	93
6.7	Summary	93
<b>7</b>	<b>Terminal Characteristics Measurements and Analysis of the Three-Phase AFE</b>	<b>95</b>
7.1	Active Front End Terminal Characteristics Measurement	95
7.1.1	Control Parameters Tuning and Control Performance	96
7.2	Terminal Characteristics Measurement System	97
7.2.1	Grid Emulator and Perturbation Injection Converter	99
7.2.2	Perturbation Signal	99
7.2.3	Voltage and Current Measurement	100
7.2.4	Data-Acquisition System	100
7.2.5	Admittance and Impedance Extraction	100
7.3	Measurement Results	101
7.4	Summary	105
<b>8</b>	<b>Flexible Medium-Voltage Perturbation Injection Converter for Ac and Dc System Identification</b>	<b>107</b>
8.1	Flexible Cascaded H-Bridge Converter	107
8.1.1	Ac Output Configuration	107
8.1.2	Dc Output Configuration	108

8.2	Output Voltage Control	111
8.3	MMC Ac and Dc Admittance Measurements	111
8.4	Summary	117
<b>9</b>	<b>Summary and Future Work</b>	<b>119</b>
9.1	Summary and Contributions	119
9.2	Future Work	121
	<b>Appendices</b>	<b>123</b>
<b>A</b>	<b>Appendix</b>	<b>125</b>
A.1	Small-Signal and State-Space Equations	125
A.2	Synchronous Reference Frame Modelling	126
A.3	Hilbert Transform	127
	<b>Bibliography</b>	<b>129</b>





# 1

## Introduction

### 1.1 Towards a Power Electronics Dominated Power Systems

The names of Nikola Tesla and Thomas Edison have been immortalized in the late 19<sup>th</sup> century after a struggle to prevail in the world of electrical engineering. At the time, during the *War of the Currents* Tesla and Edison battled over the application of the alternate current (ac) or the direct current (dc) in the domain of electrical power generation and distribution. The dc technology became popular in providing electricity for American households and street lighting, replacing the previously adopted arc lights technology which turned out to be too bright to be used outdoors and too dangerous to be used indoors, as it presented a sparking or fire hazard due to the high voltage operation [1]. Edison devised a cost-effective incandescent light bulb and went on to establish a first widespread illumination utility in Manhattan, New York.

However, soon after the rise of Edison, George Westinghouse came to the conclusion that Edison's dc technology lacked the capability to change the voltage level and was impractical for power transmission over longer distances due to the increased cost and power losses and that the inexpensive conversion technology only existed for alternating current. Subsequently, Nikola Tesla partnered with George Westinghouse and successfully demonstrated the capabilities of the ac technology at the Chicago fair. The advantage the ac possessed was the ease of changing the voltage levels using transformers and the invention of induction generators. Consequently, the ac technology was chosen by the Niagara Falls Power Company to generate electricity and thus Nikola Tesla won the first battle of the *War of the Currents*. After this victory the dc technology was cast aside and the ac shaped the power system for a considerable time.

Nevertheless, it would be unfair not to mention the name of René Thury, who being based by the work of Marcel Deprez and Charles Bush, developed the first low voltage dc (LVdc) transmission system in Bözingen in Switzerland in 1885 and afterwards the first high voltage dc (HVdc) system in Genoa in 1889 [2]–[4].

Even though the mercury valves were invented in 1901 and introduced in 1914 and certain power transmission projects were developed around the dc technology, such as the Elbe-Berlin HVdc system [5], it was not until the improvement in the semiconductor and especially power semiconductor technologies that the development of dc technology has started. The power electronics converters have enabled the conversion of ac to dc voltage and vice versa and have moreover made possible power conversion and transmission between the systems of different nature.

In the last 20 to 30 years we have witnessed the efforts to reduce the CO<sub>2</sub> emission by decreasing the share of fossil-fuel based power plants and replacing them by renewable energy sources (RES) such as

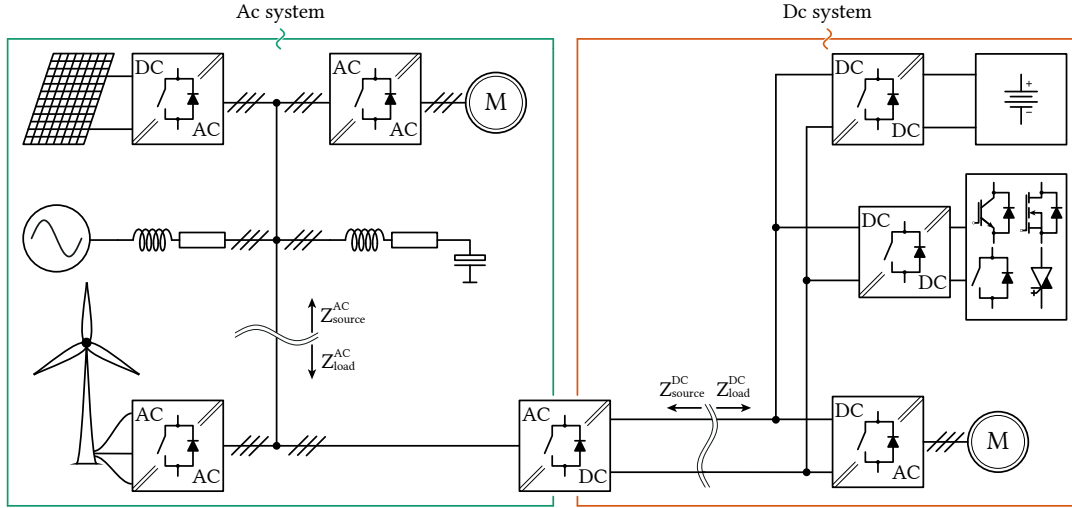


**Fig. 1.1** Modern, hybrid, ac/dc power electronics dominated energy system including loads and sources of different nature. Adaptation from [7].

solar and wind energy sources. An example of a modern power system incorporating conventional and RES, passive and active loads and energy storage elements is presented in **Fig. 1.1**. The core elements of the power grid in **Fig. 1.1** can be of different natures, either dc or ac. Additionally, voltage levels at the terminals of these subsystems can differ from one to another. The operation of such a system is mainly made possible by the presence of power electronics equipment. From the input/output standpoint of power electronic converters, depending on the topology used, any conversion can be performed, ac-dc, dc-ac, ac-ac and dc-dc. Solar energy sources, dc in nature, are a perfect example in which the power electronics converters are used to convert dc power into ac power and feed it into the grid. On the other side, power electronics converters are also used with wind energy sources where the turbines are connected to an ac generator. Depending on the application, the ac voltage either needs to be adapted to the grid level where the generator feeds the produced power or it needs to be converted into the dc voltage in order to reduce the power losses during electricity transport over long distances. The advances in the field of energy storage have subsequently lead to the installation of energy storage elements where one large scale example is the installation of 129 MWh system in South Australia [6].

It is clear that the development of power electronics equipment, RES and modern power systems go hand in hand. As a consequence, the increase in the share of RES is followed by the increase in the share of the power electronics equipment installed. This trend further leads us towards power electronics dominated power system where the heritage of both Tesla and Edison needs to coexist in harmony.

## 1.2 Stability Issues Related to Power Electronics in Power Systems

Notwithstanding, harmony is rarely reached in a war, or in peace for that matter, since disturbances are a part of life, and such is the case here as well. This absence of harmony comes from the inherent nature of power converters as they are not ideal sources and loads, and every converter has its input and output characteristics, namely input or output impedance or admittance as presented in

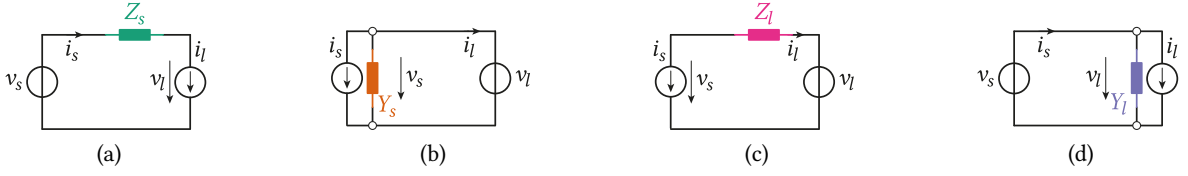


**Fig. 1.2** Illustration of non-ideal (a) voltage and (b) current sources and (c) voltage and (d) current loads. Each source or load is characterized by its input or output impedance or admittance.

**Fig. 1.2.** Interaction of their characteristics potentially poses a problem in an interconnected system of two or more converters. The first instabilities started to emerge as soon as the ac and dc systems started to interact in aircraft systems in 1950's [8] and switching-mode amplifiers, dc/dc converters or dc/ac inverters began to be used [9]. More recently, harmonic instabilities and resonances have been reported due to the integration of RES, such as wind farms or solar parks, where the voltage-source converters (VSCs) have either been a reason for the resonances or have contributed to their amplification [10], [11]. This trend of harmonic instabilities was also noticed and reported in railway networks where the low frequency oscillations have been observed [12]. One of the most notable, local, examples is the case of the the Swiss Federal Railways (SBB) network which has been brought down twice, once in 1995 and then ten years later in 2005, due to interaction between the converters installed in the new SBB locomotives [13], [14]. In this particular case, due to an improper controller software of the converters, the system became unstable and locomotives were shut down by protective equipment.

One of the reasons for the instabilities is the fact that the small-signal dynamics of power electronics converters has a tendency of introducing negative damping in the system. The frequency range in which this damping is present depends on the closed-loop control of converters as well as the operating conditions of the power system in which the converter is running [15]. There exists a wide variety of modelling techniques that can be used for the harmonic stability studies. When modelling a system with the complexity of the one given in **Fig. 1.1** many parameters such as control and physical parameters of the equipment are required. Moreover, even when an approximate model is found, every time that a new element is introduced into or removed from the system the model needs to be updated. Furthermore, due to the ever increasing number of equipment manufacturers and system component vendors, obtaining proprietary information is not always achievable. This in turns transforms the modelling of a power system, and its underlying components, into an overwhelming task. Finally, we have all at least once heard a phrase “*All models are wrong, but some are useful*”. Therefore, establishing or choosing an adequate modelling approach is essential step before commencing an in-depth analysis of the power system behaviour.

### 1.3 Impedance-Based Stability and Overview of Stability Criteria

A more practical approach compared to the analytical modelling is the impedance-based stability analysis [16]–[18]. This method has historically been successfully used for low-power, low voltage (LV) systems and converters [19]. The underlying idea behind this method is the measurement of an impedance, or an admittance, at an interface in the system and application of some stability criterion to estimate the global stability of the system. The advantage of this technique is due to the fact that the measured impedance encompasses all of the system components, as well as physical and

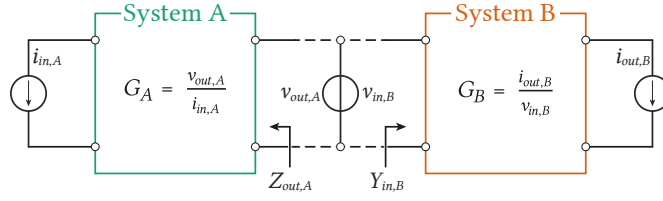


**Fig. 1.3** Block representation of interconnection of two independent systems obtained using small-signal modelling techniques.

control system features. As the stability studies themselves are out of the scope of the thesis only the overview of the most important ones, according to the author, are presented here. The criteria presented here can be described using an example shown in **Fig. 1.3**, where two independent systems are interconnected to create a new system. It is taken as an assumption that each of these systems is stable on their own. Their transfer functions are given as:

$$\begin{aligned} G_A(s) &= \frac{v_{out,A}(s)}{i_{in,A}(s)} \\ G_B(s) &= \frac{i_{out,B}(s)}{v_{in,B}(s)} \end{aligned} \quad (1.1)$$

From the physical point of view, the output and input characteristics of systems A and B are represented as their output impedance and input admittance,  $Z_{out,A}(s)$  and  $Y_{in,B}(s)$ . By connecting the two systems a new transfer function can be defined as:

$$\begin{aligned} G_{AB} &= \frac{i_{out,B}(s)}{i_{in,A}(s)} = G_A(s) G_B(s) \frac{Y_{in,B}^{-1}(s)}{Y_{in,B}^{-1}(s) + Z_{out,A}(s)} \\ &= G_A(s) G_B(s) \frac{1}{1 + Z_{out,A}(s) Y_{in,B}(s)} \end{aligned} \quad (1.2)$$

In (1.2) the product of output impedance and input admittance,  $L(s) = Z_{out,A}(s) Y_{in,B}(s)$ , is known as *minor loop gain* and is used to determine the stability of the interconnection of two already stable systems. The Nyquist Criterion can be applied on the product  $Z_{out,A}(s) Y_{in,B}(s)$ , which states that the system is stable, if and only if, the Nyquist plot of  $Z_{out,A}(s) Y_{in,B}(s)$  does not encircle the critical point of  $(-1, 0)$  [20]. Moreover, the product  $Z_{out,A}(s) Y_{in,B}(s)$  maps the dynamic interactions of two independent systems. For multi-variable systems a Generalized Nyquist Criterion can be applied, which makes use of the the number of encirclements around critical point  $(-1, 0)$  in complex plane. Namely, the number of closed-loop poles in the right-half plane ( $\mu$ ) is equal to the number of open-loop poles in the right-half plane ( $\rho$ ) plus the number of clockwise encirclements ( $\nu$ ) of the -1 point of the Nyquist plot of the minor loop gain (i.e.  $\mu = \rho + \nu$ ) [21]. Thus, system is stable if the number of encirclements (in the counter-clockwise direction) of the point  $(-1, 0)$  is equal to the number of unstable poles of the minor loop gain, i.e.  $\nu = -\rho$  (from  $\mu = \nu + \rho = 0$ ).

Based on the concept of product of output impedance and input admittance, different stability criteria have been proposed and defined to establish the stability of a system. Most noteworthy amongst these criteria are: (i) *Middlebrook criterion*, (ii) *gain margin and phase margin (GMPM) criterion* and (iii) *opposing argument criterion*.

### Middlebrook Criterion

The *Middlebrook criterion* was first defined in the 1970s and it was intended for determining the stability of a closed-loop controlled switching converter with an input filter [20], [22]. The stability of a system, at a certain frequency  $\omega$ , following this criterion can be defined as:

$$\|Z_{out,A}(\omega) Y_{in,B}(\omega)\| \ll 1 \quad (1.3)$$

What the equation (1.3) demonstrates is a design-oriented sufficient stability condition imposing a small-gain condition on the *minor loop gain* [20], which in turn provides that the product  $Z_{out,A}(s) Y_{in,B}(s)$  never encircles the critical point  $(-1, 0)$ . The application of this criterion to different systems is relatively simple since it considers only the magnitude of the *minor loop gain*. However, the constraints it imposes are rather conservative and may result in impractical design parameters.

### Gain and Phase Margin Criterion

Where the *Middlebrook criterion* fails due to its conservativeness, the *gain and phase margin criterion* appears to counter it [23]. The name of the criterion comes from the fact that it defines the limits for both the gain and the phase of the *minor loop gain* to ensure the stability of a system. The two limits are defined as:

$$\begin{aligned} \|Z_{out,A}(\omega) Y_{in,B}(\omega)\| &\leq \frac{1}{GM} \\ |\angle Z_{out,A}(\omega) + \angle Y_{in,B}(\omega)| &\leq 180^\circ - PM \end{aligned} \quad (1.4)$$

Here, two information are needed from the *minor loop gain*, which are its magnitude and its phase. The limit on the gain margin is specified as 6 dB while the phase margin is specified to be at  $60^\circ$ . However, depending on the authors and experience the phase margin of  $30^\circ$  to  $60^\circ$  is often sufficient.

### Opposing Argument Criterion

Coming back to the **Fig. 1.1**, is noticeable that there exist multiple loads, or sources, at certain points in the system. In a situation such as this one, the *opposing argument criterion* makes itself useful [24]. The *opposing argument criterion* defines a stability limit at  $-1/GM$ , denoting the forbidden region, and at the same time ensures that there is no encirclement of the critical point  $(-1, 0)$ . For a systems with  $n$  multiple loads, admittance of each load can be defined as  $Y_{in,B}^i(s)$  and mathematically the criterion is defined as:

$$\Re(Z_{out,A}(\omega) Y_{in,B}^i(\omega)) \leq -\frac{1}{GM} \cdot \frac{P_{in}^i}{P_{tot}} \quad (1.5)$$

The gain limit  $-1/GM$  for a load  $i$  is scaled with respect to its portion of the total load consumption, given by  $P_{in}^i/P_{tot}$ . If the condition given by the equation (1.5) is fulfilled there is no phase constraint, however, if the contrary is true the phase is analysed and must be equal to:

$$\phi^i = \arcsin\left(\frac{1}{GM} Z_{out,A}(\omega) Y_{in,B}^i(\omega) \frac{P_{in}^i}{P_{tot}}\right) \quad (1.6)$$

## 1.4 Impedance Measurement Methods for Ac and Dc Systems

The measurement and extraction of impedances in ac and dc systems is a particularly complex topic and there exist many approaches to this problem. Namely, the approaches can be separated based on several criteria as: (i) *type of signal used for perturbation injection*, (ii) *impedance extraction techniques* and (iii) *impedance representation techniques*.

When it comes to the type of the signal used for perturbation, the single-tone perturbation injection, or an ac-sweep, is naturally the simplest and historically was the first method to be implemented, namely for the dc/dc converters [25]. However, since a single frequency signal is injected at a time, the measurement duration can become elevated. When measuring a highly dynamical system such as the power grid for example, it is desirable that the measurement time is as short as possible due to the possibility of the system changing state during the measurement. The possibility that the impedance at a certain point changes comes from the fact that the impedance also depends on the operating point of the system. A way of addressing this issue has been by making use of wideband signals for perturbation injection and measurement. These signals contain more than a single frequency and there exist several signals that are successfully used for impedance measurements. Specifically the chirp and multi-tone signals have been used to measure the impedance of power distribution networks of electric ships operating at the medium voltage (MV) level in [26]–[28]. Another signal that has recently gained in popularity is the pseudo-random binary sequence (PRBS) signal [29], albeit its usage has so far been restricted to LV domain [30], [31]. Nevertheless, these approaches have been applied to complex systems composed of multiple converters operating at the same time showing the potential of the impedance measurement method.

Once the perturbation injection is over and the voltage and current measurements are collected, there needs to exist a way of extracting the useful information from the measurement. In the past there have been cases of time-domain identification of impedances where the black-box modelling was performed together with the stability analysis [32], [33]. However, similar applications are very few in number compared to frequency-domain identification which dominates the field. The discrete Fourier transform (DFT) algorithm is widely used to extract the frequency components from the measured voltages and currents, together with different techniques for reducing the effect of noise in the system. A successful example where the cross-power spectral density (CPSD), based on Welch's averaging algorithm, is used is presented in [28]. Methods that do not fall under this category are the neural network techniques treated in [34] and recursive least square estimation techniques presented in [35].

Eventually, whichever perturbation signal or extraction technique is used the results need to be represented in a sensible way in order for the stability criteria to be applied. This is where the representation techniques come in place. When measuring the dc impedances the choice is very simple and clear, the impedances are represented in the dc domain. However, when measuring the ac impedances there exist several possible choices. Broadly adopted representation is the one in the synchronous reference frame (SRF) or the  $dq$ -frame. This method is valid for representing both the three-phase and single-phase ac impedances [36], [37]. The advantage of this approach lies in the fact that in the rotating  $dq$ -frame there exists an equilibrium point for small-signal representation compared to the stationary  $abc$ -frame. Moreover, the ac variables from the  $abc$ -frame, when transformed into the  $dq$ -frame become dc variables and the extraction of frequency components from voltage and current measurements becomes straightforward. One of the disadvantages claimed in [38] is that this

method requires two separate injections to fully represent the system in  $dq$ -frame. However, by using wideband signals and intelligent control methods this issue can be alleviated and the measurement time is comparable with methods using a single signal injection.

Another heavily used technique for impedance representation is the sequence domain representation using symmetric components [39]–[41]. A certain advantage of this method is the usage of a single perturbation injection to obtain the impedances. This however is only true for uncoupled sequence impedance measurement, which is a characteristic of symmetrical three-phase systems [38]. Another advantage of this method is that the resulting impedance is valid for all the range of interest, below and above the fundamental ac frequency [39]. There, however, does exist a method to measure the impedances in the stationary  $abc$ -frame as well, but it is rarely used [42].

## 1.5 Perturbation Injection and Impedance Measurement Devices

All things considered, one can easily perceive that whichever criterion, perturbation signal, extraction or impedance definition method is being used, there is a common denominator to all of them. This common point is that there needs to exist a suitable hardware to perform the perturbation injection and the impedance measurement. There exist numerous possibilities for creating a perturbation or injecting it into the system under study. Most of these devices are based on power electronics converters with some exception such as the wound rotor induction machine used in [43]. However, the perturbation creation can also be based on purely passive solutions such as load-stepping, which was presented in [32], [44]. Even though the load-stepping is easily implemented, due to the decreasing energy of the step excitation as the frequency increases, the precision in higher frequency range is compromised.

Focusing solely on the power electronics solutions the means of causing a perturbation in the system are multiple and they can either be used to create a perturbation at a certain terminal of the power system or create a perturbation at the terminals of a system under test (SUT) such as another power converter that will potentially make part of a power grid. Namely, either voltage or current perturbation signal can be injected. In a case the impedance, or admittance, of a grid is measured either series voltage (see **Fig. 1.4(a)**) or shunt current perturbation injection (see **Fig. 1.4(b)**) is performed between what is considered a source and a load in the grid.

Often the voltage injection is more suitable for impedance measurement of loads due to the stiff voltage nature of sources in a power grid, while the current injection is well suited for identification of source impedance due to the low impedance of sources resulting in a better response to a current injection. When measuring the input impedance, or admittance, of an SUT both the voltage and current injections are suitable depending on the type of the SUT, i.e. whether the SUT is a grid-connected converter, an uninterruptible power supply (UPS), grid-forming inverter, and so on. Several examples of possible measurement configuration are presented in **Figs. 1.4(c) to 1.4(f)**. The perturbation injection device can either inject only small-signal voltage and current perturbation, as shown in **Figs. 1.4(c) and 1.4(d)** or a small-signal perturbation can be injected on top of a fundamental waveform, as presented in **Figs. 1.4(e) and 1.4(f)**.

Perturbation injection and impedance measurement equipment is a well established technology in the LV low-power applications with commercial equipment available such as the Bode 100 (see **Fig. 1.5(a)**) and AP 300 (see **Fig. 1.5(b)**) frequency analysers. These devices are based on the small-

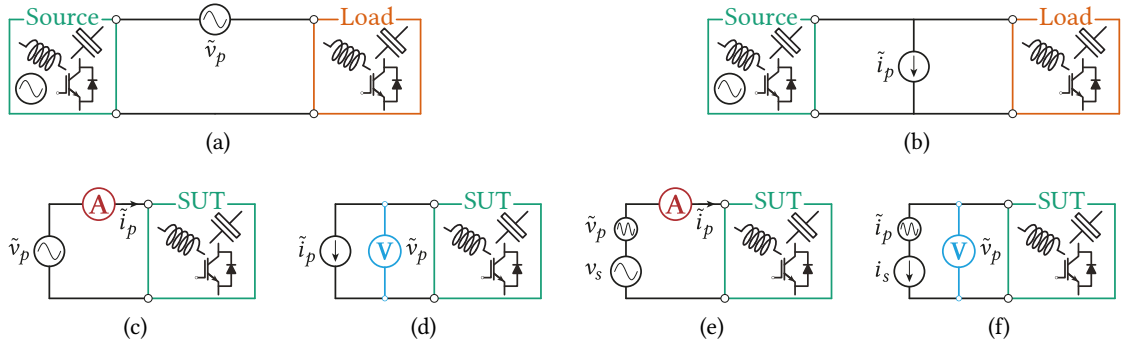


**Fig. 1.4** Representation of impedance and admittance identification by small-signal perturbation. Source and load impedance, admittance, identification by (a) series voltage injection and (b) shunt current injection, an SUT (c) impedance identification by voltage perturbation and current measurement, (d) admittance identification by current perturbation and voltage measurement, high-frequency impedance identification by (e) voltage perturbation and high-frequency admittance identification by (f) current perturbation in combination with a lower frequency main source signal  $v_s$  or  $i_s$ .

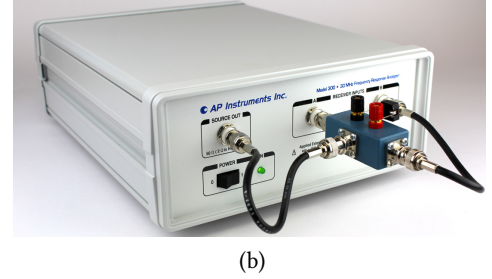
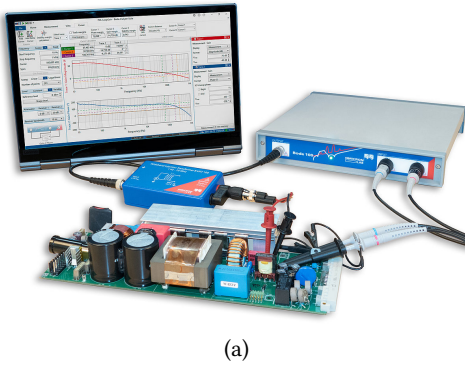


**Fig. 1.5** Commercial low voltage, low power, (a) Bode 100 by *Omicron* and (b) AP 300 by *Ridley Engineering*, frequency analysers.

signal perturbation principles and are able to provide frequency sweeps up to frequencies in the MHz range. Going to the higher power range, there exist programmable ac sources and grid emulators with specifications that correspond to the demands of the MV impedance measurement. They are designed for voltage levels up to 1 kV and power ratings of up to 200 kVA, and provide features, such as programmable harmonics or external waveform reference. Strictly speaking these solutions could be used to measure the impedance of MV systems provided that an adequate step-up voltage transformer is used at the output of such equipment. However, the leakage inductance imposed by the transformer would reduce the magnitude of measured currents which becomes even worse at higher frequencies and would impair the measurement precision. The usage of voltage step-up transformer and the limitations they impose are illustrated in **Fig. 1.7**. For this reason the equipment presented in **Fig. 1.6** still only stays a good solution for LV system measurement and hardware-in-the-loop (HIL) developments.

Based on these considerations, the most practical solution for a perturbation injection and impedance measurement device is the use of fast-switching power electronics converters directly interfaced to an MV system. Such devices are, however, very few today. The power electronics solutions for MV





**Fig. 1.6** Programmable ac sources and grid emulators (a) Regatron TC.ACS [45], (b) PAS 500 [46] and (c) Egston Compiso [47] suitable for perturbation injection and impedance measurement.

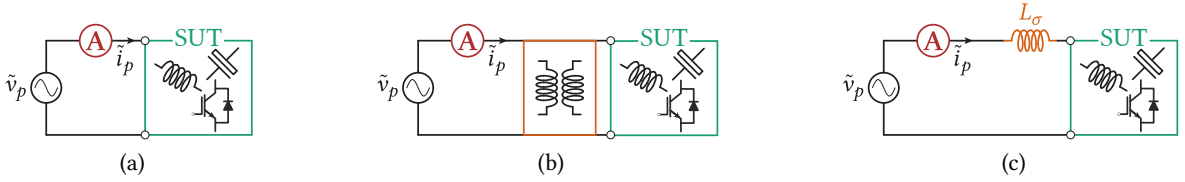


**Fig. 1.7** Limitations imposed by short-circuit power and step-up transformers (a) ideal voltage perturbation; (b) output voltage level adaptation by a step-up transformer; c) effect of transformer in the measurement: leakage impedance.

impedance measurement so far have been based on transformerless cascaded or paralleled H-bridge converter [28], [48] and on the parallel 3-level neutral point clamped (3L-NPC) topology [49].

It should still be taken into account that the perturbation injection converter (PIC) presented in [49], [50] features a transformer to step up the output voltage from 510 V to 20 kV. These PICs are mainly used for three-phase ac impedance identification but they can also be used for single-phase ac measurements [51]. A solution that approaches the most the MV impedance measurement problem definition is the passivity compliance test performed in the Swiss Railways (SBB) grid, and it is performed according to the EN-50388 standard. This procedure started to be performed directly after the second black-out of the SBB grid in 2005. Ideally, the passivity compliance test is performed as is demonstrated in **Fig. 1.8(a)**. However, the way that it is performed in practice is with a second locomotive which is used to inject small-signal perturbations into the locomotive under test and a large inductor  $L_s$  is inserted between the railways network, i.e. the source, and the perturbation injection locomotive, as is shown in **Fig. 1.8(b)**. This leads to the following problems related to this type of measurement: (i) this test can be performed only at specific locations, (e.g. train depot stations), (ii) the commercial traction power conversion systems are based on a voltage level below

the grid voltage level, so a step-up MV transformer is still needed and (iii) the perturbation signal can be amplified by including another bulky component in the circuit in front of the locomotive injecting the perturbations (i.e. inductance  $L_s$ ), so higher current harmonics are forced to be drawn by the device under test, i.e. the accuracy of the measurement is enhanced at the cost of having a rather large and impractical infrastructure and (iv) the cost of these measurements is often high. It is, however, worth mentioning that the MV transformer from the point (ii) is already a part of train system and as such is unavoidable part of the measurement setup. Another solution in the railways domain that is noteworthy is presented in [52], [53] where the set-up is based on a combination of LV power electronics and step-up transformers, which, as already discussed, strongly limits the measurements bandwidth.

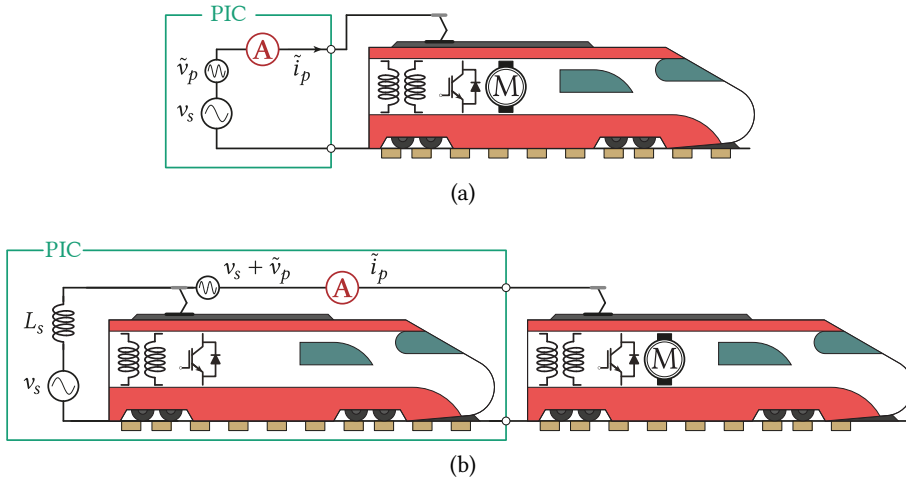


**Fig. 1.8** (a) An ideal setup for the admittance measurement of locomotives with electrical propulsion according to EN-50388 standard and (b) the realistic admittance measurement setup for the SBB locomotives with a bulky step-up transformer and inductance.

## 1.6 CHB Converter Potential in the MV Impedance Measurement and System Identification

Considering the problems outlined in the previous sections one can conclude that for the MV impedance measurement and system identification a solution is required that can cover several aspects:

- Fast-switching power electronics based device;
- Absence of step-up transformers to elevate the output voltage to MV level;
- High-power solution;
- Employment of wideband signals for system perturbation;
- Flexibility to inject perturbations into three- and single-phase system;
- Capability of injecting perturbations into ac and dc systems alike.

To this end, this thesis investigates the feasibility of the cascaded H-bridge (CHB) converter employed

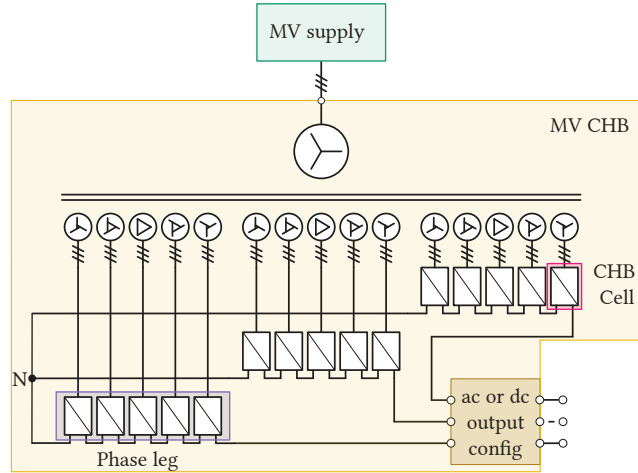


**Fig. 1.9** Cascaded H-bridge topology for high dynamic medium-voltage perturbation injection and impedance measurement. The CHB converter be configured to operate with either an ac or a dc output.

for the purposes of MV impedance measurement and system identification. The CHB topology is well known in the domain of electrical drives, already being present for several decades since it was presented for the first time in [54]. The CHB topology with a phase-shifting multi-winding transformer (MWT) is presented in **Fig. 1.9**. Even though there is a transformer present in the topology it is an input step-down transformer intended for supplying low-voltage power electronics building blocks (PEBBs), which does not limit the output bandwidth. The presence of the MWT enables stacking the low-voltage cells at their output terminals and thus expanding the voltage and current capabilities of the topology. Moreover, the recent development of the fast-switching silicon-carbide (SiC) devices enables the equivalent switching frequency to be pushed further than before which directly increases the controllable output voltage and current bandwidth and allows for higher frequency perturbation injection and impedance measurement. On top of these advantages, through intelligent hardware and control reconfiguration the CHB converter can be employed to serve the needs of both ac and dc system measurements.

## 1.7 Objectives and Contributions of the Thesis

The penetration of RES, the ever larger inclusion of power electronics and the development of medium voltage dc (MVdc) infrastructure will shape the power systems of the future. In order to properly analyze the present and future system components and their characteristics and prevent the power grid instabilities and equipment incompatibility, novel PICs and impedance measurement apparatus is needed.

As stated, the CHB converter provides outstanding output voltage and current capabilities due to the combination of multilevel waveforms and fast-switching devices and remarkable operational flexibility due to the ease of control and hardware reconfiguration and can be used for the needs of both ac and dc impedance measurement. Hence, this thesis focuses on several different topics related to the use of the CHB in the MV impedance measurement domain and its main objectives and contributions can be summarized as:

- Feasibility and suitability of the CHB converter as a solution for the MV impedance measurement

and identification;

- Small-signal modelling of the converter's PEBB;
- Study on the source-affected dynamics of the converter output;
- Investigation of the CHB capabilities when applied for the impedance measurement of both ac and dc system;
- Application of wideband signals in MV impedance identification;
- Hardware and control design, testing and commissioning of the PEBB active input rectifier.

## 1.8 Outline of the Thesis

This work is organized into nine chapters which cover different topics as follows:

**Chapter 2** provides an overview of solutions available in the domain of MV impedance measurement and system identification. All things considered, the equipment for MV impedance measurement is lacking and the need for it is growing. Making use of multilevel topologies and their fast switching frequencies and combining them with wideband injection signals shows a promising path towards the solution of MV impedance measurement problem.

**Chapter 3** treats the open-loop small-signal modelling of the input active rectifier, the active front end (AFE), and the output H-bridge (HB) inverter. The open-loop model of the three-phase AFE is verified in offline simulations. Moreover, the single-phase HB inverter model in the  $dq$ -frame is also verified using wideband signal injection. These results set the base for further closed-loop modelling.

**Chapter 4** continues on track of the **Chapter 3** and covers the control and the closed-loop modelling of the AFE and the HB inverter. The closed-loop model of the AFE is verified through the measurement of its output impedance, required for the study of the output dynamics of the HB inverter. Additionally, the HB inverter model is enhanced with the addition of the modelling of the quadrature-signal generator required for the representation of the HB in the  $dq$ -frame.

**Chapter 5** reveals the source-affected dynamics of the CHB-PEBB, i.e. show the way in which the AFE and HB interact, and shows the influence of the AFE on the HB. The output dynamics characterization is performed through real-time simulations. For the needs of the single-phase measurements and the representation of results in the  $dq$ -frame, two novel methods based on the wideband signal injection are developed and presented.

**Chapter 6** extends the discussion of **Chapter 4** and presents the hardware and control design of the AFE. Moreover, physical characteristics of the multi-winding transformer are used, and it is demonstrated how the leakage inductances of the transformer can be used as the input filter inductors for the PEBBs. This further enables the primary transformer side source synchronization, effectively alleviating the need for an increased number of voltage measurements intended for source synchronization, and saving the computation resources of the control system.

**Chapter 7** gives practical insights of the impedance and admittance measurement of the AFE. Measurements of the input ac admittance in the  $dq$ -frame, as well as the output dc impedance, of the AFE are carried out and experimental results are provided. These results are in essence the first step to experimentally confirming the findings of **Chapter 5**.

**Chapter 8** assesses the flexibility of the CHB as an impedance measurement device suitable for ac and dc applications alike. For the dc application of the CHB three different output configurations are proposed, each with their benefits and downsides. Moreover, a case study is performed where the input and output admittances of an MV-modular multilevel converter (MMC) are measured through simulations carried out in PLECS®.

**Chapter 9** provides the summary of the findings, contributions of this thesis and the future work to be carried out.

## 1.9 List of Publications

Journal papers:

- J1. **M. Petković** and D. Dujić, “Terminal Characteristics Measurements and Analysis of the Three-Phase Active Front End Converter Building Block,” *IET Electric Power Applications*, 2021, *Under review*
- J2. **M. Petković** and D. Dujić, “Hardware-in-the-Loop Characterization of Source-Affected Output Characteristics of Cascaded H-Bridge Converter,” *IEEE Journal of Emerging and Selected Topics in Power Electronics*, 2020
- J3. **M. Petković**, N. Hildebrandt, F. D. Freijedo Fernández, and D. Dujić, “Medium voltage impedance-admittance measurement system based on the cascaded h-bridge multilevel converter,” *Electronics*, vol. 22, no. ARTICLE, pp. 105–113, 2018

Conference papers:

- C1. **M. Petković** and D. Dujić, “Identification of source-affected output characteristics of a four-quadrant cascaded h-bridge converter cell,” in *2020 IEEE International Power Electronics and Motion Control Conference (IPEMC)*, IEEE, 2020, pp. 1–8
- C2. **M. Petković**, S. Milovanović, and D. Dujić, “Flexible medium-voltage perturbation injection converter for ac and dc system identification,” in *2020 IEEE Industrial Electronics Society Conference (IECON)*, IEEE, 2020, pp. 1–8
- C3. **M. Petković**, S. Milovanović, and D. Dujić, “Medium-voltage cascaded h-bridge perturbation injection converter for ac and dc system identification,” in *2020 International Symposium on Industrial Electronics (INDEL)*, IEEE, 2020, pp. 1–8
- C4. **M. Petković** and D. Dujić, “Single-Phase Measurement of the Output Impedance of the Four-Quadrant Cascaded H-Bridge Converter Cell Using Wideband Signals,” in *The 22nd European Conference on Power Electronics and Applications EPE’20 ECCE Europe*, IEEE, 2020
- C5. **M. Petković** and D. Dujić, “Benchmark study on impedance identification methods for grid connected converters,” in *PCIM Europe 2019; International Exhibition and Conference for Power Electronics, Intelligent Motion, Renewable Energy and Energy Management*, VDE, 2019, pp. 1–7
- C6. **M. Petković**, N. Hildebrandt, F. D. Freijedo, and D. Dujić, “Cascaded h-bridge multilevel converter for a high-power medium-voltage impedance-admittance measurement unit,” in *2018 International Symposium on Industrial Electronics (INDEL)*, IEEE, 2018, pp. 1–8
- C7. N. Hildebrandt, **M. Petković**, and D. Dujić, “Evaluation of 1.7 kv sic mosfets for a regenerative cascaded h-bridge multilevel converter cell,” in *2018 IEEE International Conference on Industrial*

*Technology (ICIT)*, IEEE, 2018, pp. 718–723

Other publications:

- O1. A. Christe, I. A. Polanco Lobos, **M. Petković**, M. Utvić, and D. Dujić, “Auxiliary submodule power supply for a medium voltage modular multilevel converter,” *CPSS Transaction on Power Electronics and Applications*, vol. 4, no. ARTICLE, pp. 204–2018, 2019

# Technology Overview for Medium Voltage Impedance and Admittance Identification

*This chapter provides an overview of solutions available for medium voltage impedance and admittance measurement. The solutions in the domain of impedance measurement can effectively be divided into industry-based and academia-, or research-based, solutions. The converter topologies for perturbation injection and perturbation signals are presented in more detail, followed by the proposition of a suitable topology and the signal for the impedance identification in MV domain.*

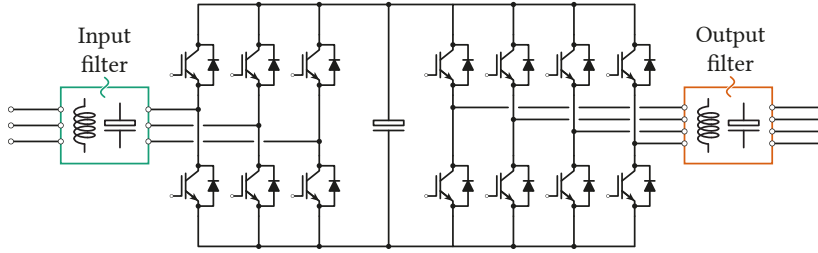
## 2.1 Industry-Based Perturbation Injection Converters

Nowadays, the devices intended for the purposes of perturbation injection into SUTs and impedance measurement usually come in the form of programmable ac sources and grid emulators. One of such devices, used primarily as an LV grid emulator, is the Regatron TC.ACS [45]. The simplified topology employed for the TC.ACS grid emulator is presented in **Fig. 2.1**. It consists of the input three-phase rectifier and output four-leg inverter, as well as the input and output filters. Such an output configuration allows for the operation with a neutral point and can be utilized to emulate a grid, or a secondary of a transformer, where the neutral point is available. The advantage of the TC.ACS is that it can follow external references and can be employed as a three-phase or single-phase ac grid emulator, or even as a dc grid emulator. Due to its high output voltage bandwidth it can also be employed as a perturbation injection converter. Namely, in the nominal voltage output range the TC.ACS has a bandwidth of  $f_{sw}^{nom} = 1$  kHz, whereas in the small-signal range it has a bandwidth of  $f_{bw}^{ss} = 5$  kHz. The small-signal output voltage level in this case is 10 % of the nominal output range, which is compatible with most of the perturbation injection methods where usually from 5 % to 10 % of nominal voltage or current is injected. Overall the TC.ACS is a good solution for perturbation injection and impedance identification in the LV domain. However, due to its maximum output voltage of  $v_{out} = 305$  V, without a step-up output transformer it is not an appropriate solution for MV impedance identification. Moreover, its limited power of  $P_{out} = 50$  kVA is not sufficient for high-power applications. Main features of the Regatron TC.ACS are summarized in **Tab. 2.1**.

Another device similar to the Regatron TC.ACS, i.e. a programmable ac source and a grid emulator, capable of injecting small-signal perturbations is the Egston COMPISO [47]. The simplified topology of the COMPISO is presented in **Fig. 2.2**. The COMPISO system consist of an input grid transformer and an input filter as well as the input rectifier, as was the case with the Regatron TC.ACS. What is particular with the COMPISO converter is its output side inverter, or the COMPISO digital amplifier. The digital amplifier is comprised of a 6-leg interleaved step-up converter with coupled inductors. This arrangement enables the increase of the output equivalent switching frequency up to  $f_{sw,eq} = 125$  kHz.

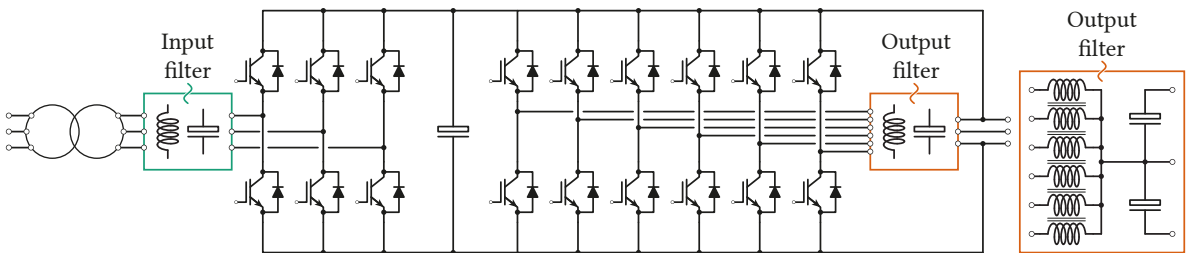
**Tab. 2.1** Regatron TC.ACS parameters

Parameter	Value
Power range	0–50 kVA
Voltage range	0–305 Vrms (L-N)
Current range	$3 \times 0\text{--}72$ A
Nominal output bandwidth	1 kHz
Small-signal bandwidth	5 kHz


**Fig. 2.1** Topology of the Regatron TC.ACS with the input filter, three-phase input active rectifier, dc-link capacitor and a four-leg inverter and the output filter.

Subsequently, with proper output voltage control methods the control bandwidth can be increased as well. The bandwidth of the nominal output voltage is in the range of  $f_{sw}^{nom} = 5$  kHz, while the small-signal range is pushed even higher compared to the Regatron TC.ACS and equals to  $f_{bw}^{ss} = 15$  kHz. The COMPISO output can be configured so that the converter operates with a three-phase or single-phase ac output or with a dc output. When operating with a three-phase output the nominal output voltage of the COMPISO is  $v_{out,3\phi} = 433$  V without the third harmonic injection, while when operating with a single-phase output it is  $v_{out,1\phi} = 500$  V. In the dc output mode, the maximum output voltage is  $v_{out,dc} = 732$  V in unipolar mode. Additionally, the output voltage in the ac output operation mode can be increased with an output transformer to 20 kV. The output power of a single unit presented in **Fig. 2.2** is  $P_{out} = 187.5$  kVA in three-phase mode and  $P_{out} = 200$  kW in dc mode, which on its own does not approach the MV high-power impedance measurement. However, the COMPISO is a highly modular system and multiple digital amplifier unit can be combined to increase its output power up to 7.2 MVA. The parameters of a single digital amplifier are given in **Tab. 2.2**.

There exist many different grid emulators capable of MV and high-power operation, such as the ones presented in [55]–[57], however, their output frequency range is extremely limited for them to be interesting for the impedance measurement applications.


**Fig. 2.2** Topology of the EGSTON Compiso system.



**Tab. 2.2** COMPISO digital amplifier parameters

Parameter	Value
Power range - dc	0–120 kW
Power range - $1\phi$ ac	0–31.5 kVA
Input dc voltage range	40–800 V
Voltage range - dc	0–732 V
Voltage range - $1\phi$ ac	0–250 Vrms
Current range - dc	0–150 A
Current range - ac	0–126 Arms
Nominal output bandwidth	5 kHz
Small-signal bandwidth	15 kHz

## 2.2 Academia-Based Perturbation Injection Converters

Both of the so far presented solutions are industrial ones. In general, there are very few perturbation injection converters developed in academia. Nevertheless, it is definitely worth mentioning the perturbation injection converters presented in [49], [50]. More interestingly this perturbation injection converter is intended for MV grid impedance identification, a problem that this thesis is addressing. This topology is presented in **Fig. 2.3** and is based on parallel connection of 3L-NPC converters. In total, two groups of three parallel connected 3L-NPCs are connected to voltage transformers stepping-up the voltage from  $v_{LV} = 510$  V to  $v_{MV} = 20$  kV.

Each 3L-NPC converter in **Fig. 2.3** is capable of handling a power of  $P_{out} = 480$  kVA with  $i_{out} = 300$  A output current. This topology resulted in successful current injection into a 20 kV grid. In this particular case 30 A was injected from a single 3L-NPC at 5 kHz. However, due to its output current control, i.e. the proportional resonant (PR) control in the  $\alpha\beta$ -frame, the PIC can inject either single-tone components or a very limited number of components at the same time. Moreover, the desire to inject a different frequency set would require the control to be adapted every time. For grid impedance identification this is not the best solution due to the time required to perform this operation and to the ever-changing grid operating conditions and subsequently its impedance.

Another PIC developed in academia is presented in [28]. This topology is presented in **Fig. 2.4** and it is essentially a single-phase CHB converter. However, the PIC presented here is used for the injection into three-phase ac and dc systems for load and source impedance identification. Depending on the output filter configuration the perturbation injection performed can be either series voltage injection or shunt current injection. When performing the series voltage injection the perturbation is injected at an interface between the source and a load. When injecting the current perturbations, the single-phase CHB is connected between two phases, phase  $a$  and phase  $b$ . The switching frequency reported in [28] is  $f_{sw} = 10$  kHz, which combined with the unipolar phase-shifted PWM (PS-PWM) yields an equivalent switching frequency of  $f_{sw,eq} = 60$  kHz. With this configuration the impedances of a 2.8 kV MV system were measured and represented in the  $dq$ -frame. The single-phase excitation of a three-phase systems, however, yields an unbalanced system response in  $abc$ -frame. Subsequently this leads to more sideband harmonics showing up in  $d$  and  $q$  axes when extracting the measurement results.

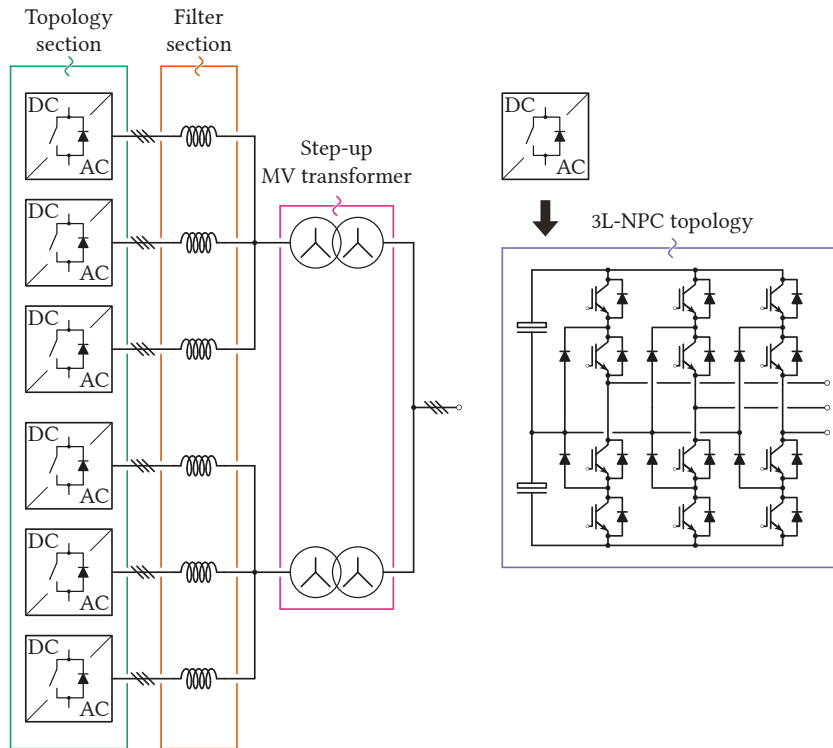


**Fig. 2.3** Topology presented in [49], [50] consisting of two groups of three parallel connected 3L-NPCs, each with their output filter, connected to the step-up voltage transformers.

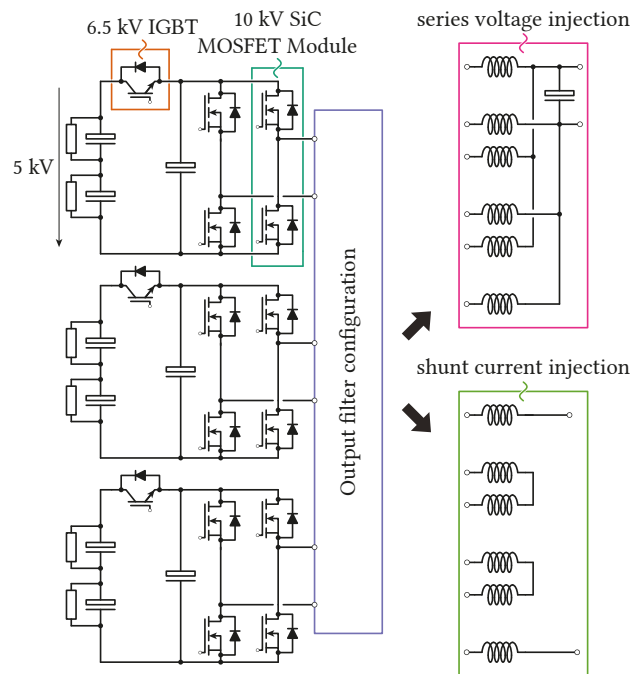


**Fig. 2.4** Transformerless CHB topology consisting of three single-phase HBs connected in parallel or in series for series voltage and shunt current injection with their dedicated output filters.

## 2.3 Perturbation Signals Overview

The measurement of the impedance of a system cannot go without some kind of perturbation signal suitable for perturbation injection. There exist a plethora of signals available and discussing them all would drag the reader from the focus of the thesis. Here, only signals that are successfully used for impedance measurement are mentioned, while the others are available for the reader to consult in [29].

### 2.3.1 Single Tone Sinusoidal Signal

The most simple perturbation signal, and historically the first that started to be used together with switching converters for impedance measurement purposes, is the single tone sinusoidal signal which falls under the category of *narrowband* signals. The ideal sinusoidal signal characterized by its amplitude  $A$ , frequency  $f_p$ , and the initial phase  $\theta_0$  is given as:

$$x_{\sin}(t) = A \sin(2\pi f_p t + \theta_0) \quad (2.1)$$

The advantage of the single tone sinusoidal signal is that in the frequency domain all of the signal energy is concentrated at the injection frequency. Naturally, this gives rise to a good system response at that frequency, better measurements and more precise impedance identification. On the other side, in order to cover a wide range of frequencies, sinusoidal perturbations with different frequencies need to be injected one at a time. Moreover, for the purpose of having a good measurement resolution, the number of frequencies increases additionally, as well. These two requirements combined may lead to long injection and measurement times which is undesirable for rapid impedance measurements of systems such as power grids. An example of a single tone sinusoidal signal and its representation in the frequency domain is given in **Fig. 2.5**.

### 2.3.2 Chirp Signal

In order to overcome the shortcoming of single tone sinusoidal, and narrowband signals in general, the *wideband* signals come into place. As their name suggests, these signals contain more than a single frequency in their spectrum, at the time of the injection. A good example of such a signal is the chirp signal where the frequency increases linearly with time. The chirp signal with linearly increasing frequency has a relatively constant energy in the frequency domain in the frequency range of interest. The frequency of the linear chirp signal is changing linearly and it is defined with the initial frequency  $f_i$ , the terminal frequency  $f_e$  at time  $T$  which is also the time duration of the signal. However, it should

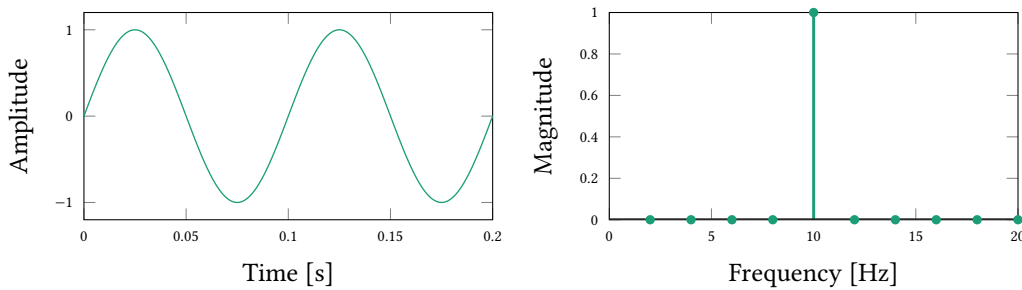


**Fig. 2.5** Single tone sinusoidal signal with  $A = 1$ ,  $f_p = 10$  Hz and  $\theta_0 = 0$  rad.

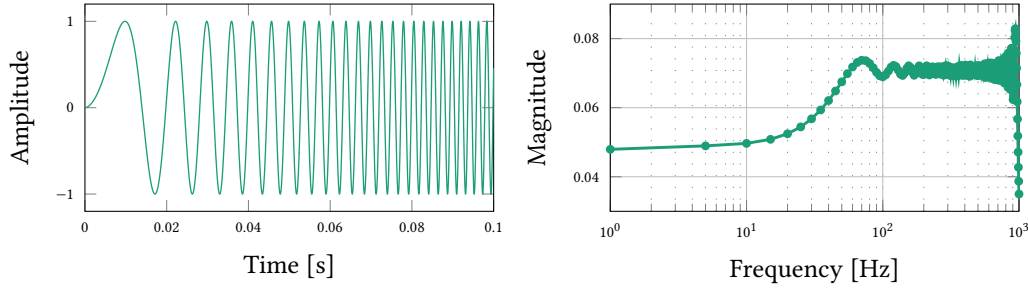


**Fig. 2.6** An example of a chirp signal with  $f_i = 10$  Hz,  $f_e = 1$  kHz and  $T = 0.1$  s.

be noted that the energy of the signal in the frequency domain depends on the terminal frequency of the signal. Practically, this means that if a chirp with too large terminal frequency is injected its energy might drop below the noise levels and might become indiscernible from the noise itself making both the measurements and the signal themselves useless. The instantaneous frequency at an arbitrary time  $t$  is given as:

$$f(t) = f_i + \frac{f_e - f_i}{T}t \quad (2.2)$$

The phase of the chirp signal is given as the integral of the frequency for an arbitrary initial phase  $\theta_0$  and equals:

$$\theta(t) = 2\pi \int_0^t \left( f_i + \frac{f_e - f_i}{T}\tau \right) d\tau + \theta_0 = 2\pi \left( f_i t + \frac{f_e - f_i}{2T}t^2 \right) + \theta_0 \quad (2.3)$$

Finally the linear chirp signal can be described as:

$$x_{\text{chirp}}(t) = \sin \left[ 2\pi \left( f_i t + \frac{f_e - f_i}{2T}t^2 \right) + \theta_0 \right] \quad (2.4)$$

A representation of the chirp signal in time and frequency domain is given in **Fig. 2.6**.

### 2.3.3 Multi-Tone Signal

Another signal falling under the wideband category is the multi-tone signal. As its name suggests it contains multiple frequencies over a period of time. Thus, having a sufficient number of tones and making the multi-tone signal resolution good enough the injection and measurement times can be drastically reduced. When choosing the frequency components of the multi-tone signal, each tone should have the same amplitude. The trade-off in choosing the amplitude comes from the fact that small enough amplitude should be chosen in order not to perturb the system in a way that it would compromise its normal operation, and on the other hand it should be chosen large enough in order to have the energy of the signal strong enough in the frequency domain. The second requirement is due to the fact that the overall energy of the signal decreases linearly with the number of tones it contains. When it comes to choice of frequency, the frequencies have to be selected appropriately to prevent overlapping of responses generated by different tones. The multi-tone signal can be expressed

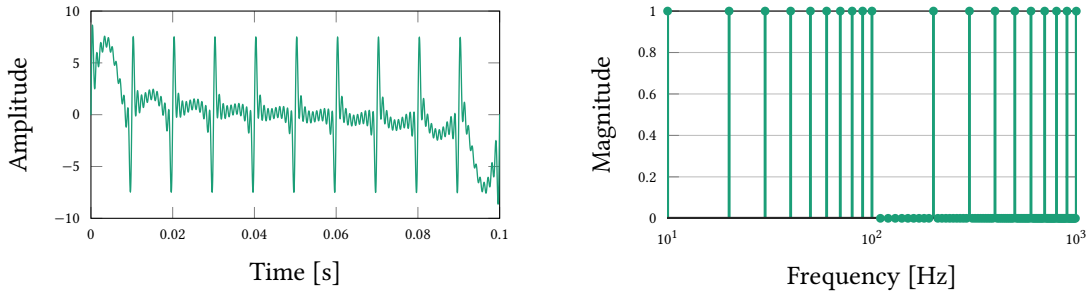


**Fig. 2.7** Multi-tone signal in time and frequency domain. Simultaneously 20 frequency components are present in the signal, ranging from 10 Hz to 1 kHz.

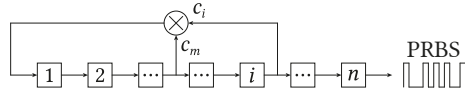


**Fig. 2.8**  $n$ -bit shift-register with XOR feedback for PRBS generation.

mathematically as:

$$\begin{aligned}
 x_{\text{mt}}(t) &= \sum_{n=1}^N \sin(2\pi f_i + \theta_{0i}) \\
 f_i &= f_0 + i\Delta f \\
 \theta_{0i} &= \frac{\pi}{N}(i-1)^2
 \end{aligned} \tag{2.5}$$

The multi-tone signal in time and in frequency domain is presented in **Fig. 2.7**.

### 2.3.4 Pseudo-Random Binary Sequence Signal

A signal that has recently gained a lot of attention and has been used extensively for impedance measurement and system identification is the PRBS signal. Namely, the PRBS signal is used for grid impedance identification and grid connected converter input admittance identification in LV systems. However, the application of the PRBS in the MV domain is still not developed well enough. The PRBS signal itself is a wideband signal based on a sequence of length  $N$ . The most commonly used pseudo-random signals are known as the maximum-length binary sequence (MLBS). Such sequences exist for  $N = 2^n - 1$ , where  $n$  is an integer. The reason for their popularity is that they can be generated using feedback shift-register circuits, as shown in **Fig. 2.8**. Essentially, the PRBS signal is a stream of pseudo-random pulses. Depending on the sought for impedance identification range and the resolution of the PRBS signal there exist two degrees of freedom. First one is the generation frequency of the signal  $f_{\text{gen}}$  which also naturally depends on the output bandwidth of the PIC. The other degree of freedom is the length of the signal,  $N$ . The resolution of the PRBS signal is related to its generation frequency and its length as:

$$f_r = \frac{f_{\text{gen}}}{N} \tag{2.6}$$

An example of a PRBS signal in the time and frequency domain is presented in **Fig. 2.9**. The PRBS signal has multiple advantages. Since it is a wideband signal it contains multiple frequency at the

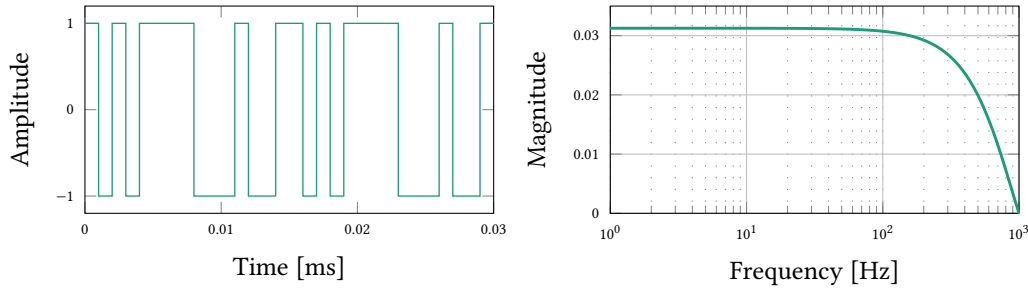


**Fig. 2.9** Wideband PRBS signal created at generation frequency of  $f_{\text{gen}} = 1 \text{ kHz}$ .

same time and the energy of the signal stays fairly constant over a wide range after which it falls to zero at its generation frequency. About one-half to two-thirds of the frequency range are useful for the perturbation injection and impedance measurement. Moreover, since the perturbation injection of a single period generally last up to 1 second, multiple perturbation can be injected sequentially. This leads to the possibility of measuring multiple periods and performing an average over these periods. Moreover, by injecting multiple periods the amplitude of the perturbation can be reduced which leads to a good trade-off between measurement accuracy and the effects on the quality of voltage and current [58].

### 2.3.5 CHB Converter Considerations for Medium Voltage Perturbation Injection and Impedance Measurement

Recalling the presented solutions for MV impedance measurement and system identification several requirements can be set for further development of a PICs. One of the requirements is naturally the sufficient output voltage level which can be achieved by using medium voltage switching devices, using a step-up transformer or by using some of the multilevel topologies such as the MMC, CHB, neutral point clamped (NPC) or the multilevel flying-capacitor inverters. The downside of medium voltage switching devices is that they are limited in their switching capabilities, i.e. the switching frequency, which in turn would limit the closed-loop control bandwidth. As discussed earlier the usage of step-up transformers should be avoided due to the limitations that they present through their leakage inductances. Finally, multilevel topologies offer themselves as a viable solution for having a medium voltage output.

Another requirement stems from the perturbation signal choice. Effectively, the wideband signals are preferred over narrowband signals and preferably the PRBS presents itself as a potentially good solution that would yield a good trade-off between its frequency content, ease of implementation and the rapidity of injection and measurements. Certainly, to profit the most from the PRBS, its generation frequency should be as high as possible which leads to the issue of closed-loop control bandwidth. High closed-loop control bandwidth requires high switching frequencies which can of course be attained with multilevel structures. However, there exists a practical limitation on the size of the topology and the number of output levels. Thus, fast switching devices in combination with multilevel structure are desirable. Fortunately, the development of fast switching SiC and gallium-nitride (GaN) has been on the rise recently [59]–[61]. However, the GaN devices are as well an impractical solution for MV domain due to their limitations in voltage and current. Therefore, the SiC MOSFET switching devices in combination with a multilevel topology are an ideal solution for

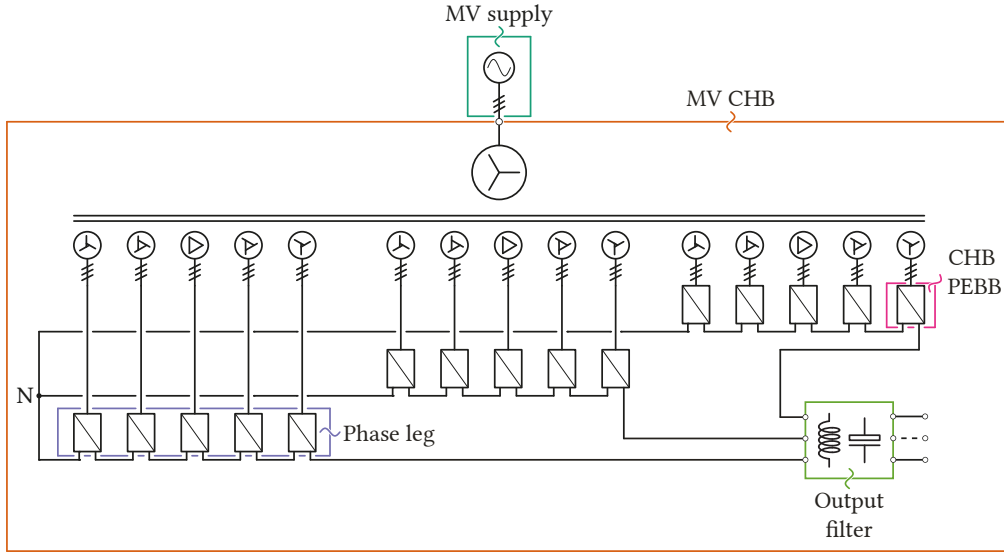


**Fig. 2.10** CHB topology consisting of a multi-winding 6.3 kV transformer with 15 phase-shifted 710 V secondaries and three groups of five PEBB connected in series to create three-phase MV output and a dedicated output filter.

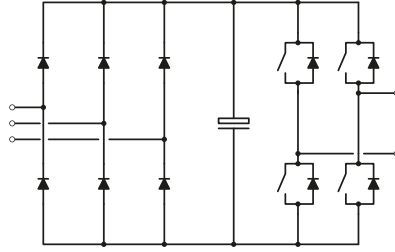


**Fig. 2.11** The PEBB of the original CHB topology with a passive diode front end (DFE) and an HB inverter.

the domain of MV impedance measurement and system identification.

A promising multilevel topology that could be employed for the purpose of MV perturbation injection and impedance measurement is the CHB topology, presented in **Fig. 2.10**. In its original form presented in [54] the CHB topology including a MWT consists of a passive DFE and an HB inverter, presented in **Fig. 2.11**. The downsides of this solution are the operation in two quadrants and the fact that the maximum output voltage per HB inverter is set by the DFE. On the other side, replacing the passive DFE by a three-phase AFE enables four-quadrant operation and boosting the dc-link voltage. Moreover, the dc-link voltage level becomes controllable leading to a more flexible and higher voltage output on the inverter side of the CHB. This is however true in the case where the voltage level of the transformer is not altered. A PEBB of the CHB with an Si-IGBT based three-phase AFE and a SiC-MOSFET HB inverter is presented in **Fig. 2.12**.

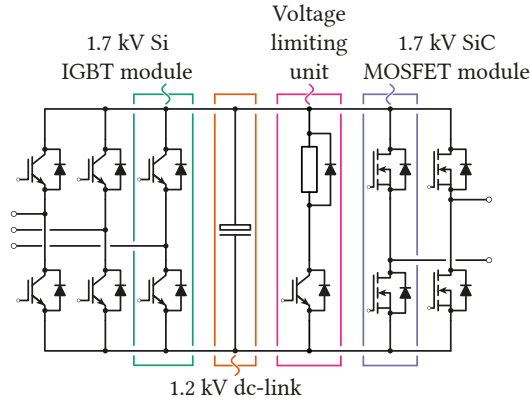


**Fig. 2.12** CHB PEBB consisting of a three-phase active rectifier, the AFE based on silicon (Si) IGBTs, a dc-link serving as an energy buffer, a voltage limiting unit and a single-phase HB inverter based on SiC MOSFETS.

## 2.4 Summary

This chapter has provided an overview of the technologies available for the MV impedance and admittance measurement and system identification, in general. The industry-based solutions generally rely on the usage of grid emulators for the purposes of impedance measurement, when the output dynamics of these grid emulators is a valid and sensible choice. On the other hand, the academia-based converters usually rely on the well-established topologies for the MV applications, and in conjunction with smart closed-loop control they could be a viable solution for the impedance and admittance measurement. Moreover, to fully benefit from efficient closed-loop control methods the choice of the perturbation signal has a high degree of importance and the wideband signals present themselves as an ideal choice. However, what is often lacking is a proper analysis and modelling of building blocks of PICs and this thesis seeks to bridge this gap and lay a foundation for future analysis of PICs as a special type of power electronics devices. Moreover, the impedance measurement devices put forward present either very limited or no flexibility at all, in the sense that they cannot be reconfigured to serve the purposes of both ac and dc systems. Thus, the work presented in the following chapters also focuses on solving the issue of lack of flexibility in impedance measurement domain. Finally, this thesis serves as a foundation for the further development of the CHB converter as a PIC.



# 3

## Power Electronics Building Block Open Loop Modelling

*This chapter presents the open-loop modelling of a single power electronics building block of the cascaded H-bridge converter. The modelling separates the active-front-end active rectifier unit and the H-bridge inverter unit and presents them as independent entities with their respective inputs and outputs and makes evident their dynamic models with different transfer functions relating the input and output variables. The chapter serves as a basis for the further control design and closed-loop modelling and load/source affected dynamics modelling.*

### 3.1 Cascaded H-Bridge Converter Power Electronics Building Block

A single, regenerative, PEBB of a CHB converter is presented in **Fig. 3.1**. When the economical aspects of CHB converter and the possibility to recover power become interesting, or when it is employed as a high-dynamics grid emulator as is the case in [62], the simple diode front-ends from **Fig. 2.11** can be replaced or extended by Si-IGBT based AFEs [63]–[65]. The AFE is one side interfaced to a three phase grid, whose impedance is at the same time the input filter for the AFE, and to a dc-link capacitor, serving as an energy buffer, on the other side.

On the output side, a SiC-MOSFET based single phase inverter or the HB inverter is present and is considered for the overall concept. High switching frequencies at which the SiC devices are able to operate in combination with properly chosen modulations strategies are able to push the output waveform frequencies higher than was the case before [28]. To filter out the switched voltage waveforms, an LC-type output filter is used, which is further connected to a certain SUT (e.g. another converter or a grid). The nature of the load is irrelevant here and it can be considered for the modelling purposes to be a controlled current source. In a practical case, multiple HBs would be connected at their outputs, but for the sake of modelling only one, equivalent, HB inverter is presented in this chapter. In order to facilitate the control and modelling one can always apply the "divide and conquer" strategy and treat and model the input and the output separately. Following sections deal with dynamic modelling of open-loop AFE and HB.

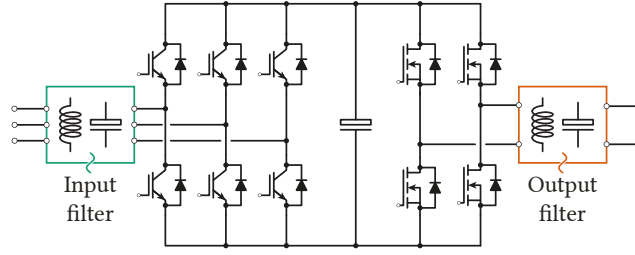


**Fig. 3.1** Regenerative PEBB of the CHB converter.

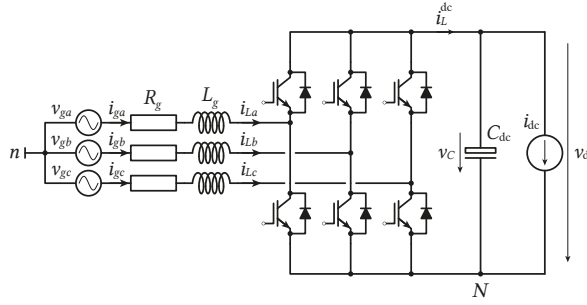


**Fig. 3.2** Ideal three-phase grid-connected current-fed AFE.

### 3.2 Active Front End Modelling

**Fig. 3.2** shows an ideal three-phase grid connected AFE. The following developments in the text give the state-space modelling of the AFE which serves as a base to understand further dynamic interactions that surround the operation of the AFE. The input variables are considered to be the three-phase grid voltages,  $v_{ga}$ ,  $v_{gb}$ ,  $v_{gc}$ , and the dc-link output current  $i_{dc}$ . The state variables are the inductor currents,  $i_{La}$ ,  $i_{Lb}$ ,  $i_{Lc}$ . Grid currents,  $i_{ga}$ ,  $i_{gb}$ ,  $i_{gc}$ , and the dc-link output voltage  $v_{dc}$  are considered to be the output variables. The control variables are the switch duty cycles,  $d_a$ ,  $d_b$ ,  $d_c$ . These duty cycles are considered to be the duty cycles of the upper side switches and the dead-time non-linear effects are not considered in the modelling. There exist eight possible switching states of the AFE (cf. **Tab. 3.1**), where  $s_x$  and  $\bar{s}_x$  are the upper and lower switches in phases  $a$ ,  $b$  and  $c$ , respectively. Current directions out of the grid and towards the current source are considered positive. The IGBT on-state voltage drop and losses are not modelled, thus there is no resistance  $R_{CE}$  present, although it can be introduced easily.

To model the AFE, one needs to formulate the time-averaged derivatives of state variables and the time-averaged values of the output variables and each phase leg of the AFE is considered separately. It is assumed that the inductors and inductor parasitic resistances are identical, i.e.  $L_{ga,b,c} = L_g$  and  $R_{ga,b,c} = R_g$ . For readability purposes,  $L_g$  and  $R_g$  are denoted simply as  $L$  and  $R$ . For modelling, two subsets of equations are considered, one during the on-time of the switch and one during the off-time.

During the on-time, following the Kirchhoff's voltage law (KVL) voltages are given by:

$$\begin{aligned} v_{La} &= v_{ga} - v_{Ra} - v_{dc} + v_{nN} \\ v_{Lb} &= v_{gb} - v_{Rb} - v_{dc} + v_{nN} \\ v_{Lc} &= v_{gc} - v_{Rc} - v_{dc} + v_{nN} \\ v_{dc} &= v_C \end{aligned} \tag{3.1}$$

**Tab. 3.1** AFE switching states

$s$	$s_a$	$s_b$	$s_c$	$\overline{s_a}$	$\overline{s_b}$	$\overline{s_c}$
0	0	0	0	1	1	1
1	1	0	0	0	1	1
2	1	1	0	0	0	1
3	0	1	0	1	0	1
4	0	1	1	1	0	0
5	0	0	1	1	1	0
6	1	0	1	0	1	0
7	1	1	1	0	0	0

where  $v_L$  and  $v_R$  are the voltage drops caused by the current flowing in, our out of, the AFE and  $v_{Rx} = Ri_{Lx}$ , where  $x$  can be each of the phases  $a$ ,  $b$  or  $c$ . The  $v_{nN}$  is the voltage between the grid neutral point and dc-link negative point voltage.

Following the Kirchhoff's current law (KCL), currents in the AFE are given by:

$$\begin{aligned}
 i_L^{\text{dc}} &= i_{La} + i_{Lb} + i_{Lc} \\
 i_C^{\text{dc}} &= i_L^{\text{dc}} - i_{\text{dc}} \\
 i_{ga} &= i_{La} \\
 i_{gb} &= i_{Lb} \\
 i_{gc} &= i_{Lc}
 \end{aligned} \tag{3.2}$$

Where  $i_L^{\text{dc}}$  is the current flowing on the dc-side of the AFE. Following the same laws the off-time voltages can be given as:

$$\begin{aligned}
 v_{La} &= v_{ga} - v_{Ra} + v_{nN} \\
 v_{Lb} &= v_{gb} - v_{Rb} + v_{nN} \\
 v_{Lc} &= v_{gc} - v_{Rc} + v_{nN} \\
 v_{\text{dc}} &= v_C
 \end{aligned} \tag{3.3}$$

The same is applied to the AFE currents, which are given by:

$$\begin{aligned}
 i_L^{\text{dc}} &= 0 \\
 i_C^{\text{dc}} &= -i_{\text{dc}} \\
 i_{ga} &= i_{La} \\
 i_{gb} &= i_{Lb} \\
 i_{gc} &= i_{Lc}
 \end{aligned} \tag{3.4}$$

To obtain the time-averaged values of equations above, one has to multiply the equations (3.1) to (3.4) by on-time and off-time duty cycles  $d_{a,b,c}^{\text{on}}$  and  $d_{a,b,c}^{\text{off}}$ , respectively, and sum them together. For further

developments  $d_{a,b,c}^{\text{off}} = 1 - d_{a,b,c}^{\text{on}}$  and  $d_{a,b,c}^{\text{on}}$  is denoted only as  $d_{a,b,c}$ . This yields:

$$\begin{aligned}
 \langle v_{La} \rangle &= \langle v_{ga} \rangle - \langle v_{Ra} \rangle - d_a \langle v_{dc} \rangle + \langle v_{nN} \rangle \\
 \langle v_{Lb} \rangle &= \langle v_{gb} \rangle - \langle v_{Rb} \rangle - d_b \langle v_{dc} \rangle + \langle v_{nN} \rangle \\
 \langle v_{Lc} \rangle &= \langle v_{gc} \rangle - \langle v_{Rc} \rangle - d_c \langle v_{dc} \rangle + \langle v_{nN} \rangle \\
 \langle i_L^{\text{dc}} \rangle &= d_a \langle i_{La} \rangle + d_b \langle i_{Lb} \rangle + d_c \langle i_{Lc} \rangle \\
 \langle i_C^{\text{dc}} \rangle &= \langle i_L^{\text{dc}} \rangle - \langle i_{dc} \rangle
 \end{aligned} \tag{3.5}$$

$$\begin{aligned}
 \langle i_{ga} \rangle &= \langle i_{La} \rangle \\
 \langle i_{gb} \rangle &= \langle i_{Lb} \rangle \\
 \langle i_{gc} \rangle &= \langle i_{Lc} \rangle \\
 \langle v_{dc} \rangle &= \langle v_C \rangle
 \end{aligned}$$

By applying well-known equations presented in **Sec. A.1**, more specifically the equation (A.5), that relate current flowing through an inductor to voltage established over it and voltage established over a capacitor to current flowing through one can obtain following equations:

$$\begin{aligned}
 \frac{d\langle i_{ga} \rangle}{dt} &= \frac{\langle v_{ga} \rangle - \langle v_{Ra} \rangle - d_a \langle v_{dc} \rangle + \langle v_{nN} \rangle}{L} \\
 \frac{d\langle i_{gb} \rangle}{dt} &= \frac{\langle v_{gb} \rangle - \langle v_{Rb} \rangle - d_b \langle v_{dc} \rangle + \langle v_{nN} \rangle}{L} \\
 \frac{d\langle i_{gc} \rangle}{dt} &= \frac{\langle v_{gc} \rangle - \langle v_{Rc} \rangle - d_c \langle v_{dc} \rangle + \langle v_{nN} \rangle}{L} \\
 \frac{d\langle v_{dc} \rangle}{dt} &= \frac{d_a \langle i_{La} \rangle + d_b \langle i_{Lb} \rangle + d_c \langle i_{Lc} \rangle - \langle i_{dc} \rangle}{C}
 \end{aligned} \tag{3.6}$$

$$\begin{aligned}
 \langle i_{ga} \rangle &= \langle i_{La} \rangle \\
 \langle i_{gb} \rangle &= \langle i_{Lb} \rangle \\
 \langle i_{gc} \rangle &= \langle i_{Lc} \rangle \\
 \langle v_{dc} \rangle &= \langle v_C \rangle
 \end{aligned} \tag{3.7}$$

The equations (3.6) and (3.7) can be represented in their vectorial or matrix form for easier transformation from  $abc$ - to  $\alpha\beta$ - or  $dq$ -frame:

$$\frac{d}{dt} \begin{bmatrix} \langle i_{ga} \rangle \\ \langle i_{gb} \rangle \\ \langle i_{gc} \rangle \end{bmatrix} = -\frac{1}{L} \begin{bmatrix} d_a \\ d_b \\ d_c \end{bmatrix} \langle v_{dc} \rangle - \frac{1}{L} \begin{bmatrix} \langle v_{Ra} \rangle \\ \langle v_{Rb} \rangle \\ \langle v_{Rc} \rangle \end{bmatrix} + \frac{1}{L} \begin{bmatrix} \langle v_{ga} \rangle \\ \langle v_{gb} \rangle \\ \langle v_{gc} \rangle \end{bmatrix} + \frac{1}{L} \begin{bmatrix} \langle v_{nN} \rangle \\ \langle v_{nN} \rangle \\ \langle v_{nN} \rangle \end{bmatrix} \tag{3.8}$$

$$\frac{d\langle v_{dc} \rangle}{dt} = \frac{1}{C} \begin{bmatrix} d_a \\ d_b \\ d_c \end{bmatrix} \begin{bmatrix} \langle i_{ga} \rangle \\ \langle i_{gb} \rangle \\ \langle i_{gc} \rangle \end{bmatrix} - \frac{\langle v_{dc} \rangle}{C} \tag{3.9}$$

When the grid voltages and currents are balanced, the common-mode voltage and current components are not present.

To avoid cluttering the chapter, the  $abc$ - to  $\alpha\beta$ -frame (Clarke)  $\alpha\beta$ - to  $dq$ -frame (Parke) transformations are presented in **Sec. A.2**. Performing the transformations on derivatives is also possible, more specifically on inductor current derivatives, as follows:

$$\frac{d}{dt} T \begin{bmatrix} \langle i_{ga} \rangle \\ \langle i_{gb} \rangle \\ \langle i_{gc} \rangle \end{bmatrix} = -\frac{1}{L} T \begin{bmatrix} d_a \\ d_b \\ d_c \end{bmatrix} \langle v_{dc} \rangle - \frac{1}{L} T \begin{bmatrix} \langle v_{Ra} \rangle \\ \langle v_{Rb} \rangle \\ \langle v_{Rc} \rangle \end{bmatrix} + \frac{1}{L} T \begin{bmatrix} \langle v_{ga} \rangle \\ \langle v_{gb} \rangle \\ \langle v_{gc} \rangle \end{bmatrix} + \frac{1}{L} T \begin{bmatrix} \langle v_{nN} \rangle \\ \langle v_{nN} \rangle \\ \langle v_{nN} \rangle \end{bmatrix} \quad (3.10)$$

$$\frac{d}{dt} \langle \mathbf{i}_g^{\alpha\beta} \rangle = -\frac{\mathbf{d}^{\alpha\beta} \langle v_{dc} \rangle}{L} - \frac{\langle \mathbf{v}_R^{\alpha\beta} \rangle}{L} + \frac{\langle \mathbf{v}_g^{\alpha\beta} \rangle}{L}$$

Transforming the capacitor voltage requires considering the product of two space vectors, one in  $\alpha$ - and one in  $\beta$ -axis:

$$\frac{d\langle v_{dc} \rangle}{dt} = \frac{3}{2K^2} \frac{d_\alpha \langle i_g \rangle + d_\beta \langle i_g \rangle}{C} - \frac{\langle i_{dc} \rangle}{C} \quad (3.11)$$

$$\frac{d\langle v_{dc} \rangle}{dt} = \frac{3}{2K^2} \frac{\Re \left( \langle \mathbf{d}^{\alpha\beta} \rangle \langle \mathbf{i}_g^{\alpha\beta} \rangle^* \right)}{C} - \frac{\langle i_{dc} \rangle}{C}$$

To transform the variables from  $\alpha\beta$ - to  $dq$ -frame one has to multiply the previous lines with  $e^{-j\omega_g t}$ , where  $\omega_g$  is the grid angular frequency. This yields replacements in the form of  $\underline{x}^{\alpha\beta} = \underline{x}^{dq} e^{j\omega_g t}$ . Thus, the averaged state-space model in  $dq$ -frame can be given as:

$$\frac{d}{dt} \left( \langle \mathbf{i}_g^{dq} \rangle e^{j\omega_g t} \right) = -\frac{\mathbf{d}^{dq} \langle v_{dc} \rangle e^{j\omega_g t}}{L} - \frac{\langle \mathbf{v}_R^{dq} \rangle e^{j\omega_g t}}{L} + \frac{\langle \mathbf{v}_g^{dq} \rangle e^{j\omega_g t}}{L} \quad (3.12)$$

$$\frac{d\langle v_{dc} \rangle}{dt} = \frac{3}{2K^2} \frac{d_d \langle i_{gd} \rangle + d_q \langle i_{gq} \rangle}{C} - \frac{\langle i_{dc} \rangle}{C}$$

Continuing with the time derivation:

$$\frac{d\langle \mathbf{i}_g^{dq} \rangle}{dt} = -j\omega_g \langle \mathbf{i}_g^{dq} \rangle - \frac{\mathbf{d}^{dq} \langle v_{dc} \rangle}{L} - \frac{\langle \mathbf{v}_R^{dq} \rangle}{L} + \frac{\langle \mathbf{v}_g^{dq} \rangle}{L} \quad (3.13)$$

$$\frac{d\langle v_{dc} \rangle}{dt} = \frac{3}{2K^2} \frac{d_d \langle i_{gd} \rangle + d_q \langle i_{gq} \rangle}{C} - \frac{\langle i_{dc} \rangle}{C}$$

Separating the previous two expressions into their real and imaginary counterparts,  $d$ - and  $q$ -axis, the averaged state-space model in  $dq$ -frame is given as:

$$\frac{d\langle i_{gd} \rangle}{dt} = \omega_g \langle i_{gq} \rangle - \frac{d_d \langle v_{dc} \rangle}{L} - \frac{R}{L} \langle i_{gd} \rangle + \frac{\langle v_{gd} \rangle}{L}$$

$$\frac{d\langle i_{gq} \rangle}{dt} = -\omega_g \langle i_{gd} \rangle - \frac{d_q \langle v_{dc} \rangle}{L} - \frac{R}{L} \langle i_{gq} \rangle + \frac{\langle v_{gq} \rangle}{L} \quad (3.14)$$

$$\frac{d\langle v_{dc} \rangle}{dt} = \frac{3}{2K^2} \frac{d_d \langle i_{gd} \rangle + d_q \langle i_{gq} \rangle}{C} - \frac{\langle i_{dc} \rangle}{C}$$

The steady-state operating point of the AFE can be obtained by setting the derivatives to zero in (3.14) and considering Park transformation as amplitude invariant, i.e.  $K = 1$ , which yields:

$$\omega_g L I_{gq} - D_d V_{dc} - R I_{gd} + V_{gd} = 0 \quad (3.15)$$

$$-\omega_g L I_{gd} - D_q V_{dc} - R I_{gq} + V_{gq} = 0 \quad (3.16)$$

$$\frac{3}{2} (D_d I_{gd} + D_q I_{gq}) - I_{dc} = 0 \quad (3.17)$$

Solving equations (3.15) to (3.17) gives the steady state values of  $D_q$ ,  $I_{gd}$  and  $D_d$ :

$$D_q = \frac{V_{gq} - I_{gq} R - \omega_g L I_{gd}}{V_{dc}} \quad (3.18)$$

$$I_{gd} = \frac{I_{gq}^2 R + \frac{2}{3} I_{dc} V_{dc} - I_{gq} V_{gq}}{D_d V_{dc} - \omega_g L I_{gq}} \quad (3.19)$$

$$D_d^2 V_{dc}^2 - D_d V_{dc} (V_{gd} + 2\omega_g L I_{gq}) + \left( I_{gq}^2 (R^2 + \omega_g^2 L^2) + \frac{2}{3} V_{dc} I_{dc} R - I_{gq} V_{gq} R + \omega_g L I_{gq} V_{gd} \right) = 0 \quad (3.20)$$

The equation (3.20) is a quadratic one and it has two solutions for  $D_d$ , but as usual, only one that makes sense is chosen afterwards. For a balanced grid and a unity power factor,  $q$ -axis voltage and current are set to zero, i.e.  $V_{gq} = 0$  and  $I_{gq} = 0$ , respectively. With this condition, equations (3.18) to (3.20) can be solved and different elements such as dc-link voltage, converter duty cycles or inductor current can be determined as follows:

$$D_d = \frac{V_{gd} + \sqrt{V_{gd}^2 - (8/3) V_{dc} I_{dc} R}}{2 V_{dc}} \quad (3.21)$$

$$I_{gd} = \frac{2}{3} \frac{I_{dc}}{D_d} \quad (3.22)$$

$$D_q = -\frac{\omega_g L I_{gd}}{V_{dc}} \quad (3.23)$$

Equations (3.21) to (3.23) represent an open-loop steady-state operating point for a three-phase grid connected current-fed AFE.

### 3.2.1 Active Front End State-Space Model and Open-Loop Dynamics

The state-space model in (3.14) is non-linear and as such does not provide much information on a first sight. Naturally, one would sought to linearise the model. Linearization techniques presented in **Sec. A.1** can be applied which yields the model in the equation (3.24) where a tilde above a variable denotes a time-varying small-signal variable.

$$\begin{aligned} \frac{d\tilde{i}_{gd}}{dt} &= \omega_g \tilde{i}_{gq} - \frac{D_d}{L} \tilde{v}_{dc} - \frac{V_{dc}}{L} \tilde{d}_d - \frac{R}{L} \tilde{i}_{gd} + \frac{1}{L} \tilde{v}_{gd} \\ \frac{d\tilde{i}_{gq}}{dt} &= -\omega_g \tilde{i}_{gd} - \frac{D_q}{L} \tilde{v}_{dc} - \frac{V_{dc}}{L} \tilde{d}_q - \frac{R}{L} \tilde{i}_{gq} + \frac{1}{L} \tilde{v}_{gq} \\ \frac{d\tilde{v}_{dc}}{dt} &= \frac{3}{2} \frac{d_d}{C} \tilde{i}_{gd} + \frac{3}{2} \frac{d_q}{C} \tilde{i}_{gq} - \frac{1}{C} \tilde{i}_{dc} + \frac{3}{2} \frac{i_{gd}}{C} \tilde{d}_d + \frac{3}{2} \frac{i_{gq}}{C} \tilde{d}_q \end{aligned} \quad (3.24)$$

The state-space model in time domain (superscript  $t$ ) can be represented in a matrix form:

$$\begin{bmatrix} \frac{d\tilde{i}_{gd}}{dt} \\ \frac{d\tilde{i}_{gq}}{dt} \\ \frac{d\tilde{v}_{dc}}{dt} \end{bmatrix}^t = \begin{bmatrix} -\frac{R}{L} & \omega_g & -\frac{D_d}{L} \\ -\omega_g & -\frac{R}{L} & -\frac{D_q}{L} \\ \frac{3}{2}\frac{D_d}{C} & \frac{3}{2}\frac{D_q}{C} & 0 \end{bmatrix} \begin{bmatrix} \tilde{i}_{gd} \\ \tilde{i}_{gq} \\ \tilde{v}_{dc} \end{bmatrix}^t + \begin{bmatrix} \frac{1}{L} & 0 & 0 & -\frac{V_{dc}}{L} & 0 \\ 0 & \frac{1}{L} & 0 & 0 & -\frac{V_{dc}}{L} \\ 0 & 0 & -\frac{1}{C} & \frac{3}{2}\frac{I_{gd}}{C} & \frac{3}{2}\frac{I_{gq}}{C} \end{bmatrix} \begin{bmatrix} \tilde{v}_{gd} \\ \tilde{v}_{gq} \\ \tilde{i}_{dc} \\ \tilde{d}_d \\ \tilde{d}_q \end{bmatrix}^t \quad (3.25)$$

The output variables are given by:

$$\begin{bmatrix} \tilde{i}_{gd} \\ \tilde{i}_{gq} \\ \tilde{v}_{dc} \end{bmatrix}^t = \begin{bmatrix} 1 & 0 & 0 \\ 0 & 1 & 0 \\ 0 & 0 & 1 \end{bmatrix} \begin{bmatrix} \tilde{i}_{gd} \\ \tilde{i}_{gq} \\ \tilde{v}_{dc} \end{bmatrix}^t + \begin{bmatrix} 0 & 0 & 0 & 0 & 0 \\ 0 & 0 & 0 & 0 & 0 \\ 0 & 0 & 0 & 0 & 0 \end{bmatrix} \begin{bmatrix} \tilde{v}_{gd} \\ \tilde{v}_{gq} \\ \tilde{i}_{dc} \\ \tilde{d}_d \\ \tilde{d}_q \end{bmatrix}^t \quad (3.26)$$

The same equation in matrix form can be represented in s-domain by applying the Laplace transform and replacing the time derivative  $d/dt$  by the operator  $s$ :

$$s \begin{bmatrix} \tilde{i}_{gd} \\ \tilde{i}_{gq} \\ \tilde{v}_{dc} \end{bmatrix}^s = \underbrace{\begin{bmatrix} -\frac{R}{L} & \omega_g & -\frac{D_d}{L} \\ -\omega_g & -\frac{R}{L} & -\frac{D_q}{L} \\ \frac{3}{2}\frac{D_d}{C} & \frac{3}{2}\frac{D_q}{C} & 0 \end{bmatrix}}_{\mathbf{A}} \begin{bmatrix} \tilde{i}_{gd} \\ \tilde{i}_{gq} \\ \tilde{v}_{dc} \end{bmatrix}^s + \underbrace{\begin{bmatrix} \frac{1}{L} & 0 & 0 & -\frac{V_{dc}}{L} & 0 \\ 0 & \frac{1}{L} & 0 & 0 & -\frac{V_{dc}}{L} \\ 0 & 0 & -\frac{1}{C} & \frac{3}{2}\frac{I_{gd}}{C} & \frac{3}{2}\frac{I_{gq}}{C} \end{bmatrix}}_{\mathbf{B}} \begin{bmatrix} \tilde{v}_{gd} \\ \tilde{v}_{gq} \\ \tilde{i}_{dc} \\ \tilde{d}_d \\ \tilde{d}_q \end{bmatrix}^s \quad (3.27)$$

The output variables are given by:

$$\begin{bmatrix} \tilde{i}_{gd} \\ \tilde{i}_{gq} \\ \tilde{v}_{dc} \end{bmatrix}^s = \underbrace{\begin{bmatrix} 1 & 0 & 0 \\ 0 & 1 & 0 \\ 0 & 0 & 1 \end{bmatrix}}_{\mathbf{C}} \begin{bmatrix} \tilde{i}_{gd} \\ \tilde{i}_{gq} \\ \tilde{v}_{dc} \end{bmatrix}^s + \underbrace{\begin{bmatrix} 0 & 0 & 0 & 0 & 0 \\ 0 & 0 & 0 & 0 & 0 \\ 0 & 0 & 0 & 0 & 0 \end{bmatrix}}_{\mathbf{D}} \begin{bmatrix} \tilde{v}_{gd} \\ \tilde{v}_{gq} \\ \tilde{i}_{dc} \\ \tilde{d}_d \\ \tilde{d}_q \end{bmatrix}^s \quad (3.28)$$

The transfer functions from the input variables to the state ones are obtained by solving the equation:

$$\mathbf{G} = \mathbf{C}(\mathbf{sI} - \mathbf{A})^{-1}\mathbf{B} + \mathbf{D}$$

$$\begin{bmatrix} \tilde{i}_{gd} \\ \tilde{i}_{gq} \\ \tilde{v}_{dc} \end{bmatrix}^s = \underbrace{\begin{bmatrix} G_{11} & G_{12} & G_{13} & G_{14} & G_{15} \\ G_{21} & G_{22} & G_{23} & G_{24} & G_{25} \\ G_{31} & G_{32} & -G_{33} & G_{34} & G_{35} \end{bmatrix}}_{\mathbf{G}} \begin{bmatrix} \tilde{v}_{gd} \\ \tilde{v}_{gq} \\ \tilde{i}_{dc} \\ \tilde{d}_d \\ \tilde{d}_q \end{bmatrix}^s \quad (3.29)$$

The matrix  $\mathbf{G}$  in the equation (3.29) can be represented in a way that they depict the physical relation between the variables as follows:

$$\mathbf{G} = \begin{bmatrix} Y_{indd,o} & Y_{indq,o} & G_{iod,o} & G_{cidd,o} & G_{cidq,o} \\ Y_{inqd,o} & Y_{inqq,o} & G_{ioq,o} & G_{ciqd,o} & G_{ciqq,o} \\ T_{oid,o} & T_{oiq,o} & -Z_{out,o} & G_{cod,o} & G_{coq,o} \end{bmatrix} \quad (3.30)$$

- $\mathbf{Y}_{in,o}$  - input admittance matrix
- $\mathbf{G}_{io,o}$  - forward transfer function matrix
- $\mathbf{G}_{co,o}$  - control-to-output transfer function matrix
- $\mathbf{T}_{oi,o}$  - input-to-output reverse transfer function matrix
- $\mathbf{Z}_{out,o}$  - output impedance
- $\mathbf{G}_{ci,o}$  - control-to-input transfer function matrix

The diagonal terms  $dd$  and  $qq$  of the matrices represent the interaction of the  $d$ - and  $q$ -axis variables on the variables in the same axis, while the anti-diagonal terms  $dq$  and the  $qd$  show the influence of the  $d$ -axis variables on the  $q$ -axis ones, and vice-versa. The reason why the output impedance  $Z_{out,o}$  has a negative sign is due to the fact that it is the impedance seen from the "point of view" of dc side and the current is defined as flowing into the dc side, thus opposite to the direction from where the impedance is seen. Another way of representing the open-loop dynamics is through a block diagram which permits to understand the influence each input variable has on the output one. Moreover, this way of representation also gives a straightforward way to confirm the model, be it in a simulation or on a real system. Block diagram depicting open-loop dynamics of an AFE can be seen in **Fig. 3.3**, from which the open-loop dynamics is obtained as:

$$\begin{aligned} \tilde{\mathbf{i}}_g &= \mathbf{G}_{io,o} \tilde{i}_{dc} + \mathbf{Y}_{in,o} \tilde{\mathbf{v}}_g + \mathbf{G}_{ci,o} \tilde{\mathbf{d}} \\ \tilde{v}_{dc} &= -Z_{out,o} \tilde{i}_{dc} + \mathbf{T}_{oi,o} \tilde{\mathbf{v}}_g + \mathbf{G}_{co,o} \tilde{\mathbf{d}} \end{aligned} \quad (3.31)$$

Solving the equation (3.29) and obtaining an analytical model of an AFE is not a straightforward task and includes a lot of mathematical manipulation, but it is nevertheless an indispensable step which later serves as a basis to confirm the validity of methods that are used to identify a model in a case where detailed knowledge of all parameters does not exist.

In following equations, the operator  $\Delta$  is the denominator of the transfer functions which is written in a way that it improves readability and is given by:

$$\Delta = s^3 + s^2 \frac{2R}{L} + s \left( \frac{3}{2} \frac{(D_d^2 + D_q^2)}{LC} + \omega_g^2 \right) + \frac{3}{2} \frac{R(D_d^2 + D_q^2)}{L^2 C} \quad (3.32)$$



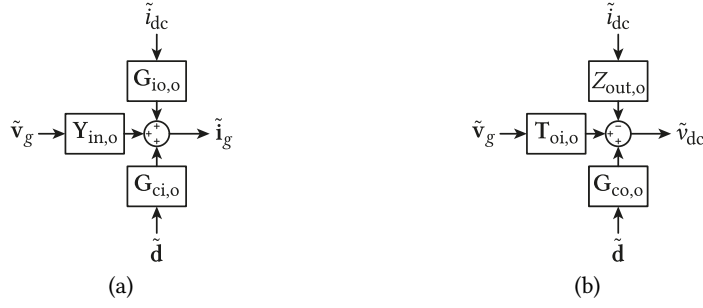


**Fig. 3.3** Open-loop dynamic for a) input, ac side, and b) output, dc side, terminals.

By solving (3.29) different transfer functions are obtained that describe the AFE dynamics. The  $d$ -axis inductor current related transfer functions are given by:

$$\begin{aligned}
 G_{11} &= \frac{1}{L} \left( s^2 + s \frac{R}{L} + \frac{3 D_q^2}{2 LC} \right) \cdot \Delta^{-1} \\
 G_{12} &= \frac{\omega_g}{L} \left( s - \frac{3 D_d D_q}{2 \omega_g LC} \right) \cdot \Delta^{-1} \\
 G_{13} &= \frac{D_d}{LC} \left( s + \frac{D_q \omega_g}{D_d} + \frac{R}{L} \right) \cdot \Delta^{-1} \\
 G_{14} &= -\frac{V_{dc}}{L} \left( s^2 + s \left( \frac{3 D_d I_{gd}}{2 C V_{dc}} + \frac{R}{L} \right) + \frac{3 D_q}{2 C} \left( \frac{D_q}{L} + \frac{I_{gq} \omega_g}{V_{dc}} + \frac{R D_d}{L V_{dc} D_q} \right) \right) \cdot \Delta^{-1} \\
 G_{15} &= -\frac{V_{dc}}{L} \left( s \left( \frac{3 D_d I_{gq}}{2 V_{dc} C} + \omega_g \right) + \frac{3}{2 C} \left( \frac{D_q I_{gq} \omega_g}{V_{dc}} - \frac{D_d D_q}{L} + \frac{R D_d I_{gd}}{L V_{dc}} \right) \right) \cdot \Delta^{-1}
 \end{aligned} \tag{3.33}$$

The  $q$ -axis inductor current related transfer functions are given by:

$$\begin{aligned}
 G_{21} &= -\frac{\omega_g}{L} \left( s + \frac{3 D_d D_q}{2 \omega_g LC} \right) \cdot \Delta^{-1} \\
 G_{22} &= \frac{1}{L} \left( s^2 + s \frac{R}{L} + \frac{3 D_d^2}{2 LC} \right) \cdot \Delta^{-1} \\
 G_{23} &= \frac{D_d}{LC} \left( s - \frac{D_d \omega_g}{D_q} + \frac{R}{L} \right) \cdot \Delta^{-1} \\
 G_{24} &= -\frac{V_{dc}}{L} \left( s \left( \frac{3 D_q I_{gd}}{2 V_{dc} C} - \omega_g \right) - \frac{3}{2 C} \left( \frac{D_d I_{gd} \omega_g}{V_{dc}} + \frac{D_d D_q}{L} + \frac{R D_q I_{gd}}{L V_{dc}} \right) \right) \cdot \Delta^{-1} \\
 G_{25} &= -\frac{V_{dc}}{L} \left( s^2 + s \left( \frac{3 D_q I_{gq}}{2 C V_{dc}} + \frac{R}{L} \right) - \frac{3 D_d}{2 C} \left( \frac{D_d}{L} - \frac{I_{gq} \omega_g}{V_{dc}} + \frac{R D_q}{L V_{dc} D_d} \right) \right) \cdot \Delta^{-1}
 \end{aligned} \tag{3.34}$$

The dc voltage related transfer functions are given by:

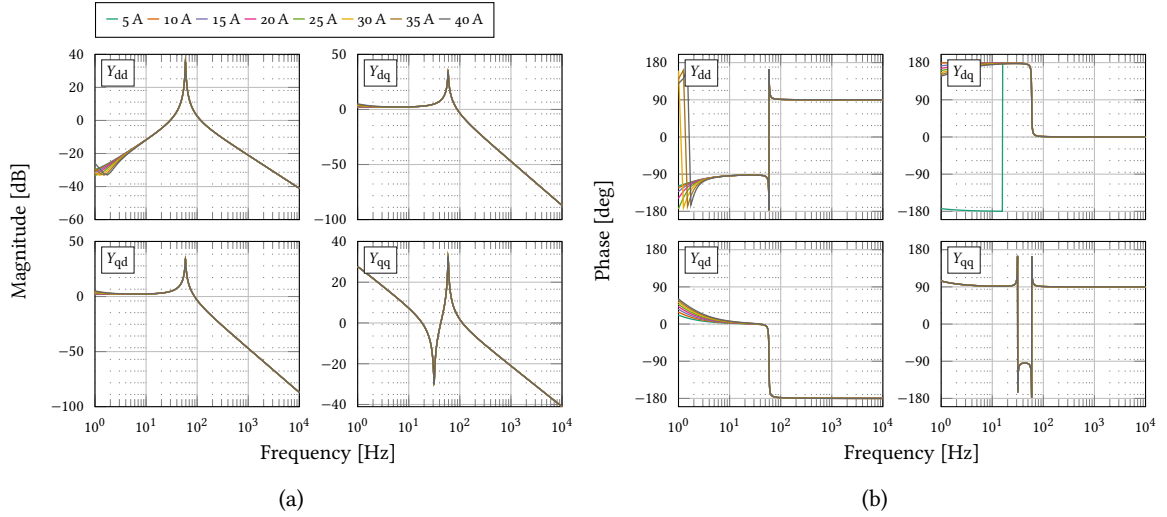
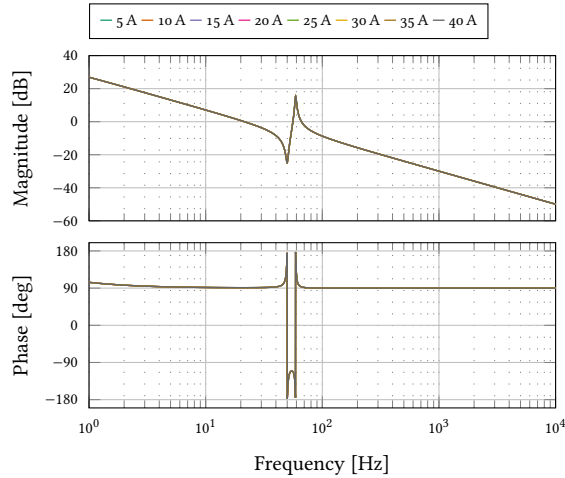
$$\begin{aligned}
G_{31} &= \frac{3D_d}{2LC} \left( s - \frac{D_q \omega_g}{D_d} + \frac{R}{L} \right) \cdot \Delta^{-1} \\
G_{32} &= \frac{3D_q}{2LC} \left( s - \frac{D_q \omega_g}{D_q} + \frac{R}{L} \right) \cdot \Delta^{-1} \\
G_{33} &= \frac{1}{C} \left( s^2 + s \frac{2R}{L} + \frac{R^2}{L^2} + \omega_g^2 \right) \cdot \Delta^{-1} \\
G_{34} &= \frac{3I_{gd}}{2C} \left( s^2 - s \left( \frac{D_d V_{dc}}{L I_{gd}} - \frac{2R}{L} \right) + \omega_g \left( \omega_g + \frac{D_q V_{dc}}{L I_{gd}} + \frac{R^2}{L^2 \omega_g} - \frac{V_{dc} D_d R}{\omega_g I_{gd} L^2} \right) \right) \cdot \Delta^{-1} \\
G_{35} &= \frac{3I_{gq}}{2C} \left( s^2 - s \left( \frac{D_q V_{dc}}{L I_{gq}} - \frac{2R}{L} \right) + \omega_g \left( \omega_g - \frac{D_d V_{dc}}{L I_{gq}} + \frac{R^2}{L^2 \omega_g} - \frac{V_{dc} D_q R}{\omega_g I_{gq} L^2} \right) \right) \cdot \Delta^{-1}
\end{aligned} \tag{3.35}$$

### 3.2.1.1 Influence of Different Parameters on the Model

From the previous developments it is clear that a number of different parameters can influence the shape and characteristics of the model, or input admittance and output impedance in this particular case. Dc-link capacitance, filter inductance and AFE operating point can all influence the model. **Tabs. 3.2 to 3.4** present the model parameters when these parameters are swept for a certain range. Dc-link capacitance is swept in the range 1–8 mF, filter inductance in the range 0.6–4.8 mH and the output current in the range 5–40 A. **Figs. 3.4 to 3.9** present the influence of each of these parameters on input admittance and output impedance. From **Fig. 3.4** it is visible that the output current affects the low-frequency region of the admittance and that the operating point in this particular case does not have influence on the output impedance. On the other side, modifying the dc-link capacitance and filter inductance influences both the admittance and the impedance over the whole frequency range. The reason for this is the absence of the closed-loop control, whose role is partially to dampen the effects of the inductance and capacitance in the low-frequency region, i.e. in the controllable region. Moreover, the change the inductance and capacitance modifies the resonant point coming from the interaction between the filter inductor and dc-link capacitor. This effect is clearly visible in **Figs. 3.6 and 3.8**.

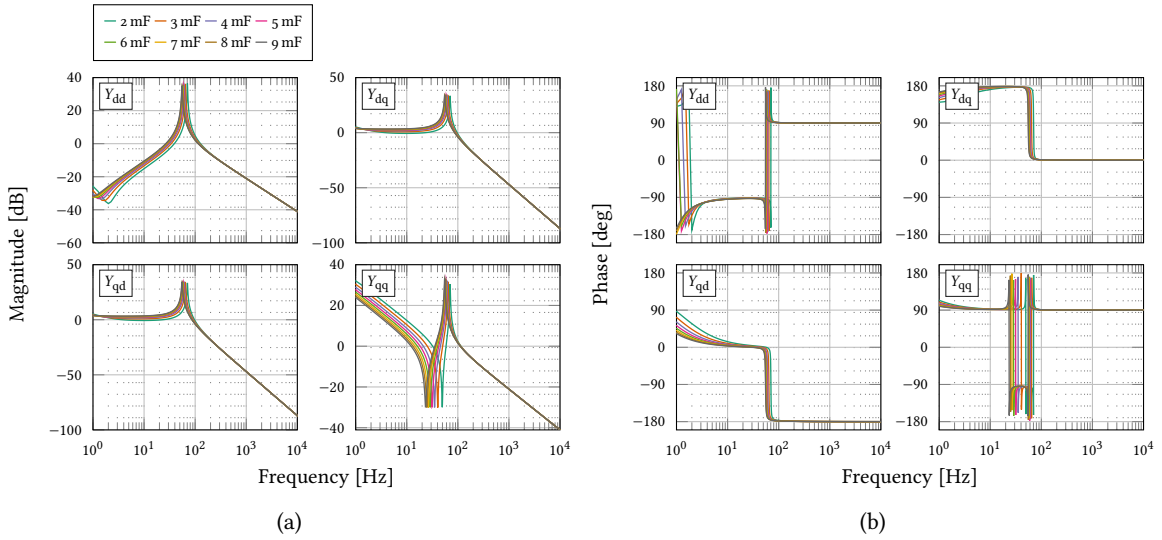
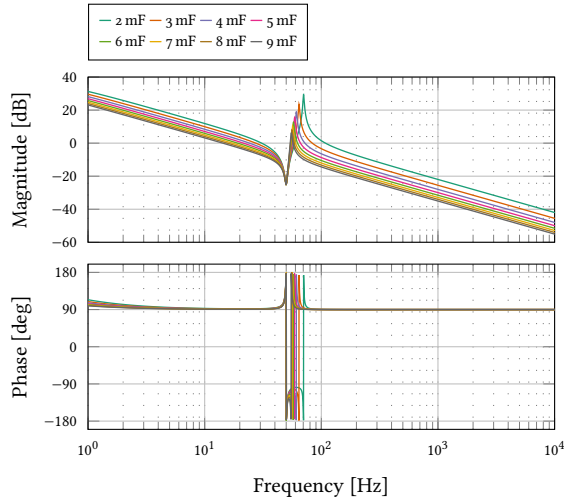
**Tab. 3.2** Model parameters for change of  $I_{dc}$ 

$P_{out} = 6-48 \text{ kW}$	$V_{dc} = 1.2 \text{ kV}$	$I_{dc} = 5-40 \text{ A}$	$C_{dc} = 5 \text{ mF}$	$f_{sw} = 10 \text{ kHz}$	$f_g = 50 \text{ Hz}$
$V_{gd} = 580 \text{ V}$	$V_{gq} = 0 \text{ V}$	$I_{gd} = 7-55 \text{ A}$	$I_{gq} = 0 \text{ A}$	$L_g = 1.8 \text{ mH}$	$R_g = 10 \text{ m}\Omega$

**Fig. 3.4** Dependence of the a) magnitude and b) phase of the input admittance  $Y_{in}$  of current-fed AFE on the change of the output side current  $I_{dc}$ .**Fig. 3.5** Dependence of the magnitude and phase of the output impedance  $Z_{out}$  of current-fed AFE on the change of the output side current  $I_{dc}$ .

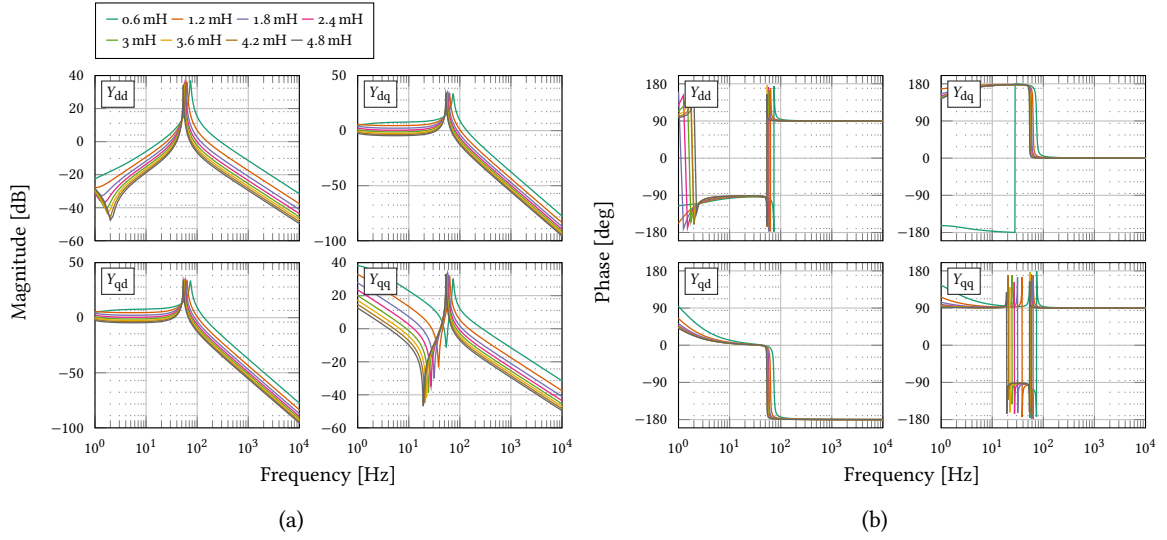
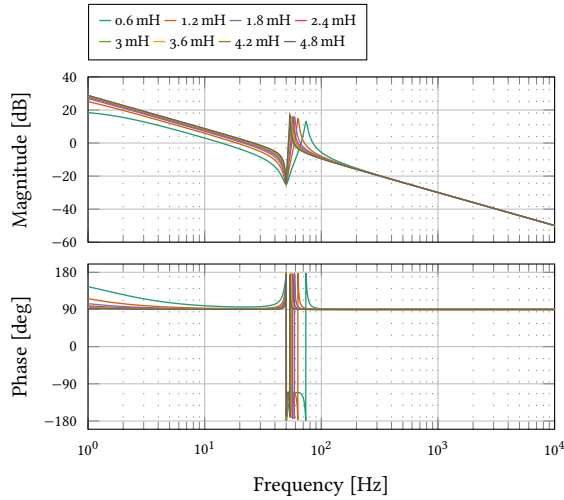
**Tab. 3.3** Model parameters for change of  $C_{dc}$ 

$P_{out} = 36 \text{ kW}$	$V_{dc} = 1.2 \text{ kV}$	$I_{dc} = 30 \text{ A}$	$C_{dc} = 1\text{--}8 \text{ mF}$	$f_{sw} = 10 \text{ kHz}$	$f_g = 50 \text{ Hz}$
$V_{gd} = 580 \text{ V}$	$V_{gq} = 0 \text{ V}$	$I_{gd} = 41 \text{ A}$	$I_{gq} = 0 \text{ A}$	$L_g = 1.8 \text{ mH}$	$R_g = 10 \text{ m}\Omega$


**Fig. 3.6** Dependence of the a) magnitude and b) phase of the input admittance  $\mathbf{Y}_{in}$  of current-fed AFE on the change of the dc-link capacitor  $C_{dc}$ .

**Fig. 3.7** Dependence of the magnitude and phase of the output impedance  $Z_{out}$  of current-fed AFE on the change of the dc-link capacitor  $C_{dc}$ .

**Tab. 3.4** Model parameters for change of  $L_g$ 

$P_{out} = 36 \text{ kW}$	$V_{dc} = 1.2 \text{ kV}$	$I_{dc} = 30 \text{ A}$	$C_{dc} = 5 \text{ mF}$	$f_{sw} = 10 \text{ kHz}$	$f_g = 50 \text{ Hz}$
$V_{gd} = 580 \text{ V}$	$V_{gq} = 0 \text{ V}$	$I_{gd} = 41 \text{ A}$	$I_{gq} = 0 \text{ A}$	$L_g = 0.6\text{--}4.8 \text{ mH}$	$R_g = 10 \text{ m}\Omega$

**Fig. 3.8** Dependence of the a) magnitude and b) phase of the input admittance  $Y_{in}$  of current-fed AFE on the change of the filter inductance  $L_f$ .**Fig. 3.9** Dependence of the magnitude and phase of the output impedance  $Z_{out}$  of current-fed AFE on the change of the filter inductance  $L_f$ .

**Tab. 3.5** Model parameters

$P_{\text{out}} = 36 \text{ kW}$	$V_{\text{dc}} = 1.2 \text{ kV}$	$V_{\text{gd}} = 580 \text{ V}$	$V_{\text{gq}} = 0 \text{ V}$	$f_g = 50 \text{ Hz}$
$I_{\text{gd}} = 41 \text{ A}$	$I_{\text{gq}} = 0 \text{ A}$	$f_{\text{sw}} = 10 \text{ kHz}$	$L_g = 1.8 \text{ mH}$	$R_g = 10 \text{ m}\Omega$

### 3.2.2 Open-Loop Model Verification

The open-loop model can be verified by creating a switching model of an AFE and using a signal of small amplitude to perturb any of the input variables presented so far and capturing the frequency response of an output variable. Comparing the small-signal response of the output variable to the perturbation gives one of the transfer functions defined in equations (3.33) to (3.35). The switching model was implemented in PLECS (c.f. **Fig. 3.10**), whereas the computations and extraction of results were performed in MATLAB. The analytical expressions of the transfer functions are also obtained through the same software. The angle  $\theta$  of the grid, used for  $dq$ -transformations, is assumed known and is generated inside the PLECS environment, thus there exists no grid synchronization algorithm. To perturb the system, a PRBS-12 [29] was used. Generation frequency of the signal is set to  $f_{\text{gen}} = 5 \text{ kHz}$ , while the frequency resolution is  $f_r = 1.221 \text{ Hz}$ . At the generation frequency the signal energy falls to zero. The parameters of the model are given in **Tab. 3.5**. Only the terminal characteristics of the open-loop model are presented here, i.e. the input admittance and output impedance. After the perturbation injection voltages and currents, both on the input and the output terminals, are collected. It should be noted that for the measurement of the input admittance two injections are required, one in the  $d$ -axis and one in the  $q$ -axis of the converter model. The input admittance can be obtained with the following equation:

$$\begin{aligned} \mathbf{Y}_{\text{in}}(s) &= \begin{bmatrix} i_{d,1}(s) & i_{d,2}(s) \\ i_{q,1}(s) & i_{q,2}(s) \end{bmatrix} \cdot \begin{bmatrix} v_{d,1}(s) & v_{d,2}(s) \\ v_{q,1}(s) & v_{q,2}(s) \end{bmatrix}^{-1} \\ &= \begin{bmatrix} Y_{dd}(s) & Y_{dq}(s) \\ Y_{qd}(s) & Y_{qq}(s) \end{bmatrix} \end{aligned} \quad (3.36)$$

Where the  $i_{x,y}$  and  $v_{x,y}$  are the measured currents and voltage in the  $dq$ -frame after the first and second injection. On the dc-side, from the voltage and current measurements the output impedance can be extracted as:

$$Z_{\text{out}}(s) = \frac{\|\tilde{v}(s)\|}{\|\tilde{i}(s)\|} [\angle \tilde{v}(s) - \angle \tilde{i}(s)] \quad (3.37)$$

The obtained characteristics are illustrated in **Figs. 3.11** and **3.12**. As the frequency is approaching the generation one, large oscillations appear due to the very low, almost zero, energy of the signal. This demonstrates that the useful frequency range for system identification using the PRBS is lower than its generation frequency and to identify a system over a larger range, PRBS with larger generation frequency needs to be used. Nevertheless, in the frequency range of interest, the PRBS manages to indicate points of interest, such as resonance points and phase jumps.

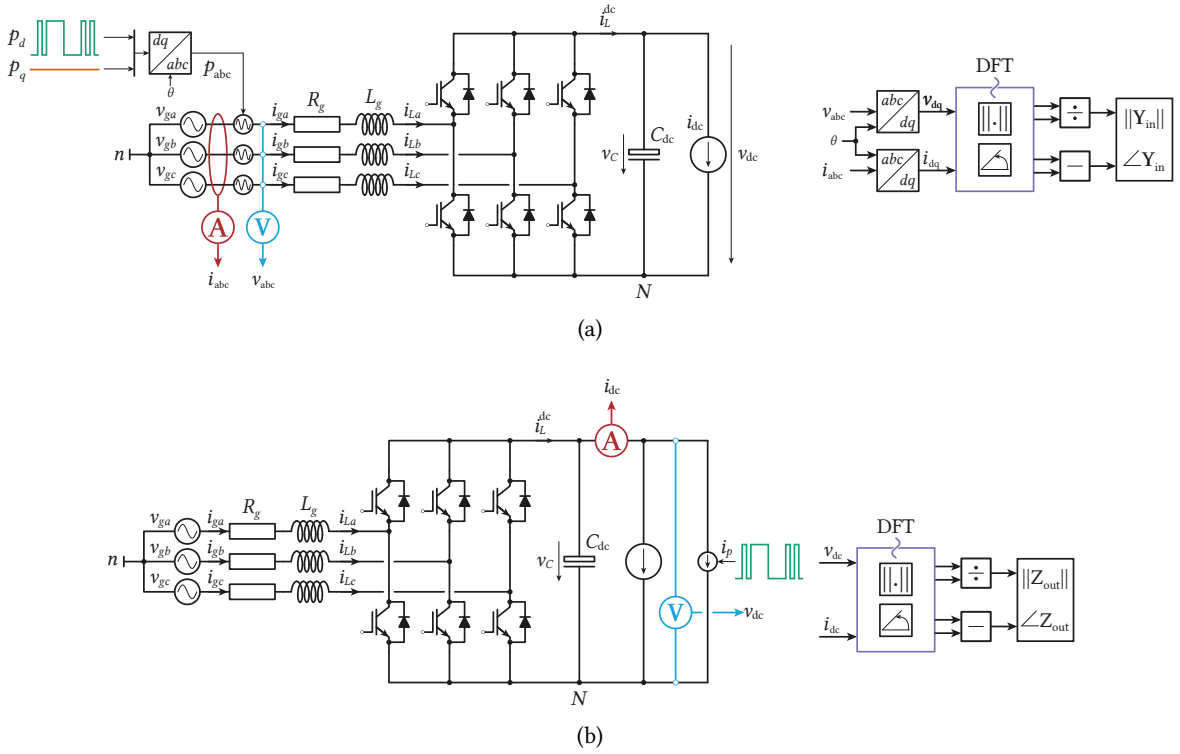


**Fig. 3.10** Schematics of the a) voltage and b) current perturbation injection for the measurement of the a) input admittance and b) output impedance. Only the  $d$ -axis injection is shown, but the principle is the same for  $q$ -axis injection.

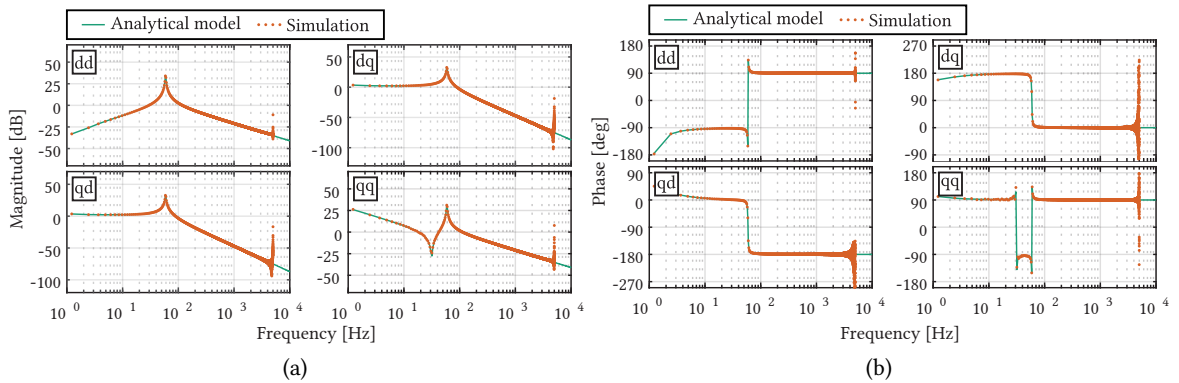


**Fig. 3.11** a) Magnitude and b) phase of the input admittance of current-fed AFE.

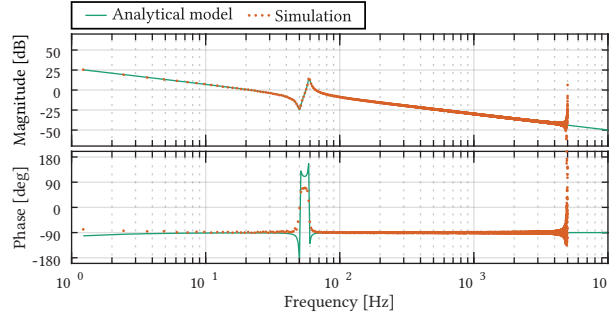


Fig. 3.12 Output impedance of the AFE.

### 3.3 H-Bridge Inverter Modelling

The modelling of the HB (c.f. Fig. 3.13) inverter follows relatively similar and simple approach as the modelling of the AFE. The main difference, but not at all a limiting one, is that the HB inverter modelling starts from a single-phase system, but by creating an imaginary axis the modelling process ends up in the  $dq$ -frame. As the dc-link voltage control is performed on the AFE side, the inverter input is considered to be an ideal voltage source. The inverter output stage is an LC-type filter and the load is considered to be an ideal current source (or sink). As in the case of the AFE, state-space modelling approach is applied. Input variables are considered to be the input voltage  $v_{dc}$  and the load current  $i_o$ . State variables are the filter inductor current and capacitor voltage,  $i_L$ , and  $v_C$ , respectively. The load voltage is essentially the filter capacitor voltage. For readability purposes,  $L_f$ ,  $R_f$  and  $C_f$  are simply denoted as  $L$ ,  $R$  and  $C$ . The control variable is the duty cycle  $d$ . The dead-time nonlinear effect is not considered in HB modelling either. There exist four possible switching states of the AFE (cf. Tab. 3.6), where  $s_x$  and  $\bar{s}_x$  are the upper and lower switches in left and right inverter leg, respectively. The positive current direction is considered to be the one flowing into the load.

As with the AFE modelling, one needs to establish the time-averaged derivatives of state variables and the time-averaged values of the output variables. Two subsets of equations are established, one for the on-time and one for the switch off-time.

During the on-time, voltages are given by:

$$\begin{aligned} v_L &= v_{dc} - v_R - v_f + v_N \\ v_f &= v_o \end{aligned} \tag{3.38}$$

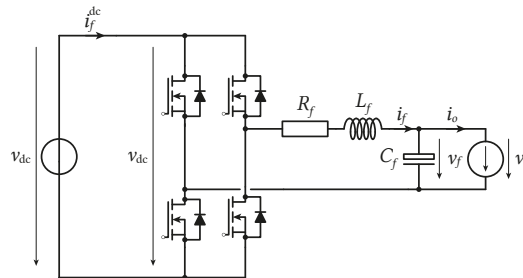


Fig. 3.13 HB inverter with an output LC filter.



Tab. 3.6 HB switching states

$s$	$s_L$	$s_R$	$\overline{s_L}$	$\overline{s_R}$
0	0	0	1	1
1	1	0	0	1
2	0	1	1	0
3	1	1	0	0

While the currents are given by

$$\begin{aligned} i_f^{\text{dc}} &= i_f \\ i_C &= i_f - i_o \end{aligned} \quad (3.39)$$

During the off-time, voltages and currents are given by:

$$\begin{aligned} v_L &= -v_R - v_f + v_N \\ v_f &= v_o \end{aligned} \quad (3.40)$$

while the currents are given by:

$$\begin{aligned} i_f^{\text{dc}} &= 0 \\ i_C &= i_f - i_o \end{aligned} \quad (3.41)$$

To obtain the averaged values of the equations above, one must multiply the equations (3.38) and (3.39) and (3.40) and (3.41) by on-time and off-time duty cycles  $d^{\text{on}}$  and  $d^{\text{off}}$ , respectively, and summing them together. For further developments  $d^{\text{off}} = 1 - d^{\text{on}}$  and  $d^{\text{on}}$  is denoted only as  $d$ . These manipulations yield time-averaged equations for voltage and current:

$$\begin{aligned} \langle v_L \rangle &= -\langle v_R \rangle - \langle v_f \rangle + d\langle v_{\text{dc}} \rangle + \langle v_N \rangle \\ \langle v_f \rangle &= \langle v_o \rangle \\ \langle i_f^{\text{dc}} \rangle &= d\langle i_f \rangle \\ \langle i_C \rangle &= \langle i_f \rangle - \langle i_o \rangle \end{aligned} \quad (3.42)$$

Again, by applying (A.5) one obtains:

$$\begin{aligned} \frac{d\langle i_f \rangle}{dt} &= \frac{-\langle v_R \rangle - \langle v_f \rangle + d\langle v_{\text{dc}} \rangle + \langle v_N \rangle}{L} \\ \frac{d\langle v_f \rangle}{dt} &= \frac{\langle i_f \rangle - \langle i_o \rangle}{C} \\ \langle i_f^{\text{dc}} \rangle &= d\langle i_f \rangle \end{aligned} \quad (3.43)$$

The equations given here are single-phase equations and Clarke and Park transformation cannot be applied directly in this case. However, there exist quadrature signal generators (QSGs) [66]–[68] used

to create a signal orthogonal to ones in (3.43). Considering that a QSG has been applied to a signal in (3.43), new set of equation is obtained in  $\alpha\beta$ -frame:

$$\begin{aligned}\frac{d}{dt}\langle \mathbf{i}_f^{\alpha\beta} \rangle &= -\frac{\langle \mathbf{v}_R^{\alpha\beta} \rangle}{L} - \frac{\langle \mathbf{v}_f^{\alpha\beta} \rangle}{L} + \frac{\langle \mathbf{d}^{\alpha\beta} \rangle \langle v_{dc} \rangle}{L} + \langle v_N \rangle \\ \frac{d}{dt}\langle \mathbf{v}_f^{\alpha\beta} \rangle &= \frac{\langle \mathbf{i}_f^{\alpha\beta} \rangle - \langle \mathbf{i}_o^{\alpha\beta} \rangle}{C} \\ \langle i_f^{dc} \rangle &= \mathbf{d}^{\alpha\beta} \langle \mathbf{i}_f^{\alpha\beta} \rangle\end{aligned}\quad (3.44)$$

As before, to transform the variables from  $\alpha\beta$ - to  $dq$ -frame, one has to multiply (3.44) by  $e^{j\omega_s t}$ , where  $\omega_s$  is the output rotating frequency, which gives:

$$\begin{aligned}\frac{d}{dt} \left( \langle \mathbf{i}_f^{dq} \rangle e^{j\omega_s t} \right) &= \frac{\mathbf{d}^{dq} \langle v_{dc} \rangle e^{j\omega_s t}}{L} - \frac{\langle \mathbf{v}_R^{dq} \rangle e^{j\omega_s t}}{L} - \frac{\langle \mathbf{v}_f^{dq} \rangle e^{j\omega_s t}}{L} \\ \frac{d}{dt} \left( \langle \mathbf{v}_f^{dq} \rangle e^{j\omega_s t} \right) &= \frac{\langle \mathbf{i}_f^{dq} \rangle e^{j\omega_s t} - \langle \mathbf{i}_o^{dq} \rangle e^{j\omega_s t}}{C} \\ \langle i_f^{dc} \rangle &= \mathbf{d}^{dq} \langle \mathbf{i}_f^{dq} \rangle\end{aligned}\quad (3.45)$$

Performing the derivation and canceling  $e^{j\omega_s t}$  in (3.45) and recalling that  $v_R = Ri_f$  gives:

$$\begin{aligned}\frac{d}{dt} \langle \mathbf{i}_f^{dq} \rangle &= -j\omega_s \langle \mathbf{i}_f^{dq} \rangle + \frac{\mathbf{d}^{dq} \langle v_{dc} \rangle}{L} - \frac{R}{L} \langle \mathbf{i}_f^{dq} \rangle - \frac{\langle \mathbf{v}_f^{dq} \rangle}{L} \\ \frac{d}{dt} \langle \mathbf{v}_f^{dq} \rangle &= -j\omega_s \langle \mathbf{v}_f^{dq} \rangle + \frac{\langle \mathbf{i}_f^{dq} \rangle}{C} - \frac{\langle \mathbf{i}_o^{dq} \rangle}{C}\end{aligned}\quad (3.46)$$

The equation (3.46) can be split into  $d$ - and  $q$ -axis which gives:

$$\begin{aligned}\frac{d\langle i_{fd} \rangle}{dt} &= \omega_s \langle i_{fq} \rangle + \frac{d_d \langle v_{dc} \rangle}{L} - \frac{R}{L} \langle i_{fd} \rangle - \frac{\langle V_{fd} \rangle}{L} \\ \frac{d\langle i_{fq} \rangle}{dt} &= -\omega_s \langle i_{fd} \rangle + \frac{d_q \langle v_{dc} \rangle}{L} - \frac{R}{L} \langle i_{fq} \rangle - \frac{\langle V_{fq} \rangle}{L} \\ \frac{d\langle v_{fd} \rangle}{dt} &= \omega_s \langle v_{fq} \rangle + \frac{\langle I_{fd} \rangle}{C} - \frac{\langle i_{od} \rangle}{C} \\ \frac{d\langle v_{fq} \rangle}{dt} &= -\omega_s \langle v_{fd} \rangle + \frac{\langle I_{fq} \rangle}{C} - \frac{\langle i_{oq} \rangle}{C} \\ \langle i_f^{dc} \rangle &= d_d \langle i_{fd} \rangle + d_q \langle i_{fq} \rangle\end{aligned}\quad (3.47)$$

The steady-state operating point of the HB can be obtained by setting the derivatives to zero in previous equation, which yields:

$$\omega_s L I_{fq} + D_d V_{dc} - R I_{fd} - V_{fd} = 0 \quad (3.48)$$

$$-\omega_s L I_{gd} + D_q V_{dc} - R I_{fq} - V_{fq} = 0 \quad (3.49)$$

$$\omega_s CV_{fq} + I_{fd} - I_{od} = 0 \quad (3.50)$$

$$-\omega_s CV_{fd} + I_{fq} - I_{oq} = 0 \quad (3.51)$$

Aligning the voltage vector to the  $d$ -axis,  $V_{fq}$  is set to zero, the steady-state operating point of the HB is given with:

$$\begin{aligned} I_{fd} &= I_{od} \\ I_{fq} &= \omega_s CV_{fd} \\ D_d &= \frac{V_{fd} - \omega_s LI_{fq} + RI_{od}}{V_{dc}} \\ D_q &= \frac{\omega_s LI_{fd} + RI_{fq}}{V_{dc}} \end{aligned} \quad (3.52)$$

### 3.3.1 H-Bridge State-Space Model and Open-Loop Dynamics

In order to present the HB dynamics in the open-loop, the state-space model is first created by linearising (3.47) following the method presented in **Sec. 3.2.1**.

$$\begin{aligned} \frac{d\tilde{i}_{fd}}{dt} &= \omega_s \tilde{i}_{fq} + \frac{V_{dc}}{L} \tilde{d}_d + \frac{D_d}{L} \tilde{v}_{dc} - \frac{R}{L} \tilde{i}_{fd} - \frac{1}{L} \tilde{v}_{fd} \\ \frac{d\tilde{i}_{fq}}{dt} &= -\omega_s \tilde{i}_{fd} + \frac{V_{dc}}{L} \tilde{d}_q + \frac{D_q}{L} \tilde{v}_{dc} - \frac{R}{L} \tilde{i}_{fq} - \frac{1}{L} \tilde{v}_{fq} \\ \frac{d\tilde{v}_{fd}}{dt} &= \omega_s \tilde{v}_{fq} + \frac{\tilde{i}_{fd}}{C} - \frac{\tilde{i}_{od}}{C} \\ \frac{d\tilde{v}_{fq}}{dt} &= -\omega_s \tilde{v}_{fd} + \frac{\tilde{i}_{fq}}{C} - \frac{\tilde{i}_{oq}}{C} \\ \tilde{i}_f^{dc} &= \tilde{d}_d I_{fd} + D_d \tilde{i}_{fd} + \tilde{d}_q I_{fq} + D_q \tilde{i}_{fq} \end{aligned} \quad (3.53)$$

The state-space model in time domain (superscript  $t$ ) can be represented in a matrix form:

$$\begin{bmatrix} \frac{d\tilde{i}_{fd}}{dt} \\ \frac{d\tilde{i}_{fq}}{dt} \\ \frac{d\tilde{v}_{fd}}{dt} \\ \frac{d\tilde{v}_{fq}}{dt} \end{bmatrix}^t = \begin{bmatrix} -\frac{R}{L} & \omega_s & -\frac{1}{L} & 0 \\ -\omega_s & -\frac{R}{L} & 0 & -\frac{1}{L} \\ \frac{1}{C} & 0 & 0 & \omega_s \\ 0 & \frac{1}{C} & -\omega_s & 0 \end{bmatrix} \begin{bmatrix} \tilde{i}_{fd} \\ \tilde{i}_{fq} \\ \tilde{v}_{fd} \\ \tilde{v}_{fq} \end{bmatrix}^t + \begin{bmatrix} \frac{D_d}{L} & 0 & 0 & \frac{V_{dc}}{L} & 0 \\ \frac{D_q}{L} & 0 & 0 & 0 & \frac{V_{dc}}{L} \\ 0 & -\frac{1}{C} & 0 & 0 & 0 \\ 0 & 0 & -\frac{1}{C} & 0 & 0 \end{bmatrix} \begin{bmatrix} \tilde{v}_{dc} \\ \tilde{i}_{od} \\ \tilde{i}_{oq} \\ \tilde{d}_d \\ \tilde{d}_q \end{bmatrix}^t \quad (3.54)$$

The output variables are given by

$$\begin{bmatrix} \tilde{i}_f^{dc} \\ \tilde{i}_{fd} \\ \tilde{i}_{fq} \\ \tilde{v}_{fd} \\ \tilde{v}_{fq} \end{bmatrix}^t = \begin{bmatrix} D_d & D_q & 0 & 0 \\ 1 & 0 & 0 & 0 \\ 0 & 1 & 0 & 0 \\ 0 & 0 & 1 & 0 \\ 0 & 0 & 0 & 1 \end{bmatrix} \begin{bmatrix} \tilde{i}_{fd} \\ \tilde{i}_{fq} \\ \tilde{v}_{fd} \\ \tilde{v}_{fq} \end{bmatrix}^t + \begin{bmatrix} 0 & 0 & 0 & I_d & I_q \\ 0 & 0 & 0 & 0 & 0 \\ 0 & 0 & 0 & 0 & 0 \\ 0 & 0 & 0 & 0 & 0 \\ 0 & 0 & 0 & 0 & 0 \end{bmatrix} \begin{bmatrix} \tilde{v}_{dc} \\ \tilde{i}_{od} \\ \tilde{i}_{oq} \\ \tilde{d}_d \\ \tilde{d}_q \end{bmatrix}^t \quad (3.55)$$

The same equation in matrix form can be represented in s-domain by replacing the time derivative  $d/dt$  by the operator  $s$ :

$$s \begin{bmatrix} \tilde{i}_{fd} \\ \tilde{i}_{fq} \\ \tilde{v}_{fd} \\ \tilde{v}_{fq} \end{bmatrix} = \underbrace{\begin{bmatrix} -\frac{R}{L} & \omega_s & -\frac{1}{L} & 0 \\ -\omega_s & -\frac{R}{L} & 0 & -\frac{1}{L} \\ \frac{1}{C} & 0 & 0 & \omega_s \\ 0 & \frac{1}{C} & -\omega_s & 0 \end{bmatrix}}_{\mathbf{A}} \begin{bmatrix} \tilde{i}_{fd} \\ \tilde{i}_{fq} \\ \tilde{v}_{fd} \\ \tilde{v}_{fq} \end{bmatrix} + \underbrace{\begin{bmatrix} -\frac{D_d}{L} & 0 & 0 & -\frac{V_{dc}}{L} & 0 \\ -\frac{D_q}{L} & 0 & 0 & 0 & -\frac{V_{dc}}{L} \\ 0 & -\frac{1}{C} & 0 & 0 & 0 \\ 0 & 0 & -\frac{1}{C} & 0 & 0 \end{bmatrix}}_{\mathbf{B}} \begin{bmatrix} \tilde{v}_{dc} \\ \tilde{i}_{od} \\ \tilde{i}_{oq} \\ \tilde{d}_d \\ \tilde{d}_q \end{bmatrix} \quad (3.56)$$

$$\begin{bmatrix} \tilde{i}_f^{dc} \\ \tilde{i}_{fd} \\ \tilde{i}_{fq} \\ \tilde{v}_{fd} \\ \tilde{v}_{fq} \end{bmatrix}^s = \underbrace{\begin{bmatrix} D_d & D_q & 0 & 0 \\ 1 & 0 & 0 & 0 \\ 0 & 1 & 0 & 0 \\ 0 & 0 & 1 & 0 \\ 0 & 0 & 0 & 1 \end{bmatrix}}_{\mathbf{C}} \begin{bmatrix} \tilde{i}_{fd} \\ \tilde{i}_{fq} \\ \tilde{v}_{fd} \\ \tilde{v}_{fq} \end{bmatrix}^s + \underbrace{\begin{bmatrix} 0 & 0 & 0 & I_d & I_q \\ 0 & 0 & 0 & 0 & 0 \\ 0 & 0 & 0 & 0 & 0 \\ 0 & 0 & 0 & 0 & 0 \\ 0 & 0 & 0 & 0 & 0 \end{bmatrix}}_{\mathbf{D}} \begin{bmatrix} \tilde{v}_{dc} \\ \tilde{i}_{od} \\ \tilde{i}_{oq} \\ \tilde{d}_d \\ \tilde{d}_q \end{bmatrix}^s \quad (3.57)$$

The transfer functions from the input variable to the state ones are obtained by solving the equation:

$$\mathbf{G} = \mathbf{C}(\mathbf{sI} - \mathbf{A})^{-1}\mathbf{B} + \mathbf{D}$$

$$\begin{bmatrix} \tilde{i}_f^{dc} \\ \tilde{i}_{fd} \\ \tilde{i}_{fq} \\ \tilde{v}_{fd} \\ \tilde{v}_{fq} \end{bmatrix}^s = \underbrace{\begin{bmatrix} G_{11} & G_{12} & G_{13} & G_{14} & G_{15} \\ G_{21} & G_{22} & G_{23} & G_{24} & G_{25} \\ G_{31} & G_{32} & G_{33} & G_{34} & G_{35} \\ G_{41} & -G_{42} & -G_{43} & G_{44} & G_{45} \\ G_{51} & -G_{52} & -G_{53} & G_{54} & G_{55} \end{bmatrix}}_{\mathbf{G}} \begin{bmatrix} \tilde{v}_{dc} \\ \tilde{i}_{od} \\ \tilde{i}_{oq} \\ \tilde{d}_d \\ \tilde{d}_q \end{bmatrix}^s \quad (3.58)$$

The matrix  $\mathbf{G}$  can again be represented in a way that the transfer functions depict the physical relation between the variables as follows:

$$\mathbf{G} = \begin{bmatrix} Y_{in,o} & T_{oid,o} & T_{oiq,o} & G_{ci,d} & G_{ci,q} \\ G_{iLd,o} & T_{oLdd,o} & T_{oLdq,o} & G_{cLdd,o} & G_{cLdq,o} \\ G_{iLq,o} & T_{oLqd,o} & T_{oLqq,o} & G_{cLqd,o} & G_{cLqq,o} \\ G_{iCd,o} & -Z_{outdd,o} & -Z_{outdq,o} & G_{codd,o} & G_{codq,o} \\ G_{iCq,o} & -Z_{outqd,o} & -Z_{outqq,o} & G_{coqd,o} & G_{coqq,o} \end{bmatrix} \quad (3.59)$$

- $G_{iL,o}$  - input voltage-to-inductor current transfer function matrix
- $G_{iC,o}$  - input voltage-to-capacitor voltage transfer function matrix

- $Y_{in,o}$  - input admittance
- $G_{cL,o}$  - control-to-inductor current transfer function matrix
- $G_{co,o}$  - control-to-output voltage transfer function matrix
- $G_{ci,o}$  - control-to-input current transfer function matrix
- $T_{oL,o}$  - output current-to-inductor current reverse transfer function matrix
- $T_{oi,o}$  - output current-to-input current reverse transfer function matrix
- $Z_{out,o}$  - output impedance

The open-loop dynamics representation through a block diagram is fairly simple and reveals the influence of input variables to output ones. The block diagram depicting the open-loop dynamics of the HB is presented in **Fig. 3.14** from which the open-loop dynamics can be obtained as:

$$\tilde{i}_f^{dc} = \tilde{i}_o T_{oi,o} + \tilde{v}_{dc} Y_{in,o} + \tilde{d} G_{ci,o} \quad (3.60)$$

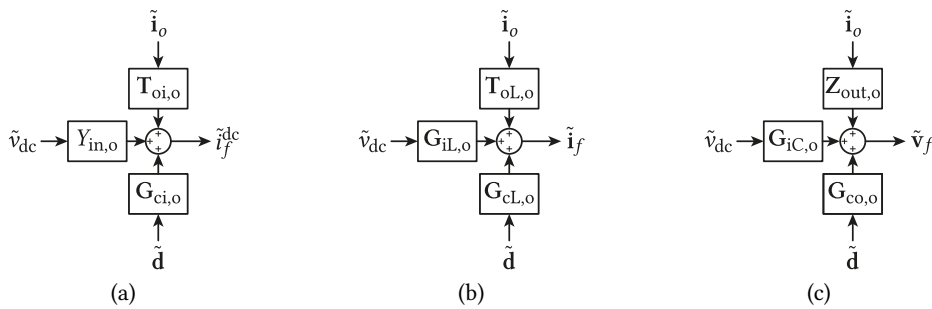
$$\tilde{i}_f = \tilde{i}_o T_{oL,o} + \tilde{v}_{dc} G_{iL,o} + \tilde{d} G_{cL,o} \quad (3.61)$$

$$\tilde{v}_f = \tilde{i}_o Z_{out,o} + \tilde{v}_{dc} G_{iC,o} + \tilde{d} G_{co,o} \quad (3.62)$$

Identically to the AFE modelling, solving (3.58) gives transfer functions that describe the HB dynamics. However, their analytical forms are not given here due to their complexity. The advantage of the model developed here is in the fact that when used to describe the dynamics of a single-phase inverter, one can remove the transfer functions related to the  $q$ -axis components. On the other hand, the model can be used as presented here to illustrate the dynamics of a three-phase inverter.

### 3.3.1.1 Influence of Different Parameters on the Model

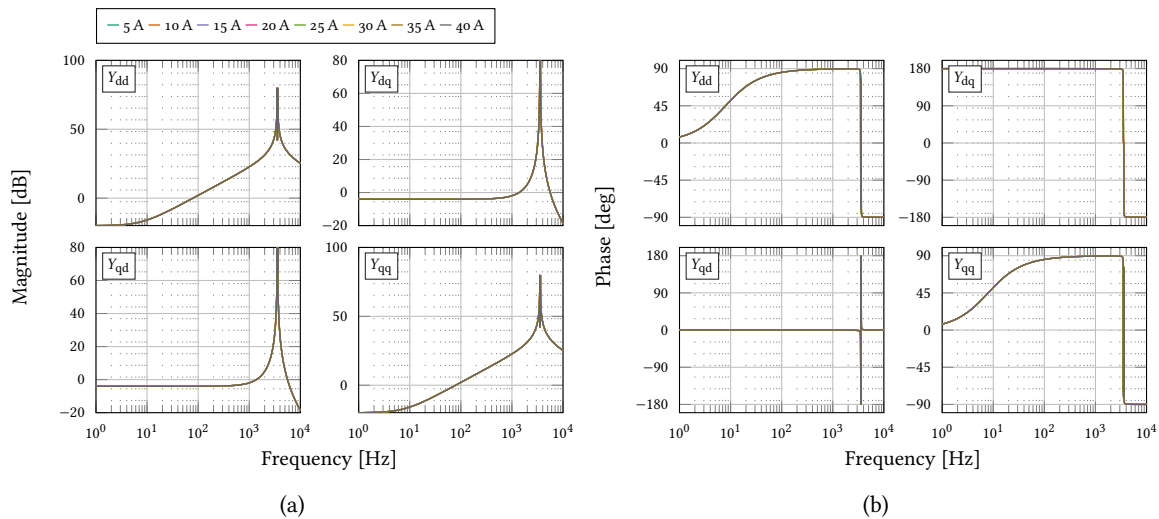
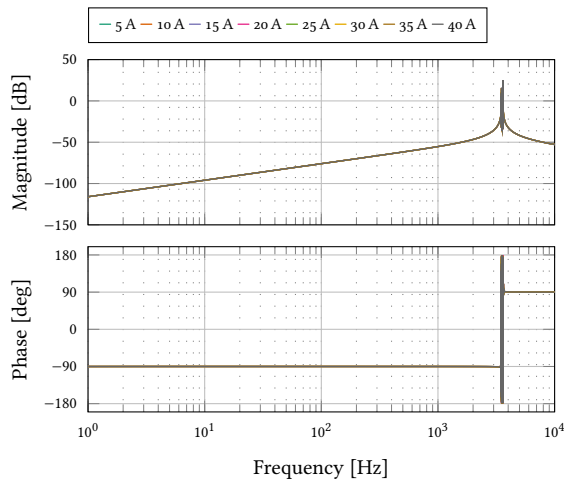
From the previous developments it is clear that a number of different parameters can influence the shape and characteristics of the model, or input admittance and output impedance in this particular case. Output capacitance, filter inductance, and HB operating point have the most influence. **Tabs. 3.7** to **3.9** present the model parameters when these parameters are swept for a certain range. Output filter capacitance is swept in the range 0.2–1.6  $\mu\text{F}$ , filter inductance in the range 1–8 mH and the output current in the range 5–40 A. **Figs. 3.15, 3.17** and **3.19** present the influence of each of these parameters on output impedance, while **Figs. 3.16, 3.18** and **3.20** shows the influence of the same parameters on the input admittance. As was the case with the AFE, modifying the inductance of the capacitance of the output  $LC$  filter shifts the characteristics in the frequency range of interest. This, naturally, comes from the resonance frequency of the  $LC$  filter that is being modified with the inductance and capacitance.



**Fig. 3.14** Open-loop dynamic for a) input dc and b,c) output ac terminals.

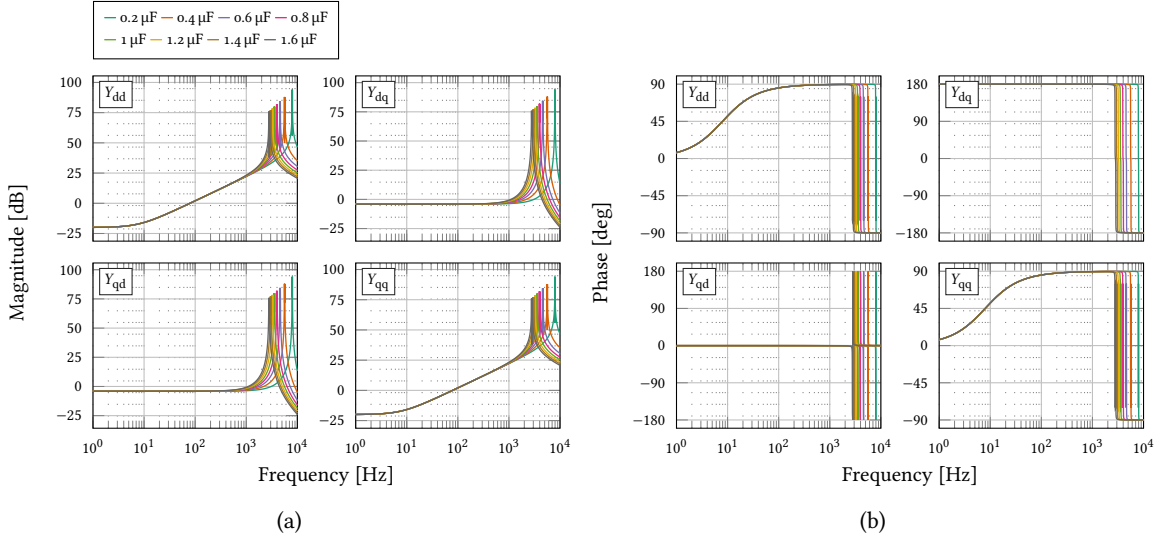
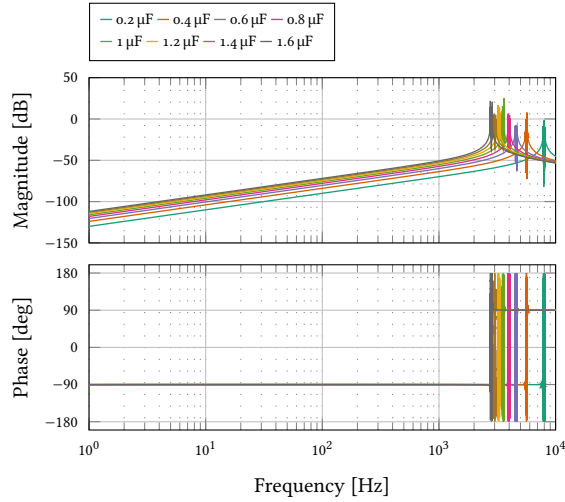
**Tab. 3.7** Model parameters for change of output current

$P_{out} = 3\text{--}24\text{ kW}$	$V_{dc} = 1.2\text{ kV}$	$I_{dc} = 5\text{--}40\text{ A}$	$C_{dc} = 1.6\text{ }\mu\text{F}$	$f_{sw} = 20\text{ kHz}$	$f_s = 50\text{ Hz}$
$V_{fd} = 600\text{ V}$	$V_{fq} = 0\text{ V}$	$I_{fd} = 5\text{--}40\text{ A}$	$I_{fq} = 0.2\text{ A}$	$L_f = 1.8\text{ mH}$	$R_f = 100\text{ m}\Omega$


**Fig. 3.15** Dependence of the a) magnitude and b) phase of the output impedance  $Z_{out}$  of current-fed AFE on the change of the  $d$ -axis current  $I_{fd}$ .

**Fig. 3.16** Dependence of the magnitude and phase of the input admittance  $Y_{in}$  of the voltage-fed HB inverter on the change of the  $d$ -axis current  $I_{fd}$ .

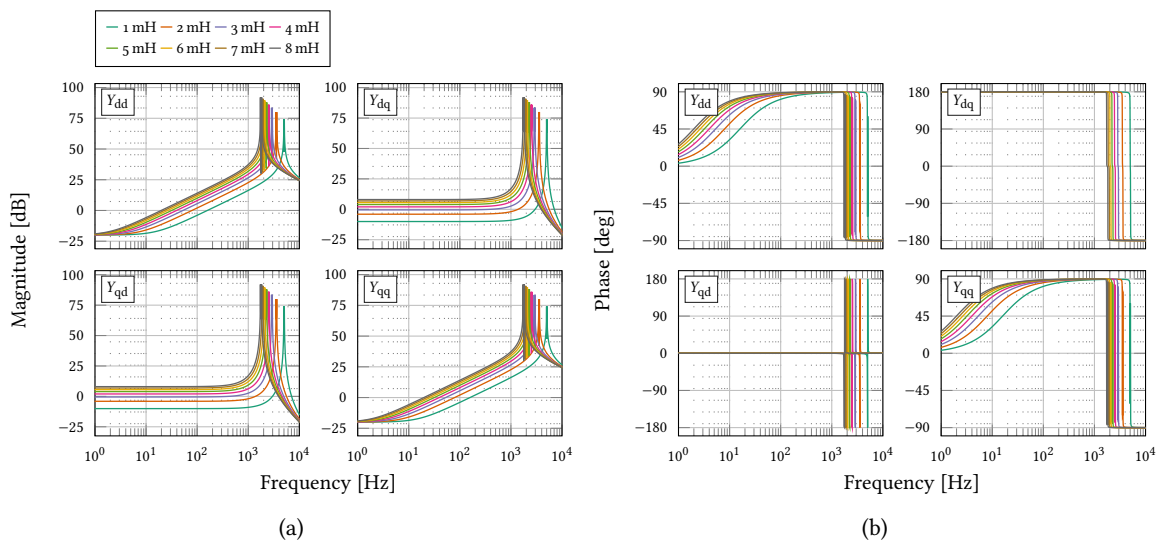
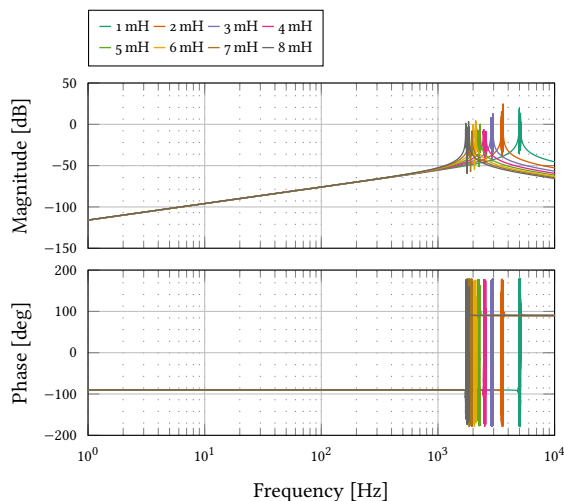
**Tab. 3.8** Model parameters for change of  $C_f$ 

$P_{\text{out}} = 18 \text{ kW}$	$V_{\text{dc}} = 1.2 \text{ kV}$	$I_{\text{dc}} = 30 \text{ A}$	$C_f = 0.2\text{--}1.6 \text{ }\mu\text{F}$	$f_{\text{sw}} = 20 \text{ kHz}$	$f_s = 50 \text{ Hz}$
$V_{\text{fd}} = 600 \text{ V}$	$V_{\text{fq}} = 0 \text{ V}$	$I_{\text{fd}} = 30 \text{ A}$	$I_{\text{fq}} = 0.2 \text{ A}$	$L_f = 2 \text{ mH}$	$R_f = 100 \text{ m}\Omega$

**Fig. 3.17** Dependence of the a) magnitude and b) phase of the output impedance  $Z_{\text{out}}$  of current-fed AFE on the change of the output filter capacitance  $C_f$ .**Fig. 3.18** Dependence of the magnitude and phase of the input admittance  $Y_{\text{in}}$  of the voltage-fed HB inverter on the change of the output filter capacitance  $C_f$ .

**Tab. 3.9** Model parameters for change of  $L_f$ 

$P_{\text{out}} = 18 \text{ kW}$	$V_{\text{dc}} = 1.2 \text{ kV}$	$I_{\text{dc}} = 30 \text{ A}$	$C_f = 1.6 \text{ } \mu\text{F}$	$f_{\text{sw}} = 20 \text{ kHz}$	$f_s = 50 \text{ Hz}$
$V_{\text{fd}} = 600 \text{ V}$	$V_{\text{fq}} = 0 \text{ V}$	$I_{\text{fd}} = 30 \text{ A}$	$I_{\text{fq}} = 0.2 \text{ A}$	$L_f = 1\text{--}8 \text{ mH}$	$R_f = 100 \text{ m}\Omega$


**Fig. 3.19** Dependence of the a) magnitude and b) phase of the output impedance  $Z_{\text{out}}$  of current-fed AFE on the change of the output filter inductance  $L_f$ .

**Fig. 3.20** Dependence of the magnitude and phase of the input admittance  $Y_{\text{in}}$  of the voltage-fed HB inverter on the change of the output filter inductance  $L_f$ .

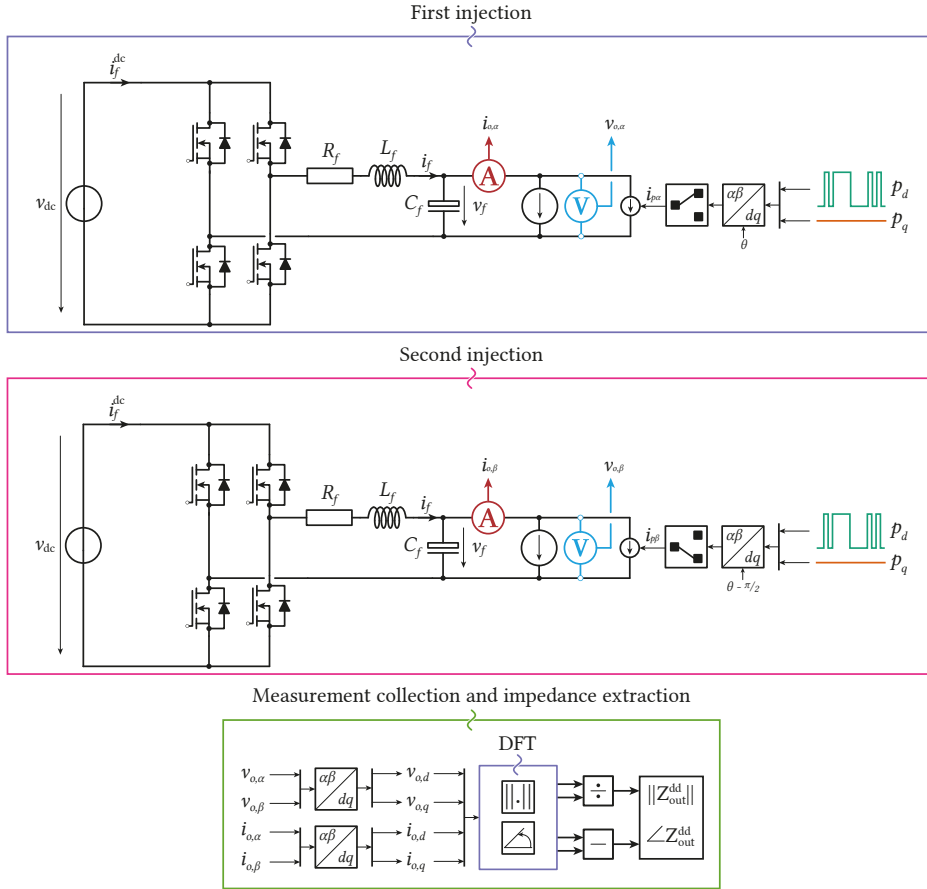




**Fig. 3.21** Schematics of the current perturbation injection for the measurement of the output impedance of the HB inverter.

### 3.3.2 Open-Loop Model Verification

The open-loop model can be verified by creating a switching model of an HB and using a signal of small amplitude to perturb any of the input variables presented so far and capturing the frequency response of an output variable. The switching model was implemented in PLECS, whereas the computations and extraction of results were performed in MATLAB. As opposed to the verification of the open-loop model, and any related measurement of the  $dq$ -frame characteristics, of the AFE which requires two perturbation injections to describe the whole characteristics, when measuring the characteristics of the HB two injections are required to describe the only one term of  $2 \times 2$  transfer function matrices, i.e. to measure the  $Z_{out}^{dd}$  two perturbation injections and measurements are required. To perturb the system, a PRBS-12 [29] was used as was the case with the open-loop model verification of the AFE and again the generation frequency of the signal is set to  $f_g = 5$  kHz, while the frequency resolution is  $f_r = 1.221$  Hz. The perturbation is injected into the  $d$ -axis, while the  $q$ -axis is kept at zero value. Subsequently, the perturbation is transferred from the  $dq$ -frame to the  $\alpha\beta$ -frame.

In the first perturbation injection the  $\alpha$ -axis perturbation is injected into the current sink, while the second one, the  $\beta$ -axis perturbation is injected. If the converter and the current sink are driven with an angle  $\theta$  in the first injection, they are driven with the angle  $\theta - \pi/2$  in the second one, i.e. an

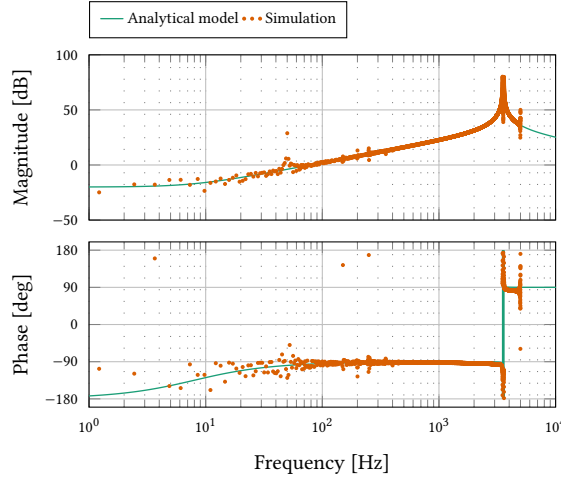


**Fig. 3.22**  $d$ -axis  $Z_{\text{out}}^{\text{dd}}$  output impedance magnitude and phase of the HB.

orthogonal system is simulated. Thus, two sets of measurements are obtained, one  $\alpha$ -axis set, and the other, orthogonal,  $\beta$ -axis set. The two measurement sets obtained in the  $\alpha\beta$ -frame can then be transferred into the  $dq$ -frame from where the frequency responses can be extracted. This technique is depicted in **Fig. 3.21**. The  $d$ -axis output impedance of the HB inverter obtained through analytical developments is compared against the impedance obtained with the method summarized in **Fig. 3.21** and is presented in **Fig. 3.22**. From the results presented it is clearly visible that the theoretical output impedance is confirmed by the PLECS simulation.

### 3.4 Summary

This chapter presented the open-loop models of the AFE and the HB inverter which serve as a basis for the closed-loop modelling and further development of the load-source interactions of the PEBB of the CHB converter. To verify the models, the wideband PRBS signal is used to verify both the three-phase AFE and the single-phase HB inverter. The application of wideband signals for verification of the models of three-phase converter developed in  $dq$ -frame is already a well-established technique. However, the verification of the models surrounding single-phase converters was so far reserved for the narrowband signals such as the single-tone sinusoidal signals. By using the methods to artificially create a switching model of the HB orthogonal to its original counterpart, the wideband signal injection and measurement is made possible and the open-loop models of single-phase inverter can be confirmed as well.

# 4

## Closed-Loop Control Modelling

*This chapters presents the control design and closed-loop modelling of a cascaded H-bridge converter power electronics building block. The closed-loop modelling takes into account the addition of the input current and dc-link voltage control as well as synchronization loop on the active-front-end side. On the H-bridge side, filter capacitor voltage and inductor current loops are studied, and their overall effect on the inverter model. A verification of the closed-loop control model of the active front end is provided through the verification of its output impedance, further required for the assessment of source-affected dynamics of the cascaded H-bridge power electronics building block.*

### 4.1 Active-Front-End Closed-Loop Control and Synchronization Design

The control of the AFE follows a today already classical approach of cascaded control in which the inner loop is the input current control and the outer loop is the dc-link voltage control. Assuming there are no unbalances in the input voltage, synchronization is performed using the SRF-phase-locked loop (PLL).

#### 4.1.1 Synchronous Reference Frame Phase-Locked-Loop

So far it has been assumed that the input, or grid, voltage frequency and angle were known and there was no synchronization loops present. This also meant that the synchronization loop dynamics were not taken into account. However, in any real system there has to exist a mean of synchronizing the converter to the grid. There exist many different synchronization techniques, with the most relevant for the grid connected systems being the SRF-PLL [69], [70]. The method is based on the amplitude-invariant Park transformation that is used to sense the magnitude of grid voltage  $d$ - and  $q$ -axis components. The control block diagram of SRF-PLL is shown in **Fig. 4.1**. The SRF-PLL is composed of a combined Clarke and Park transformation, proportional integral (PI) regulator, controlling the  $v_{g,q}$  value to zero. Output of the PI controller is the grid frequency which is fed into the integrator which gives the grid angle  $\theta^c$ .

In ideal conditions the angle sensed by the PLL and the real grid angle should be identical, but due to

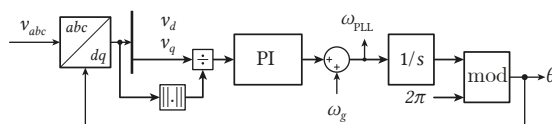


**Fig. 4.1** Control block diagram of SRF-PLL.

the limited bandwidth of the PLL there exists a small deviation,  $\tilde{\theta}$ , between the two. This causes the sensed grid voltages to lag behind the real grid voltages by the same angle deviation. Consequently, all the reference frame transformations and controllers are as well affected by this difference. The effect that the angle deviation has on the real transformed  $dq$ -frame components can be interpreted as a rotation by an angle  $\tilde{\theta}$ . Thus, an arbitrary signal in  $dq$ -frame affected by the misalignment can be given as:

$$\begin{bmatrix} X_d^c + \tilde{x}_d^c \\ X_q^c + \tilde{x}_q^c \end{bmatrix} = \begin{bmatrix} \cos \tilde{\theta} & \sin \tilde{\theta} \\ -\sin \tilde{\theta} & \cos \tilde{\theta} \end{bmatrix} \begin{bmatrix} X_d + \tilde{x}_d \\ X_q + \tilde{x}_q \end{bmatrix} \quad (4.1)$$

By solving the (4.1) and assuming that for very small values of  $\tilde{\theta}$ ,  $\cos \tilde{\theta} = 1$  and  $\sin \tilde{\theta} = \tilde{\theta}$  and that the steady-state values are equal, i.e.  $\mathbf{X}^c = \mathbf{X}$ , one obtains the relation revealing the effect the grid synchronization has on a system variable:

$$\begin{aligned} \tilde{x}_d^c &= \tilde{x}_d + X_q \tilde{\theta} \\ \tilde{x}_q^c &= \tilde{x}_q - X_d \tilde{\theta} \end{aligned} \quad (4.2)$$

From the PLL control loop, not taking into account the frequency feed-forward for improved angle tracking, the relation between the output angle and input  $q$ -axis voltage is given as

$$\tilde{\theta} = \tilde{v}_q^c \underbrace{\left( K_{p,PLL} + \frac{K_{i,PLL}}{s} \right)}_{G_{PI}^{PLL}(s)} \frac{1}{s} = \tilde{v}_q^c \underbrace{\frac{K_{p,PLL}s + K_{i,PLL}}{s^2}}_{H_{PLL,ol}(s)} \quad (4.3)$$

Where  $H_{PLL,ol}(s)$  is the PLL open-loop transfer function. From (4.2), replacing the  $q$ -axis signal by voltage and plugging it in (4.3) gives the relation between the angle  $\tilde{\theta}$  and unaffected voltage as

$$\tilde{\theta} = \frac{H_{PLL,ol}}{1 + V_d H_{PLL,ol}} \tilde{v}_q \quad (4.4)$$

When this equation is replaced in (4.1), it gives the effect of the PLL dynamics on the small-signal variables  $\tilde{x}_d^c$  and  $\tilde{x}_q^c$  as:

$$\begin{aligned} \tilde{x}_d^c &= \tilde{x}_d + X_q \frac{H_{PLL,ol}}{1 + V_d H_{PLL,ol}} \tilde{v}_q \\ \tilde{x}_q^c &= \tilde{x}_q - X_d \underbrace{\frac{H_{PLL,ol}}{1 + V_d H_{PLL,ol}}}_{G_{PLL}(s)} \tilde{v}_q \end{aligned} \quad (4.5)$$

#### 4.1.1.1 PLL Closed-Loop Control Design

The closed loop of the PLL is given as:

$$H_{PLL,cl}(s) = \frac{H_{PLL,ol}}{1 + H_{PLL,ol}} = \frac{K_{p,PLL}s + K_{i,PLL}}{s^2 + K_{p,PLL}s + K_{i,PLL}} = \frac{2\xi\omega_n s + \omega_n^2}{s^2 + 2\xi\omega_n s + \omega_n^2} \quad (4.6)$$

Where  $\omega_n = \sqrt{K_{i,PLL}}$  and  $\xi = 1/2 K_{p,PLL} \sqrt{1/K_{i,PLL}}$ . The PI regulator gains can be sized as:

$$K_{p,PLL} = \frac{9.2}{t_s} \quad \text{and} \quad K_{i,PLL} = \frac{21.16}{t_s^2 \xi^2} \quad (4.7)$$

Where  $t_s$  and  $\xi$  are the settling time and the damping factor respectively.

### 4.1.2 Grid Current Control

The grid current control can be performed in different reference frames, such as synchronous  $dq$ -, stationary  $\alpha\beta$ - or reference  $abc$ -frame [71]. As the modelling introduced so far was performed in  $dq$ -frame, the control principle inherits this approach and is performed in the  $dq$ -frame as well. Apart from this, quantities in the  $dq$ -frame are dc quantities and using a simple PI regulator is sufficient. Moreover, the advantage of SRF control lies in the fact that controlling active and reactive power is possible through the use of PI controllers [72]. Nevertheless, using controllers in  $\alpha\beta$ - and  $abc$ - and representing them in  $dq$ -frame is also possible but is out of scope of this work.

In the following developments it should be noted that the  $s$ -domain operator ( $s$ ) is omitted to ease the readability. The controller action, affected by the PLL dynamics and with the cross coupling between axes and input voltage feed-forward can be formulated as:

$$\mathbf{v}_{dq}^* = \underbrace{\left( K_{p,gcc} + \frac{K_{i,gcc}}{s} \right)}_{G_{PI}^i(s)} (\mathbf{i}_{g,dq}^* - \mathbf{H}_i \tilde{\mathbf{i}}_{g,dq}^c) + \mathbf{G}_{dec} \mathbf{H}_i \tilde{\mathbf{i}}_{g,dq}^c + \tilde{\mathbf{v}}_{g,dq}^c \quad (4.8)$$

Where the PI regulator coefficients  $K_{p,gcc}$  and  $K_{i,gcc}$  can be sized using Magnitude Optimum Criterion [73],  $\mathbf{H}_i$  is the matrix representing the current transducer and  $\mathbf{G}_{dec}$  is the decoupling matrix given as:

$$\mathbf{H}_i = \begin{bmatrix} H_{i,d} & 0 \\ 0 & H_{i,q} \end{bmatrix} \quad (4.9)$$

$$\mathbf{G}_{dec} = \begin{bmatrix} 0 & -\omega_g L_g \\ \omega_g L_g & 0 \end{bmatrix} \quad (4.10)$$

The abbreviation “gcc” stands for *grid current control*. The grid current and voltage in  $dq$ -frame are given in the control system reference frame as:

$$\begin{bmatrix} \tilde{i}_{g,d}^c \\ \tilde{i}_{g,q}^c \end{bmatrix} = \begin{bmatrix} \tilde{i}_{g,d} \\ \tilde{i}_{g,q} \end{bmatrix} + \underbrace{\begin{bmatrix} 0 & I_{g,q} G_{PLL} \\ 0 & -I_{g,d} G_{PLL} \end{bmatrix}}_{\mathbf{G}_{PLL}^i} \cdot \begin{bmatrix} \tilde{v}_{g,d} \\ \tilde{v}_{g,q} \end{bmatrix} \quad (4.11)$$

$$\begin{bmatrix} \tilde{v}_{g,d}^c \\ \tilde{v}_{g,q}^c \end{bmatrix} = \begin{bmatrix} \tilde{v}_{g,d} \\ \tilde{v}_{g,q} \end{bmatrix} + \underbrace{\begin{bmatrix} 0 & V_{g,q} G_{PLL} \\ 0 & -V_{g,d} G_{PLL} \end{bmatrix}}_{\mathbf{G}_{PLL}^v} \cdot \begin{bmatrix} \tilde{v}_{g,d} \\ \tilde{v}_{g,q} \end{bmatrix} \quad (4.12)$$

To obtain the duty cycles in the controller reference frame one has to divide the  $\tilde{\mathbf{v}}_{dq}^*$  by the dc-link voltage giving the  $dq$ -frame duty cycles:

$$\tilde{\mathbf{d}}_{dq}^c = \frac{\tilde{\mathbf{v}}_{dq}^*}{V_{dc}} \quad (4.13)$$

Similarly to (4.11), the duty cycle in the grid reference frame is defined as;

$$\begin{bmatrix} \tilde{d}_d \\ \tilde{d}_q \end{bmatrix} = \begin{bmatrix} \tilde{d}_d^c \\ \tilde{d}_q^c \end{bmatrix} + \underbrace{\begin{bmatrix} 0 & -D_q G_{PLL} \\ 0 & D_d G_{PLL} \end{bmatrix}}_{\mathbf{G}_{PLL}^d} \cdot \begin{bmatrix} \tilde{v}_{g,d} \\ \tilde{v}_{g,q} \end{bmatrix} \quad (4.14)$$

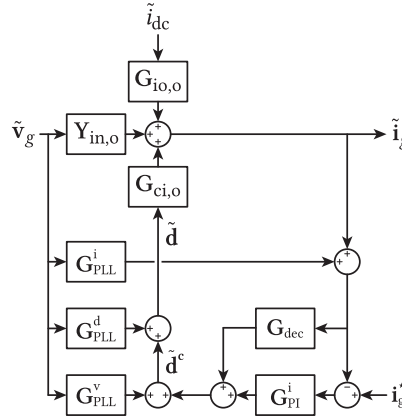


**Fig. 4.2** Small-signal output dynamics of the AFE with the influence of the PLL and under the current control.

The reason why the duty cycle is given in the grid reference frame is that it is the one that will directly influence the converter voltage. The converter duty cycle can be solved from **Fig. 4.2** and is given as:

$$\ddot{\mathbf{d}}_{dq} = \mathbf{G}_{\text{PI}}^{\text{i}} \dot{\mathbf{i}}_{g,dq}^* + (\mathbf{G}_{\text{dec}} - \mathbf{G}_{\text{PI}}^{\text{i}}) \ddot{\mathbf{i}}_{g,dq} + \underbrace{\left[ \mathbf{I} + (\mathbf{G}_{\text{dec}} - \mathbf{G}_{\text{PI}}^{\text{i}}) \mathbf{G}_{\text{PLL}}^{\text{i}} + \mathbf{G}_{\text{PLL}}^{\text{d}} + \mathbf{G}_{\text{PLL}}^{\text{v}} \right]}_{\mathbf{G}_{\text{PLL}}^{\text{vd}}} \tilde{\mathbf{v}}_{g,dq} \quad (4.15)$$

With the duty cycle defined by equation (4.15) the closed loop dynamics under current control can be solved. To solve the closed-loop dynamics one has to take a look back to **Fig. 3.3** from which two equations were defined as:

$$\tilde{\mathbf{i}}_g = \mathbf{G}_{\text{io},0} \tilde{i}_{\text{dc}} + \mathbf{Y}_{\text{in},0} \tilde{\mathbf{v}}_{g,dq} + \mathbf{G}_{\text{ci},0} \tilde{\mathbf{d}}_{dq} \quad (4.16)$$

$$\tilde{v}_{dc} = -Z_{out,o}\tilde{i}_{dc} + \mathbf{T}_{oi,o}\tilde{\mathbf{v}}_{g,dq} + \mathbf{G}_{co,o}\tilde{\mathbf{d}}_{dq} \quad (4.17)$$

When (4.15) is replaced into these two equations the input dynamics is given as

$$\mathbf{G}_{\text{io,cl}}^{\text{gcc}} = [\mathbf{I} + \mathbf{G}_{\text{ci,o}} (\mathbf{G}_{\text{PI}}^{\text{i}} - \mathbf{G}_{\text{dec}})]^{-1} \mathbf{G}_{\text{io,o}} \quad (4.18)$$

$$\mathbf{Y}_{\text{in,cl}}^{\text{gcc}} = \left[ \mathbf{I} + \mathbf{G}_{\text{ci,o}} \left( \mathbf{G}_{\text{PI}}^{\text{i}} - \mathbf{G}_{\text{dec}} \right) \right]^{-1} \left[ \mathbf{Y}_{\text{in,o}} + \mathbf{G}_{\text{ci,o}} \left( \mathbf{I} + \left( \mathbf{G}_{\text{dec}} - \mathbf{G}_{\text{PI}}^{\text{i}} \right) \mathbf{G}_{\text{PLL}}^{\text{i}} + \mathbf{G}_{\text{PLL}}^{\text{d}} + \mathbf{G}_{\text{PLL}}^{\text{v}} \right) \right] \quad (4.19)$$

$$\mathbf{G}_{\text{ci,cl}}^{\text{gcc}} = [\mathbf{I} + \mathbf{G}_{\text{ci,o}} (\mathbf{G}_{\text{PI}}^{\text{i}} - \mathbf{G}_{\text{dec}})]^{-1} \mathbf{G}_{\text{ci,o}} \mathbf{G}_{\text{PI}}^{\text{i}} \quad (4.20)$$

While the output dynamics is given as:

$$Z_{\text{out,cl}}^{\text{gcc}} = -Z_{\text{out},0} + \mathbf{G}_{\text{co},0} \left( \mathbf{G}_{\text{dec}} - \mathbf{G}_{\text{Pl}}^{\text{i}} \right) \mathbf{G}_{\text{io,cl}}^{\text{gcc}} \quad (4.21)$$

$$\mathbf{G}_{\text{co,cl}}^{\text{gcc}} = \mathbf{G}_{\text{co,o}} \mathbf{G}_{\text{PI}}^{\text{i}} + \mathbf{G}_{\text{co,o}} \left( \mathbf{G}_{\text{dec}} - \mathbf{G}_{\text{PI}}^{\text{i}} \right) \mathbf{G}_{\text{ci,cl}}^{\text{gcc}} \quad (4.22)$$

$$\mathbf{T}_{\text{oi,cl}}^{\text{gcc}} = \mathbf{T}_{\text{oi,o}} + \mathbf{G}_{\text{co,o}} \left[ \left( \mathbf{G}_{\text{dec}} - \mathbf{G}_{\text{PI}}^{\text{i}} \right) \mathbf{Y}_{\text{in,cl}}^{\text{gcc}} + \mathbf{G}_{\text{PLL}}^{\text{vd}} \right] \quad (4.23)$$

It should be noted that the input of  $\mathbf{G}_{\text{ci,cl}}^{\text{gcc}}$  and  $\mathbf{G}_{\text{co,cl}}^{\text{gcc}}$  is the current reference  $\mathbf{i}_{g,dq}^*$

### 4.1.3 Dc-link Voltage Control

From the model established in **Sec. 4.1** it is evident that the dc-link voltage, or the output voltage, is an output variable. The role of the dc-link voltage controller is dual. The first one is to stabilise the

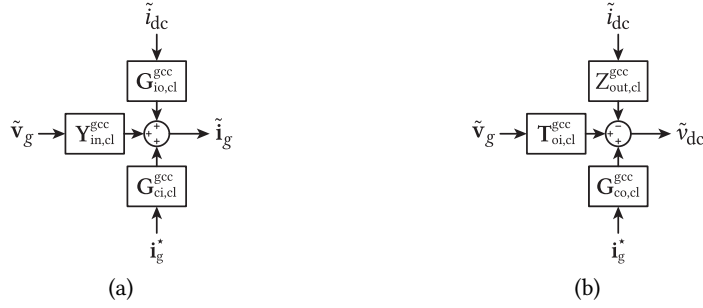


**Fig. 4.3** Closed-loop dynamic for a) input, ac side, and b) output, dc side, terminals under grid current control.

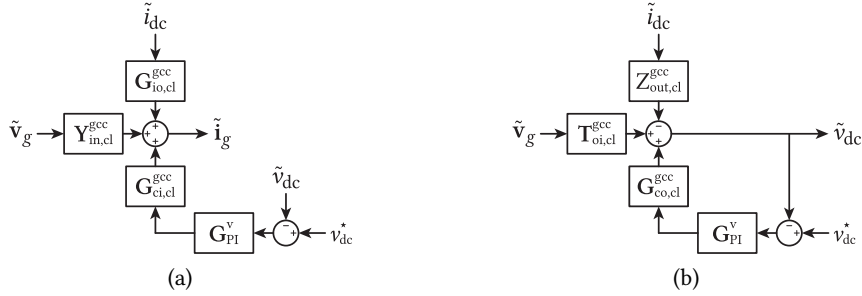


**Fig. 4.4** Closed-loop dynamics for a) input, ac side, and b) output, dc side, terminals with the addition of the dc-link voltage regulator.

unstable control dynamics [74], while the second one is to provide a reference to the other output variable control loop, which is the grid current control loop. More precisely, the reference provided is the  $d$ -axis current reference  $i_{g,d}^*$ , which is directly responsible for the exchange of active power between the grid and the AFE. The controller action can be formulated as:

$$i_{g,d}^* = \underbrace{\left( K_{p,dvc} + \frac{K_{i,dvc}}{s} \right)}_{G_{PI}^v(s)} (v_{dc}^* - H_v \tilde{v}_{dc}) \quad (4.24)$$

The "dvc" in the previous equation stands for *dc-link voltage control*. The closed-loop dynamics under cascaded control and dc-link voltage control can be solved by first solving the dc-side, or output

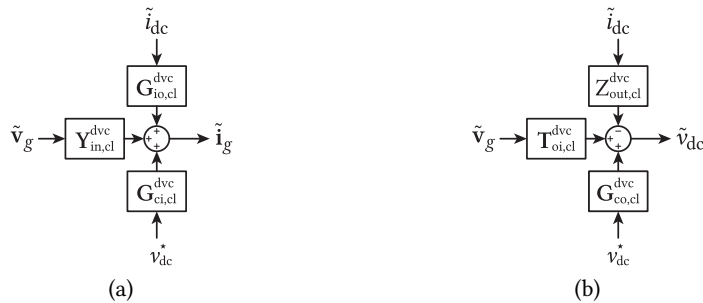


**Fig. 4.5** Closed-loop dynamics for a) input, ac side, and b) output, dc side, terminals.

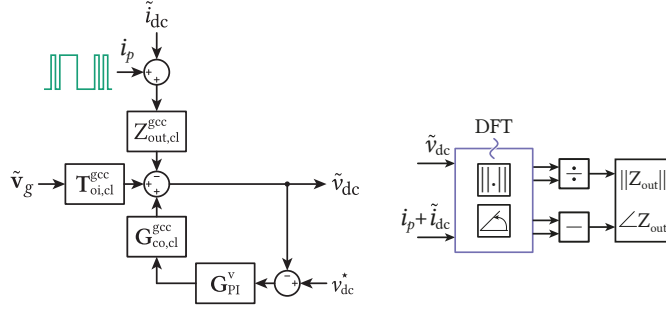


**Fig. 4.6** Schematics of small-signal perturbation injection and output impedance extraction of the closed-loop output impedance  $Z_{out,cl}^{dvc}$ .

dynamics, and then solving the input side dynamics. The output side dynamics is represented as:

$$Z_{out,cl}^{dvc} = -\left(\mathbf{I} + \mathbf{G}_{co,cl}^{gcc} \mathbf{G}_{PI}^v\right)^{-1} Z_{out,cl}^{gcc} \quad (4.25)$$

$$\mathbf{G}_{co,cl}^{dvc} = \left(\mathbf{I} + \mathbf{G}_{co,cl}^{gcc} \mathbf{G}_{PI}^v\right)^{-1} \mathbf{G}_{co,cl}^{gcc} \mathbf{G}_{PI}^v \quad (4.26)$$

$$\mathbf{T}_{oi,cl}^{dvc} = \left(\mathbf{I} + \mathbf{G}_{co,cl}^{gcc} \mathbf{G}_{PI}^v\right)^{-1} \mathbf{T}_{oi,cl}^{gcc} \quad (4.27)$$

While the input side dynamics is given as:

$$\mathbf{G}_{io,cl}^{dvc} = \mathbf{G}_{io,cl}^{gcc} + \mathbf{G}_{ci,cl}^{gcc} \mathbf{G}_{PI}^v Z_{out,cl}^{dvc} \quad (4.28)$$

$$\mathbf{Y}_{in,cl}^{dvc} = \mathbf{Y}_{in,cl}^{gcc} + \mathbf{G}_{ci,cl}^{gcc} \mathbf{G}_{PI}^v \mathbf{T}_{oi,cl}^{dvc} \quad (4.29)$$

$$\mathbf{G}_{ci,cl}^{dvc} = \mathbf{G}_{ci,cl}^{gcc} \mathbf{G}_{PI}^v - \mathbf{G}_{ci,cl}^{gcc} \mathbf{G}_{PI}^v \mathbf{G}_{co,cl}^{dvc} \quad (4.30)$$

The closed-loop dynamics under dc-link voltage control can be represented by block diagrams in **Fig. 4.5**.

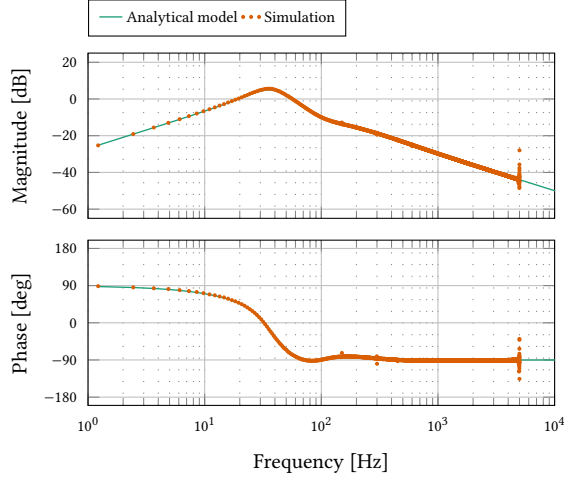
#### 4.1.4 Closed-loop Control Model Verification of the AFE

The closed-loop control model of the AFE can be verified by applying the techniques for open-loop verification provided in **Sec. 3.2**. The process follows the same logic used in the previous chapter, i.e. a small-signal current perturbation is injected into the output, or dc-side, current  $i_{dc}$ . The closed-loop operating point is identical to the one presented in **Tab. 3.5**, while the regulator gains are given in **Tab. 4.1**. The signal injected is the PRBS signal with the generation frequency of  $f_{gen} = 5$  kHz and the frequency resolution of  $f_r = 1.221$  Hz. An important characteristics of the closed-loop control model of the AFE to verify is its output impedance. The importance of the output impedance comes from the fact that it is the coupling element of the AFE and the HB inverter and as such can possibly influence the output dynamics of the CHB converter. A block diagram of the verification method is given in **Fig. 4.6**. The output impedances obtained on the basis of analytical developments, as well as from the simulation model of the AFE, are presented in **Fig. 4.7**. It can be seen that the output impedance obtained through the simulations corresponds extremely well to its analytical counterpart, thus confirming its mathematical validity.



**Tab. 4.1** Closed-loop control parameters

Gain	$K_{p, gcc}$	$K_{i, gcc}$	$K_{p, dvc}$	$K_{i, dvc}$	$K_{p, PLL}$	$K_{i, PLL}$
Value	18	33.4	1.4	192.9	46	4232

**Fig. 4.7** AFE output impedance magnitude and phase under the grid-current control and dc-link voltage control loops closed.

## 4.2 H-Bridge Control

As in the case of the AFE, the control of HB can be performed in cascaded manner, i.e. the current control loop is the inner, while the voltage control loop is the outer one. First the output voltage, or filter capacitor is controlled in  $dq$ -frame, including the decoupling. The voltage controller provides a reference current for the inductor current control as well in  $dq$ -frame. In the following sections first the current control is presented and its influence on the HB dynamics after which the influence of the voltage control is presented.

### 4.2.1 Inductor Current Control

The current control can be performed in SRF as was the case with the AFE. The control law is given as:

$$\mathbf{v}_{dq}^* = \underbrace{\left( K_{p,icc} + \frac{K_{i,icc}}{s} \right)}_{G_{PI}^i(s)} \left( \mathbf{i}_{f,dq}^* - \mathbf{H}_i \tilde{\mathbf{i}}_{f,dq} \right) + \mathbf{G}_{dec}^i \mathbf{H}_i \tilde{\mathbf{i}}_{f,dq} \quad (4.31)$$

Where the abbreviation stands for *inductor current control* and PI controller coefficients  $K_{p,icc}$  and  $K_{i,icc}$  can be sized using Magnitude Optimum Criterion [73],  $\mathbf{H}_i$  is the matrix representing the current transducer and  $\mathbf{G}_{dec}$  is the decoupling matrix.

$$\mathbf{H}_i = \begin{bmatrix} H_{i,d} & 0 \\ 0 & H_{i,q} \end{bmatrix} \quad (4.32)$$

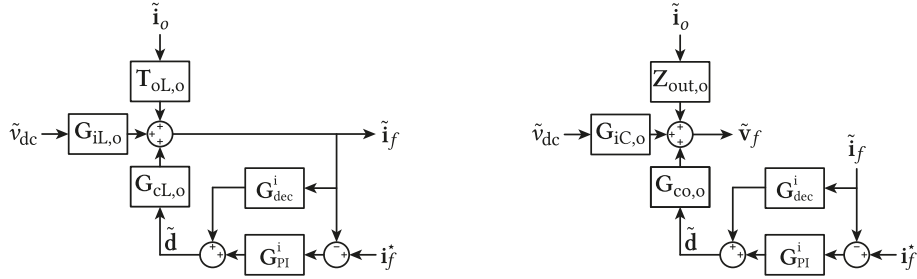


**Fig. 4.8** Small-signal closed-loop model of the HB under the inductor current control.

$$\mathbf{G}_{\text{dec}}^i = \begin{bmatrix} 0 & -\omega_s L_f \\ \omega_s L_f & 0 \end{bmatrix} \quad (4.33)$$

To obtain the duty cycles in the controller reference frame one has to divide the  $\tilde{v}_{dq}^*$  by the dc-link voltage giving the  $dq$ -frame duty cycles:

$$\tilde{d}_{dq} = \frac{\tilde{v}_{dq}^*}{V_{\text{dc}}} \quad (4.34)$$

Similarly to AFE control, the closed-loop dynamics under inductor current control can be solved from **Fig. 4.8**. The first step in the solution process is to find the duty cycle  $\tilde{d}_{dq}$  which is given as:

$$\tilde{d}_{dq} = \Delta_i \left[ \left( \mathbf{G}_{\text{dec}}^i - \mathbf{G}_{\text{PI}}^i \right) \mathbf{T}_{\text{oL,o}} \tilde{\mathbf{i}}_o + \left( \mathbf{G}_{\text{dec}}^i - \mathbf{G}_{\text{PI}}^i \right) \mathbf{G}_{\text{iL,o}} \tilde{v}_{\text{dc}} + \mathbf{G}_{\text{PI}}^i \tilde{\mathbf{i}}_f^* \right] \quad (4.35)$$

Where  $\Delta_i$  is given as:

$$\Delta_i = \mathbf{I} - \left( \mathbf{G}_{\text{PI}}^i - \mathbf{G}_{\text{dec}}^i \right) \mathbf{G}_{\text{cL,o}} \quad (4.36)$$

With the duty cycle defined as in (4.35) the closed-loop dynamics under current control can be solved. To solve the closed-loop dynamics one has to take a look back to **Fig. 3.14** from which three equations can be defined as:

$$\tilde{\mathbf{i}}_f^{\text{dc}} = \mathbf{T}_{\text{io,o}} \tilde{\mathbf{i}}_o + \mathbf{Y}_{\text{in,o}} \tilde{v}_{\text{dc}} + \mathbf{G}_{\text{ci,o}} \tilde{d}_{dq} \quad (4.37)$$

$$\tilde{\mathbf{i}}_f = \mathbf{T}_{\text{oL,o}} \tilde{\mathbf{i}}_o + \mathbf{G}_{\text{iL,o}} \tilde{v}_{\text{dc}} + \mathbf{G}_{\text{cL,o}} \tilde{d}_{dq} \quad (4.38)$$

$$\tilde{v}_f = -\mathbf{Z}_{\text{out,o}} \tilde{\mathbf{i}}_o + \mathbf{G}_{\text{iC,o}} \tilde{v}_{\text{dc}} + \mathbf{G}_{\text{co,o}} \tilde{d}_{dq} \quad (4.39)$$

When (4.35) is replaced in these three equations, input dynamics is given as:

$$\mathbf{T}_{\text{oi,cl}}^{\text{icc}} = \mathbf{T}_{\text{oi,o}} + \mathbf{G}_{\text{ci,o}} \Delta_i^{-1} \left( \mathbf{G}_{\text{dec}}^i - \mathbf{G}_{\text{PI}}^i \right) \mathbf{T}_{\text{oL,o}} \quad (4.40)$$

$$\mathbf{Y}_{\text{in,cl}}^{\text{icc}} = \mathbf{Y}_{\text{in,o}} + \mathbf{G}_{\text{ci,o}} \Delta_i^{-1} \left( \mathbf{G}_{\text{dec}}^i - \mathbf{G}_{\text{PI}}^i \right) \mathbf{G}_{\text{iL,o}} \quad (4.41)$$

$$\mathbf{G}_{\text{ci,cl}}^{\text{icc}} = \mathbf{G}_{\text{ci,o}} \Delta_i^{-1} \mathbf{G}_{\text{PI}}^i \quad (4.42)$$

While the output side dynamics is given as:

$$\mathbf{T}_{oL,cl}^{icc} = \mathbf{T}_{oL,o} + \mathbf{G}_{cL,o} \Delta_i^{-1} (\mathbf{G}_{dec}^i - \mathbf{G}_{PI}^i) \mathbf{T}_{oL,o} \quad (4.43)$$

$$\mathbf{G}_{iL,cl}^{icc} = \mathbf{G}_{iL,o} + \mathbf{G}_{cL,o} \Delta_i^{-1} (\mathbf{G}_{dec}^i - \mathbf{G}_{PI}^i) \mathbf{G}_{iL,o} \quad (4.44)$$

$$\mathbf{G}_{cL,cl}^{icc} = \mathbf{G}_{cL,o} \Delta_i^{-1} \mathbf{G}_{PI}^i \quad (4.45)$$

For the inductor current, while for the capacitor voltage it given as:

$$\mathbf{Z}_{out,cl}^{icc} = \mathbf{Z}_{out,o} + \mathbf{G}_{co,o} \Delta_i^{-1} (\mathbf{G}_{dec}^i - \mathbf{G}_{PI}^i) \mathbf{T}_{oL,o} \quad (4.46)$$

$$\mathbf{G}_{iC,cl}^{icc} = \mathbf{G}_{iC,o} + \mathbf{G}_{co,o} \Delta_i^{-1} (\mathbf{G}_{dec}^i - \mathbf{G}_{PI}^i) \mathbf{G}_{iL,o} \quad (4.47)$$

$$\mathbf{G}_{co,cl}^{icc} = \mathbf{G}_{co,o} \Delta_i^{-1} \mathbf{G}_{PI}^i \quad (4.48)$$

#### 4.2.2 Output Voltage Control

Similarly to the current control, the output voltage control can also be performed in the  $dq$ -frame. The control law can be formulated as:

$$\mathbf{i}_{f,dq}^* = \underbrace{\left( K_{p,cvc} + \frac{K_{i,cvc}}{s} \right)}_{\mathbf{G}_{PI}^v(s)} (\mathbf{v}_{f,dq}^* - \mathbf{H}_v \tilde{\mathbf{v}}_{f,dq}) + \mathbf{G}_{dec}^v \mathbf{H}_v \tilde{\mathbf{v}}_{f,dq} \quad (4.49)$$

Where the abbreviation “cvc” stands for *capacitor voltage control*, and the PI controller coefficients  $K_{p,cvc}$  and  $K_{i,cvc}$  can be sized using Magnitude Optimum Criterion [73],  $\mathbf{H}_v$  is the matrix representing the voltage transducer and  $\mathbf{G}_{dec}^v$  is the decoupling matrix.

$$\mathbf{H}_v = \begin{bmatrix} H_{v,d} & 0 \\ 0 & H_{v,q} \end{bmatrix} \quad (4.50)$$

$$\mathbf{G}_{dec}^v = \begin{bmatrix} 0 & -\omega_s C_f \\ \omega_s C_f & 0 \end{bmatrix} \quad (4.51)$$

The closed-loop dynamics under cascaded voltage and current control can be solved by first solving the dynamics at the output voltage side, then at the inductor side and finally at the input side. The voltage output dynamics is given as:

$$\mathbf{Z}_{out,cl}^{cvc} = \mathbf{Z}_{out,cl}^{icc} + \mathbf{G}_{co,cl}^{icc} \Delta_v^{-1} (\mathbf{G}_{dec}^v - \mathbf{G}_{PI}^v) \mathbf{Z}_{out,cl}^{icc} \quad (4.52)$$

$$\mathbf{G}_{iC,cl}^{cvc} = \mathbf{G}_{iC,cl}^{icc} + \mathbf{G}_{co,cl}^{icc} \Delta_v^{-1} (\mathbf{G}_{dec}^v - \mathbf{G}_{PI}^v) \mathbf{G}_{iC,cl}^{icc} \quad (4.53)$$

$$\mathbf{G}_{co,cl}^{cvc} = \mathbf{G}_{co,cl}^{icc} \Delta_v^{-1} \mathbf{G}_{PI}^v \quad (4.54)$$

The inductor current dynamic is given as:

$$\mathbf{T}_{oL,cl}^{cvc} = \mathbf{T}_{oL,cl}^{icc} + \mathbf{G}_{cL,cl}^{icc} \Delta_v^{-1} (\mathbf{G}_{dec}^v - \mathbf{G}_{PI}^v) \mathbf{Z}_{out,cl}^{icc} \quad (4.55)$$

$$\mathbf{G}_{iL,cl}^{cvc} = \mathbf{G}_{iL,cl}^{icc} + \mathbf{G}_{cL,cl}^{icc} \Delta_v^{-1} (\mathbf{G}_{dec}^v - \mathbf{G}_{PI}^v) \mathbf{G}_{iC,cl}^{icc} \quad (4.56)$$

$$\mathbf{G}_{cL,cl}^{cvc} = \mathbf{G}_{cL,cl}^{icc} \Delta_v^{-1} \mathbf{G}_{PI}^v \quad (4.57)$$

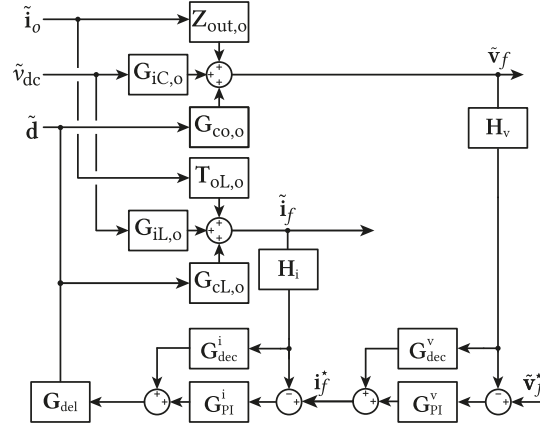


**Fig. 4.9** Output side closed-loop dynamics of the HB inverter with cascaded inductor current and capacitor voltage control.

While for the input side it is given as:

$$\mathbf{T}_{oi,cl}^{cvc} = \mathbf{T}_{oi,cl}^{icc} + \mathbf{G}_{ci,cl}^{icc} \Delta_v^{-1} (\mathbf{G}_{dec}^v - \mathbf{G}_{PI}^v) \mathbf{Z}_{out,cl}^{icc} \quad (4.58)$$

$$\mathbf{Y}_{in,cl}^{cvc} = \mathbf{Y}_{in,cl}^{icc} + \mathbf{G}_{ci,cl}^{icc} \Delta_v^{-1} (\mathbf{G}_{dec}^v - \mathbf{G}_{PI}^v) \mathbf{G}_{IC,cl}^{icc} \quad (4.59)$$

$$\mathbf{G}_{ci,cl}^{cvc} = \mathbf{G}_{ci,cl}^{icc} \Delta_v^{-1} \mathbf{G}_{PI}^v \quad (4.60)$$

Finally, the output side closed-loop dynamics of the HB inverter can be represented with the block diagram in **Fig. 4.9**

### 4.2.3 Second Order Generalised Integrator in the $dq$ -Frame

The previous developments and the model in the  $dq$ -frame were based on the assumption that there exists a signal that is in quadrature with the single-phase signal. Moreover, it was taken as an assumption that the dynamics of the QSG does not influence the overall dynamics of the HB inverter. While this is true in the frequency region above twice the output frequency, in the lower frequency region this hypothesis does not stand and the influence of the QSG needs to be taken into account [75]. The second-order generalized integrator (SOGI) transfer function matrix is given as:

$$\begin{aligned} \mathbf{H}_{SOGI} &= \begin{bmatrix} \frac{K_S \omega_s s}{s^2 + K_S \omega_s s + \omega_s^2} & 0 \\ 0 & \frac{K_S \omega_s s}{s^2 + K_S \omega_s s + \omega_s^2} \end{bmatrix} \\ &= \begin{bmatrix} H_{SOGI}(s) & 0 \\ 0 & H_{SOGI}(s) \end{bmatrix} \end{aligned} \quad (4.61)$$

The SOGI transfer function matrix presented in the equation (4.61) in  $\alpha\beta$ -frame can be described in the  $dq$ -frame as well. The SOGI transfer function in the  $dq$ -domain is obtained by combining the transfer function matrix in the  $\alpha\beta$ -frame and the Park transformation, with the remark that the first one is an  $s$ -domain matrix and the second one is a time-domain matrix. For a time-domain function  $x_\alpha(t)$  and its orthogonal counterpart  $x_\beta(t)$ , its  $dq$ -frame counterpart can be obtained by applying the

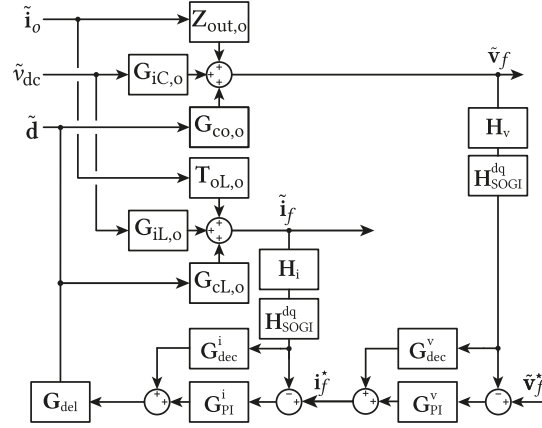


**Fig. 4.10** Output side closed-loop dynamics of the HB inverter with cascaded inductor current and capacitor voltage control and with the  $dq$ -frame SOGI model in the current and voltage path.

Park transformation as:

$$\begin{aligned} \begin{bmatrix} x_d \\ x_q \end{bmatrix} &= \begin{bmatrix} \cos \theta_s & \sin \theta_s \\ -\sin \theta_s & \cos \theta_s \end{bmatrix} \begin{bmatrix} h_{\text{SOGI}} * x_\alpha \\ h_{\text{SOGI}} * x_\beta \end{bmatrix} \\ &= \begin{bmatrix} \cos \theta_s (h_{\text{SOGI}} * x_\alpha) + \sin \theta_s (h_{\text{SOGI}} * x_\beta) \\ -\sin \theta_s (h_{\text{SOGI}} * x_\alpha) + \cos \theta_s (h_{\text{SOGI}} * x_\beta) \end{bmatrix} \end{aligned} \quad (4.62)$$

Where  $*$  is the convolution operation. In the following developments the subscript "SOGI" is omitted to avoid clutter. Here, a property of the Laplace transform for a product can be applied as

$$\begin{aligned} h(t) \cos \theta_s &= \frac{1}{2} (H(s + j\omega_s) + H(s - j\omega_s)) \\ h(t) \sin \theta_s &= \frac{j}{2} (H(s + j\omega_s) - H(s - j\omega_s)) \end{aligned} \quad (4.63)$$

Subsequently, this product can be replaced into the equation (4.62). Finally, the SOGI modelling in  $dq$ -frame is given as:

$$\begin{aligned} \begin{bmatrix} X_d(s) \\ X_q(s) \end{bmatrix} &= \begin{bmatrix} \frac{1}{2} (H(s + j\omega_s) X_\alpha(s + j\omega_s) + H(s - j\omega_s) X_\alpha(s - j\omega_s)) \\ -\frac{j}{2} (H(s + j\omega_s) X_\alpha(s + j\omega_s) - H(s - j\omega_s) X_\alpha(s - j\omega_s)) \\ + \frac{j}{2} (H(s + j\omega_s) X_\beta(s + j\omega_s) - H(s - j\omega_s) X_\beta(s - j\omega_s)) \\ + \frac{1}{2} (H(s + j\omega_s) X_\beta(s + j\omega_s) + H(s - j\omega_s) X_\beta(s - j\omega_s)) \end{bmatrix} \\ &= \underbrace{\begin{bmatrix} A(s) & -B(s) \\ B(s) & A(s) \end{bmatrix}}_{\mathbf{H}_{\text{SOGI}}^{\text{dq}}(s)} \begin{bmatrix} \frac{1}{2} (X_\alpha(s + j\omega_s) + X_\alpha(s - j\omega_s)) + \frac{j}{2} (X_\beta(s + j\omega_s) - X_\beta(s - j\omega_s)) \\ \frac{j}{2} (X_\alpha(s + j\omega_s) - X_\alpha(s - j\omega_s)) + \frac{1}{2} (X_\beta(s + j\omega_s) + X_\beta(s - j\omega_s)) \end{bmatrix} \end{aligned} \quad (4.64)$$

Where  $A(s)$  and  $B(s)$  are defined as:

$$A(s) = \frac{1}{2} [H(s + j\omega_s) + H(s - j\omega_s)] \quad B(s) = \frac{j}{2} [H(s + j\omega_s) - H(s - j\omega_s)] \quad (4.65)$$

Finally, the modified output side closed-loop dynamics of the HB with the SOGI modelled in the  $dq$ -frame can be represented with **Fig. 4.10**.

### 4.3 Summary

This chapter presented the closed-loop control modelling of the AFE and the HB inverter with the further goal of establishing their connected model in order to study the load-source interactions of two converters. The AFE closed-loop control modelling revolves around the modelling of the closed-loop control of the input, or grid, current and the dc-link voltage and their cascaded link. Moreover, the influence of the PLL is taken into account and modelled into the closed-loop control. On the other side, the modelling of the HB focuses on the cascaded control of the filter inductor current and filter capacitor voltage which is at the same time the output voltage of the HB inverter. Moreover, as the HB modelling is performed with the assumption that there exists a QSG which creates an orthogonal signal required for the modelling in the  $dq$ -frame, the SOGI-QSG is also modelled in the  $dq$ -frame and included in the overall closed-loop model. Thus, all elements required for the load-source interaction investigation are put into place.

# 5

## Load and Source Affected Dynamics

*This chapter presents the assessment of the impact that the AFE on the input side has on the HB output side, which is responsible for the realization of the perturbation signal of the topology realized in thesis.. Small-signal model in the  $dq$ -frame is developed, and to validate the theoretical developments, a new method to measure the single-phase output dynamics in the  $dq$ -frame is proposed and the measurement is performed using offline and real-time simulations on a hardware-in-the-loop platform. It is shown that the AFE and the HB are perfectly decoupled and that there is no influence of the AFE closed-loop dynamics on the HB inverter.*

### 5.1 Source-Affected Dynamics Characterization

The motivation for the evaluation of the load and source affected dynamics comes from the requirement that for precise injection of perturbation signal into the SUT, one needs to ensure that the input side of the CHB does not in any way limit the output, and that there are no other frequency components present that may impact the measurements. The methodology to respond to this question puts to use the state-space source-affected modelling and presents the model of the PEBB in the  $dq$ -frame. To confirm the model there needs to exist a method to measure the single-phase characteristics and represent them in  $dq$ -frame. Ideally, for the best possible impedance identification of the SUT, the output stage should be completely decoupled from the input one, and the presence of the active element with its closed-loop control should not be a limiting factor for impedance measurement.

In **Sec. 3.3** it was stated that the dc-link voltage source is ideal with respect to the fact that the voltage was controlled on the AFE side. However, in practice control loops do not have an infinite bandwidth and as such the voltage source cannot be considered ideal. This means that the source contains a non-zero internal impedance, which is the same closed-loop control output impedance  $Z_{out,cl}^{dvc}$  obtained in the equation (4.25). The modified schematics with the  $Z_{out,cl}^{dvc}$  present is depicted **Fig. 5.1**.

In order to redefine the HB inverter model taking into account the  $Z_{out,cl}^{dvc}$  first the dc-side current can be redefined to reflect the presence of the impedance. Thus, from **Fig. 5.1** the dc-side current can be obtained as:

$$i_f^{dc} = \frac{v_{dc}^s - v_{dc}}{Z_{out,cl}^{dvc}} \quad (5.1)$$

Where  $v_{dc}^s$  is the dc-link voltage controlled by the AFE control system, i.e. by the source side and

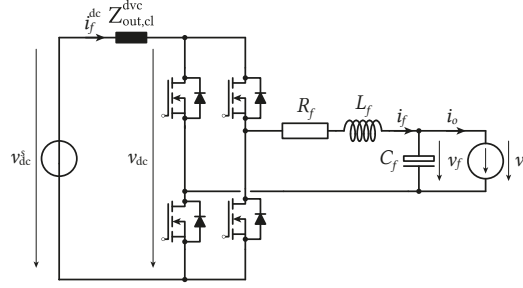


**Fig. 5.1** HB with an output LC filter and internal source impedance resulting in the closed-loop control of the AFE.

hence the superscript “s”. As a reminder, closed loop dynamics of the HB is given as:

$$\begin{bmatrix} \tilde{\mathbf{i}}_{f,dq} \\ \tilde{\mathbf{v}}_{f,dq} \\ \tilde{i}_f^{\text{dc}} \end{bmatrix} = \begin{bmatrix} \mathbf{G}_{iL,cl}^{\text{cvc}} & \mathbf{G}_{cL,cl}^{\text{cvc}} & \mathbf{T}_{oL,cl}^{\text{cvc}} \\ \mathbf{G}_{iC,cl}^{\text{cvc}} & \mathbf{G}_{co,cl}^{\text{cvc}} & \mathbf{Z}_{out,cl}^{\text{cvc}} \\ \mathbf{Y}_{in,cl}^{\text{cvc}} & \mathbf{G}_{ci,cl}^{\text{cvc}} & \mathbf{T}_{oi,cl}^{\text{cvc}} \end{bmatrix} \begin{bmatrix} \tilde{v}_{dc} \\ \tilde{\mathbf{v}}_{f,dq}^* \\ \tilde{\mathbf{i}}_{o,dq} \end{bmatrix} \quad (5.2)$$

From the equation (5.2) the  $\tilde{i}_f^{\text{dc}}$  can be obtained as:

$$\tilde{i}_f^{\text{dc}} = \mathbf{Y}_{in,cl}^{\text{cvc}} \tilde{v}_{dc} + \mathbf{G}_{ci,cl}^{\text{cvc}} \tilde{\mathbf{v}}_{f,dq}^* + \mathbf{T}_{oi,cl}^{\text{cvc}} \tilde{\mathbf{i}}_{o,dq} \quad (5.3)$$

Plugging (5.1) into (5.3) gives the  $\tilde{v}_{dc}^s$  expressed in terms of  $\tilde{v}_{dc}$  as:

$$\tilde{v}_{dc} = \frac{\tilde{v}_{dc}^s - \mathbf{Z}_{out,cl}^{\text{dvc}} \mathbf{G}_{ci,cl}^{\text{cvc}} \tilde{\mathbf{v}}_{f,dq}^* - \mathbf{Z}_{out,cl}^{\text{dvc}} \mathbf{T}_{oi,cl}^{\text{cvc}} \tilde{\mathbf{i}}_{o,dq}}{1 + \mathbf{Z}_{out,cl}^{\text{dvc}} \mathbf{Y}_{in,cl}^{\text{cvc}}} \quad (5.4)$$

Replacing  $\tilde{v}_{dc}$  in (5.2) by (5.4) gives:

$$\begin{bmatrix} \tilde{\mathbf{i}}_{f,dq} \\ \tilde{\mathbf{v}}_{f,dq} \\ \tilde{i}_f^{\text{dc}} \end{bmatrix} = \begin{bmatrix} \mathbf{G}_{iL,cl}^{\text{cvc}} & \mathbf{G}_{cL,cl}^{\text{cvc}} & \mathbf{T}_{oL,cl}^{\text{cvc}} \\ \mathbf{G}_{iC,cl}^{\text{cvc}} & \mathbf{G}_{co,cl}^{\text{cvc}} & \mathbf{Z}_{out,cl}^{\text{cvc}} \\ \mathbf{Y}_{in,cl}^{\text{cvc}} & \mathbf{G}_{ci,cl}^{\text{cvc}} & \mathbf{T}_{oi,cl}^{\text{cvc}} \end{bmatrix} \begin{bmatrix} \mathbf{I} & \frac{-\mathbf{Z}_{out,cl}^{\text{dvc}} \mathbf{G}_{ci,cl}^{\text{cvc}}}{1 + \mathbf{Z}_{out,cl}^{\text{dvc}} \mathbf{Y}_{in,cl}^{\text{cvc}}} & \frac{-\mathbf{Z}_{out,cl}^{\text{dvc}} \mathbf{T}_{oi,cl}^{\text{cvc}}}{1 + \mathbf{Z}_{out,cl}^{\text{dvc}} \mathbf{Y}_{in,cl}^{\text{cvc}}} \\ 0 & \mathbf{I} & 0 \\ 0 & 0 & \mathbf{I} \end{bmatrix} \begin{bmatrix} \tilde{v}_{dc}^s \\ \tilde{\mathbf{v}}_{f,dq}^* \\ \tilde{\mathbf{i}}_{o,dq} \end{bmatrix} \quad (5.5)$$

Finally, the closed loop dynamics of the HB under the influence of the AFE output dynamics is obtained as:

$$\begin{bmatrix} \tilde{\mathbf{i}}_{f,dq} \\ \tilde{\mathbf{v}}_{f,dq} \\ \tilde{i}_f^{\text{dc}} \end{bmatrix} = \begin{bmatrix} \frac{\mathbf{G}_{iL,cl}^{\text{cvc}}}{1 + \mathbf{Z}_{out,cl}^{\text{dvc}} \mathbf{Y}_{in,cl}^{\text{cvc}}} & \mathbf{G}_{cL,cl}^{\text{cvc}} - \frac{\mathbf{G}_{iL,cl}^{\text{cvc}} \mathbf{Z}_{out,cl}^{\text{dvc}} \mathbf{G}_{ci,cl}^{\text{cvc}}}{1 + \mathbf{Z}_{out,cl}^{\text{dvc}} \mathbf{Y}_{in,cl}^{\text{cvc}}} & \mathbf{T}_{oL,cl}^{\text{cvc}} - \frac{\mathbf{G}_{iL,cl}^{\text{cvc}} \mathbf{Z}_{out,cl}^{\text{dvc}} \mathbf{T}_{oi,cl}^{\text{cvc}}}{1 + \mathbf{Z}_{out,cl}^{\text{dvc}} \mathbf{Y}_{in,cl}^{\text{cvc}}} \\ \frac{\mathbf{G}_{iC,cl}^{\text{cvc}}}{1 + \mathbf{Z}_{out,cl}^{\text{dvc}} \mathbf{Y}_{in,cl}^{\text{cvc}}} & \mathbf{G}_{co,cl}^{\text{cvc}} - \frac{\mathbf{G}_{iC,cl}^{\text{cvc}} \mathbf{Z}_{out,cl}^{\text{dvc}} \mathbf{G}_{ci,cl}^{\text{cvc}}}{1 + \mathbf{Z}_{out,cl}^{\text{dvc}} \mathbf{Y}_{in,cl}^{\text{cvc}}} & \mathbf{Z}_{out,cl}^{\text{cvc}} - \frac{\mathbf{G}_{iL,cl}^{\text{cvc}} \mathbf{Z}_{out,cl}^{\text{dvc}} \mathbf{T}_{oi,cl}^{\text{cvc}}}{1 + \mathbf{Z}_{out,cl}^{\text{dvc}} \mathbf{Y}_{in,cl}^{\text{cvc}}} \\ \frac{\mathbf{Y}_{in,cl}^{\text{cvc}}}{1 + \mathbf{Z}_{out,cl}^{\text{dvc}} \mathbf{Y}_{in,cl}^{\text{cvc}}} & \frac{\mathbf{G}_{ci,cl}^{\text{cvc}}}{1 + \mathbf{Z}_{out,cl}^{\text{dvc}} \mathbf{Y}_{in,cl}^{\text{cvc}}} & \frac{\mathbf{T}_{oi,cl}^{\text{cvc}}}{1 + \mathbf{Z}_{out,cl}^{\text{dvc}} \mathbf{Y}_{in,cl}^{\text{cvc}}} \end{bmatrix} \begin{bmatrix} \tilde{v}_{dc}^s \\ \tilde{\mathbf{v}}_{f,dq}^* \\ \tilde{\mathbf{i}}_{o,dq} \end{bmatrix} \quad (5.6)$$



## 5.2 Single-Phase Measurements in the $dq$ -Frame

When it comes to characterizing a single PEBB of a MV-CHB converter, two characteristics are worth mentioning and investigating. The first one is the closed-loop output impedance of a PEBB,  $\mathbf{Z}_{\text{out,cl}}^{\text{cvc}}$ , while the second one is the control-to-output characteristics,  $\mathbf{G}_{\text{co,cl}}^{\text{cvc}}$ . The challenge put forward when trying to measure these characteristics comes from the fact that both of them are small-signal characteristics at the dc level, while the actual system is an ac system, and as such the characteristics cannot be directly measured in the  $dq$ -frame. Instead, an approach in which the measurements from a single-phase system are transferred into a  $dq$ -frame needs to be devised. As the output impedance is an external characteristics and the control-to-output characteristics is an internal one, the methods for measuring the two will be different. In any case, the use of wideband signals such as the PRBS is preferable as opposed to the method using an ac sweep.

### 5.2.1 Single-Phase Output Impedance Measurement in $dq$ -Frame

Recently, PRBS signals have seen substantial use for system identification and impedance measurement [76]–[78]. The advantage of these signals lies in the fact that they are well suited for characterization of dynamics systems where rapid measurement is necessary due to the possibility of variation of system state in time. What is common for measurements in [76]–[78] is that they are performed in dc or three-phase ac systems after which the results are represented in  $dq$ -frame even though they represent ac measurements. Hilbert transform was successfully applied to single-phase measurement and representation in  $dq$ -frame in [79]. However, the transform was applied to a single tone perturbation and an ac sweep was performed. The reason for using the Hilbert transform is to create an orthogonal signal to the original one, which is obviously beneficial when trying to perform  $dq$ -frame measurements. A description of the Hilbert transform is presented in **Sec. A.3**

Measurement process of  $\mathbf{Z}_{\text{out,cl}}^{\text{cvc}}$  requires two perturbation injections and two measurement sets. First perturbation is created in the  $dq$ -frame and then transformed into the  $\alpha\beta$ -frame as:

$$\begin{bmatrix} i_{p,d}(t) \\ i_{p,q}(t) \end{bmatrix} = \begin{bmatrix} p(t) \\ 0 \end{bmatrix} \xrightarrow{\text{inv. Park}} \begin{bmatrix} i_{p,\alpha}(t) \\ i_{p,\beta}(t) \end{bmatrix} = \begin{bmatrix} i_{p,d}(t) \cos \omega_s t - i_{p,q}(t) \sin \omega_s t \\ i_{p,d}(t) \sin \omega_s t + i_{p,q}(t) \cos \omega_s t \end{bmatrix} = \begin{bmatrix} p(t) \cos \omega_s t \\ p(t) \sin \omega_s t \end{bmatrix} \quad (5.7)$$

Afterwards only the  $\alpha$ -axis is injected into, or by, the current source in **Fig. 5.1**, where the  $p(t)$  is the PRBS signal in time domain. The resulting voltage measured would be equal to (5.9).

The second perturbation is created as:

$$\begin{bmatrix} \hat{i}_{p,d}(t) \\ \hat{i}_{p,q}(t) \end{bmatrix} = \begin{bmatrix} 0 \\ -\hat{p}(t) \end{bmatrix} \xrightarrow{\text{inv. Park}} \begin{bmatrix} \hat{i}_{p,\alpha}(t) \\ \hat{i}_{p,\beta}(t) \end{bmatrix} = \begin{bmatrix} \hat{i}_{p,d}(t) \cos \omega_s t - \hat{i}_{p,q}(t) \sin \omega_s t \\ \hat{i}_{p,d}(t) \sin \omega_s t + \hat{i}_{p,q}(t) \cos \omega_s t \end{bmatrix} = \begin{bmatrix} \hat{p}(t) \sin \omega_s t \\ -\hat{p}(t) \cos \omega_s t \end{bmatrix} \quad (5.8)$$

Where  $\hat{p}(t)$  is the Hilbert transform of  $p(t)$ , and the  $\hat{i}_{p,\beta}$  is injected into the current source as a small-signal perturbation. This would cause the resulting voltage to be equal to (5.10).

$$v_f(t) = V_m \cos \omega_s t + v_p(t) \cos \omega_s t \quad (5.9)$$

$$\hat{v}_f(t) = V_m \cos \omega_s t - \hat{v}_p(t) \cos \omega_s t \quad (5.10)$$

**Tab. 5.1** AFE parameters

$v_{g,d} = 580 \text{ V}$	$f_g = 50 \text{ Hz}$
$v_{g,q} = 0 \text{ V}$	$L_g = 5.4 \text{ mH}$
$i_{g,d} = 41.5 \text{ A}$	$R_g = 10 \text{ m}\Omega$
$i_{g,q} = 0 \text{ A}$	$v_{dc} = 1.2 \text{ kV}$
$K_{p,gcc} = 18$	$K_{i,gcc} = 33$
$K_{p,dvc} = 1.4$	$K_{i,dvc} = 192$

**Tab. 5.2** HB parameters

$v_{f,d} = 600 \text{ V}$	$f_s = 50 \text{ Hz}$
$v_{f,q} = 0 \text{ V}$	$L_f = 1.4 \text{ mH}$
$i_{o,d} = 60 \text{ A}$	$R_f = 100 \text{ m}\Omega$
$i_{o,q} = 0 \text{ A}$	$C_f = 24 \text{ }\mu\text{H}$
$K_{p,lcc} = .25$	$K_{i,lcc} = 5$
$K_{p,cvc} = 1$	$K_{i,cvc} = 52$

Applying the Hilbert transform to (5.10) and combining the resulting voltage with voltage from (5.9) gives a set of voltages in the  $\alpha\beta$ -frame. Subsequently, these voltage can then be transformed into to the  $dq$ -frame as:

$$\begin{bmatrix} v_{f,\alpha}(t) \\ v_{f,\beta}(t) \end{bmatrix} = \begin{bmatrix} V_m \cos \omega_s t + v_{p,\alpha}(t) \cos \omega_s t \\ V_m \sin \omega_s t + v_{p,\beta}(t) \sin \omega_s t \end{bmatrix} \xrightarrow{\text{Park}} \begin{bmatrix} v_{f,d}(t) \\ v_{f,q}(t) \end{bmatrix} = \begin{bmatrix} V_m + v_{p,d}(t) \\ v_{p,q}(t) \end{bmatrix} \quad (5.11)$$

The same procedure can be applied for the resulting current, which would be equal to:

$$i_o(t) = I_o \cos \omega_s t + p(t) \cos \omega_s t \quad (5.12)$$

$$\hat{i}_o(t) = I_o \cos \omega_s t - \hat{p}(t) \cos \omega_s t \quad (5.13)$$

Now, the Hilbert transform is applied to (5.13) and combined with (5.12). These two equations can be transformed to the  $dq$ -frame as:

$$\begin{bmatrix} i_{o,\alpha}(t) \\ i_{o,\beta}(t) \end{bmatrix} = \begin{bmatrix} I_o \cos \omega_s t + p(t) \cos \omega_s t \\ I_o \sin \omega_s t + p(t) \sin \omega_s t \end{bmatrix} \xrightarrow{\text{Park}} \begin{bmatrix} i_{o,d}(t) \\ i_{o,q}(t) \end{bmatrix} = \begin{bmatrix} I_o + p(t) \\ p(t) \end{bmatrix} \quad (5.14)$$

This method can be effectively illustrated using **Fig. 5.2**. In order to put the proposed method to test, two simulations were performed. The first simulation considered only the HB operating with an ideal voltage source on the dc side, while in the second simulation the full PEBB was simulated. The PEBB parameters are given in **Tabs. 5.1** and **5.2**. The  $d$ -axis closed-loop output impedance, extracted using the proposed method, is given in **Fig. 5.3**. From the presented results it can be concluded that there is no influence of the AFE on the output impedance of the single-phase HB inverter. However, it can also be noted that the method proposed gives a good match for frequencies above 100 Hz. Below that frequency there are some discrepancies between the proposed model and the measurement.

### 5.2.2 Single-Phase Control-to-Output Characteristics Measurement in $dq$ -Frame

To measure the control-to-output characteristics in the  $dq$ -frame of a single-phase HB inverter, one needs to perform two sets of perturbation injections and output voltage measurements. Thus, the  $\mathbf{G}_{co,cl}^{cvc}$  can be uniquely defined. The  $\mathbf{G}_{co,cl}^{cvc}$  can be defined as a relation between the output voltage reference and the measured voltage as:

$$\begin{bmatrix} \tilde{v}_{f,d} \\ \tilde{v}_{f,q} \end{bmatrix} = \mathbf{G}_{co,cl}^{cvc} \begin{bmatrix} \tilde{v}_{f,d}^* \\ \tilde{v}_{f,q}^* \end{bmatrix} \quad (5.15)$$

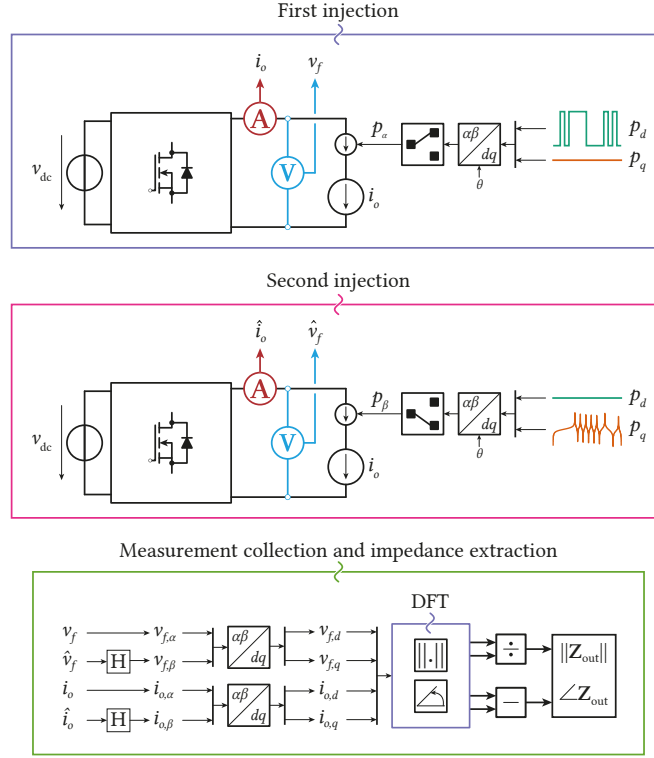


**Fig. 5.2**  $dq$ -frame output impedance measurement principle of a single-phase HB inverter

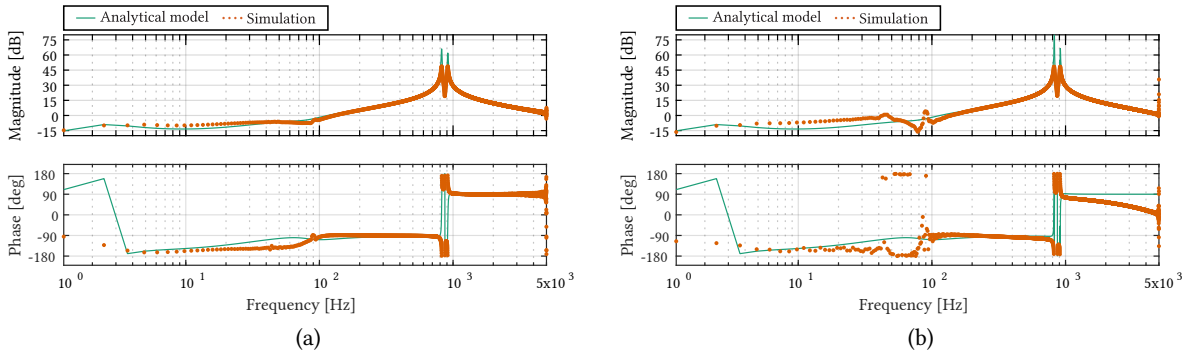


**Fig. 5.3**  $d$ -axis output impedance  $Z_{\text{out,cl,dd}}^{\text{cvc}}$  with a) standalone-operation of the HB-inverter compared to the same characteristics, b) when the AFE is operating at the input stage.

Taking into account that two injections are required, the  $\mathbf{G}_{\text{co,cl}}^{\text{cvc}}$  can be calculated as:

$$\mathbf{G}_{\text{co,cl}}^{\text{cvc}} = \begin{bmatrix} \tilde{v}_{\text{fd},1} & \tilde{v}_{\text{Cd},2} \\ \tilde{v}_{\text{fq},1} & \tilde{v}_{\text{Cq},2} \end{bmatrix} \begin{bmatrix} \tilde{v}_{\text{fd},1}^* & \tilde{v}_{\text{fd},2}^* \\ \tilde{v}_{\text{fq},1}^* & \tilde{v}_{\text{fq},2}^* \end{bmatrix}^{-1} \quad (5.16)$$

Moreover,  $[\tilde{v}_{\text{fd},1}, \tilde{v}_{\text{fq},1}]$  and  $[\tilde{v}_{\text{fd},2}, \tilde{v}_{\text{fq},2}]$  are linearly independent as well as  $[\tilde{v}_{\text{fd},1}^*, \tilde{v}_{\text{fq},1}^*]$  and  $[\tilde{v}_{\text{fd},2}^*, \tilde{v}_{\text{fq},2}^*]$ . The perturbation can be injected directly in the reference voltage  $\tilde{v}_{\text{f,dq}}^*$  in the control system, but the response can only be measured on the inverter terminals in the single-phase system. First perturbation

is injected into the  $d$ -axis voltage reference, while the  $q$ -axis perturbation is kept at zero value. For the second injection, the opposite holds. Thus the perturbation matrix  $\mathbf{P}(t)$  in the  $dq$ -frame is designed as:

$$\mathbf{P}(t) = \begin{bmatrix} v_{pd,1} & v_{pd,2} \\ v_{pq,1} & v_{pq,2} \end{bmatrix} = \begin{bmatrix} p(t) & 0 \\ 0 & p(t) \end{bmatrix} \quad (5.17)$$

Where the  $p(t)$  is the PRBS signal in time domain, and the perturbation is injected into the voltage reference  $\hat{\mathbf{v}}_{f,dq}^*$ .

The idea behind the single-phase measurement of  $\mathbf{G}_{co,cl}^{cvc}$  in  $dq$ -frame lies in measuring the response of two systems, one original and one orthogonal to it. For the original system, considering  $\theta_s = \omega_s t$ , the Park transform and its inverse are given as:

$$\mathbf{T}_\Theta = \begin{bmatrix} \cos \theta_s & \sin \theta_s \\ -\sin \theta_s & \cos \theta_s \end{bmatrix} \quad (5.18)$$

$$\mathbf{T}_\Theta^{-1} = \begin{bmatrix} \cos \theta_s & -\sin \theta_s \\ \sin \theta_s & \cos \theta_s \end{bmatrix}$$

While for the orthogonal system all the transformations and its inverse in the control algorithm are rotated by  $\pi/2$  and are given as:

$$\bar{\mathbf{T}}_\Theta = \begin{bmatrix} \cos(\theta_s - \frac{\pi}{2}) & \sin(\theta_s - \frac{\pi}{2}) \\ -\sin(\theta_s - \frac{\pi}{2}) & \cos(\theta_s - \frac{\pi}{2}) \end{bmatrix} = \begin{bmatrix} \sin \theta_s & -\cos \theta_s \\ \cos \theta_s & \sin \theta_s \end{bmatrix} \quad (5.19)$$

$$\bar{\mathbf{T}}_\Theta^{-1} = \begin{bmatrix} \sin \theta_s & \cos \theta_s \\ -\cos \theta_s & \sin \theta_s \end{bmatrix}$$

After injecting the perturbation and measuring the output voltages, the original system will provide the voltage  $v_{f,\alpha}$ , while the orthogonal one will provide  $v_{f,\beta}$ . The two voltage measurements are then combined and transformed into their  $dq$ -frame counterparts, thus effectively providing a way to perform single-phase measurements in  $dq$ -frame. Once the measurements are obtained one needs to extract the frequency spectrum of the measurements and the perturbation signal using fast Fourier transform (FFT) algorithm upon which the equation (5.16) can be applied. For this approach to be possible it is considered that one has the access to the control system to which the system designers and converter manufacturers usually do. The approach of the output characteristics measurement can graphically be depicted using the schematics presented in **Fig. 5.4**.

For the purposes of obtaining trustworthy results that would support mathematical modelling and offline simulations, real-time HIL system is created. The physical system is presented in **Fig. 5.5**. Two main parts of the system are the RT-Box real-time simulator and the TMS320F28069 MCU. The switching models of the PEBB and the single-phase HB are implemented in the RT-Box and are used to simulate the converter structures in the real-time. The grid synchronization and control of the models is deployed on the MCU as well as the perturbation signal that is injected in the output voltage reference. The signal was generated by a 12-bit-length shift register resulting in 4095-bit-long PRBS signal. The sequence was generated at 5 kHz generation frequency which sets the injection time at 0.819 s. Only one sequence was injected due to the limitations in capturing the signals inside the

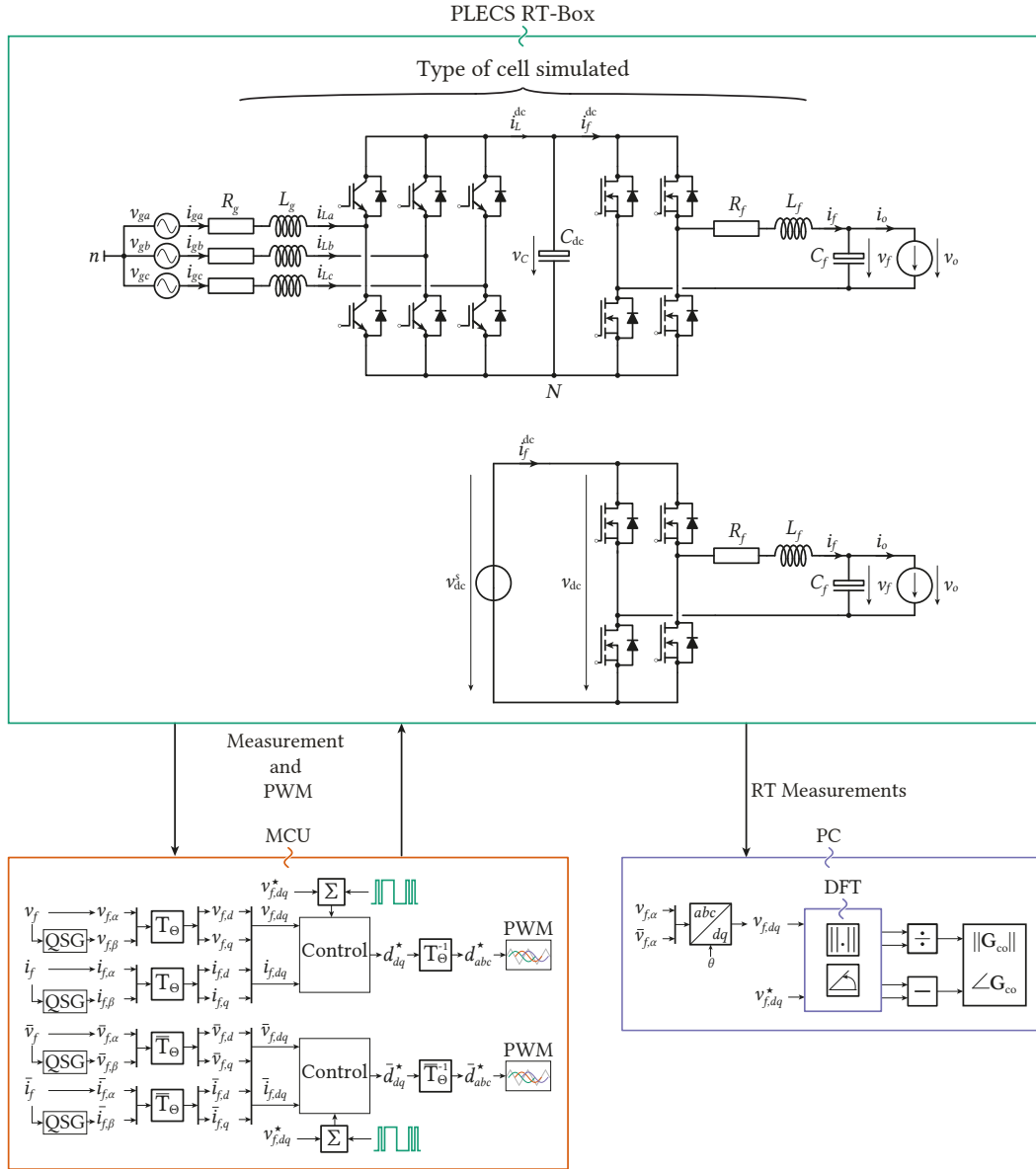


**Fig. 5.4** Schematics of the hardware-in-the-loop system, where the switching models of the converters are implemented inside the PLECS environment and are simulated in real-time on the RT-Box platform. The control for the converters is implemented on the MCU which sends the PWM signals to the RT-Box and receives the measurements from the RT-Box. Finally, the measurements from the RT-Box are extracted to a PC where the data is processed and results are obtained.

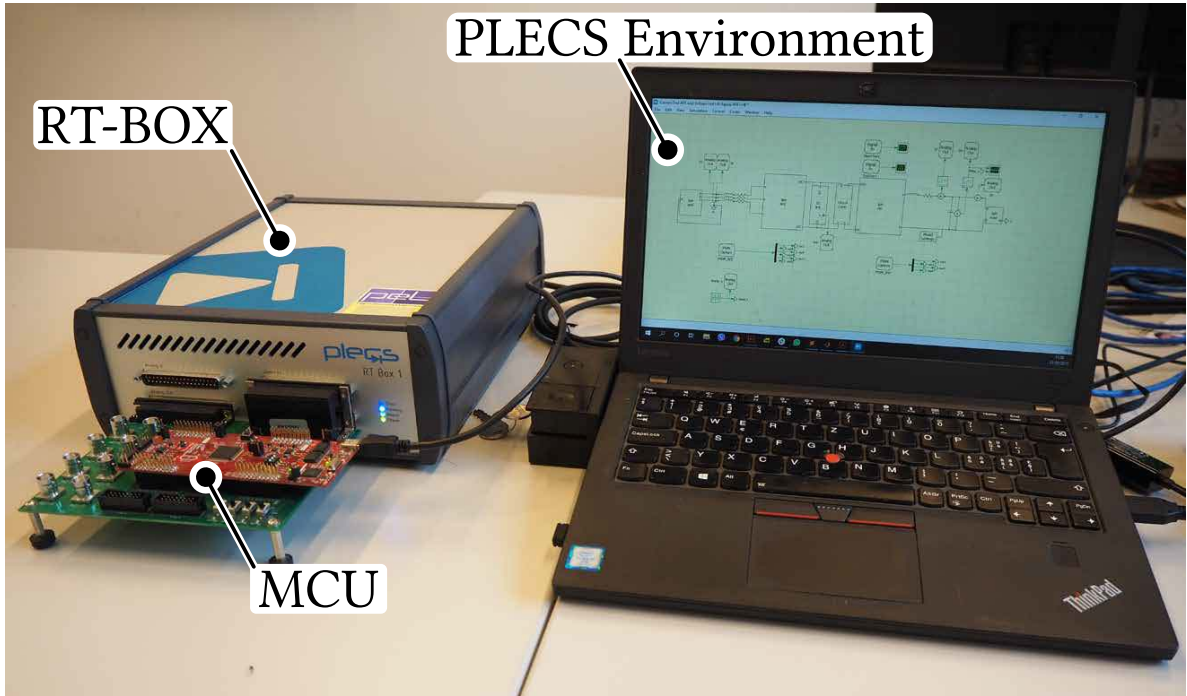


**Fig. 5.5** Hardware-in-the-loop system, where the switching models of the converters are implemented inside the PLECS environment and are simulated in real-time on the RT-Box platform.

RT-Box and in order to avoid using an external acquisition system that would require additional scaling and conversion and thus would reduce the measurement precision.

As the measurement process requires two separate systems to be implemented and perturbed there has to exist a mean of assuring that the systems are perturbed at the same operating point. This requirement is achieved by the synchronization scheme presented in **Fig. 5.6**. After the perturbation is enabled by an external signal the scheme waits until the angle of the output voltage,  $\theta_s$  is zero. In this way, the original system is perturbed at the peak of the output voltage and the orthogonal at the zero voltage. Once the zero angle is detected the perturbation signal is created inside the MCU using shift-registers. Additionally, at the start and at the end of the perturbation signal two flag signals are raised which are passed to the RT-Box. These flags serve as a mean of knowing which portion of the output voltage is perturbed and thus the extraction of the response to the perturbation is performed only on that part of the output voltage measurement.

By comparing the two frequency responses it is easy to notice that there is either none or very slight difference in two characteristics. The difference in the phase angle can be attributed to the modelling of the transducer and delay transfer functions as these are an approximation of the real transfer functions. Moreover, it is clearly distinguishable the characteristics exhibits two resonant peaks at approximately  $f_{res,1} = 818 \text{ Hz}$  and  $f_{res,2} = 918 \text{ Hz}$  which come from the  $LC$ -type filter resonant frequency. The resonant frequency is  $f_{LC} = 868 \text{ Hz}$  in the single-phase domain but when represented in the  $dq$ -frame it is split into two points and shifted by  $-f_s$  and  $+f_s$ , which in this particular case is  $f_s = 50 \text{ Hz}$ , showing that the method is precise enough to characterize resonant points that are not far away from each other on the frequency spectrum.

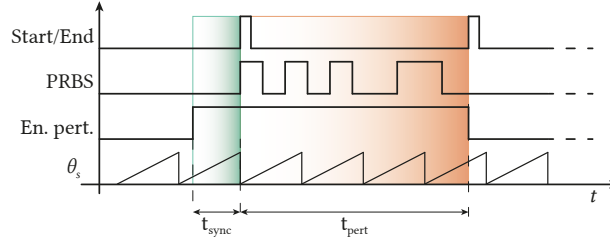


**Fig. 5.6** Perturbation injection synchronization process. After the perturbation signal is enabled, the scheme waits for the angle to become zero after which the PRBS signal is created and injected.

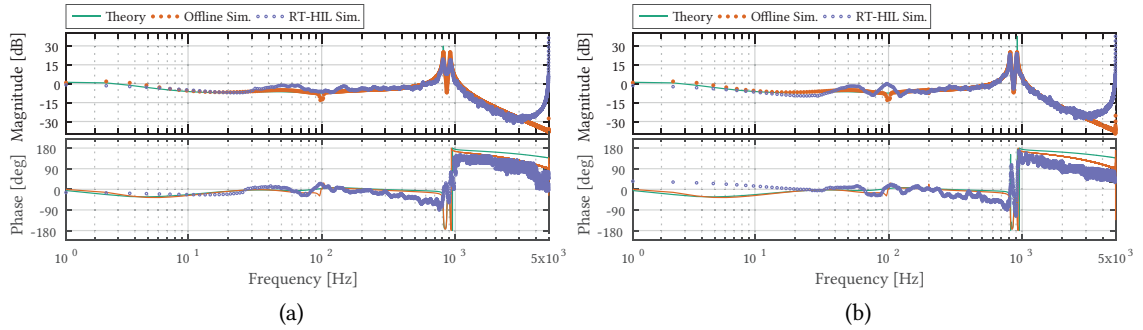


**Fig. 5.7** (a)  $d$ -axis control-to-output characteristics  $G_{co,cl,dd}^{cvc}$  with the standalone-operation of the HB-inverter compared to the same characteristics, (b) when the AFE is operating at the input stage.

### 5.3 Summary

From the results presented in this chapter, it can be drawn as a conclusion that the presence of an active input stage does not hinder the performance of the output one, i.e. the HB stage, and that the two are perfectly decoupled. Practically, this means that all future analyses of the CHB as a topology employed for the impedance/admittance measurement can be undertaken without taking into consideration the source effects on the output stage. It should be also noted that only the  $d$ -axis output impedance and control-to-output characteristics  $G_{co,cl,dd}^{cvc}$  are presented here. The reason for this is the fact that in reality the output of the single-phase HB inverter depends only on the characteristics in the  $d$ -axis and presenting the cross-axis characteristics would be redundant.





# 6

## Power Electronics Building Block Testing and Power Circulation Test

*This chapter describes the common phase-locked loop voltage synchronization for multiple active front ends, taking into account the transformer voltage transformation ratios and phase-shift angles of the transformer. The active front end hardware and control implementations are presented in more detail. Furthermore, the transformation ratios and phase-shift angles are based on the measurements of the primary transformer side voltages which is further used in the control implementation of the active front end. Finally, a full-power testing of the active front end is performed in order to validate the design. The control method applied shows robust performance when applied to active front ends connected to different windings, each having different leakage inductance. The full-power test, performed by circulating the power between two active front ends, demonstrates that the electrical and thermal design perform well.*

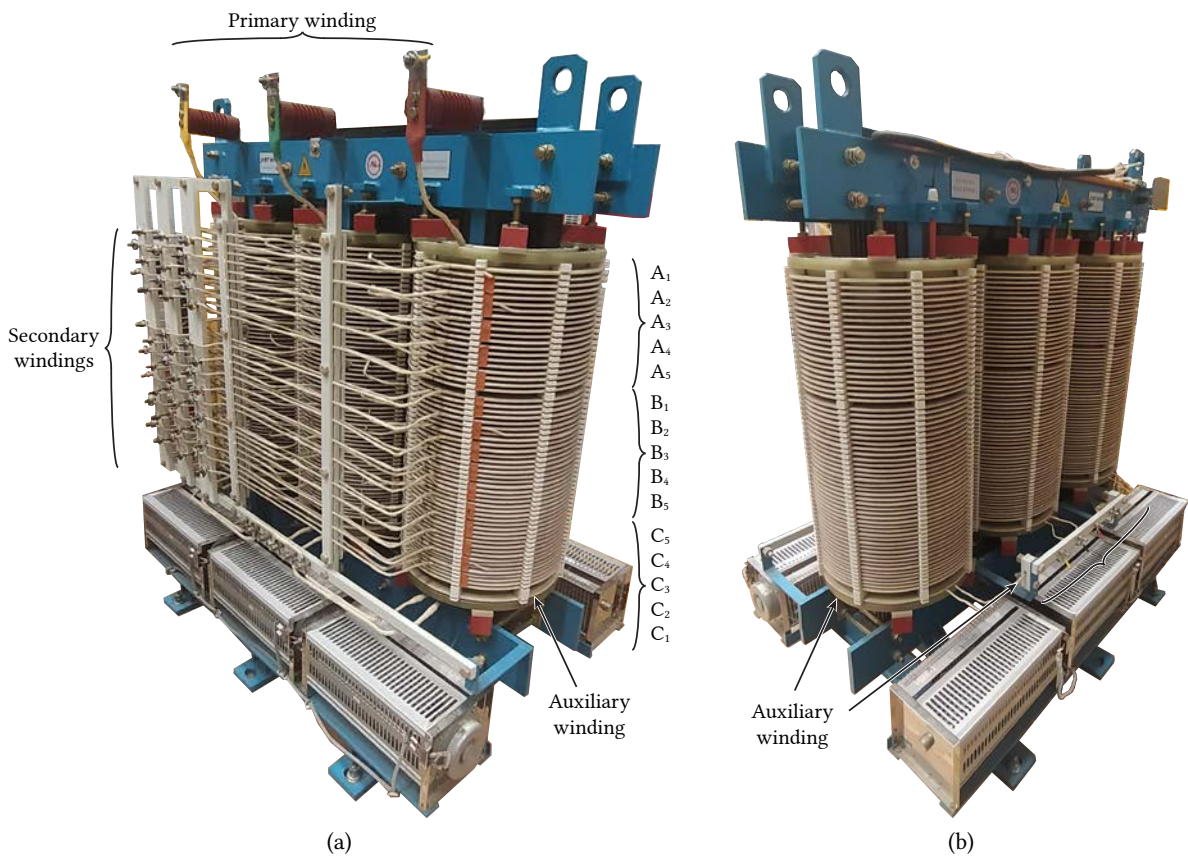
### 6.1 Multi-Winding Phase-Shifting Transformer Measurements

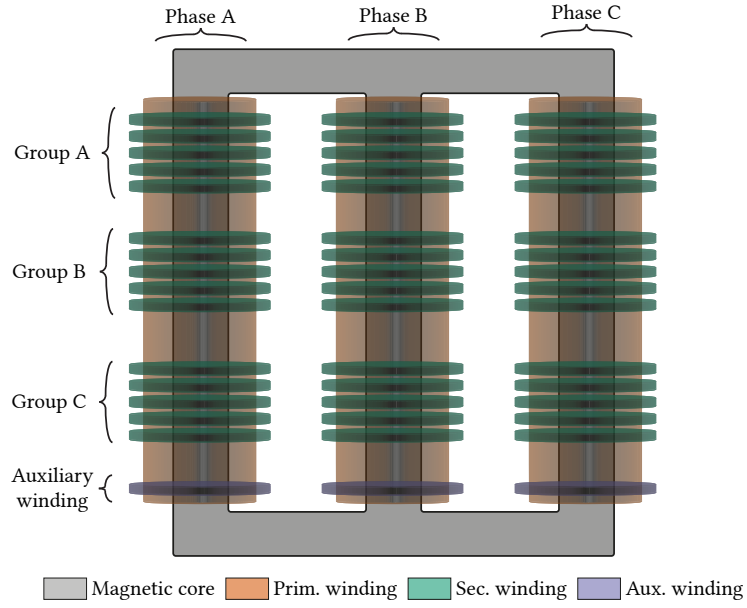
The phase-shifting multi-winding transformer with the parameters in **Tab. 6.1**, which is at the basis of the CHB converter development, is depicted in **Figs. 6.1** and **6.2**. Apart from its primary, MV winding and the secondary, LV windings there exists also an auxiliary winding for supplying auxiliary equipment of the MV-CHB converter, as well as the cooling system of the transformer. In the absence of an appropriate MV source for supplying the primary winding, the auxiliary winding is used in order to obtain phase-shifted voltages at the LV secondary windings, albeit with an extremely reduced power ratings. Nevertheless, the presence of this winding still allows for the full power testing of CHB PEBBs. More specifically, the power circulation between two PEBBs can be performed through the windings of the transformer.

In order to use the auxiliary winding as the supply winding, first the leakage inductance of each secondary winding needs to be measured as well as the voltage transformation ratio and the phase-shift angle between the primary and the secondary windings. The leakage inductance measurements have already been performed in [80] and they show a characteristic *U*-shape curve as revealed in **Fig. 6.3(a)**. The *U*-shape of the leakage inductance comes from the fact that the windings that are more centralized with respect to the primary winding achieve stronger coupling and have lower leakage inductance [81]. The measurements presented in **Fig. 6.3(a)** are obtained by supplying the MV primary winding with a three-phase voltage source. However, the coupling between the MV primary winding to the secondary winding and the coupling between the auxiliary and secondary windings are different due to the winding structure and the location of the windings, thus these measurements results cannot be reused directly.

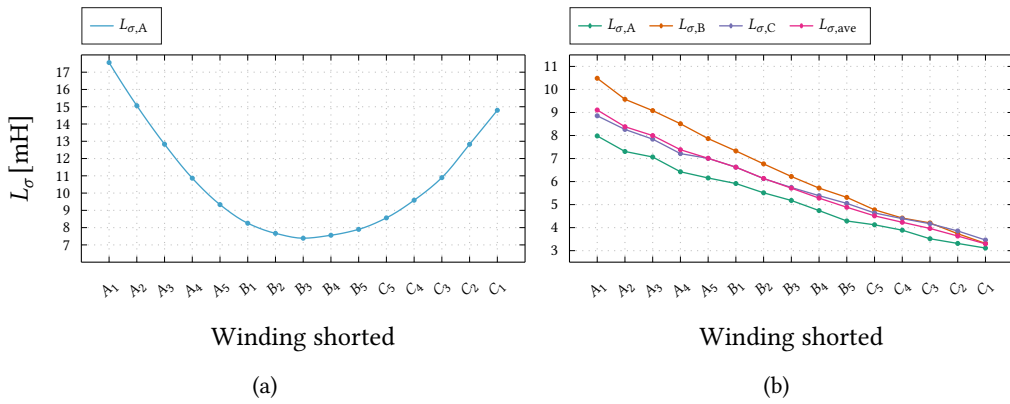
**Tab. 6.1** Multi-winding transformer parameters

Parameter	Value
Apparent power rating	1 MVA
Primary side line voltage	6–6.3 kV
Secondary side line voltage rating	710 V
Secondary side current rating	54 A
Grid frequency	50 Hz
Star primary windings	1
Extended-delta secondary windings	15
Phase shift of the secondaries	$-18^\circ, -6^\circ, 6^\circ, 18^\circ, 30^\circ$
Auxiliary winding line voltage rating	400 V
Auxiliary winding line current rating	14 A

**Fig. 6.1** (a) Front and (b) back of the phase-shifting transformer with 6.3 kV MV primary winding, 15 phase-shifted 710 V LV secondary windings and an auxiliary 400 V winding.



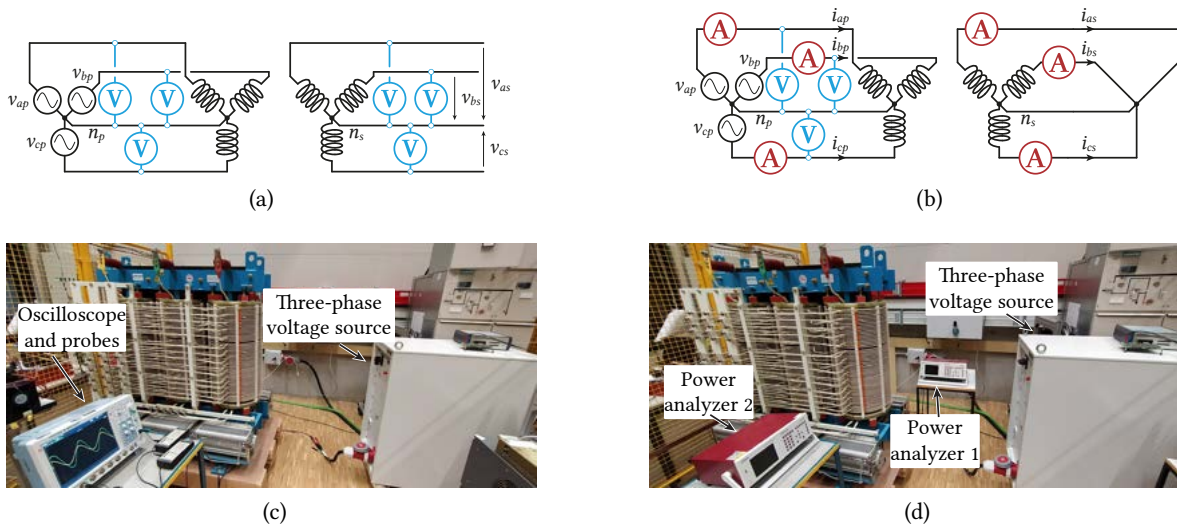
**Fig. 6.2** Transformer drawing with the primary windings, secondary windings and an auxiliary winding. The secondary and auxiliary windings can be seen as concentric to the primary winding which runs the whole length of the transformer core limb.



**Fig. 6.3** Leakage inductance of the secondary winding looking into the primary side of the transformer when the latter is supplied from the (a) MV primary winding and (b) from the auxiliary winding.

**Tab. 6.2** Short-circuit measurements

Shorted w.	$v_{p,AB}$ [V]	$v_{p,BC}$ [V]	$v_{p,CA}$ [V]	$i_{p,A}$ [A]	$i_{p,B}$ [A]	$i_{p,C}$ [A]	$L_{\sigma,A}$ [mH]	$L_{\sigma,B}$ [mH]	$L_{\sigma,C}$ [mH]
A1	19.1	18.8	19.4	18.2	13.6	16.6	7.9	10.5	8.8
A2	19.2	18.6	19.6	19.3	14.2	17.4	7.3	9.6	8.3
A3	20.3	19.9	20.5	21.1	16.1	19.2	7.1	9.1	7.8
A4	19.3	19.1	20.3	21.7	16.1	20.3	6.4	8.5	7.2
A5	19.1	18.4	19.4	22.3	16.9	20.1	6.1	7.8	6.9
B1	18.6	18.2	18.7	22.8	18.2	20.7	5.9	7.3	6.6
B2	15.6	15.2	15.7	20.5	16.4	18.8	5.5	6.7	6.1
B3	16.8	16.5	17.1	23.4	19.3	21.5	5.1	6.2	5.7
B4	14.9	14.7	15.4	22.6	18.5	20.6	4.7	5.7	5.4
B5	13.9	13.8	15.1	23.2	18.5	21.3	4.2	5.3	5.1
C5	14.5	14.3	14.9	25.1	21.4	22.9	4.1	4.8	4.6
C4	10.2	10.1	10.7	18.9	16.3	17.6	3.8	4.4	4.4
C3	10.6	10.4	11.8	22.1	18.2	20.8	3.5	4.2	4.2
C2	11.6	11.3	12.7	25.7	22.2	24.1	3.3	3.7	3.8
C1	11.1	10.8	11.8	26.1	23.9	24.9	3.1	3.3	3.5


**Fig. 6.4** (a) Open-circuit and (b) short-circuit schematics and their (c) and (d) implemented test setup for the measurement of the transformer parameters.

The short- and open-circuit measurements are performed using the following equipment:

- A variable three-phase voltage source to generate 50 Hz sinusoidal voltages at the auxiliary winding;
- Two power analyzers to measure the winding voltages and currents;
- Voltage probes for open-circuit winding voltage measurement;
- An oscilloscope to estimate the voltage transformation ratio and phase-shift.

The open- and short-circuit measurement schematics and their laboratory setups are presented in **Fig. 6.4**. The measured voltage and current values obtained from the short-circuit test are shown in **Tab. 6.2**. In order to verify the phase-shift and voltage transformation rate nameplate data of the transformer, an open-circuit test needs to be performed. As a matter of fact, the phase-shift angles and the voltage transfer ratios are quantized and may deviate from the ideal ones given by the nominal

**Tab. 6.3** Open-circuit measurements

Winding tested	$v_{p,AB}$ [V]	$v_{s,AB}$ [V]	$\phi_w$ [°]	$N_s/N_p$
A1	98.9	175.5	-18	1.774
A2	96.1	173.3	-7	1.803
A3	97.1	175.1	7	1.803
A4	96.3	175.1	18	1.818
A5	98.5	179.1	29	1.818
B1	95.9	173.3	-18	1.807
B2	95.9	173.3	-7	1.807
B3	96.7	175.4	7	1.813
B4	97.5	177.8	20	1.823
B5	96.1	175.8	29	1.831
C5	97.6	178.9	29	1.832
C4	97.4	177.1	20	1.818
C3	95.9	173.1	7	1.805
C2	96.9	174.8	-9	1.803
C1	96.1	173.6	-20	1.806

phase-shifts due to the discrete turns number. The nominal phase-shifts are given as:

$$\phi_{i,nom} = 30^\circ - 60^\circ \cdot \frac{K-i}{K} \quad (6.1)$$

Where  $i = [1, 2, 3, 4, 5]$  and  $K = 5$ . Thus the nominal phase-shift angles of different windings are  $\phi_w = [-18, -6, 6, 18, 30]^\circ$ . The nominal voltage transformation ratio is given as  $N = N_s/N_p = 710/400 = 1.775$ . The voltage transformation ratios obtained from the open-circuit measurements are presented in **Tab. 6.3**. In general the phase-shift angles show a good match with the nominal angles and the discrepancies may also be due to the precision of the measurement which is performed using voltage probes and an oscilloscope. On the other side the voltage transformation ratios show up to 7 % relative error compared to the nominal ratio of 1.775. These discrepancies do not play an important role as they should be properly compensated by the control implementation. With the results of both measurements the leakage inductance can be calculated. Namely, the leakage inductance seen from the LV secondaries can be obtained as:

$$L_k = \frac{15}{2 \cdot 2\pi f} \cdot \frac{v_p}{i_p} \cdot \left( \frac{N_s}{N_p} \right)^2 [\text{mH}] \quad (6.2)$$

where  $k$  is the winding shorted, i.e.  $k = [A_1, A_2, A_3, \dots, C_1]$ . The results of the measurements are presented in **Tab. 6.2** and **Fig. 6.3(b)** show that there is a relatively large difference in the leakage inductance among the three phases of each winding, which might lead to unwanted oscillations and harmonics in the PEBB voltages and currents if not properly compensated.

## 6.2 Primary-Based Source Synchronization

There exist multiple ways of performing source synchronization among which the PLL implemented in the SRF is the most commonly used one for three-phase grid connected converters. The primary-based synchronization approach is based on the work presented in [82]. Namely, the voltage required for the PLL need to be free of switching harmonics which can be achieved by using electrical or analog filters. Both of these methods can potentially introduce delays and reduce overall stability. Moreover, considering the nominal power of the PEBB of 66.7 kVA the required three-phase filter would turn out to be bulky and costly for the application and a decision was made that the filter-less design approach is used [82].

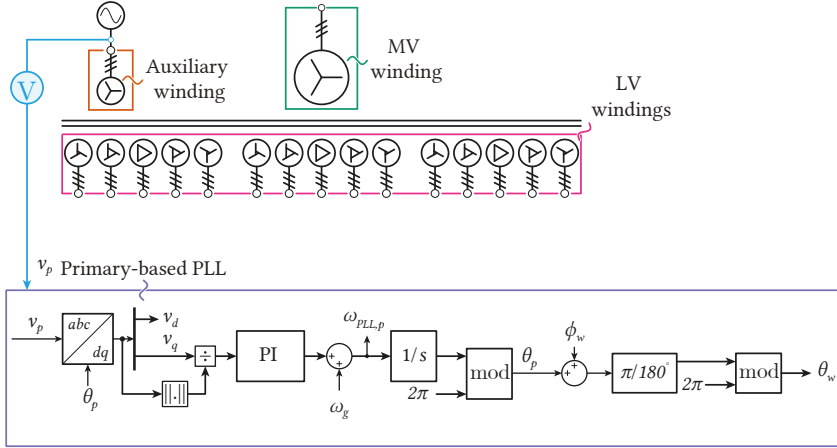


**Fig. 6.5** Schematics of a primary-based PLL where the auxiliary winding is supplied by a three-phase voltage source for the PEBC testing. The output of the PLL,  $\theta_p$ , is shifted by winding phase-shift angle  $\phi_w$  in order to obtain secondary side angle  $\theta_w$ .

Therefore, a filter-less approach that makes use of the transformer leakage inductances is a preferred solution to this issue. In order to perform the filter-less synchronization the auxiliary winding voltages are used as the input of the PLL, in combination with the phase-shift angles between the auxiliary and secondary windings. The auxiliary winding here plays a role of the primary winding from where the secondary windings are supplied. The primary-based PLL concept can be depicted with the **Fig. 6.5**, first presented in [82], where the auxiliary winding voltages are used to obtain the grid angle  $\theta_p$ . With the  $\theta_p$  obtained from the PLL and with the phase-shift angle a secondary side angle  $\theta_w$  can be obtained according to the **Fig. 6.5**. In the configuration portrayed in **Fig. 6.5**, the leakage inductances of the transformer are intrinsically positioned between the auxiliary winding and the AFEs connected to the secondaries of the transformer. In an MV implementation of the CHB converter, the PLL would be performed by making use of the MV primary winding voltages, which would in turn give different set and the shape of the inductances between MV and LV windings, thus also presenting a different control challenge of the input side of the MV-CHB. However, in the case of the synchronization to the auxiliary winding, a different inductance shape is relevant. Additionally, such arrangement simplifies the testing as LV voltage sensors can be used to provide voltages to the PLL.

To test the method presented in [82], the winding  $A_5$  was supplied with three-phase voltage and the primary and secondary voltage were measured. The nominal phase-lag of the secondary winding is  $\phi_{w,nom} = 30^\circ$  for this particular winding, while the measured phase-lag is reported to be  $\phi_{w,meas} = 29^\circ$ . The  $\theta_p$  angle was obtained from the PLL which uses the primary side voltages, while the angle  $\theta_s$  was obtained from the secondary side voltages. At the same time the angle  $\theta_p$  was shifted by  $\phi_{w,nom} = 30^\circ$  in order to obtain the angle  $\theta_w$  and compare it to the angle  $\theta_s$ . The waveforms of the angles are presented in **Fig. 6.6(a)**, showing that the  $\theta_s$  and the shifted version of the  $\theta_p$ , the  $\theta_w$ , match closely confirming that the proposed method is valid.

In order to verify the voltage transformation ratio, the primary side voltages are transformed into the  $dq$ -frame using the angle  $\theta_p$  and scaled with the nominal voltage transformation ratio of  $N = 1.775$ . At the same time the secondary side voltages are measured and transformed into  $dq$ -frame using the secondary side angle  $\theta_w$ . The comparison of the primary and secondary voltages in the  $dq$ -frame is presented in **Fig. 6.6(b)** and there exists a slight deviation between the scaled and measured voltages.

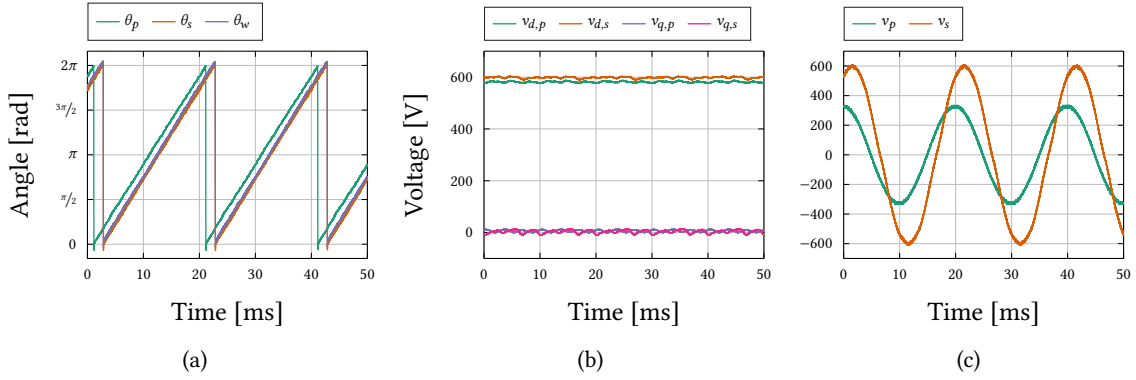


**Fig. 6.6** a) Comparison of the primary side angle  $\theta_p$ , secondary side angle  $\theta_s$  and the shifted primary side angle by the phase shift  $\phi_w$ , b) primary and secondary side voltages in the  $dq$ -frame and (c) phase A primary and secondary voltages.

This does not come as a surprise as the measured voltage transformation ratio is  $N_{\text{meas}} = 1.818$  according to the **Tab. 6.3**.

### 6.3 Cascaded H-Bridge Converter Power Electronics Building Block

With the theoretical modelling of the PEBB already been examined in the early chapters of this thesis the focus can shift to its hardware and control implementation that have not yet been considered. A single PEBB of the CHB converter is depicted in **Fig. 6.7**. It consists of an input,  $L$ -type filter, three-phase active rectifier, the AFE based on Si-IGBT modules, a dc-link serving as an energy buffer, a single-phase HB inverter based on SiC-MOSFET modules, and an output,  $LC$ -type, filter. Taking into account the MWT secondary winding voltage ratings and the voltage boosting capabilities of three-phase AFE, the dc-link is sized for the nominal voltage of  $v_{dc} = 1.2$  kV. Subsequently, the voltage class of the IGBT and MOSFET modules is chosen to be the 1.7 kV-class. Considering the switching capabilities of the 1.7 kV-class Si-IGBT and SiC-MOSFET modules, as well as the evaluation performed in [62], the switching frequency chosen for the three-phase AFE is set at  $f_{sw}^{\text{AFE}} = 10$  kHz and at  $f_{sw}^{\text{HB}} = 20$  kHz for the HB inverter unit (INU). Taking into account the nominal power rating of the MWT, the CHB converter is sized for a power of  $S_{\text{CHB}} = 1$  MVA. Consequently, with 15 PEBBs forming the CHB converter, the power of a single PEBB is set at  $S_{\text{PEBB}} = 66.7$  kVA. The parameters of single PEBB, not including the filter parameters, are presented in **Tab. 6.4**. The  $L$ -type input filter of the three-phase AFE can effectively be replaced by the leakage inductances of the MWT, thus achieving volumetric and monetary saving for the CHB converter realization. In order to verify the hardware and control design of the PEBB, as well as the effectiveness of using the transformer leakage inductance as a filter inductance, a test needs to be performed in which the rated power of the PEBB is processed by its constituent elements.

Considering the size and the complexity of the system, i.e. the MV-CHB converter being formed of 15 low-voltage cells, the converter control concept requires a platform capable of supporting demanding computational power and increased number of different inputs and outputs (I/Os). Usually, large-scale industrial control platforms are capable of handling such requirements. For the control of the input side of the CHB, i.e. the AFEs, the ABB AC 800PEC control system is employed together



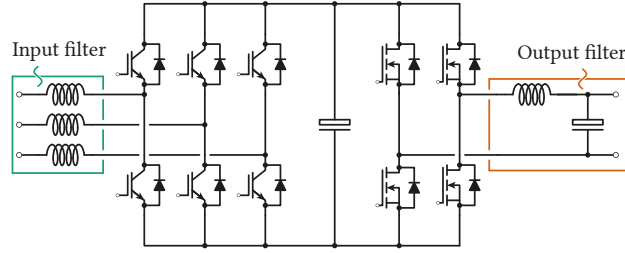


**Fig. 6.7** CHB PEBB consisting of a three-phase active rectifier, the AFE based on 1.7 kV Si IGBTs, a 1.2 kV dc-link serving as an energy buffer and a single-phase HB inverter based on 1.7 kV SiC MOSFETS.

**Tab. 6.4** CHB PEBB parameters

Parameter	Value
Apparent Power Rating	66.7 kVA
AFE Nominal Current	54 A
Inverter HB Nominal Current	96 A
Nominal dc-link voltage	1200 V
Semiconductor blocking voltage	1700 V
Inverter HB Modulation	PSC-PWM

with its peripheral units for various measurements and auxiliary functions. The task of driving the IGBT switches of the AFE is performed by the PEC gate driver unit (PEC-GDU) with intelligent functions deployed on an FPGA platform, such as the dc-link voltage and input currents sensing and filtering and integrated protection functions. The protection functions are namely the over-voltage and over-current protection, and short-circuit protection.

The systems commands are issued from the command and supervisory unit, essentially a human user interface, with which the AC 800PEC continuously communicates, while simultaneously exchanging information with its peripheral units and the PEC-GDU. There exist two sources of measurements required for control tasks in the AC 800PEC. First source is the PEC measurement interface (PEC-MI), which provide the ac voltage measurements required for the grid synchronization. The second source is the PEC-GDU which provides the measurement of the dc-link voltage and the input current. Both the dc-link voltage and the current are passed either through a moving average filter or a low-pass filter in order to reduce the control sensitivity to noise and sensor imprecision. Each unit in the control structure has its own execution time which are added on top of the communication time between the PEC and its peripheral units. These times combined act as delay in the control system and affect the overall performance of the implemented control and they need to be properly compensated.

### 6.3.1 Back-to-Back Setup for Active Front End Testing

In order to test the hardware and control design of the AFE a back-to-back setup is built. At the same time the primary-based source synchronization is put to the test. The general schematic layout of this setup is given in **Fig. 6.8**. Here, one AFE is operating as it is intended, i.e. as a three-phase active rectifier, while the other one operates as a three-phase INU. A three-phase voltage source supplies the auxiliary windings and provides the power to cover the losses of the system. At the same time, the voltage source also provides the magnetization current for the transformer. In the system presented in **Fig. 6.8**, for the control purposes, the voltages of the primary side of the transformer,  $v_p$ ,



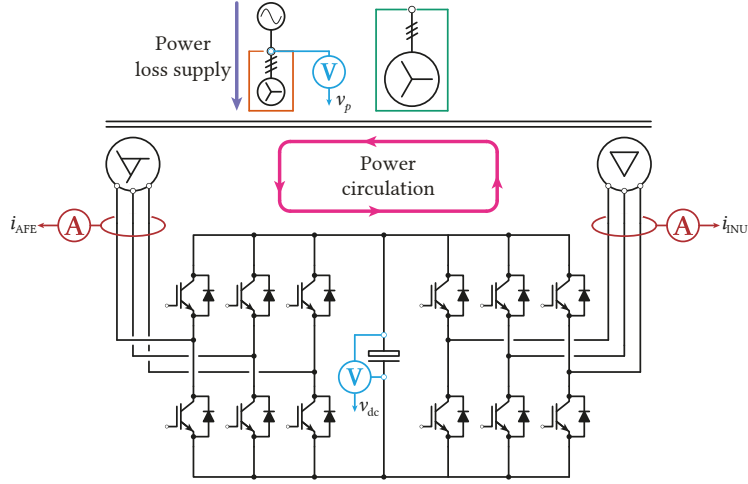


**Fig. 6.8** Schematics of the back-to-back setup for hardware and control design testing of the AFE. The AFE and the INU are connected to separate secondary side windings.

are measured as well as the currents of the AFE and the three-phase INU,  $i_{AFE}$  and  $i_{INU}$ . Finally, the dc-link voltage  $v_{dc}$  is measured as well.

A PI regulator structure is used to control the voltage of the dc-link. The output of the regulator,  $i_{dc}^*$  is multiplied with the measured dc-link voltage  $v_{dc}$  in order to obtain the active power reference  $P_{AFE}^*$ , as displayed in **Fig. 6.9**. On the other side, the reactive power reference is set independently in order to obtain the desired power factor at the terminals of the AFE. The input current control (ICC) of the AFE is performed in the decoupled SRF, i.e. the  $d$ - and  $q$ -axis are separately controlled using a PI regulator structure. The measured input current of the AFE is transformed into the  $dq$ -frame using the angle  $\theta_{w,AFE}$ , which is the angle obtained from the primary-based PLL which is additionally shifted with respect to the winding to which the AFE is connected, i.e. according to the **Fig. 6.5**. The active and reactive current references,  $i_d^*$  and  $i_q^*$ , are obtained from the active and reactive power reference and the  $dq$ -frame voltages of the three-phase source. These voltages are obtained in the same manner as the AFE currents in the  $dq$ -frame, i.e. by transforming the  $abc$ -frame voltages with the angle  $\theta_{w,AFE}$  and additionally scaling them with the nominal voltage transformation ratio. The current references are calculated using the following equation:

$$\begin{bmatrix} i_d^* \\ i_q^* \end{bmatrix} = \frac{2}{3} \frac{1}{v_{d,AFE}^2 + v_{q,AFE}^2} \begin{bmatrix} v_{d,AFE} & -v_{q,AFE} \\ v_{q,AFE} & v_{d,AFE} \end{bmatrix} \begin{bmatrix} P_{AFE}^* \\ Q_{AFE}^* \end{bmatrix} \quad (6.3)$$

This equation stems directly from the equation for the active and reactive power in the  $dq$ -frame:

$$\begin{bmatrix} P \\ Q \end{bmatrix} = \frac{3}{2} \begin{bmatrix} v_d & v_q \\ -v_q & v_d \end{bmatrix} \begin{bmatrix} i_d \\ i_q \end{bmatrix} \quad (6.4)$$

Once the  $dq$ -frame voltage references for the AFE are obtained, they are transformed into the  $abc$ -frame by again using the angle  $\theta_{w,AFE}$  and they are divided by the measured dc-link voltage to obtain the modulation indices. The control schematic for the AFE can be represented using the **Fig. 6.9**. On the other side, the control of the three-phase INU is performed in a similar manner with the exception

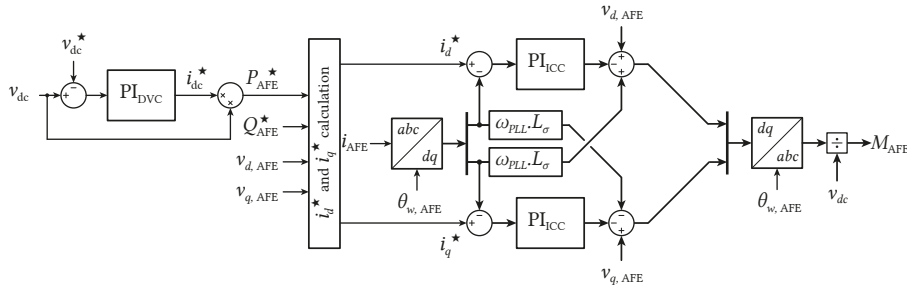


**Fig. 6.9** Schematic of the input current control of the AFE with the current references obtained from the active and reactive power reference and the voltages in the  $dq$ -frame.

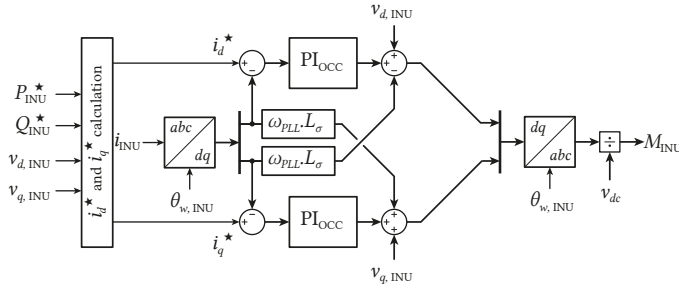


**Fig. 6.10** Schematic of the output current control of the three-phase INU with the current references obtained from the active and reactive power reference and the voltages in the  $dq$ -frame.

that both the active and reactive references are set directly in the control software and in essence the output current of the INU is controlled. The control schematic for the three-phase INU is given in **Fig. 6.10**.

## 6.4 Control Parameter Tuning

The PI regulator gains of the PLL can be set using the closed loop transfer function of the PLL given as:

$$\begin{aligned}
H_{CL,PLL}(s) &= \frac{K_{p,PLL}s + \frac{K_{p,PLL}}{T_{i,PLL}}}{s^2 + K_{p,PLL}s + \frac{K_{p,PLL}}{T_{i,PLL}}} \\
&= \frac{2\xi\omega_n s + \omega_n^2}{s^2 + 2\xi\omega_n s + \omega_n^2}
\end{aligned} \tag{6.5}$$

Subsequently the gains are obtained according to the sought settling time of the second-order system which is approximated as:

$$t_s = 4.6\tau \quad \tau = \frac{1}{\xi\omega_n} \quad (6.6)$$

From here, the PI controller gains can be set as a function of the settling time as follows [83]:

$$K_{p,PLL} = 2 \cdot \xi \omega_n = \frac{9.2}{t_s} \quad T_{i,PLL} = \frac{2\xi}{\omega_n} = \frac{t_s \xi^2}{2.3} \quad (6.7)$$

The damping factor is chosen as  $\xi = \frac{1}{\sqrt{2}}$  while the settling time is  $t_s = 100$  ms.

The PI regulator parameters for the voltage and current controllers can be tuned according to Magnitude Optimum for the ICC and the output current control (OCC) and according to Symmetrical Optimum for the dc-link voltage control (DVC) [84]–[86]. The ICC is tuned according to the following equations:

$$\begin{aligned} T_{n,ICC} &= \frac{L_\sigma}{R_\sigma} \\ T_{i,ICC} &= \frac{2 \cdot T_{d\Sigma,ICC}}{R_\sigma} \\ K_{p,ICC} &= \frac{T_{n,ICC}}{T_{i,ICC}} \\ K_{i,ICC} &= \frac{1}{T_{i,ICC}} \end{aligned} \quad (6.8)$$

Where the  $T_{d\Sigma,ICC}$  is the total delay of the current control loop which can be established according to the switching and sampling frequencies and communication delays between the control platform, measurement devices and the gate driver unit for the AFE, i.e. between the PEC and PECMI and the GDU. The tuning of the OCC can be performed according to the same equation, taking into account of the leakage inductance and the parasitic resistance of the corresponding winding. The tuning of the DVC is performed according to the following equations:

$$\begin{aligned} T_{\Sigma,DVC} &= 10 \cdot T_{d\Sigma,ICC} \\ T_{d\Sigma,DVC} &= 2 \cdot T_{d\Sigma,ICC} + T_{\Sigma,DVC} \\ T_{n,DVC} &= 4 \cdot T_{d\Sigma,DVC} \\ T_{i,DVC} &= \frac{8 \cdot T_{d\Sigma,DVC}^2}{C_{dc}} \\ K_{p,DVC} &= \frac{T_{n,ICC}}{T_{i,ICC}} \\ K_{i,DVC} &= \frac{1}{T_{i,ICC}} \end{aligned} \quad (6.9)$$

Where the  $T_{d\Sigma,DVC}$  is the total delay of the dc-link voltage control loop. The total delay of the current control loop is be given as:

$$T_{d\Sigma,ICC} = 2 \cdot T_{GD} + 2 \cdot T_{comm} + T_{CP} + T_{PWM} \quad (6.10)$$

Where the different delays and their time durations are:

- $T_{GD}$  - gate driver ADC and calculation time;
- $T_{comm}$  - communication delay between the gate driver unit and the control platform;
- $T_{CP}$  - calculation time of the control platform;
- $T_{PWM}$  - PWM delay.

From the equation (6.8) and from the **Tab. 6.2** it can be seen how the proportional gain  $K_p$  of the current controller changes with respect to the winding to which the AFE is connected. Namely, with the increase of the leakage inductance the proportional gain increases as well, leading to a conclusion that for different windings different control parameters need to be set for different AFEs. However, this is undesirable as it makes it harder to keep track of the control parameters in the system. There exist two possible solutions to this problem. The first one is to add additional inductances in series with the transformer secondaries in order to increase the overall inductance of windings. However, due to the difference between the leakage inductances of the windings  $C_1$  and  $A_1$  a large inductance would need to be added. Moreover, this would beat the purpose of implementing the primary-based PLL, i.e. the overall system size and cost would increase.

Another inexpensive and much simpler technique would simply be to have all the parameters the same for all the AFEs. Depending on the winding to which an individual AFE is connected, the control performance could be compromised, however, not to a degree where it would impair the overall operation of the CHB. Moreover, in this particular application the control performance of the input, i.e. the AFE, side is not of utmost importance compared to the output side control performance. The following problem which arises is the choice of the winding for which the control parameters are tuned. Tuning the parameters according to the leakage inductance of the winding  $A_1$  would possibly provoke instabilities in the control system of the AFEs connected to lower leakage inductance windings simply due to the fact that the control would be too aggressive, i.e. the regulator gains would be too high. Hence, intuitively the optimal choice would be to tune the parameters according to the leakage inductance of the winding  $C_1$ .

An alternative, more mathematical, argument for the choice of winding for which the gains are tuned for can be made using the sought for phase margin. According to [87] a set of maximal allowable gains can be found. If the transfer function of the PI regulator is given as:

$$G_s(s) = K_p \left( 1 + \frac{1}{sT_i} \right) \quad (6.11)$$

and the plant, that is the leakage inductance together with its parasitic resistance, is given as:

$$G_p(s) = \frac{1}{R_\sigma} \left( \frac{1}{1 + sT_p} \right) \quad (6.12)$$

where  $T_p = L_\sigma / R_\sigma$ , the open-loop transfer function is obtained as:

$$G_s(s) G_p(s) = \frac{K_p}{R_\sigma T_i} \frac{1 + sT_i}{s(1 + sT_p)} \quad (6.13)$$

Taking the overall communication, calculation and actuator delays into account, the open-loop transfer function can be rewritten as:

$$G_{ol}(s) = G_s(s) G_p(s) G_d(s) = \frac{K_p}{R_\sigma T_i} \frac{1 + sT_i}{s(1 + sT_p)} e^{-sT_{d\Sigma}} \quad (6.14)$$

The goal objective here is to maximize the proportional gain  $K_p$  and minimize the integrator time constant  $T_i$ , while taking into account the effects of the delay  $T_{d\Sigma}$  and maintaining the sought for

phase margin  $\phi_m$  at a crossover frequency  $\omega_c$ . The phase of the (6.14) at  $\omega_c$  with the phase margin taken into account is obtained as:

$$\begin{aligned} & \angle [G_s(j\omega_c) G_p(j\omega_c) G_d(j\omega_c)] \\ &= \angle \left[ \frac{K_p}{R_\sigma T_i} \frac{1 + j\omega_c T_i}{j\omega_c (1 + j\omega_c T_p)} e^{-j\omega_c T_{d\Sigma}} \right] \\ &= -\pi + \phi_m \\ &= \arctan(\omega_c T_i) - \pi/2 - \omega_c T_{d\Sigma} - \arctan(\omega_c T_p) \end{aligned} \quad (6.15)$$

As the crossover frequency is almost exclusively beyond the frequency of the plant pole, the  $\arctan(\omega_c T_p)$  can be approximated as  $\pi/2$ , thus from (6.15) the phase margin becomes:

$$\phi_m \approx \arctan(\omega_c T_i) - \omega_c T_{d\Sigma} \quad (6.16)$$

giving the crossover frequency as:

$$\omega_c = \frac{\arctan(\omega_c T_i) - \phi_m}{T_{d\Sigma}} \quad (6.17)$$

The maximum crossover frequency occurs when  $\arctan(\omega_c T_i) = \pi/2$  resulting in:

$$\omega_{c,\max} = \frac{\pi/2 - \phi_m}{T_{d\Sigma}} \quad (6.18)$$

The maximum gain  $K_p$  can be found by setting (6.14) to unity at  $\omega_{c,\max}$  giving:

$$K_p = R_\sigma T_i \omega_{c,\max} \sqrt{\frac{1 + \omega_{c,\max}^2 T_p^2}{1 + \omega_{c,\max}^2 T_i^2}} \quad (6.19)$$

which, taking into account that  $\omega_{c,\max} T_i \gg 1$  and  $\omega_{c,\max} T_p \gg 1$ , the equation (6.18) and the fact that the lowest leakage inductance must be considered gives:

$$K_p \leq \frac{\pi/2 - \phi_m}{T_{d\Sigma}} L_{\sigma,\min} \quad (6.20)$$

The integrator time constant and the integrator gain can, on the other side be obtained by setting the  $\arctan(\omega_c T_i)$  close to  $\pi/2$ ,  $89.7^\circ$  for example, leading to:

$$\begin{aligned} T_i &= \frac{200}{\omega_{c,\max}} \\ K_i &= \frac{K_p \omega_{c,\max}}{200} \end{aligned} \quad (6.21)$$

The PI regulator parameters can be tuned according to (6.8) and (6.9) and the current control gains can later be compared with (6.20) in order to verify if the obtained parameters violate the previously set constraints. A parameter needed for the tuning is the winding parasitic resistance  $R_\sigma$  which has not been directly measured but can be estimated from its base impedance. Namely, parasitic resistance  $R_\sigma$

**Tab. 6.5** Control tuning parameters

$L_\sigma$	$R_\sigma$	$T_{GD}$	$T_{comm}$	$T_{CP}$	$T_{PWM}$	$f_{sw,AFE}$	$f_{sw,INV}$
3.1 mH	56 m $\Omega$	25 $\mu$ s	25 $\mu$ s	100 $\mu$ s	$1/4 T_{sw}$	10 kHz	8 kHz

**Tab. 6.6** Controller gains

Gain	$K_{p,ICC}$	$K_{i,ICC}$	$K_{p,DVC}$	$K_{p,DVC}$	$K_{p,OCC}$	$K_{i,OCC}$
Value	7.31	132.11	0.98	96.57	5.85	105.66

is in the order of less than 0.9 % of the base impedance for the 1 MVA-class transformers [88]. Thus, the parasitic resistance is calculated as:

$$R_\sigma = \frac{V_n^2}{S_n} = \frac{(6.3 \text{ kV})^2}{1 \text{ MVA}} = 56 \text{ m}\Omega \quad (6.22)$$

All the parameters needed for the control gains tuning are given in **Tab. 6.5**. With the control tuning parameters from **Tab. 6.5** the gains are obtained presented in **Tab. 6.6**. For the sake of comparison, the gains of the current controller of the AFE with the phase margin of  $\phi_m = \pi/3$  are obtained as  $K_{p,ICC} = 8.93$  and  $K_{i,ICC} = 128.69$ , showing that the gains obtained using the Magnitude Optimum do not violate the maximum allowable proportional gain and assures the required phase margin.

### 6.4.1 Control Performance

In order to examine the control method put forward, where the same control parameters are applied to the control system independent of the secondary winding supplying the AFE, several tests are performed. Namely, the AFE is connected to either the uppermost winding,  $A_1$ , or the lowermost,  $C_1$ , while the INU is connected to the middle-point winding  $B_3$ . In total, four tests are performed per configuration. More specifically, the dc-link voltage charge and discharge tests and the power-up and power-down tests were performed.

The **Fig. 6.11** shows the dc-link charge and discharge test when the AFE is connected to the winding  $A_1$ . In the first part of the test, the dc-link voltage is regulated at its nominal value of  $v_{dc} = 1.2 \text{ kV}$ . In the following step the new reference of  $v_{dc}^* = 1.3 \text{ kV}$  is issued. Similarly, in the dc-link discharge test, the voltage is regulated at 1.3 kV and is then discharged to 1.2 kV. It should be noted that to perform the test the output of the dc-link voltage regulator is limited to  $i_{lim} = \pm 15 \text{ A}$  in order not to trip the protection circuits of the three-phase voltage source. From **Fig. 6.11** it is discernible that the input current regulator has sub-par performance in the sense of the dynamics and reference tracking. This is easily explained by the fact that the gains of the current regulator are sub-optimal for the winding to which the AFE is connected. However, the end-goal of regulating the dc-link voltage is achieved.

The **Fig. 6.12** shows the power-up and power-down test, which can be understood as the disturbance rejection test. Here, the dc-link voltage is controlled at  $v_{dc} = 1.2 \text{ kV}$  when the active power reference of the INU is issued at  $P_{INU}^* = 20 \text{ kW}$ , which represents a load of the same power for the AFE. The dc-link voltage regulator performance shown here is satisfactory, i.e. the voltage is regulated at  $v_{dc} = 1.2 \text{ kV}$  and the current regulator reference tracking performs well which is understandable given that the rate of change of power demand is relatively slow.

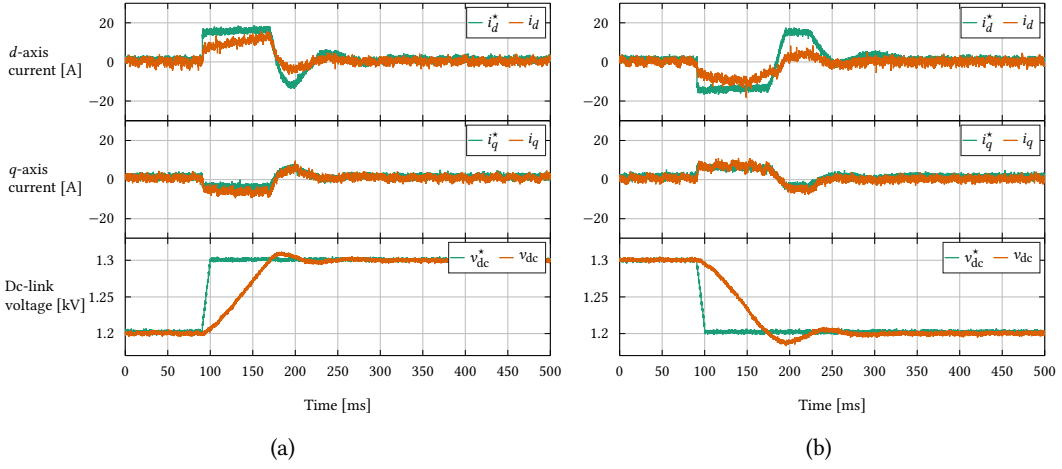


**Fig. 6.11** AFE current and dc-link voltage waveforms for the (a) dc-link charge and (b) dc-link discharge test for the AFE connected to the winding  $A_1$ .

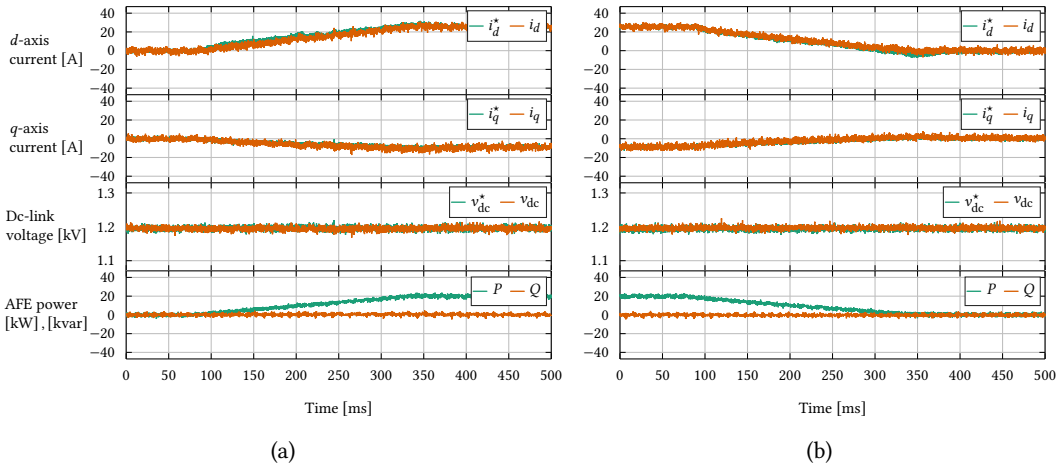


**Fig. 6.12** AFE current and dc-link voltage waveforms for the (a) power-up and (b) power-down test for the AFE connected to the winding  $A_1$ .

The same tests of the dc-link charge and discharge and power-up and power-down are performed while the AFE is connected to the winding  $C_5$ . The control performance with this arrangement is presented in **Figs. 6.13** and **6.14**. The dc-link voltage regulation and the reference tracking are performed well, as well as the disturbance rejection during the power-up and power-down test, which is straightforward given that the regulator gains are well optimized for this particular winding. However, the current ripple in this arrangement is much larger compared to the previous one. This comes as a direct consequence of the leakage inductance of the winding  $C_1$ , which is in average three times lower than the one of the winding  $A_1$ .

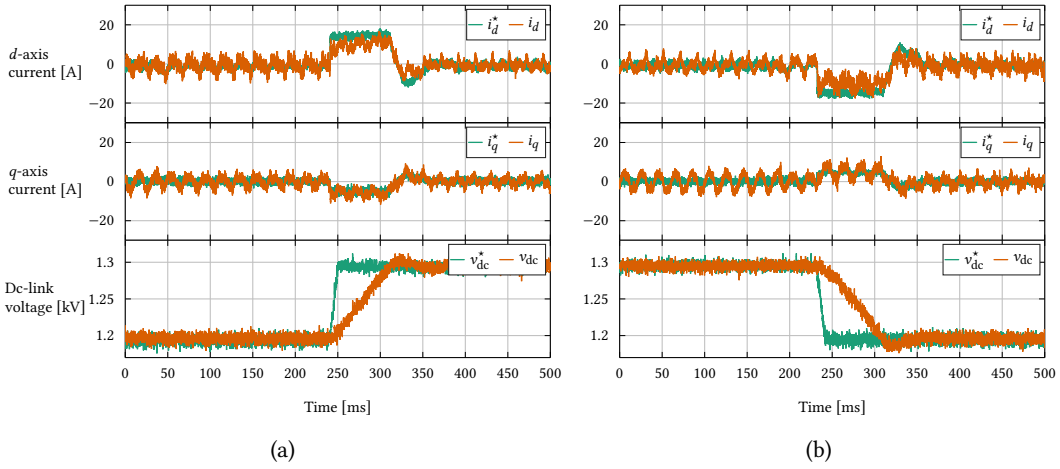


**Fig. 6.13** AFE current and dc-link voltage waveforms for the (a) dc-link charge and (b) dc-link discharge test for the AFE connected to the winding  $C_1$ .

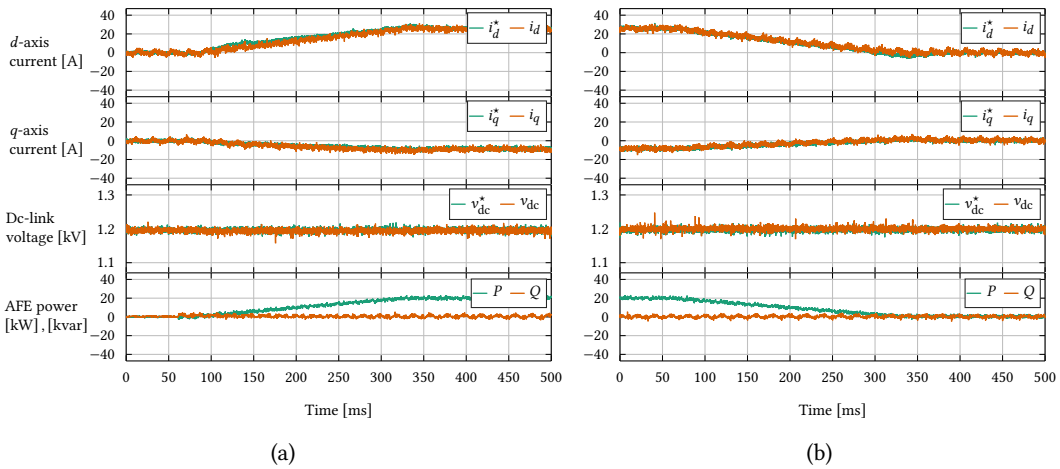


**Fig. 6.14** AFE current and dc-link voltage waveforms for the (a) power-up and (b) power-down test for the AFE connected to the winding  $C_1$ .

## 6.5 Power Electronics Building Block Thermal System Design

One of the requirements for performing the power circulation between the AFE and its three-phase inverting counterpart in the back-to-back setup presented in **Fig. 6.8** is to design an efficient thermal system for heat extraction. The thermal system design is based on estimation of losses obtained in [62] using a combination of PLECS and MATLAB software. Namely, in PLECS a detailed simulation of the AFE is performed where the IGBT models are based on the data-sheet provided by the manufacturer. From the waveforms obtained in PLECS the losses can subsequently be calculated in MATLAB. The loss estimation was performed for  $f_{sw} = 10$  kHz switching frequency. Apart from the switching frequency the losses also depend on the operating point of the AFE, i.e. on the power factor at which the AFE is operating. The power losses for different power factors are presented in **Fig. 6.15**. The



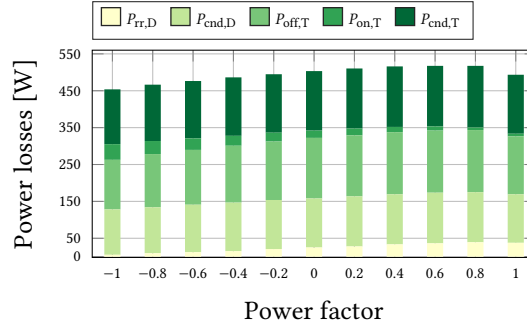


**Fig. 6.15** Power losses of a single IGBT and its freewheeling diode of the AFE depending on the power factor. The power loss contributions come from diode reverse-recovery and conduction losses and from IGBT turn-off, turn-on and conduction losses.

**Tab. 6.7** IGBT and freewheeling diode loss distribution

$P_{loss,sw}$	$P_{loss,IGBT}$	$P_{loss,D}$	$P_{rr,D}$	$P_{cnd,D}$	$P_{off,T}$	$P_{on,T}$	$P_{cnd,T}$
495 W	325 W	170 W	37.7 W	131.6 W	157.1 W	7.1 W	159.9 W

power factor of  $\cos \phi = 1$  is chosen as a point for the thermal system design. The losses are estimated at  $P_{loss,AFE} = 2.97$  kW for a full power operation, i.e. at  $S = 66.7$  kVA. The power loss of a single IGBT and its freewheeling diode amounts to  $P_{loss,sw} = 495$  W of which 325 W are the IGBT losses and 170 W are the diode losses. The more detailed loss distribution between the freewheeling diode and IGBT losses are given in **Tab. 6.7**.

The case temperature of the IGBT module,  $T_c$ , can be calculated as:

$$T_c = n_1 P_{loss,AFE} R_{th,s-a} + T_a \quad (6.23)$$

While the heatsink temperature,  $T_s$ , is calculated as:

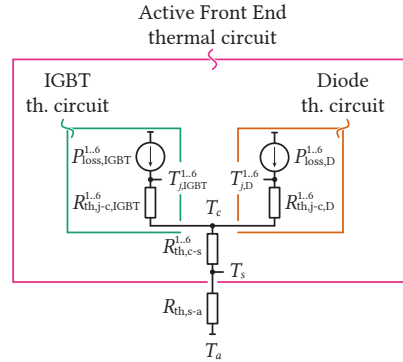
$$T_s = n_2 P_{loss,AFE} R_{th,c-s} + T_c \quad (6.24)$$

Where the  $R_{th,s-a}$  is the heatsink-to-ambient thermal resistance,  $R_{th,c-s}$  is the case-to-sink thermal resistance,  $T_a$  is the ambient temperature,  $n_1$  is the number of semiconductor devices per heatsink and  $n_2$  is the number of sources of power loss in an IGBT module, i.e.  $n_2$  IGBTs and  $n_2$  freewheeling diodes. For the case of the three-phase AFE there are  $n_1 = 6$  devices on the heatsink and  $n_2 = 2$  IGBTs and diodes in a module. Finally, the junction temperature is obtained as:

$$T_j = P_{loss}^x R_{th,c-j}^x + T_c \quad (6.25)$$

Where  $x$  is either the IGBT or the freewheeling diode and  $R_{th,c-j}$  is the case-to-junction thermal resistance. Combining the equations (6.23) to (6.25) and the simplified thermal circuit of the AFE, presented in **Fig. 6.16**, the required heatsink-to-ambient thermal resistance  $R_{th,s-a}$  can be calculated as:

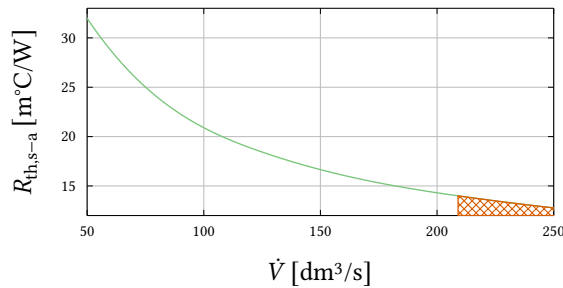
$$R_{th,s-a} = \frac{T_{j,max} - T_a - P_{loss}^x R_{th,c-j}^x - n_2 P_{loss,AFE} R_{th,c-s}}{n_1 P_{loss,AFE}} \quad (6.26)$$


**Fig. 6.16** Thermal circuit of the Active Front End.

**Tab. 6.8** Cooling system design parameters

$R_{th,c-j}^{IGBT}$	$R_{th,c-j}^{diode}$	$R_{th,c-s}$	$T_{j,max}$	$T_a$
161 m°C/W	356 m°C/W	17 m°C/W	150 °C	30 °C

Depending on the loss contribution from the IGBT or the diode and their respective  $R_{th,c-j}$  a different  $R_{th,s-a}$  might be calculated. Naturally, the lower value needs to be taken as a design parameter since it is the thermal resistance for which the junction temperature of either the IGBT or diode will not surpass the maximum value allowed. The Si-IGBT module used to realize the AFE is the SEMIKRON SKM150GB17E4G [89] and its thermal resistances, as well as the ambient and maximum junction temperatures, are given in **Tab. 6.8**. With the parameters from **Tab. 6.8** and using the equation (6.25) the maximum sink-to-ambient heatsink thermal resistance is  $R_{th,s-a} = 14 \text{ m}^\circ\text{C/W}$ . The heatsink chosen for the design is the Constelium HKH-A 120 aluminum heatsink with two air ducts. The dimensions of the heatsink are  $W \times H \times L = 240 \text{ mm} \times 121 \text{ mm} \times 350 \text{ mm}$ , allowing to accommodate three IGBT modules of the AFE. The thermal resistance profile of the heatsink is presented in **Fig. 6.17**. Obviously, the passive cooling here is not an option and the system must be cooled actively using fans. The maximum sink-to-ambient thermal resistance is met for the volumetric flow of  $\dot{V} = 210 \text{ dm}^3/\text{s}$ , thus two fans, each with the volumetric flow of  $120 \text{ dm}^3/\text{s}$  are mounted on the heatsink in order to meet the cooling system requirements.


**Fig. 6.17** Heatsink-to-ambient thermal resistance  $R_{th,s-a}$  with the shaded area representing the area which satisfies the maximum acceptable thermal resistance for which the maximum junction temperature requirement is met.

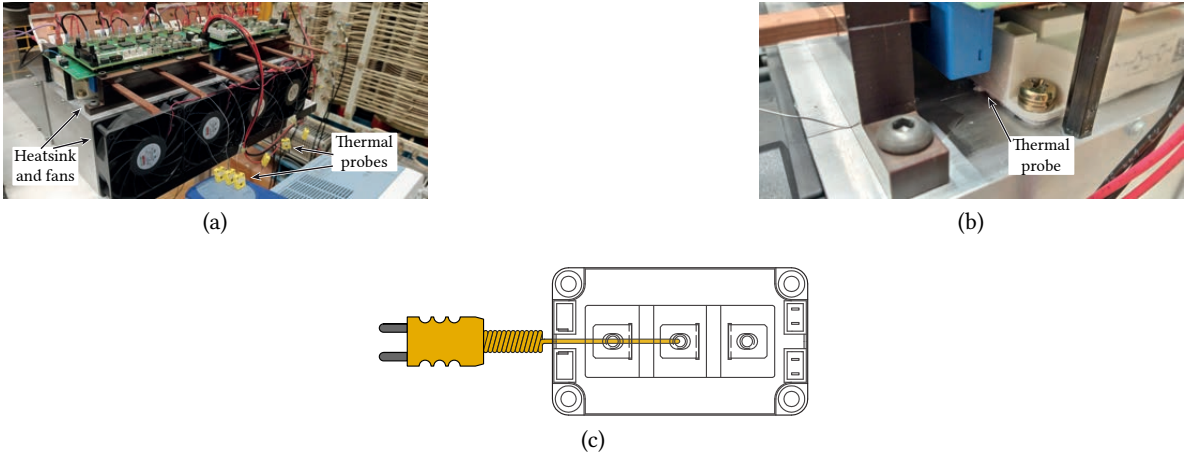


**Fig. 6.18** Cooling system for the AFE and the INU with (a) and (b) the aluminium heatsink and fans for heat extraction and thermal probes for the cooling system performance tracking. (c) The thermal probes are placed beneath the center-point of the IGBT modules.

## 6.6 Power Circulation Testing

The power circulation test in the back-to-back configuration presented in **Figs. 6.8** and **6.19** mainly serves a purpose of verifying the AFE hardware design. To perform this test the AFE and its inverting counterpart are connected to the secondaries of the MWT phase-shifting transformer, while the three-phase voltage source supplies the auxiliary winding. The test results corresponding to the configurations presented in **Tab. 6.9** are presented here. However, the power circulation test can be performed between any winding and there are 15 combinations in total, but they are not presented here in order to keep the presentation of results clear and concise. The waveforms of the AFE and the INU voltages, currents, the active and reactive powers are presented in **Figs. 6.20** to **6.22**. From the experimental results associated with different winding combinations it is visible that the current ripple of the AFE or the INU changes depending on the winding to which they are connected to, respectively. This naturally comes from a different leakage inductance of each winding. The power processed in all three tests was set at approximately  $S_{PEBB} = 66.7 \text{ kVA}$ , i.e. at the rated power. The power factor of the AFE is set at unity, i.e.  $\cos \phi = 1$ , while the INU power setpoint is changed depending on the winding combination on which the test is performed. The active and reactive power are calculated according to (6.4) in the control software in PEC using the voltages and currents of the AFE and the INU in the  $dq$ -frame. From the results presented it is evident that the connection configuration does not influence the operation of the back-to-back setup and that the power is successfully circulated between the AFE and the INU, through the transformer, using the primary-based synchronization.

**Tab. 6.9** Connection configurations

	Winding		
	$A_1$	$A_5$	$B_2$
Active Front End	$-18^\circ$	$30^\circ$	$-6^\circ$
Inverter	$B_2$	$C_4$	$C_5$
	$-6^\circ$	$18^\circ$	$30^\circ$

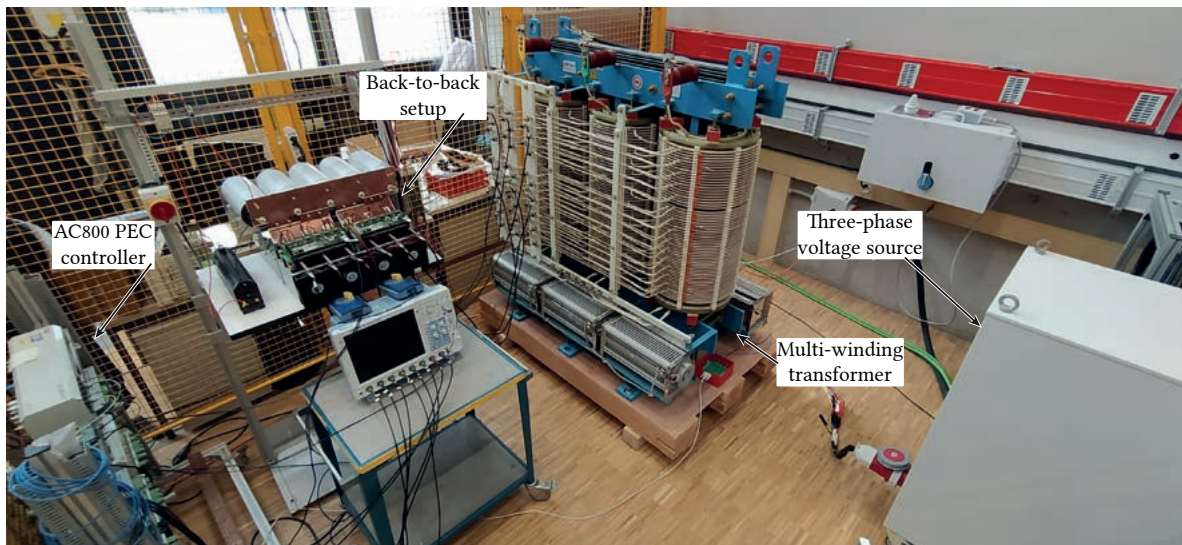


**Fig. 6.19** Back-to-back setup for full power circulation and AFE testing.

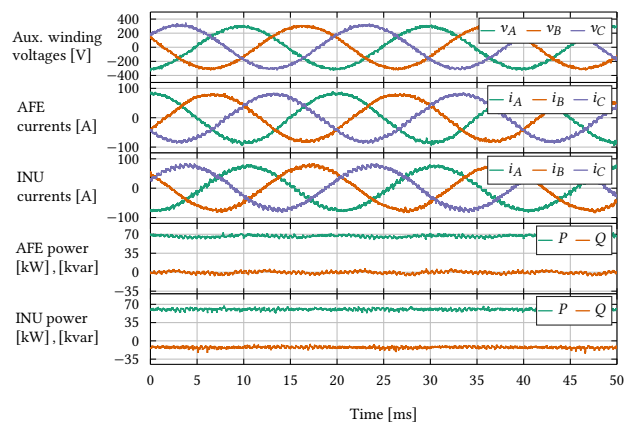


**Fig. 6.20** Voltage, current and active and reactive power waveforms for the power circulation test between windings  $A_1$  and  $B_2$ .

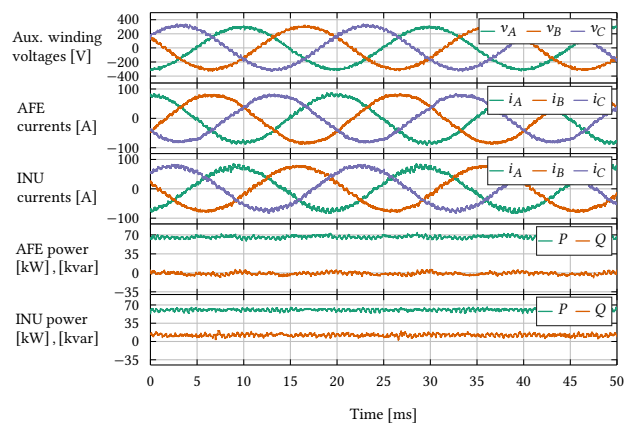


**Fig. 6.21** Voltage, current and active and reactive power waveforms for the power circulation test between windings  $A_5$  and  $C_4$ .

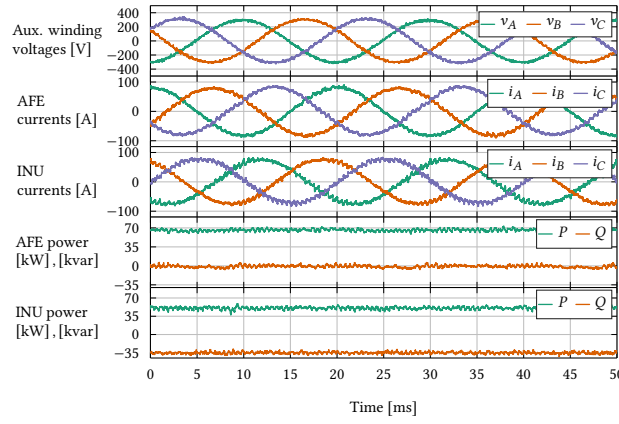


**Fig. 6.22** Voltage, current and active and reactive power waveforms for the power circulation test between windings  $B_2$  and  $C_5$ .

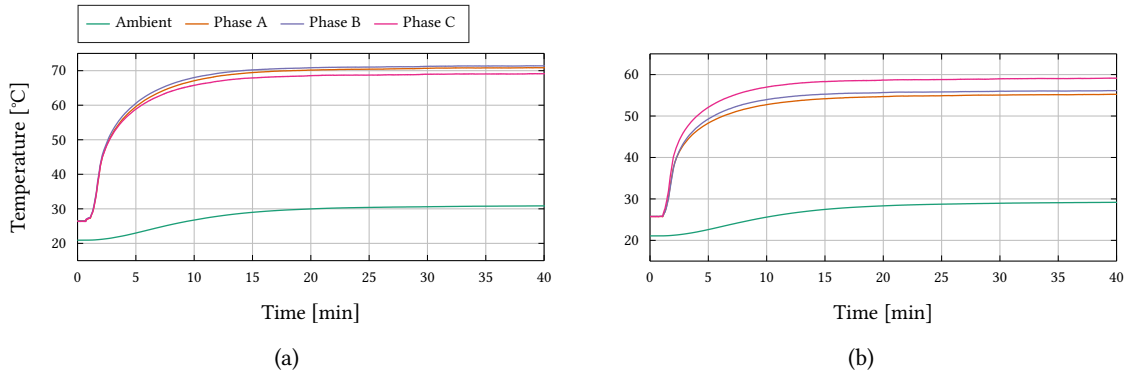


**Fig. 6.23** Case temperatures of the IGBT modules of the (a) AFE and (b) the three-phase INU.

### 6.6.1 Cooling System Performance

In order to measure the efficiency of the cooling system, the case temperature of each IGBT module was measured. This requires six thermal probes to be used in combination with a Pico Technology Tc-o8 Data Logger. The thermal probes are placed beneath the IGBT modules and in a way that the center point temperature of the module is measured (c.f. **Fig. 6.18**). Together with the case temperatures the logger also measures the ambient air temperature around the AFE and the INU. The case temperatures of six IGBT modules are presented in **Fig. 6.23** and it can be seen that for the full power operation the case temperature does not exceed  $72^\circ\text{C}$ . Together with the equations (6.23) to (6.25) it can be deduced that the junction temperature does not exceed  $125^\circ\text{C}$  for the IGBT and  $132^\circ\text{C}$  for the freewheeling diode, respectively.

## 6.7 Summary

This chapter has verified the hardware and control design of a single AFE of the CHB converter. On one side, the control design and verification was based on the synchronization to the primary of the transformer in combination with its leakage inductance being used as an input filter for the PEBB and on the other side on employing an industrial control system. Moreover, the method put

forward for robust control parameter identification was confirmed by testing the PEBB with identical control parameters on transformer windings with different physical characteristics such as the leakage inductance of voltage transformation ratio. The hardware design of the three-phase AFE was carried out through the power circulation test where two identical AFEs exchanged the rated power of a PEBB through the windings of the transformer and its magnetized core, while being supplied by an external three-phase active source. With the hardware and control designs verified and being in place the further development of the CHB converter is made possible.

# Terminal Characteristics Measurements and Analysis of the Three-Phase AFE

*To support the development of the cascaded H-bridge topology from the system level standpoint the active front end hardware and control platforms require implementation and testing. The testing aspect of the process additionally includes the measurement of terminal characteristics such as the input admittance and the output impedance, which are of particular importance for proper understanding and operation of the cascaded H-bridge system as a whole. This chapter presents the system for measuring its input admittance and output impedance. The system put in place can successfully measure both the input admittance, an ac side characteristics, and the output impedance, a dc side characteristics, and is sensible enough to the change of operation point and system parameters.*

## 7.1 Active Front End Terminal Characteristics Measurement

In order to further support the hardware and control development of the CHB, a testing and measurement platform for the identification of the input admittance and the output impedance of the AFE is required. The measurement platform should ideally make use of small-signal wideband voltage perturbation injection. For this purpose an experimental setup is assembled and presented. The system presented here includes industrial controllers and components presented in **Chap. 6** and the direct impedance measurement is needed. The theoretical developments are out of the scope of this chapter and they are already presented in more detail in **Chap. 4**, and in other external references [36], [90], [91]. Modelling and predicting the impedance of large systems is complex, and might lead to flaws, due to the ever changing nature of the system and constant inclusion of new devices and power converters as well as due to the limited information about the converters given by the manufacturers. In this case, the direct measurement is the only sensible way of obtaining an impedance of a system.

On one side, owing to the fact that the CHB topology is supplied from another medium voltage ac (MVac) system the converter requires the understanding and an assessment of its terminal characteristics for proper and safe operation. First step in characterizing the CHB converter is by acquiring the knowledge of the input admittance of its PEBBs, i.e. the input admittance of the AFE. On the other side, the AFE and the HB need to be decoupled and the AFE should not limit the output bandwidth of the HB stage. The element linking the two converters is the output impedance of the AFE [92], as discussed earlier.

For the purpose of the terminal characteristics measurement, the control system presented in **Chap. 6** is reused, i.e. the ABB AC 800PEC control system is employed together with its peripheral units and the same gate driver unit (GDU) is used to drive the Si-IGBTs. However, supplying the AFE through the MWT and injecting the small-signal perturbation through the transformer would not be the best

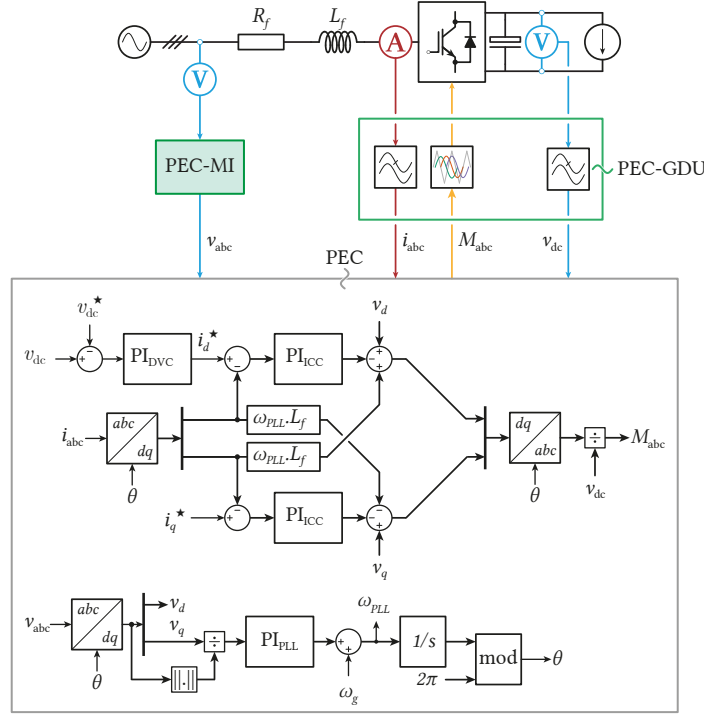


**Fig. 7.1** Control system with where the grid synchronization, dc-link voltage and input current regulation are implemented on the AC800 PEC and the IGBT switches are driven from the gate driver unit.

approach due to the reasons outlined at the introductory chapter of the thesis. Thus, an external device emulating a three-phase grid can be used together with a dedicated  $L$ -type filter.

The control system of the AFE comprises a PLL performing synchronization to the device emulating a three-phase grid. Moreover, the DVC is, in this case as well, performed using a PI regulator that provides the active current reference,  $i_d^*$ , for the ICC, while the reactive current reference,  $i_q^*$  is set independently. The current control is implemented using the SRF decoupled control after which the voltage references from the  $dq$ -frame are transformed into the  $abc$ -frame references. Finally, the modulation indices for the switching legs of the AFE are sent to the PEC-GDU. The control concept can be summarized using **Fig. 7.1**.

### 7.1.1 Control Parameters Tuning and Control Performance

The PI regulator gains of the PLL can be set according to the already established equation (6.7). For both the DVC and the ICC the PI regulator is taken as a regulator structure and the regulator parameters are tuned according to Magnitude Optimum for the ICC and according to Symmetrical Optimum for the DVC [84]–[86], i.e. according to the equations (6.8) and (6.9).

The responses of the control system to step changes of dc-link voltage reference, output load and  $q$ -axis current reference  $i_q^*$  are given in **Fig. 8.7**. The PI regulator parameters were tuned with the following parameters,  $L_f = 5$  mH,  $R_f = 100$  m $\Omega$  and  $C_{dc} = 5$  mF. To test DVC, the AFE dc-link is passively charged to  $v_{dc} = 565$  V after which the reference is set to  $v_{dc}^* = 750$  V. From **Fig. 7.2(a)** it is visible that the steady-state and the issued voltage reference are reached in about 100 ms, which is due to the regulator output limits which need to be set low in the first phase of the operation of



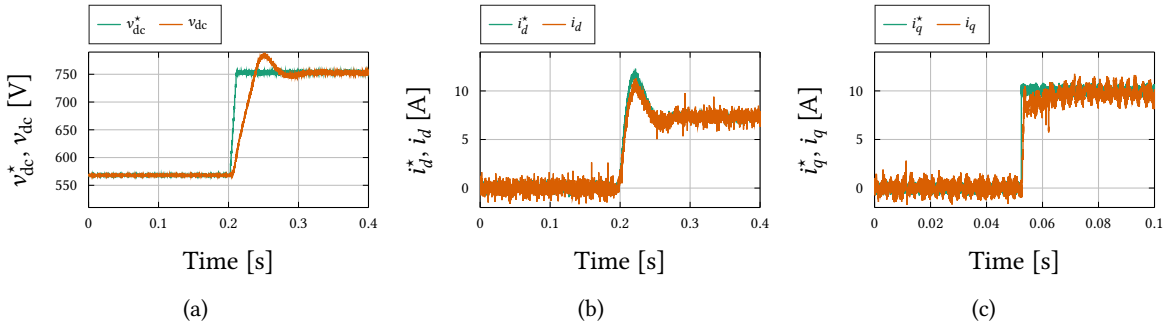


**Fig. 7.2** Voltage and current response waveforms for the step change of (a) the dc-link voltage reference, (b) the output load and (c) the  $q$ -axis current.

the converter, i.e. after the dc-link is charged actively. The ICC is tested by stepping the output load and maintaining the  $i_q^* = 0$  A which influences only the  $d$ -axis regulator. It should be remarked from **Fig. 7.2(b)** that in this test the sudden change in the output load causes a drop in the dc-link voltage to which the DVC reacts by increasing the  $i_d^*$  and that the ICC itself does present an overshoot which can be seen in **Fig. 7.2(c)** where at  $t = 50$  ms the  $i_q^*$  is set at  $i_q^* = 10$  A to test the response of the  $q$ -axis regulator. The ICC regulator performance can be evaluated from **Fig. 7.2(c)** where it can be seen that the newly issued reference is reached at  $t = 70$  ms, i.e. the steady-state is achieved in 20 ms, showing exceptionally good tracking performance of the regulators. However, a downside of the implemented control is the absence of the disturbance compensation which is visible from the **Fig. 7.2(b)**. On the other side, for the disturbance compensation to be implemented, another current sensor measuring the load current would need to be added to the system, which would in turn increase the system cost. As for the sought for application, i.e. impedance measurement, the disturbance compensation is not a priority in the control system and it does not pose an important issue.

## 7.2 Terminal Characteristics Measurement System

The measurement of terminal characteristics of the AFE, i.e. the input admittance and output impedance, requires a system consisting of several components and is represented using the schematic in **Fig. 7.3**. Since the admittance is the ac-side characteristics in this particular case while the impedance is the dc-side the methods in which the measurements are performed are somewhat different. For the measurement of the input admittance, the first component needed is a device capable of injecting small-signal voltage perturbations at the ac or the dc terminals of the AFE. A grid emulator such as Regatron TC.ACS, presented as the ACS source in **Fig. 7.3**, is capable of supplying the fundamental voltage and injecting the perturbation on top of the fundamental component and is chosen as a PIC [45]. The same grid emulator can be used as a dc source and can be used to inject small-signal perturbations. The second part of the system are the current and voltage transducers measuring the input voltage and its small-signal components, and the current resulting as a response of the AFE control system. The following element of the system is a high sample rate data-acquisition instrument, presented as DAQ block in **Fig. 7.3**, collecting the measured voltages and currents for further processing. Finally, once collected, different frequency component extraction techniques can be applied to the measured voltages and currents from which the admittance and impedance can be calculated using MATLAB software in the command and supervisory unit (CSU) in **Fig. 7.3**.

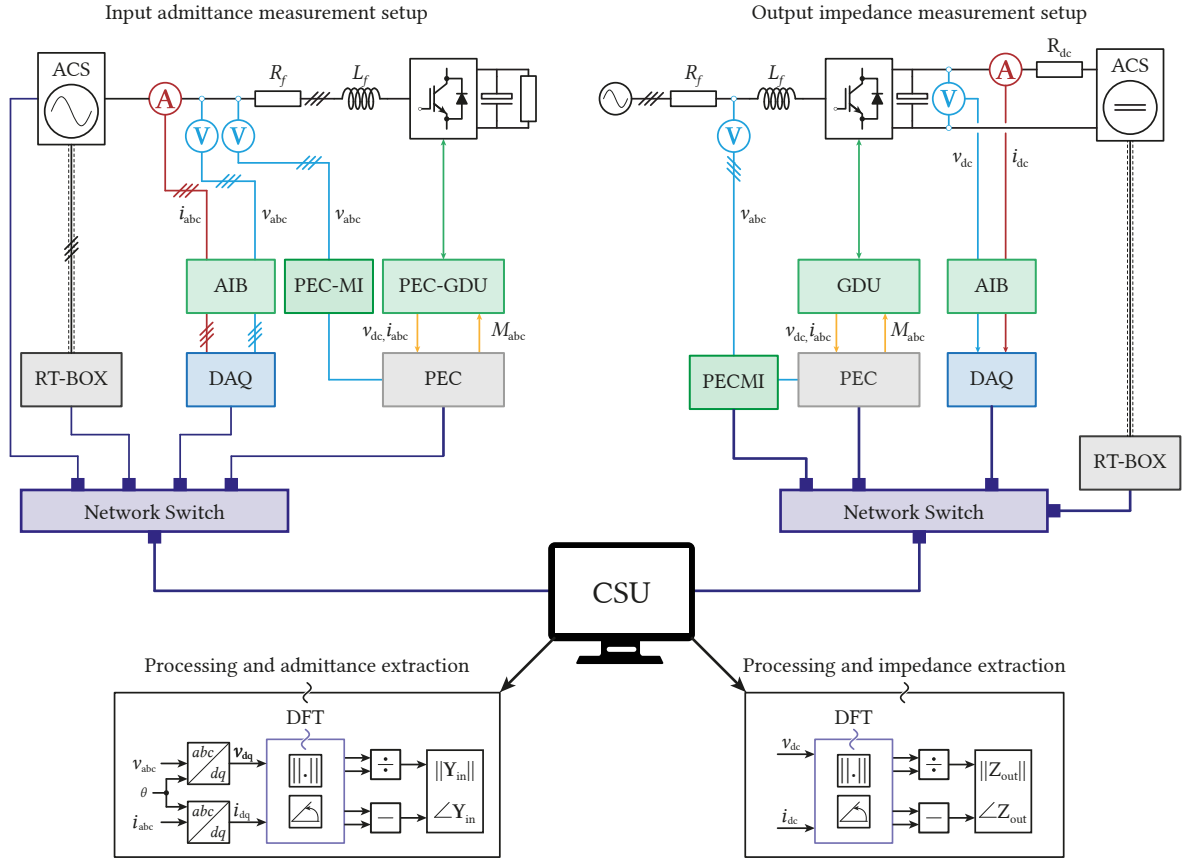


**Fig. 7.3** Schematics of the experimental setup for the measurement of the input admittance and the output impedance of the AFE.

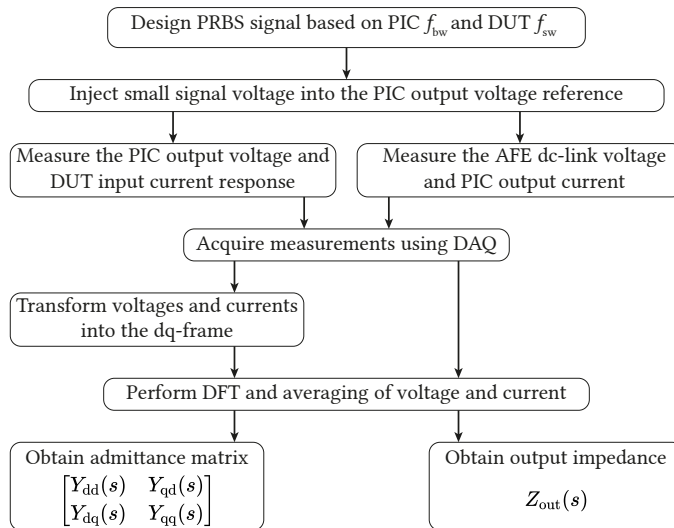


**Fig. 7.4** Flowchart for input admittance and output impedance measurement of the AFE.

### 7.2.1 Grid Emulator and Perturbation Injection Converter

Measuring the terminal characteristics of a grid connected converter is performed by injecting a small-signal voltage or current perturbations and measuring the resulting current or voltage response. The Regatron TC.ACS is capable of emulating an ac grid and acting as a dc voltage source and at the same time injecting small-signal perturbations. Since the perturbation signals are not usually readily available in the grid emulator control software, another external signal generator is needed in order to provide references and drive the TC.ACS. For this role, the Plexim RT-Box is chosen as a versatile device that can perform the duty of the signal generator. In the RT-Box, the ac grid and dc voltage source models are established and its analog outputs are used as the analog inputs for the Regatron TC.ACS output voltage references.

Measuring the input admittance is performed by injecting small-signal voltage perturbation in the output voltage reference of the TC.ACS. These perturbations give rise to current response as a consequence of the AFE control system upon which the ac-side voltage and current measurements are collected.

On the other hand, measuring the output impedance can either be performed having a controllable current source or combining a controllable voltage source with an inductor or a resistor in series. The TC.ACS combined with the resistor  $R_{dc}$  acts as a controllable current source. By controlling the output voltage of the TC.ACS and injecting small-signal perturbations in this voltage, a current perturbation for the AFE is created. This provokes a response from the AFE dc-link voltage control after which the dc-side voltage and current measurements are collected.

### 7.2.2 Perturbation Signal

A method that is widely adopted in impedance/admittance measurements of grid-connected converters, such as the three-phase AFE is the sine sweep, which requires one by one frequency small-signal perturbation injection and collection of response, thus requiring large number of measurements and time to be executed. If the measurement time is too long, the measured object may as well be disturbed and change its operating point and subsequently the impedance or admittance would change. This is somewhat improved with multi-tone signals but the energy of this signal is reduced with the number of tones it consists of. Recently, PRBS signals have seen substantial use for system identification and impedance measurement [30], [31], [58]. The advantage of these signals lies in the fact that they are well suited for the characterization of dynamics systems where rapid measurement is necessary due to the possibility of variation of the system state in time. The maximum frequency of the perturbation signals needs to be chosen with respect to PIC output bandwidth as well as the device under test (DUT) switching frequency, thus some preliminary knowledge of the DUT parameters is needed. In this particular case, the PRBS-9 signal is used resulting in a 511-bit-long signal. Taking into account the Regatron ACS output voltage control bandwidth, the sequence was generated at  $f_{gen} = 2$  kHz, which sets the injection time at about  $t_p = 250$  ms and the resolution frequency at  $f_{res} = 3.914$  Hz. For the sake of comparison between the PRBS and ac sweep injection the following analysis can be performed. Performing an ac sweep with 511 different frequencies which are given as  $f_p = 3.914, 2 \cdot 3.914, 3 \cdot 3.914, \dots, 2000$  Hz and performing 16 injections yields the total injection time of  $t_{sweep} = 27.85$  s. Performing the same perturbation injection with the PRBS signal yields the total time of  $t_{PRBS} = 4.088$  s. Thus, performing the PRBS perturbation signal injection in this particular case takes seven times less. Moreover, when performing the frequency analysis and frequency component extraction using the FFT methods in combination with the PRBS signal

injection all of the 511 components are extracted in a single iteration while the ac sweep method requires that each dataset is analysed separately and that a single frequency is extracted at a time.

### 7.2.3 Voltage and Current Measurement

Even though the input admittance is represented in the  $dq$ -frame, the only available voltage and current measurements are in the  $abc$ -frame. These measurements are implemented using voltage and current transducers. The issue of choice of transducers is related to the fact that they need to be able to measure the nominal voltage and current values of the system while at the same time being able to measure the small-signal portion of the measurand with a good enough precision. Moreover, depending on the choice of the PRBS type signal and its generation frequency, the perturbation signal may often have high frequency components which in turn requires that the transducers chosen have a large enough bandwidth for the measurement. Likewise, the PRBS signals contain low-frequency components resulting in the need that the transducers need to reliably measure the low-frequency signals. The sensors chosen for the voltage and current measurements are the ABB VS1500B [93] and LEM LF210-S [94] transducers, respectively. In total, there are six sensors, three for voltage and three for currents. Since the neutral point is available at the output terminals of the Regatron ACS, the line-to-neutral voltages and line currents are measured. When measuring the output impedance the same transducers can be used, however this time measuring the dc-link voltage of the AFE and the output, or load, current. In order to interface the transducer output to the data-acquisition system an intermediate board is added to the system that simultaneously incorporates a  $f_c = 10$  kHz low-pass analog filter and voltage limiters in order not to damage the data-acquisition system.

### 7.2.4 Data-Acquisition System

In order to follow up with the requirements for having high-bandwidth, precise voltage and current transducers for measurements the data-acquisition system employed needs to have a high sampling rate as well. Due to the number of signals acquired the sampling of each signal needs to be performed simultaneously in order to avoid delays between the signals sampled. Furthermore, having a system capable of storing large amounts of data, namely more than one perturbation period is sought for. The reason for this is the fact that having multiple periods measured and acquired allows for averaging over these multiple periods. This greatly improves the quality of results in systems where unwanted noise is unavoidably present. A data-acquisition system fulfilling these requirements is the Elsys Tranet 408s [95] transient recorder capable of performing sampling at a rate of up to  $M = 80$  MS/s. The voltage and current measurements are acquired over a time period of about  $t_r = 4$  s which, taking into account the resolution frequency, leads to 16 perturbation periods acquired.

### 7.2.5 Admittance and Impedance Extraction

Once measured and collected with the data-acquisition instrument, the voltage and current measurement can be used for processing. In this particular case this is done offline using MATLAB software. In order to extract the frequency components, namely magnitude and phase, from the measurements the DFT is performed. The acquired data is split into 16 periods of identical length and the DFT is performed on these periods upon which the data are averaged. Here, the geometric mean is used to

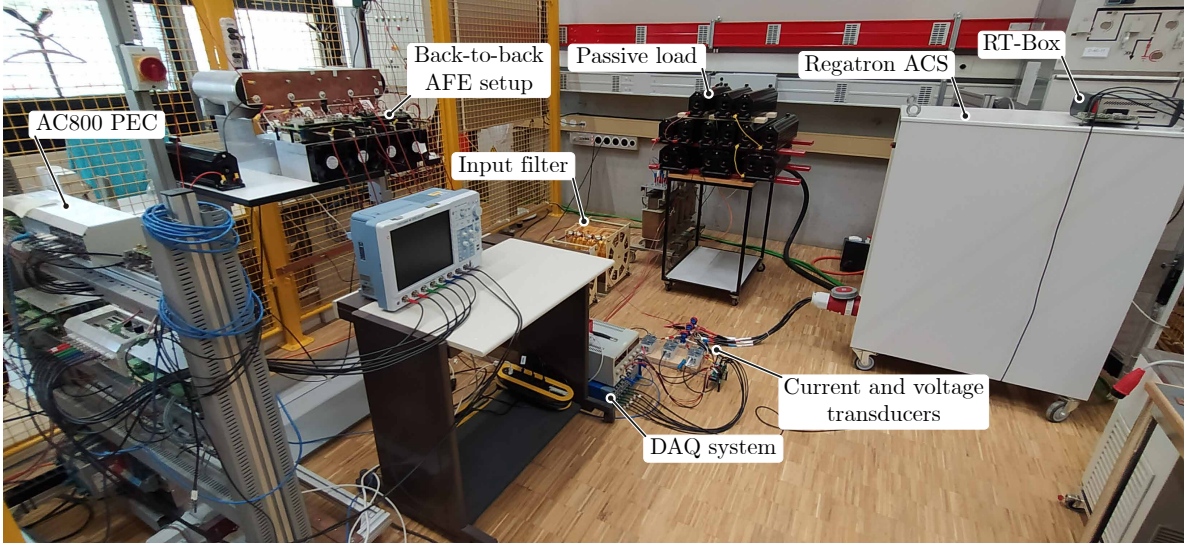


**Fig. 7.5** Experimental setup for the input admittance and output impedance measurement including the RT-Box driving TC.ACS employed as a PIC, the input  $L$ -type filter, the AC800 PEC controller, back-to-back AFE setup and the passive load.

average the measurements which is given as:

$$\bar{x} = \left( \prod_{i=1}^n x_i \right)^{\frac{1}{n}} \quad (7.1)$$

Where the  $x$  is the voltage or current measurement and  $i = 1, 2, \dots, 16$  denoting the  $i^{\text{th}}$  period of the data. Following the averaging of the data the admittance matrix in the  $dq$ -frame is extracted as:

$$\begin{aligned} \mathbf{Y}_{\text{in}}(s) &= \begin{bmatrix} i_{d,1}(s) & i_{d,2}(s) \\ i_{q,1}(s) & i_{q,2}(s) \end{bmatrix} \cdot \begin{bmatrix} v_{d,1}(s) & v_{d,2}(s) \\ v_{q,1}(s) & v_{q,2}(s) \end{bmatrix}^{-1} \\ &= \begin{bmatrix} Y_{dd}(s) & Y_{dq}(s) \\ Y_{qd}(s) & Y_{qq}(s) \end{bmatrix} \end{aligned} \quad (7.2)$$

Where the  $i_{x,y}$  and  $v_{x,y}$  are the measured currents and voltage in the  $dq$ -frame after the first and second injection. Similarly, the DFT is performed on the dc-side voltage and current measurements and the output impedance can be extracted as:

$$Z_{\text{out}}(s) = \frac{\|\tilde{v}(s)\|}{\|\tilde{i}(s)\|} [\angle \tilde{v}(s) - \angle \tilde{i}(s)] \quad (7.3)$$

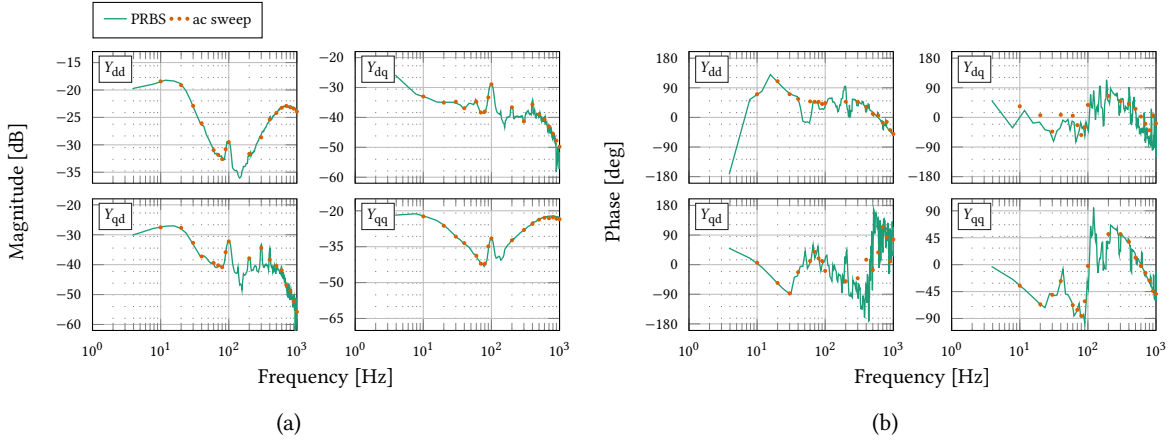
The admittance and impedance measurement method can be summarized using the flowchart presented in **Fig. 7.4**.

### 7.3 Measurement Results

The implemented experimental setup for the ac-side input admittance measurement using the elements outlined is presented in **Fig. 7.5** while for the setup for the measurement of the dc-side output

**Tab. 7.1** Input admittance measurement parameters

Measurement	$K_{p,ICC}$	$K_{i,ICC}$	$K_{p,DVC}$	$K_{i,DVC}$	$K_{p,PLL}$	$K_{i,PLL}$	$P_{in}$	$L_f$	$R_f$	$f_{sw}$	$C_{dc}$
I	9.43	118.7	0.8	61.8	92	4232	22 kW	5 mF	100 mΩ	8 kHz	5 mF
II	9.43	118.7	0.8	61.8	92	4232	11 kW	5 mF	100 mΩ	8 kHz	5 mF
III	7.1	141.5	0.6	34.8	92	4232	22 kW	5 mF	100 mΩ	6 kHz	5 mF
IV	5.1	94.4	0.8	61.8	92	4232	22 kW	2.7 mF	100 mΩ	8 kHz	5 mF

**Fig. 7.6** (a) magnitude and (b) phase of input admittance matrix  $\mathbf{Y}_{in}$  of the AFE with parameters of measurement I presented in **Tab. 7.1**. Two sets of measurements are shown, one obtained using the PRBS injection and another, a reference set, obtained using the ac sweep injection.

impedance one can refer itself to the right hand side of **Fig. 7.3**. The same elements from **Fig. 7.5** are reused for output impedance measurement but respecting the layout of **Fig. 7.3**. The amount of small-signal voltage injected is about 5–6 % of the nominal voltage. Even though injecting more voltage is desirable from the standpoint of obtaining better measurements, it is in turn undesirable from the perspective of the system protection, thus the level of injected voltage must be carefully chosen in order not to perturb the normal operation of the AFE.

For the admittance measurements two injections are performed, one in the  $d$ -axis of the reference voltage and the second in the  $q$ -axis. In total, four different measurements were performed in which the AFE was operating with different parameters, such as a different inductance of the input filter, a different switching frequency, or a different operating point, i.e. a different value of the load. Both the value of the filter and the switching frequency influence the DVC and ICC PI regulator gains, which in turn influences the shape of the admittance. In all four measurements the input line-to-line voltage was established at  $v_g = 400$  V. The reduced input voltage compared to the nominal voltage of the AFE is due to the limitations of the TC.ACS output voltage level. Different parameters of the performed measurements are summarized in **Tab. 7.1**.

From results presented in **Figs. 7.6** to **7.9** it is noticeable that there is a difference in measured input admittance depending on the parameters from **Tab. 7.1**. The operating point mostly influences the low frequency region which is clearly visible by comparing **Figs. 7.6** and **7.7**. The difference in switching frequency alters the regulator gains and reduces the control bandwidth which is interpreted as having a slightly lower admittance in **Fig. 7.8** and the characteristics shifting to the left in the frequency range compared to **Fig. 7.6**. Additionally, in **Fig. 7.6** a set of measured impedances obtained using the

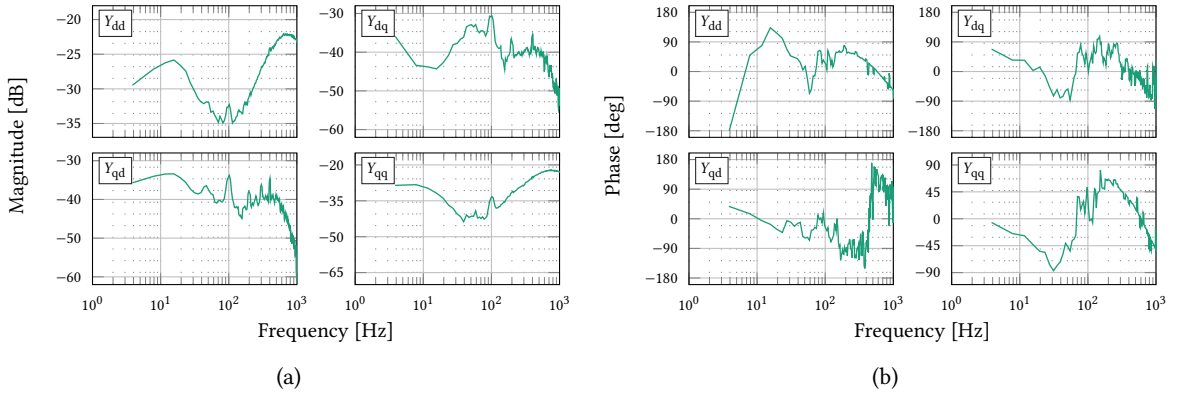


**Fig. 7.7** (a) magnitude and (b) phase of input admittance matrix  $\mathbf{Y}_{in}$  of the AFE with parameters of measurement II presented in **Tab. 7.1**.

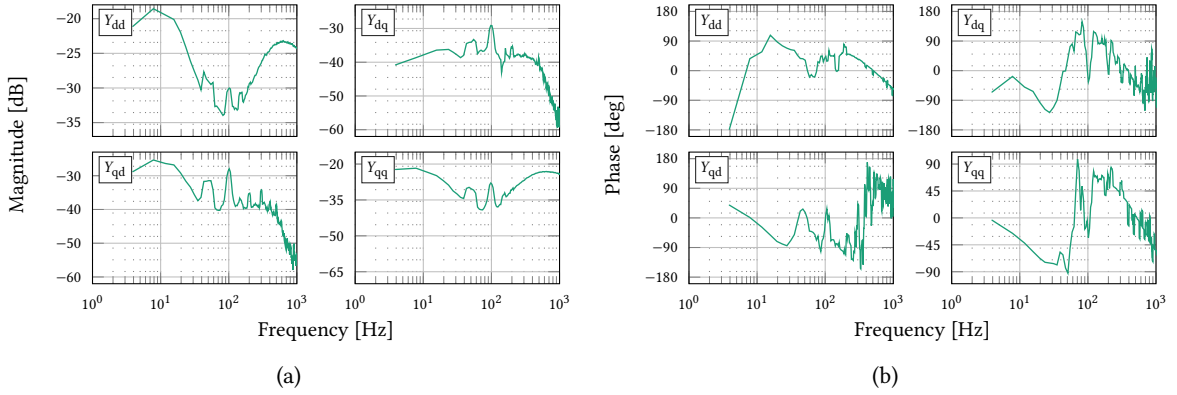


**Fig. 7.8** (a) magnitude and (b) phase of input admittance matrix  $\mathbf{Y}_{in}$  of the AFE with parameters of measurement III presented in **Tab. 7.1**.

ac sweep injection, which serves as a reference measurement, is added on top of the results obtained with the PRBS injection.

When it comes to the impedance measurements four different measurements were performed as well. The load current was varied between 5 A and 12.5 A, resulting in the power variation between 3.75 kW and 9.4 kW. The experimental measured output impedances are presented in **Fig. 7.10** for four different loads. It can be discerned between **Figs. 7.10(a) to 7.10(d)** that the impedance shape or rather its value changes in the low frequency range. The variation is between  $-1$  dB and  $3$  dB which is characteristic for the change of operation point of the converter. Moreover, the impedance shape presents a drop after 20 Hz which indicates the bandwidth of the DVC. However, the output impedance has a highest value between the dc value and 50 Hz after which the impedance decreases sharply with a rate of  $-25$  dB/dec. Thus it can be concluded that outside of this range, and in general, outside of the output voltage control range, the output impedance has little influence on the system. In conjunction with the results from [92] it can be concluded that the output impedance has little effect on the control-to-output characteristics of the CHB beyond 50 Hz.



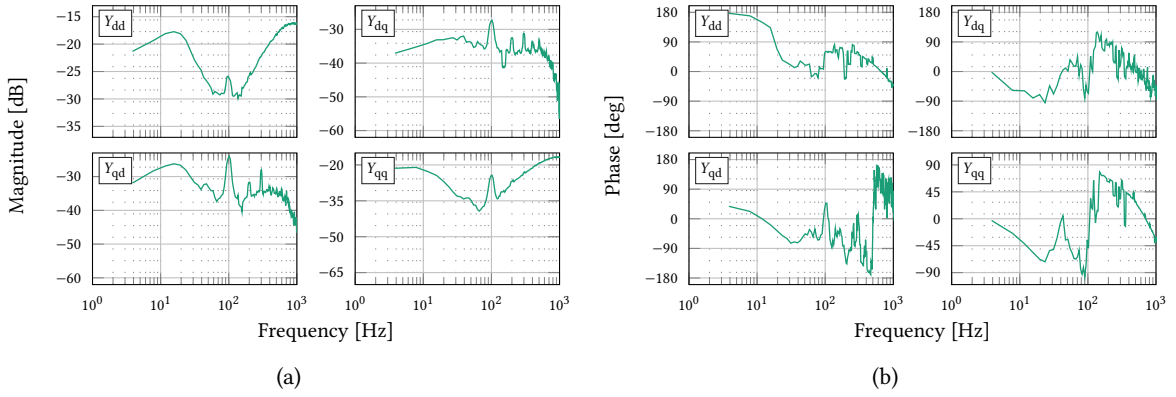


**Fig. 7.9** (a) magnitude and (b) phase of input admittance matrix  $\mathbf{Y}_{in}$  of the AFE with parameters of measurement IV presented in **Tab. 7.1**.

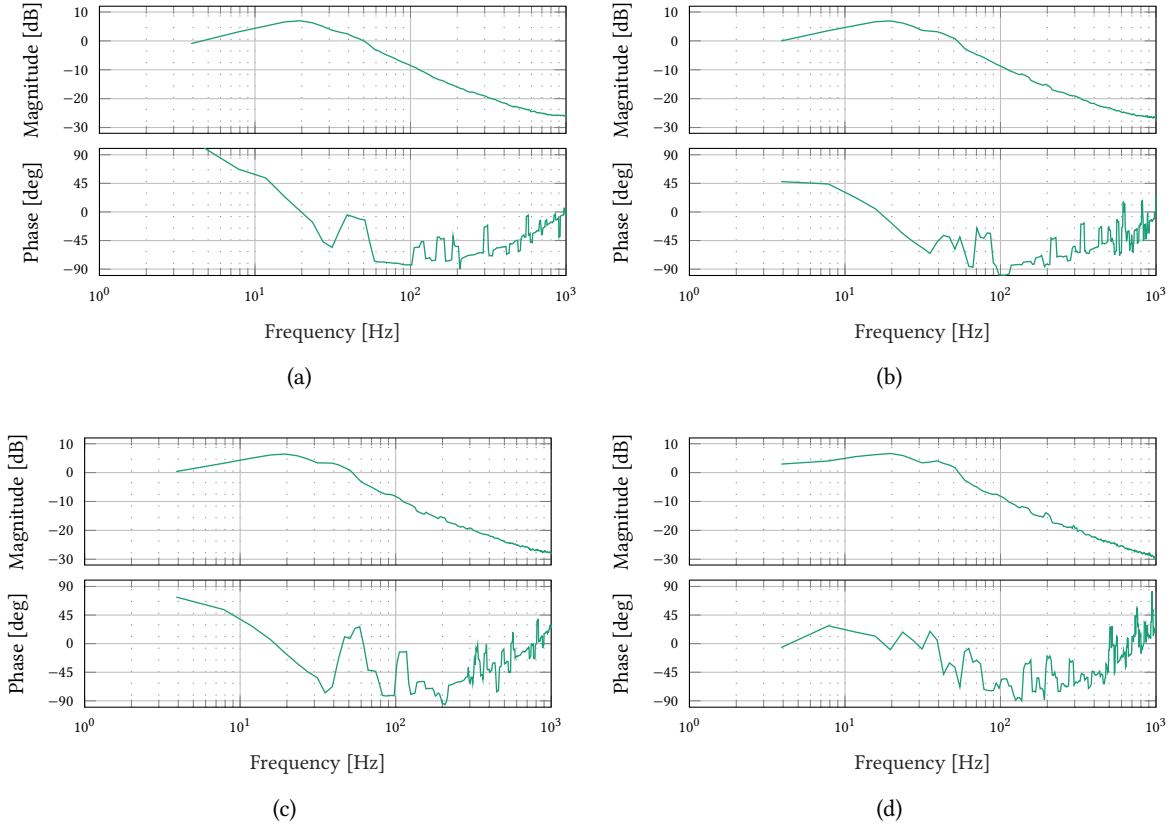


**Fig. 7.10** Magnitude and phase of output impedance  $Z_{out}$  of the AFE with **a)**  $I_{dc} = 5$  A, **b)**  $I_{dc} = 7.5$  A, **c)**  $I_{dc} = 10$  A and **d)**  $I_{dc} = 12.5$  A.

Nevertheless, the presented system does feature certain limitations such as the limited frequency range in which the measurement is performed. This, however, depends on the perturbation injection device employed for the process, and since it is a commercial device it is one of the drawbacks that is



not solved easily. Another limitation is the fact that the measurements were performed on a system with lower ratings than the nominal ones presented in [92], which is also due to the limited output voltage of the supply source used.

## 7.4 Summary

This chapter discussed the design and implementation of the measurement platform for input admittance and output impedance measurement of the AFE of a PEBB of the MV-CHB converter. The presented results indicate that the measurement platform and methods applied can clearly distinguish different admittance shapes arising as a result of the change of parameters of the AFE. Moreover, due to the frequent lack of knowledge of all parameters of industrial equipment employed for the control of the converter, practical measurements are usually the only trustworthy method of admittance or impedance identification for power electronics converters. Furthermore, the use of wideband signals for measurements has double benefit. One benefit is the significant reduction in measurement time and complexity compared to standard methods such as an ac frequency sweep while the other one is preventing that the converter on which the measurements are performed changes its operation point during the measurement. Namely, the measurement time is reduced sevenfold compared to the use of ac sweep signal injection and measurement. Moreover, the post-processing time and impedance extraction time is reduced. Presented measurement platform and results serve as a basis for proper understanding and operation of the MV-CHB as well as experimental verification of the way in which the AFE influence the HB in the MV-CHB PEBB, and its output overall.



# 8

## Flexible Medium-Voltage Perturbation Injection Converter for Ac and Dc System Identification

*This chapter builds on the previous developments, presents and discusses the flexible medium voltage cascaded H-bridge converter for impedance/admittance measurement of ac and dc systems. The effectiveness and flexibility of the topology is shown through a simulation case study where the terminal characteristics of a modular multilevel converter are measured. It has been shown how the cascaded H-bridge can be reconfigured to measure both the ac and dc characteristics of the modular multilevel converter. Moreover, three different dc output configurations with different parameters can be used depending on the voltage and power levels required.*

### 8.1 Flexible Cascaded H-Bridge Converter

The lack of flexibility within the PICs present in the field, inherently limits the range of systems that they cover. Namely, the constraints come in the form of the limited output voltage level and the type of the output voltage, i.e. they are mainly used for ac systems. However, with the development of MVdc systems there comes a need for devices suitable for their impedance measurement and identification, as well. Instead of having separate PICs for ac and dc systems, a sort of a *Swiss-knife* fitting for both, is preferable. The solutions presented in the overview of the perturbation injection converters do not satisfy these criteria, and in general have a very low degree of flexibility and they are hard to employ outside of their intended area of use. Even though the CHB topology is originally intended to be operated as an ac motor drive [54], and quite often as a static synchronous compensator (STATCOM) device [96]–[98] for three-phase ac systems, and it does not fit under the group of *modular* converters, strictly speaking, it is still a highly flexible topology and it can be reconfigured to generate dc output voltages as well. In addition, in order to fully achieve the dc voltage output of the CHB the voltage control algorithm needs to be adapted. The flexible MV-CHB presented in this chapter is an effective mean of measuring the impedances and admittances of MVac and MVdc systems alike.

#### 8.1.1 Ac Output Configuration

When the CHB converter, presented in **Fig. 8.1**, is operated with an ac output, the phase-shifting MWT secondary windings enable stacking up to 5 PEBBs per phase and thus create a three-phase ac output with an increased output voltage level and high effective switching frequency, provided a proper modulation scheme is used. This allows for higher output voltage bandwidth and thus higher frequency perturbation injection and measurements. The switching frequency of an individual HB equals

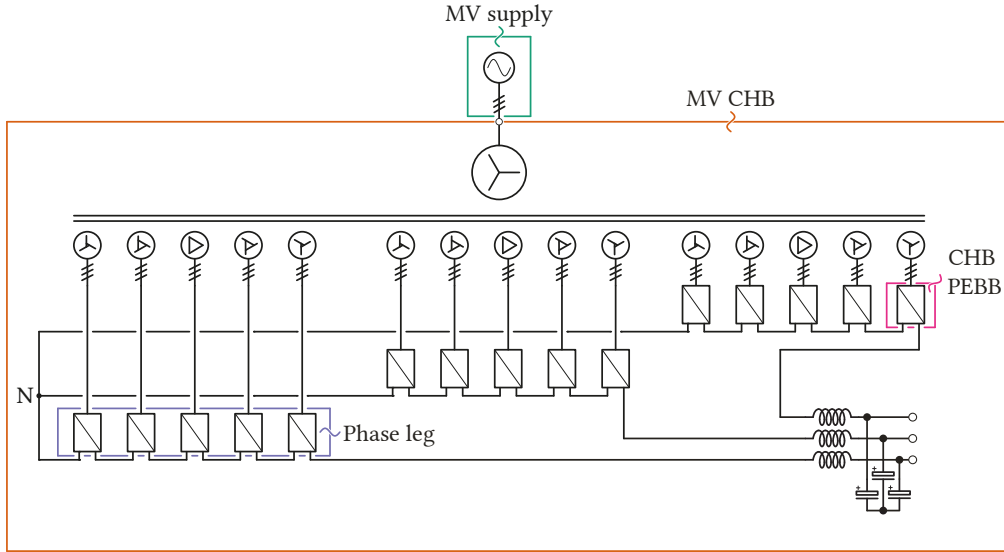


**Fig. 8.1** CHB topology consisting of a multi-winding 6.3 kV transformer with 15 phase-shifted 710 V secondaries and three groups of five PEBB connected in series to create three-phase MV output and a dedicated output filter.

$f_{sw}^{HB} = 20$  kHz. Using the bipolar PS-PWM, by shifting the carriers modulating two neighbouring cells, the equivalent switching frequency of the phase-leg can be increased to  $N_{cell} \times f_{sw}^{HB} = f_{sw}^{CHB} = 100$  kHz. As a result, an outstanding performance and bandwidth can be ensured allowing for high-fidelity voltage perturbations to be injected into an unknown network or the DUT through an LC-type filter. The presence of the MWT on the input side is one of the advantages of this topology, at least from the output stage bandwidth point of view. Having the MWT at the input means that there is no need to have a step-up transformer on the output side to elevate the voltage to MV level. As a result, the output stage high-frequency bandwidth is not limited by the leakage inductance of the output transformer. In a three-phase ac configuration the CHB cells outputs are interfaced to a three-phase LC-type filter where the output voltage is controlled. The converter is sized for a total dc-link voltage of  $v_{dc,\Sigma} = 6$  kV, per phase leg, and the power of  $S_{out}^{CHB} = 1$  MVA. Hence, the converter can be operated with an output voltage of anywhere between zero and  $v_{out}^{CHB} = 6$  kV, again provided appropriate output voltage control algorithm is used.

### 8.1.2 Dc Output Configuration

For the needs of measuring an impedance, or an admittance, of a dc system, the CHB output stage can be easily reconfigured into an arrangement that allows the dc output voltage generation at the terminals of the converter. The flexibility of the CHB is emphasized by the fact that there exist several possibilities of hardware reconfiguration depending on the sought for output voltage and current ratings. From the modulation standpoint, the PS-PWM is inherited from the ac output CHB and it can be used for the dc output as well. All of the configurations outlined here consider that the output voltage is controlled to have a dc value.

A fairly simple and straightforward mean of achieving a dc operation with a CHB converter is done by interleaving the individual phases into one single phase. In this way, the total dc-link voltage does not

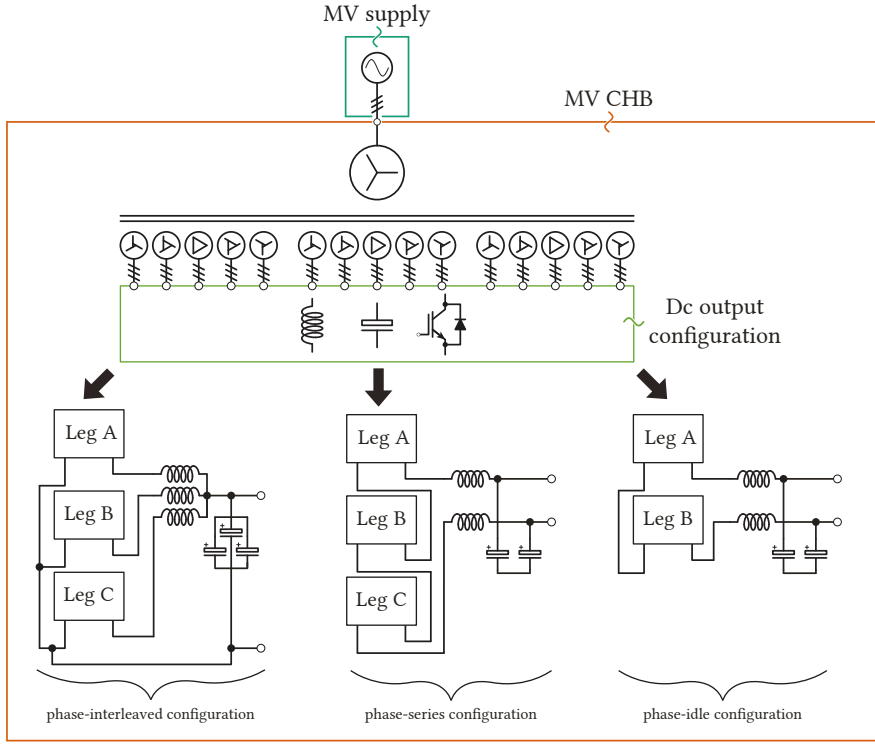


**Fig. 8.2** CHB topology with three different hardware reconfigurations for the dc operation of the converter.

exceed the rated voltage and the maximum output voltage is equal to  $v_{\text{out}}^{\text{CHB}} = 6 \text{ kV}$ . Moreover, each phase shares  $1/3$  of total current, thus the original power rating can be preserved. Furthermore, by interleaving the phase legs of the CHB the current ripple is reduced threefold. From the modulation point of view, the interleaving can be achieved by shifting the groups of carriers by  $f_{\text{sw}}^{\text{CHB}}/3$ . This configuration is presented as phase-interleaved in **Fig. 8.2**.

Another manner of obtaining a dc operation with the CHB converter is by connecting the phase legs, of a previously three-phase converter, in series and replacing the three-phase filter with a single-phase one. In this case the input voltage of the MV supply would need to be reduced in order to obtain a total dc-link voltage of  $v_{\text{dc},\Sigma} = 12 \text{ kV}$ . The reason for this particular voltage choice is the fact that it does not violate the voltage insulation constraints of the converter as the MWT is designed to support voltage this high [82]. In turn, operating the converter with lower dc-link voltage leads to lower power processing capabilities as the rated power becomes reduced to  $2/3$  of the initial one. Since the perturbation injection converters usually do not supply the main power of the system this does not arise as an issue. It would come as a problem only if the CHB would be used to supply the main power and the rated power of the SUT would surpass the  $2/3$  of the CHB power. The phase-series configuration is suitable for systems for which the output voltage of the phase-interleaved configuration is not sufficiently high to perform the perturbation injection. Theoretically, the dc-link voltage could be elevated to  $v_{\text{dc},\Sigma} = 18 \text{ kV}$ , provided that another transformer is used whose insulation is capable of withstanding this voltage. This proposition is presented as the phase-series configuration in **Fig. 8.2**.

Finally, a third possibility is presented as phase-idle configuration in **Fig. 8.2**. The advantage of the

**Tab. 8.1** Dc output configuration summary

Phase configuration	$v_{out}^{CHB}$	$i_{out}^{CHB}$	$S_{out}^{CHB}$
interleaved	6 kV	166 A	1 MVA
series	12 kV	55.5 A	667 kVA
idle	12 kV	55.5 A	667 kVA

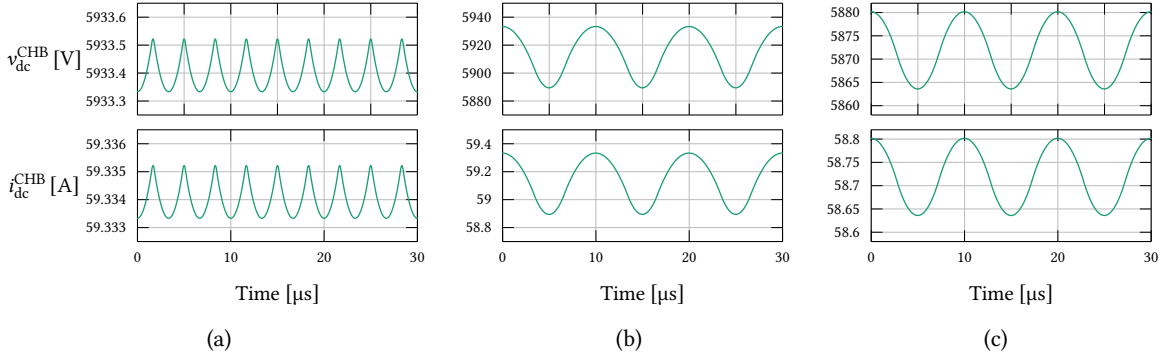


**Fig. 8.3** Voltage and current waveforms of (a) phase-interleaved, (b) phase-series and (c) phase-idle configurations of flexible CHB converter.

following proposition lies in the fact that it requires less hardware reconfiguration and it uses the original layout of the CHB topology. The output can be used in a way that only two out of three converter phases are utilized and the output is driven to be a dc output through the control. As in the previous case, in this case as well the output voltage is higher than in the first case. However, as only two out of three phases are used here the total power of the system is reduced to  $2/3$  of the original power rating. An additional challenge is the operational state of the third phase leg. The simplest option stays to charge it through the AFE control and not operate the phase leg, i.e. not perform the modulation and switching. A potential advantage when operating the CHB using the phase-idle configuration is cycling the phase which is not active for each individual measurement. In this manner, the stress on the CHB semiconductors and capacitors is reduced and it potentially prolongs the lifetime of the converter itself.

The voltage and power ratings of different dc output configurations are summarized in **Tab. 8.1**. The voltage and current simulation waveforms for the three different configurations are presented in **Fig. 8.3**. It can be noticed that all the configuration were both operated with almost 6 kV output voltage, even though the phase-series and phase-idle configurations can be operated with 12 kV output. The output voltage was reduced in order to have a fair comparison with the phase-interleaved configuration where the maximum output voltage is 6 kV. Here, a simple  $R$  load was used as a SUT and interfaced to the flexible cascaded H-bridge (FlexCHB). From **Fig. 8.3** it is visible that the phase-interleaved configuration largely outperforms the two other configurations in terms of voltage ripples. This comes as a natural consequence of interleaving the phases, thus reducing the current ripple on one side and on the other side by additionally shifting the modulation carriers which additionally reduced the voltage and current ripple. Nevertheless, the other two configurations present a voltage ripple of  $\Delta v = 15 - 25$  V, which is negligible taken into the voltage output of almost 6 kV in the presented case.

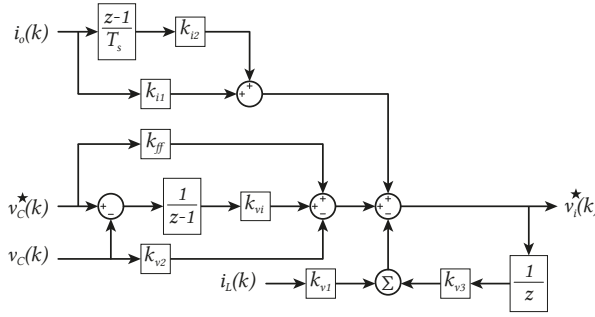


**Fig. 8.4** Control block diagram of the output voltage controller.

**Tab. 8.2** State-space controller gains

Gain	ac output	dc output
$k_{v1}$	$6.32 - j0.04$	9.1
$k_{v2}$	$-0.1 + j0.0006$	0.3
$k_{v3}$	$0.86 - j0.006$	0.98
$k_{vi}$	$0.0700 + j0.0034$	0.21
$k_{ff}$	$0.58 + j0.0156$	1.88
$k_{i1}$	$15.17 + j0.035$	18.2
$k_{i2}$	$(1.9754 + j0.005) \cdot 10^{-4}$	$2 \cdot 10^{-4}$

## 8.2 Output Voltage Control

The high equivalent switching frequency at the converter output is beneficial for the quality of the voltage output as well as the closed-loop bandwidth. In order to gain from this extended bandwidth single-loop voltage control is preferred over double-loop one. The reason is the fact that double-loop control limits the bandwidth as it is constrained by the bandwidth of the inner control loop and the output control loop bandwidth should be set up to ten times lower than the inner loop bandwidth. The bandwidth of the inner control loop, on the other hand, should be set below the  $LC$  filter resonance frequency. In order to overcome this problem, the single-loop voltage control implemented is based on the method presented in [99] where the controller gains are obtained from system parameters and design specifications based on direct pole placement. Moreover, adopting such an approach guarantees a passive output impedance of the FlexCHB, which is essential for perturbation injection converters since this method is required to be non-invasive to the SUT [100]. The control method can be applied to the control of both ac and dc variables making it ideal for the needs of the CHB perturbation injection converter. Here, phase-interleaved configuration is taken as the dc output configuration. The control block diagram is presented in **Fig. 8.4**, while the gain values for ac and dc outputs are given in **Tab. 8.2**. This choice of gains results in a theoretical bandwidth of up to  $f_{BW} = 7$  kHz, following the developments provided in [99].

## 8.3 MMC Ac and Dc Admittance Measurements

An example of a system that is both MVac and MVdc is the MMC, presented in **Fig. 8.5**. From the power electronics side point of view, the MMCs have been used extensively to support the expansion of the MVdc infrastructure, as they offer a high degree of flexibility in terms of power and voltage

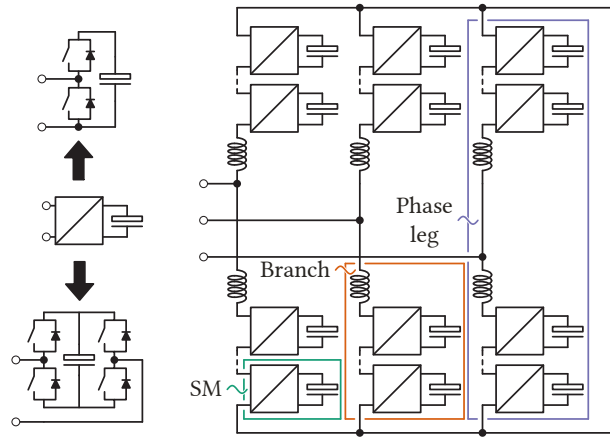


**Fig. 8.5** Modular multilevel converter

**Tab. 8.3** MMC Parameters

Parameter	$S_{nom}$	$\cos \phi$	$v_{g,l-1}$	$i_g$	$f_g$	$v_{dc}$	$L_{br}$	$C_{sm}$	$f_{sw,sm}$	# of SMs
Value	500 kVA	1	3.3 kV	87.5 A	50 Hz	5.6 kV	2.5 mH	2.25 mF	2 kHz	8

levels [101]. However, from the equipment integration standpoint there exists an issue when it comes to terminal characteristics, i.e. impedance and admittance, measurement of the MMCs [102]. Due to its flexibility, the CHB converter is reconfigured and used in a case study to measure either the ac or the dc side characteristics of the MMC. The detailed description of the control implementation of the MMC is out of the scope of this thesis as the MMC control system comprises many different layers. However, for the completeness of the thesis, the main control layers of the MMC are outlined here. The ac terminal current control [83], [103] presents itself as a highest priority control layer as it assures the control of the power at which the energy is delivered to the ac grid [104]. Additionally, the dc terminal current control and the circulating current control [105]–[107] are required for proper balancing of the converter arms. Finally, the energy balance in the MMC needs to be maintained, a task managed by the total and internal energy control layer [106]. Moreover, references [104], [108] provide an excellent overview of control methods for the MMC.

In order to examine the effectiveness of the CHB as a perturbation injection converter, measurements of the input and output admittances of the MMC were performed in PLECS simulation environment. The measurement setup can be illustrated with **Fig. 8.6**, while the operating parameters of the MMC are given in **Tab. 8.3**. It can be noticed that the measured input admittance is represented in the  $dq$ -frame. Even though the ac and dc rated voltages of the MMC are lower than the rated voltages of the CHB, this does not pose an issue as the CHB converter can establish any voltage between zero and rated voltage at its terminals. The CHB converter is used to supply the MMC either from the ac or from the dc side. Here, the MMC is operating as a grid-connected inverter and is driven either to supply the power to the CHB operating as an ac source or draw the power from the dc CHB. When supplying the MMC from the dc side, the CHB can be reconfigured using one of the methods already mentioned. While interfaced to the MMC, from either the ac or the dc side, the CHB is at the same time driven to inject small-signal voltage perturbations into the MMC.

The signal injected is a wideband PRBS signal, namely the PRBS-12 signal [29], with a generation



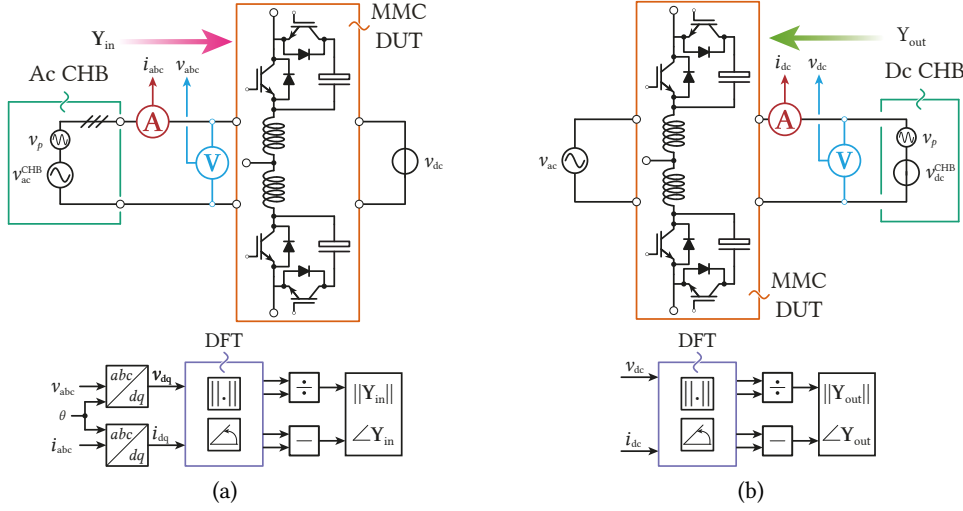


**Fig. 8.6** Schematics for the (a) input and (b) output admittance matrix  $\mathbf{Y}_{in}$  measurement of the MMC.

frequency of  $f_{gen} = 4$  kHz which sets the frequency resolution of the measurement at about  $f_{res} = 1$  Hz. Following the perturbation injection, current and voltage sensors are used to measure the resulting current response, as well as the voltages at the ac and dc terminals of the MMC. Subsequently the measurements are collected and processed. A DFT algorithm is performed to extract the frequency components from the current and voltage measurements. The typical CHB ac and dc output waveforms, before and after the perturbation injection, are presented in **Fig. 8.7**. The admittances themselves are extracted as

$$\mathbf{Y}_{in}(s) = \begin{bmatrix} i_{d,1}(s) & i_{d,2}(s) \\ i_{q,1}(s) & i_{q,2}(s) \end{bmatrix} \cdot \begin{bmatrix} v_{d,1}(s) & v_{d,2}(s) \\ v_{q,1}(s) & v_{q,2}(s) \end{bmatrix}^{-1} = \begin{bmatrix} Y_{dd}(s) & Y_{dq}(s) \\ Y_{qd}(s) & Y_{qq}(s) \end{bmatrix} \quad (8.1)$$

where the  $i_{x,y}$  and  $v_{x,y}$  are the measured currents and voltage in the  $dq$ -frame after the first and second injection. Similarly, the DFT is performed on the dc-side voltage and current measurements and the output admittance can be extracted as:

$$Y_{out}(s) = \frac{\|i_{dc}(s)\|}{\|v_{dc}(s)\|} [\angle i_{dc}(s) - \angle v_{dc}(s)] \quad (8.2)$$

where  $\tilde{v}(s)$  and  $\tilde{i}(s)$  are the small-signal voltage perturbation and the resulting current response. This process is illustrated using **Fig. 8.6**.

The measured input and output admittances measured are presented in **Figs. 8.8** and **8.9**. From **Fig. 8.8** it can be noticed that the diagonal terms of the input admittance matrix,  $Y_{in,dd}$  and  $Y_{in,qq}$ , do not contain a large quantity of noise, whereas the off-diagonal elements are much less precise. This is due to the fact that the MMC was operated with power factor of  $\cos \phi = 1$  resulting in zero current in the  $q$ -axis, meaning it becomes difficult to discern the response to the perturbation from the simulation noise. The output admittance was measured using three dc output configurations presented in this work and it is seen that all three give notably similar results, which in the end should be the case as the reconfiguration mode should not affect the measurements.

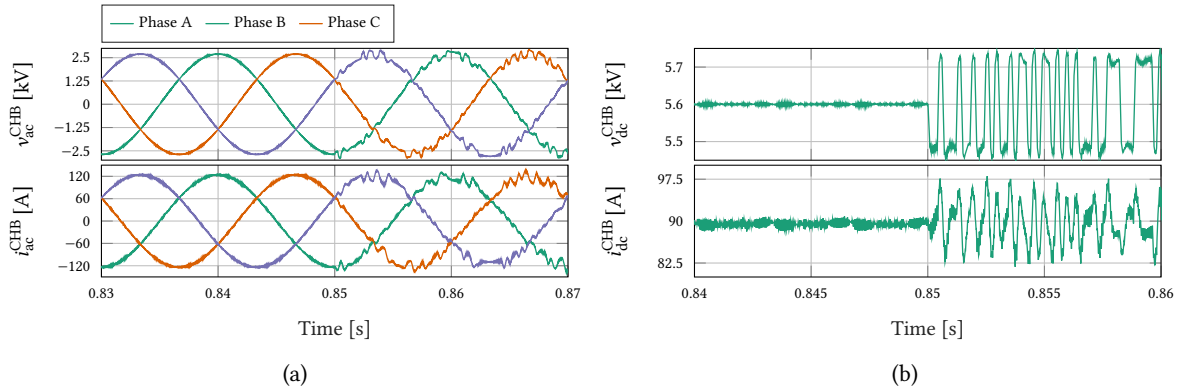


**Fig. 8.7** Ac and dc voltage and current waveforms of the CHB before and after the start of the perturbation injection at  $t_s = 0.85$  s.

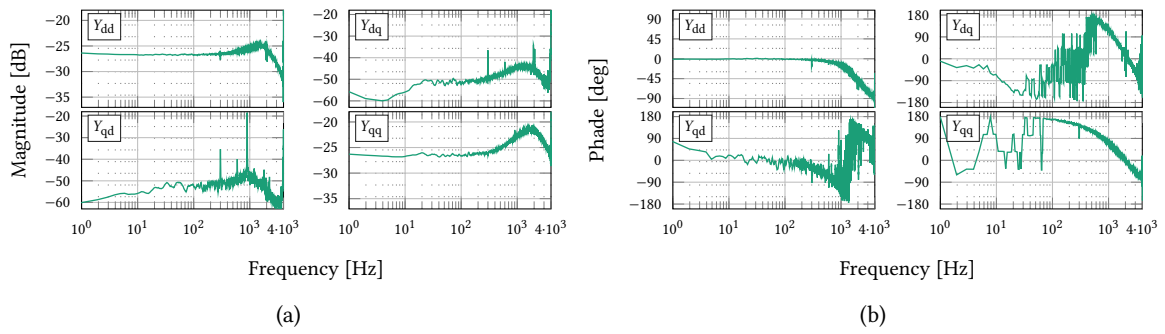


**Fig. 8.8** Ac side measurements results showing the (a) magnitude and (b) phase of input admittance matrix  $Y_{in}$  of the MMC.

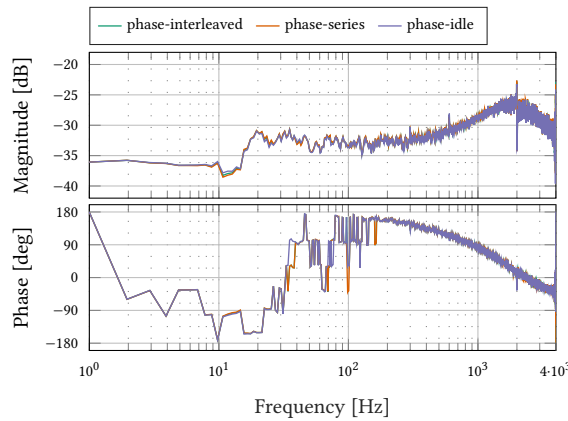


**Fig. 8.9** Dc side measurement results showing the output admittance  $Y_{out}$  of the MMC.

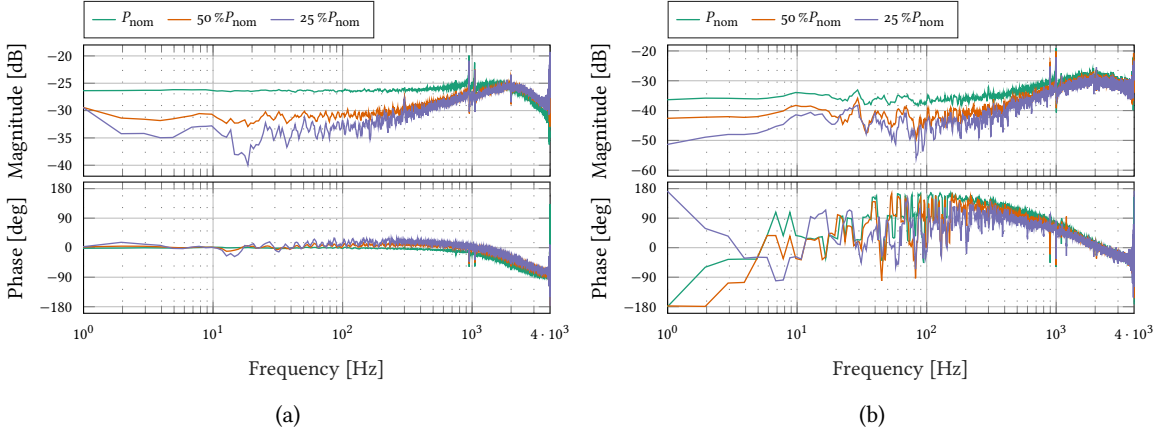


**Fig. 8.10** a)  $d$ -axis input admittance  $Y_{dd,in}$  and b)  $Y_{out}$  output admittances of the MMC operating with half-bridge submodules (SMs).

As the MMC can operate with two different types of submodules (SMs), the half-bridge and full-bridge ones, the input and output admittances were measured while the MMC was operated with these two different types of SMs. It is noticeable from the results in **Figs. 8.10** and **8.13** that the type of the submodule used does not affect the shape of the admittances, which should be the case as the submodule type does not change the way that the converter operates. It is however noticeable that the resonant peaks appear at  $2 \cdot f_{sw,sm} = 2$  kHz when the MMC operates with full-bridge submodule and at  $f_{sw} = 1$  kHz when it operates with half-bridge one. From the presented results it is also visible that the admittance does truly depend on the operating point of the converter. This is in particular visible in the frequency range lower than the  $f_{sw,sm}$  and can be perceived as the influence of the control loops that operate in this range.

In order to assess the influence of different MMC parameters on the shape of the admittances several parameters were changed and the measurements were repeated. Namely, MMC operating power was modified, the branch inductance and submodule capacitance as well as the operating point, i.e. operating power of the MMC. The results of these measurements are presented in **Figs. 8.11** to **8.13**. From **Fig. 8.11** it is apparent that the branch inductance has an influence on the shape of the input admittance in the frequency range above the  $f_{sw,sm}$  as this range is above the input side control bandwidth. When it comes to the output admittance the  $L_{br}$  affects the output admittance over the whole frequency range. This is due to the fact that the dc-side control has no effect on the  $L_{br}$  and has no compensation.

The effect of changing of the submodule capacitance  $C_{sm}$ , visible in **Fig. 8.12**, is not manifested on either the input or output admittance, at least not in the measured frequency range. This is due to the fact that the sizing of the SM capacitors is normally performed according to the desired amplitude of the low frequency oscillations in the sub-module voltage. In other words, reducing the SM capacitance increases the SM voltage ripple and vice versa. However, closed-loop control of the MMC implies that generation of the SM modulation indices, takes the total branch voltage into account as  $M = v_{dc}^* / v_{dc}^{MMC}$ , meaning that MMC voltage oscillations, being dependent on the  $C_{sm}$ , are always properly compensated.

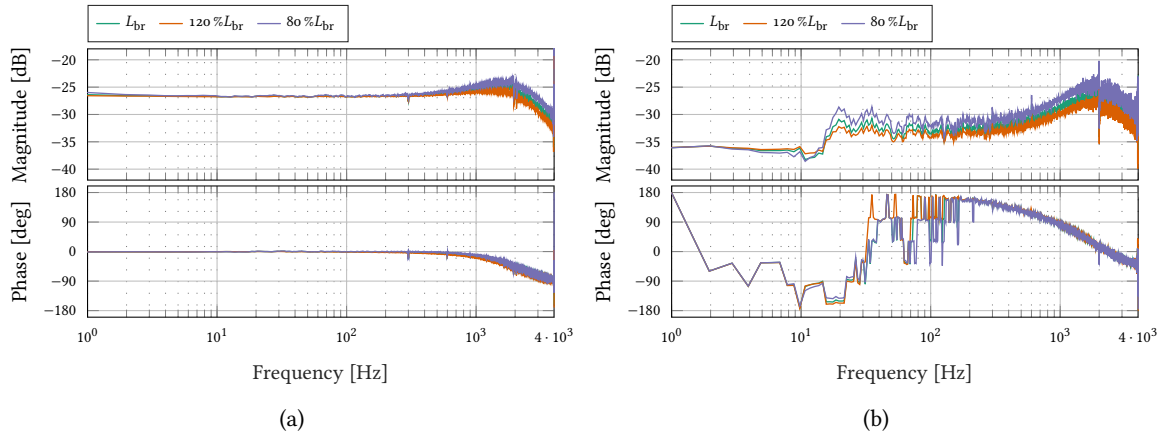


**Fig. 8.11** a)  $d$ -axis input admittance  $Y_{dd,in}$  and b)  $Y_{out}$  output admittances of the MMC with branch inductance modified.

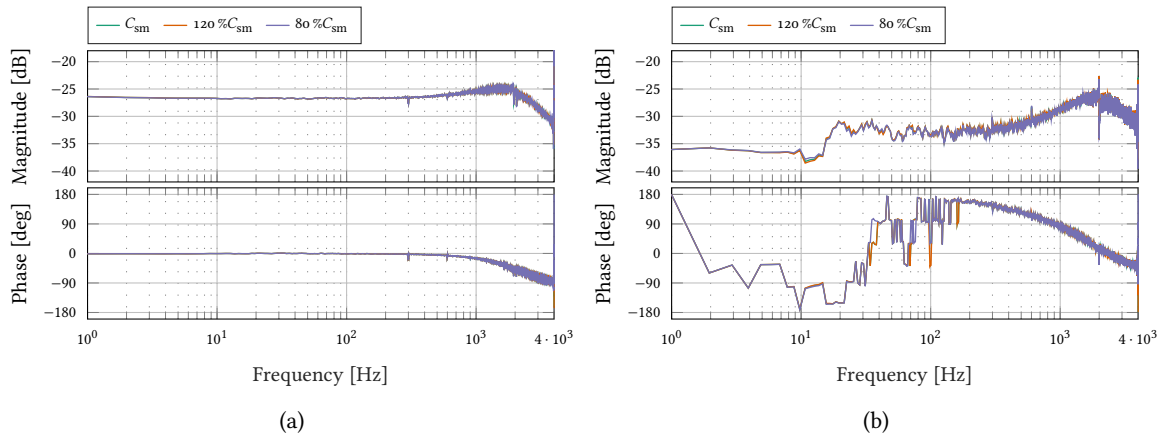


**Fig. 8.12** a)  $d$ -axis input admittance  $Y_{dd,in}$  and b)  $Y_{out}$  output admittances of the MMC operating with submodule capacitance modified.

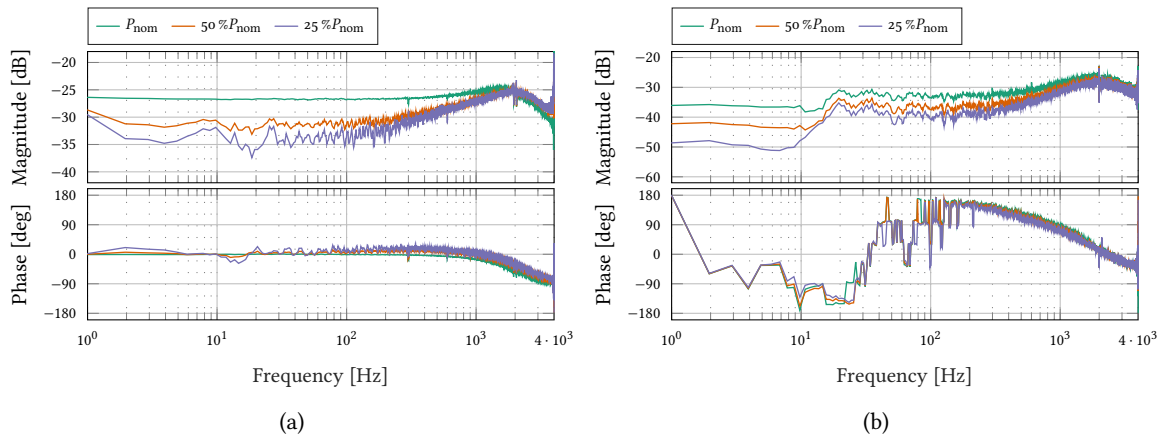


**Fig. 8.13** a)  $d$ -axis input admittance  $Y_{dd,in}$  and b)  $Y_{out}$  output admittances of the MMC operating with full-bridge SMs.

From **Fig. 8.13** it is evident that the admittance does depend on the operating point of the converter. This is in particular visible in the frequency range lower than the  $f_{sw,sm}$  and can be perceived as the influence of the control loops that operate in this range. Such a result is also expected intuitively, since the increase in power for a constant supply voltage leads to the increase in current, hence to the increase of the admittance.

## 8.4 Summary

This chapter presented the reconfiguration capabilities of the CHB converter. Originally intended as an ac output converter, the CHB can be reconfigured to serve the purposes of measuring the characteristics of the dc systems as well. Depending on the converter and transformer voltage insulation constraints and power handling capabilities, several reconfiguration methods can be applied, that have different levels of complexity and different benefits. In terms of control methods, the ac output methods are effectively applied to the the control of dc variables, which simplifies the process of changing the mode of operation of the CHB converter. The use of efficient control methods permits the CHB unit to perform wideband signal injection, in the range of several kHz, and rapid measurements making it fitting for applications where the operating point of a DUT can change in a very short time. The MMC is taken as an example of a DUT that is supplied from both ac and dc sides by a CHB converter while simultaneously injecting small-signal perturbations into the MMC and measuring the ac and dc admittances. The results presented show that the measurement method using the CHB converter is sensitive enough to capture the parameter change in the DUT whilst operating at the MV range. The solution put forward shows itself as a promising one for solving the issue of MV impedance/admittance measurements and an enabling technology for greater and faster integration of MVac and MVdc applications.



# 9

## Summary and Future Work

*The net sum of steps taken forward should always remain positive and larger than zero. It is the only way to assure progress.*

### 9.1 Summary and Contributions

This thesis focused on various concepts and topics related to the domain of MV impedance measurement and system identification, while putting the CHB converter in the spotlight.

**Chap. 2** provided a critical overview of the impedance measurement instruments and methods available today. The market of impedance measurement devices and perturbation injection converters is nowadays limited to grid emulators that are often employed as perturbation injection converters. However, as these devices are not designed with the same design goals such as having a large output voltage bandwidth, they stay a feasible but not a viable solution in the long term. On the other side, the devices developed for research purposed often lack flexibility in term of systems they can serve, i.e. they cater the needs of ac system measurement. From the standpoint of perturbation signals used, the wideband signals have found their place in the LV domain of impedance measurement but rarely in the MV domain due to the limited output voltage and current bandwidth of perturbation injection converters. Thus, a CHB converter was proposed as a universal solution to these issues.

In **Chap. 3** the path was paved for the small-signal modelling of the PEBB of the CHB converter. Namely, open-loop control modelling of both the three-phase AFE and the single-phase HB inverter unit were provided. Additionally, the open-loop models were verified in simulation environment. While the modelling and model verification of the three-phase AFE is already well-established, the verification of single-phase models in the  $dq$ -frame required developing additional methods. Specifically, wideband perturbation signal injection was used to verify the open-loop model, a technique that was so far reserved only for narrowband signals such as the sinusoidal ac sweep. The importance of open-loop models and their verification is seen in the continuation of modelling process, i.e. closed-loop control modelling.

In **Chap. 4**, the models provided in **Chap. 3** were developed further with the inclusion of closed-loop control loop such as the synchronization loop and input current and dc-link voltage loops for the three-phase AFE, which essentially acts as a grid-connected converter. On the other side, the open-loop model of the single-phase HB inverter was completed with the addition of inductor current and capacitor, or output, voltage control loops.

The requirement to define the closed-loop models was made clear in **Chap. 5**. Namely, the closed-loop control of the AFE does not have an infinite bandwidth which in turn signifies that the dc voltage

source of the HB inverter is not completely stiff. Additionally, there exists an output impedance of the AFE which actually modifies the closed-loop model and the dynamics of the HB inverter. Thus, **Chap. 5** presented the modified closed-loop model of the HB taking into account the closed-loop dynamics of the AFE. A mean to estimate the degree of influence of the AFE on the HB was through the measurement of the output impedance of the HB, as well as through its control-to-output characteristics, essentially a closed-loop output voltage control characteristics. **Chap. 5** resulted in two new methods for the identification the output impedance and the control-to-output characteristics and more importantly showed that there is practically no influence of the AFE on the HB. This result is extremely insightful and beneficial for further development and analysis of the CHB converter as a perturbation injection device for MV systems.

Power electronics is an applied field and thus the **Chap. 6** focused on the hardware and control design of the three-phase AFE of a single PEBB. Owing to the complexity and the size of the CHB converter, the control system needs to be deployed on a large scale industrial control platform. Thus, the ABB AC800PEC controller is chosen as the control platform as it is able to support the control requirements. In order to perform the cascaded control of the AFE, the source synchronization is based on the voltages measured on the primary winding of the MWT in combination with the phase-shift angles and voltage transformation ratios of MWT secondary windings. Moreover, the input filter of the AFE is realized through the leakage inductance of transformer windings, resulting in smaller and more cost-effective CHB PEBB. The hardware design is verified through the power exchange test between two identical AFEs and power circulation through the transformer.

The methods and results provided in **Chap. 7** were twofold. On one side, the CHB converter needs to be a non-invasive peace of equipment seen from the point of view of the SUT that is being identified, and on the other side, there exists a need to experimentally verify the results obtained in **Chap. 5**. Thus, **Chap. 7** discussed the implementation of a system used to measure the terminal characteristics of the AFE, i.e. its input admittance and the output impedance. Namely, the knowledge of the input admittance is required in order to estimate the passivity of the CHB, while the output impedance is required to confirm the results of **Chap. 5**. The system implemented consists of multiple elements, each crucial for proper measurement of the terminal characteristics. Moreover, it has been shown that the measurement platform implemented can distinguish between different operating point of the AFE, thus confirming its validity. The theoretical modelling was not provided in **Chap. 7** as the control algorithm was implemented on an industrial control platform and without the proprietary knowledge it becomes challenging to know all of the elements of the control that subsequently influence the shape of the input admittance and output impedance.

Finally, the issue of the lack of flexibility surrounding MV perturbation injection converters and impedance measurement devices was addressed in **Chap. 8**. Commonly used as an ac output converter, the CHB can be reconfigured through its control, modulation and hardware to operate as a dc output converter. Furthermore, three different dc output configurations are discussed and they can be used depending on the power and voltage levels required, however, always taking into consideration the insulation capabilities of the MWT. The ideas provided and the results obtained from the case study of terminal characteristics of the MMC are extremely promising and show a great potential of the CHB.



## 9.2 Future Work

Research is like an iceberg and we can only see a tip of it but there always stays a large hidden from our eyes and such is the case with this thesis as well. Work can always be improved and perfected and there always stay points to be treated in the future. It is the view of the author that there exist two main groups where the focus should be put in the future. The first group is a local one and is related directly to the hardware and control development of the CHB, as well as a more detailed study on the best practices of perturbation injection and the analysis of results. The second group takes into consideration the topics that were superficially, or not at all, addressed to over the course of this thesis such as the further study in the field of flexibility of PICs, overall system stability study and the integration of PICs and impedance measurement devices into the future grids.

Even though the hardware and control implementation of a single AFE were performed successfully and presented in **Chaps. 6** and **7**, the complete hardware system still remains undeveloped and the full control concept for the AFE is not deployed. There still remain opened questions such as impact of the synchronous operation of fifteen AFEs on the MV grid supplying the CHB, as well as the impact of AFEs between themselves. As a starting point, the methods and results presented in **Chap. 6** can be generalized and extended on a full-scale system.

Much theory has been developed around the HB inverter unit of the CHB, however, no hardware development has been provided and the challenge remains. First, a single unit needs to be prototyped and tested and subsequently the full-scale hardware implementation concept needs to be implemented. Moreover, as was the case with the AFE group, the CHB output also requires an industrial control platform on which the control principles are to be deployed. This is not yet answered to, and an optimal way of operating the CHB converter output stage needs to be devised, tested and commissioned.

In the domain of the perturbation injection and impedance measurement it is taken as a good practice and a rule of thumb that the perturbation signal should not surpass 5-10 % of the nominal voltage or current, depending which physical quantity is injected. However, there is no study evaluating the effects of different injection levels. For a proper understanding and interpretation of obtained results, such a study would be more than beneficial, and even required. Additionally, this thesis has not addressed the measurement precision based on the voltage and current transducer sensing capabilities as their errors also depend on the voltage and current levels. Furthermore, a statistical analysis of the results is also required to fully understand the impedance measurements.

The flexibility concept for the CHB as an ac and dc system impedance measurement device was outlined in this thesis. However, no deeper analysis and comparison of the solutions proposed was provided. Moreover, the practical aspects of the reconfiguration were not deeply discussed. Thus, it is a point that is worth addressing in the future. On the other side, the reconfiguration capabilities of other topologies employed as PICs were not addressed. It is surely worthwhile investigating them as well and performing a fair comparison between the CHB and other topologies, not only when the flexibility is concerned but also an overall performance comparison is required in order to reveal a best possible solution for the MV impedance measurement domain.

With the development of fast-switching SiC devices the power density of the power electronics equipment increases, i.e. for the same power rating the converters are becoming smaller in size. This provides an open-door for a broader installation of PICs in a modern power system. Their intended use should be to monitor the state of the system and measure its impedance continuously in order

to estimate the system stability in real time. This information is paired particularly well with the on-line adaptive control methods where the control parameters are regularly modified to obtain the best possible performance based on the system model.

In the cases where the installation of PICs is not possible due to the the system architecture or due to the cost, the control software modification and retrofitting should be made possible. Namely, the control software should be modified in the way that it supports intermittent perturbation injection at the terminals of the power electronics converters, as well as the data acquisition and feed-in to the supervisory system of the power system operator. Similarly to the previous case, this would enable the constant stability monitoring and the system parameter estimation at the terminals of power converters.

# **Appendices**



# A

## Appendix

### A.1 Small-Signal and State-Space Equations

In order to lay the foundation for understanding following sections and converter modelling, basic small-signal and state-space equations have to be introduced. Moreover, since in general these models are nonlinear, a linearization method is given. The dynamic behaviour of a converter, or any similar system for that matter, can be reduced to a set of state-space equations consisting of output variables,  $(y_i)$ , and input or control variables,  $(u_i)$ . Physically, input and output variables are voltages and currents, while the addition of the control variables in the model which are as well input variable by their nature, is convenient for power electronic converters since their state always depends on the duty cycle as a control signal. In general, a state-space equation of a system is given as:

$$\begin{aligned} \left[ \frac{d\tilde{x}_i(t)}{dt} \right] &= [A][\tilde{x}_i(t)] + [B][\tilde{u}_i(t)] \\ [\tilde{y}_i(t)] &= [C][\tilde{x}_i(t)] + [D][\tilde{u}_i(t)] \end{aligned} \quad (\text{A.1})$$

The variables expressed in previous equation are time-varying while the coefficient matrices are time invariant. The tilde  $\sim$  over the variables denotes a small-signal variable. Solving these equations requires that they be transformed into the Laplace domain as follows:

$$\begin{aligned} [s\tilde{x}_i(s)] &= [A][\tilde{x}_i(s)] + [B][\tilde{u}_i(s)] \\ [\tilde{y}_i(s)] &= [C][\tilde{x}_i(s)] + [D][\tilde{u}_i(s)] \end{aligned} \quad (\text{A.2})$$

To obtain the input-to-state and input-to-output transfer characteristics this equation is solved as:

$$[\tilde{x}_i(s)] = [sI - [A]]^{-1} [B][\tilde{u}_i(s)] \quad (\text{A.3})$$

$$[\tilde{y}_i(s)] = \left[ [C][sI - [A]]^{-1} [B] + [D] \right] [\tilde{u}_i(s)] \quad (\text{A.4})$$

As the output variables are physically currents or voltages, their derivatives can be found by following the equations for voltages across a capacitor and currents through an inductor, given as:

$$\begin{aligned} \frac{di_{L,i}}{dt} &= \frac{1}{L_i} v_{L,i} \\ \frac{dv_{C,i}}{dt} &= \frac{1}{C_i} i_{C,i} \end{aligned} \quad (\text{A.5})$$

The averaged counterparts of these equations can be found by:

$$\begin{aligned}\frac{d\langle i_{L,i} \rangle}{dt} &= \frac{1}{L_i} (d_i v_{L,i,on} + \bar{d}_i v_{L,i,off}) \\ \frac{d\langle v_{C,i} \rangle}{dt} &= \frac{1}{C_i} (d_i i_{C,i,on} + \bar{d}_i i_{C,i,off}) \\ \langle \tilde{y}_i \rangle &= d_i \tilde{y}_{i,on} + \bar{d}_i \tilde{y}_{i,off}\end{aligned}\tag{A.6}$$

Since the state-space model is usually non-linear it needs to be linearised by replacing the averaged values by the means of the sum of a dc value and a small perturbation [109].

## A.2 Synchronous Reference Frame Modelling

Sinusoidal-signals, being time-varying signals, make it difficult to model three-phase grid-connected converters as there does not exist a time-invariant steady-state operating point. Luckily, by using mathematical transformations such a point can be created. Three-phase signals can first be transformed into stationary reference frame, or  $\alpha\beta$ -frame, by using Clarke transformation and space vectors and subsequently into a synchronous reference frame, or  $dq$ -frame, by using Park transformation. In the  $dq$ -frame three-phase ac variables become dc variables and a steady-state operating point can be defined. This is equivalent to observing the ac variables and rotating at an grid angular frequency  $\omega_g$ . In order to be systematic and perform the modelling, said transformations are given in the following subsections.

### Clarke and Park Transformations

In order to understand and perform Clarke transformation, one has to be acquainted with the notion of space vectors [110]. Three-phase signal  $x$  can be represented by its space vector, given by:

$$\underline{x} = \frac{2K}{3} \left( x_a + e^{j2\pi/3} x_b + e^{j4\pi/3} x_c \right) = x_\alpha + jx_\beta\tag{A.7}$$

And the gamma component by:

$$x_\gamma = \frac{1}{3} (x_a + x_b + x_c)\tag{A.8}$$

Where the scaling factor  $K$  can be 1,  $\sqrt{1/2}$  or  $\sqrt{3/2}$  depending on the transformation invariance that is sought for, i.e. peak value, root mean square value or power invariance.

The matrix form for the Clarke transformation in (A.7) is given by:

$$\begin{bmatrix} x_\alpha \\ x_\beta \\ x_\gamma \end{bmatrix} = \frac{2K}{3} \begin{bmatrix} 1 & -\frac{1}{2} & -\frac{1}{2} \\ 0 & \frac{\sqrt{3}}{2} & -\frac{\sqrt{3}}{2} \\ \frac{1}{2K} & \frac{1}{2K} & \frac{1}{2K} \end{bmatrix} \begin{bmatrix} x_a \\ x_b \\ x_c \end{bmatrix}\tag{A.9}$$

The inverse Clarke transformation matrix is given by:

$$\begin{bmatrix} x_a \\ x_b \\ x_c \end{bmatrix} = \frac{3}{2K} \begin{bmatrix} \frac{2}{3} & 0 & \frac{2K}{3} \\ -\frac{1}{3} & \frac{1}{\sqrt{3}} & \frac{2K}{3} \\ -\frac{1}{3} & -\frac{1}{\sqrt{3}} & \frac{2K}{3} \end{bmatrix} \begin{bmatrix} x_\alpha \\ x_\beta \\ x_\gamma \end{bmatrix} \quad (\text{A.10})$$

The  $\alpha\beta$ -frame signals can be further transformed and represented in the synchronous  $dq$ -frame as:

$$\underline{x}^s = \underline{x} e^{-j\omega_g t} \quad (\text{A.11})$$

Which has its equivalent matrix form:

$$\begin{bmatrix} x_d \\ x_q \\ x_z \end{bmatrix} = \frac{3}{2K} \begin{bmatrix} \cos \omega_g t & \sin \omega_g t & 0 \\ -\sin \omega_g t & \cos \omega_g t & 0 \\ 0 & 0 & 1 \end{bmatrix} \begin{bmatrix} x_\alpha \\ x_\beta \\ x_\gamma \end{bmatrix} \quad (\text{A.12})$$

Combining Clarke and Park transformations gives direct and inverse  $abc$ - to  $dq$ -frame ( $dq$ - to  $abc$ -frame) transformation as:

$$\begin{bmatrix} x_d \\ x_q \\ x_z \end{bmatrix} = \frac{2K}{3} \begin{bmatrix} \cos \omega_g t & \cos \left( \omega_g - \frac{2\pi}{3} \right) & \cos \left( \omega_g - \frac{4\pi}{3} \right) \\ -\sin \omega_g t & -\sin \left( \omega_g - \frac{2\pi}{3} \right) & -\sin \left( \omega_g - \frac{4\pi}{3} \right) \\ \frac{1}{2K} & \frac{1}{2K} & \frac{1}{2K} \end{bmatrix} \begin{bmatrix} x_a \\ x_b \\ x_c \end{bmatrix} \quad (\text{A.13})$$

$$\begin{bmatrix} x_a \\ x_b \\ x_c \end{bmatrix} = \frac{2K}{3} \begin{bmatrix} \cos \omega_g t & -\sin \omega_g t & \frac{2K}{3} \\ \cos \left( \omega_g - \frac{2\pi}{3} \right) & -\sin \left( \omega_g - \frac{2\pi}{3} \right) & \frac{2K}{3} \\ \cos \left( \omega_g - \frac{4\pi}{3} \right) & -\sin \left( \omega_g - \frac{4\pi}{3} \right) & \frac{2K}{3} \end{bmatrix} \begin{bmatrix} x_d \\ x_q \\ x_z \end{bmatrix} \quad (\text{A.14})$$

### A.3 Hilbert Transform

Hilbert transform, denoted  $\mathcal{H}$ , of a signal  $x(t)$  is defined as the transform in which phase angle of all components of the signal is shifted by  $\pm\pi/2$ . Hilbert transform of  $x(t)$  can also be represented with  $\hat{x}(t)$ , and it is given by:

$$\mathcal{H}[x(t)] = \hat{x}(t) = \frac{1}{\pi} \int_{-\infty}^{\infty} \frac{x(\tau)}{t-\tau} d\tau = x(t) * \frac{1}{\pi t} \quad (\text{A.15})$$

Where " $*$ " denotes a convolution operation. The Hilbert transform of an already transformed signal is defined as  $\mathcal{H}[\mathcal{H}[x(t)]] = -x(t)$ . Signals  $x(t)$  and its transform  $\hat{x}(t)$  are known as *the Hilbert pair*. The Hilbert pair signals,  $x(t)$  and  $\hat{x}(t)$ , have the following properties:

- Signals have the same amplitude spectrum;
- Signals have the same autocorrelation function;
- Signals have the same energy spectral density;
- If Fourier transform exist then Hilbert transform also exists for energy and power signals.



# Bibliography

- [1] H. B. Rockman, *Intellectual property law for engineers and scientists*. John Wiley & Sons, 2004.
- [2] D. Tiku, "Dc power transmission: Mercury-arc to thyristor hvdc valves [history]," *IEEE Power and Energy Magazine*, vol. 12, no. 2, pp. 76–96, 2014.
- [3] J. Arrillaga and J. Arrillaga, *High voltage direct current transmission*. Iet, 1998, vol. 29.
- [4] R. M. Black, *The history of electric wires and cables*, 4. IET, 1983.
- [5] M. Guarnieri, "The alternating evolution of dc power transmission [historical]," *IEEE Industrial Electronics Magazine*, vol. 7, no. 3, pp. 60–63, 2013.
- [6] G. Megan, *Tesla beats deadline, switches on gigantic australian battery array*, Online, Jan. 2017. [Online]. Available: <https://arstechnica.com/cars/2017/12/tesla-beats-deadline-switches-on-gigantic-australian-battery-array/>.
- [7] B. Wen, "Stability analysis of three-phase ac power systems based on measured dq frame impedances," Ph.D. dissertation, Virginia Tech, 2015.
- [8] R. E. Thomas, "The stability of aircraft d-c power systems with inverter loads," *Transactions of the American Institute of Electrical Engineers, Part II: Applications and Industry*, vol. 76, no. 4, pp. 183–188, 1957.
- [9] N. O. Sokal, "System oscillations from negative input resistance at power input port of switching-mode regulator, amplifier, dc/dc converter, or dc/dc inverter," in *1973 IEEE Power Electronics Specialists Conference*, 1973, pp. 138–140.
- [10] M. Bradt, B. Badrzadeh, E. Camm, D. Mueller, J. Schoene, T. Siebert, T. Smith, M. Starke, and R. Walling, "Harmonics and resonance issues in wind power plants," in *2011 IEEE Power and Energy Society General Meeting*, 2011, pp. 1–8.
- [11] C. Li, "Unstable operation of photovoltaic inverter from field experiences," *IEEE Transactions on Power Delivery*, vol. 33, no. 2, pp. 1013–1015, 2018.
- [12] Z. Liu, G. Zhang, and Y. Liao, "Stability research of high-speed railway emus and traction network cascade system considering impedance matching," *IEEE Transactions on Industry Applications*, vol. 52, no. 5, pp. 4315–4326, 2016.
- [13] M. Meyer and J. Schöning, "Netzstabilität in grossen bahnnetzen," *Eisenbahn-revue*, vol. 7, no. 8, pp. 312–317, 1999.
- [14] A. Bomhauer-Beins and U. Weidmann, "Bahnstromversorgung, quo vadis?" *Eisenbahntechnische Rundschau*, vol. 10, pp. 84–88, 2015.
- [15] X. Wang and F. Blaabjerg, "Harmonic stability in power electronic-based power systems: Concept, modeling, and analysis," *IEEE Transactions on Smart Grid*, vol. 10, no. 3, pp. 2858–2870, 2019.
- [16] J. Sun, "Impedance-based stability criterion for grid-connected inverters," *IEEE Transactions on Power Electronics*, vol. 26, no. 11, pp. 3075–3078, 2011.
- [17] H. Liu and J. Sun, "Impedance-based stability analysis of vsc-based hvdc systems," in *2013 IEEE 14th Workshop on Control and Modeling for Power Electronics (COMPEL)*, IEEE, 2013, pp. 1–8.
- [18] S. Vesti, T. Suntio, J. Oliver, R. Prieto, and J. Cobos, "Impedance-based stability and transient-performance assessment applying maximum peak criteria," *IEEE Transactions on Power Electronics*, vol. 28, no. 5, pp. 2099–2104, 2012.
- [19] R. D. Middlebrook, "Measurement of loop gain in feedback systems," *International Journal of Electronics Theoretical and Experimental*, vol. 38, no. 4, pp. 485–512, 1975.
- [20] A. Riccobono and E. Santi, "Comprehensive review of stability criteria for dc power distribution systems," *IEEE Transactions on Industry Applications*, vol. 50, no. 5, pp. 3525–3535, 2014.
- [21] R. Brockett and C. Byrnes, "Multivariable nyquist criteria, root loci, and pole placement: A geometric viewpoint," *IEEE Transactions on Automatic Control*, vol. 26, no. 1, pp. 271–284, 1981.
- [22] R. D. Middlebrook, "Input filter considerations in design and application of switching regulators," *IAS'76*, 1976.
- [23] C. M. Wildrick, F. C. Lee, B. H. Cho, and B. Choi, "A method of defining the load impedance specification for a stable distributed power system," *IEEE Transactions on power Electronics*, vol. 10, no. 3, pp. 280–285, 1995.
- [24] X. Feng, J. Liu, and F. C. Lee, "Impedance specifications for stable dc distributed power systems," *IEEE Transactions on Power Electronics*, vol. 17, no. 2, pp. 157–162, 2002.
- [25] C. Fernández, A. Fernandez-Herrero, P. Zumel, A. Lázaro, and A. Barrado, "Measuring bode plots of switching power converters from a single simulation in the time domain: Application to a digital control implemented on an fpga," in *2010 IEEE 12th Workshop on Control and Modeling for Power Electronics (COMPEL)*, IEEE, 2010, pp. 1–7.
- [26] Z. Shen, M. Jaksic, P. Mattavelli, D. Boroyevich, J. Verhulst, and M. Belkhatat, "Three-phase ac system impedance measurement unit (imu) using chirp signal injection," in *2013 Twenty-Eighth Annual IEEE Applied Power Electronics Conference and Exposition (APEC)*, IEEE, 2013, pp. 2666–2673.
- [27] Z. Shen, M. Jaksic, P. Mattavelli, D. Boroyevich, J. Verhulst, and M. Belkhatat, "Design and implementation of three-phase ac impedance measurement unit (imu) with series and shunt injection," in *2013 Twenty-Eighth Annual IEEE Applied Power Electronics Conference and Exposition (APEC)*, IEEE, 2013, pp. 2674–2681.

- [28] M. Jakšić, Z. Shen, I. Cvetković, D. Boroyevich, R. Burgos, C. DiMarino, and F. Chen, "Medium-voltage impedance measurement unit for assessing the system stability of electric ships," *IEEE Transactions on Energy Conversion*, vol. 32, no. 2, pp. 829–841, 2017.
- [29] K. Godfrey, *Perturbation signals for system identification*. Prentice Hall International (UK) Ltd., 1993.
- [30] T. Roinila, T. Messo, R. Luhtala, R. Scharrenberg, E. C. de Jong, A. Fabian, and Y. Sun, "Hardware-in-the-loop methods for real-time frequency-response measurements of on-board power distribution systems," *IEEE Transactions on Industrial Electronics*, vol. 66, no. 7, pp. 5769–5777, 2018.
- [31] T. Roinila, H. Abdollahi, S. Arrua, and E. Santi, "Real-time stability analysis and control of multiconverter systems by using mimo-identification techniques," *IEEE Transactions on Power Electronics*, vol. 34, no. 4, pp. 3948–3957, 2018.
- [32] V. Valdivia, A. Lázaro, A. Barrado, P. Zumel, C. Fernández, and M. Sanz, "Impedance identification procedure of three-phase balanced voltage source inverters based on transient response measurements," *IEEE Transactions on Power Electronics*, vol. 26, no. 12, pp. 3810–3816, 2011.
- [33] V. Valdivia, A. Lazaro, A. Barrado, P. Zumel, C. Fernandez, and M. Sanz, "Black-box modeling of three-phase voltage source inverters for system-level analysis," *IEEE Transactions on Industrial Electronics*, vol. 59, no. 9, pp. 3648–3662, 2011.
- [34] P. Xiao, G. Venayagamoorthy, and K. Corzine, "A novel impedance measurement technique for power electronic systems," in *2007 IEEE Power Electronics Specialists Conference*, IEEE, 2007, pp. 955–960.
- [35] S. Cobrecas, F. Huerta, D. Pizarro, F. J. Rodriguez, and E. J. Bueno, "Three-phase power system parametric identification based on complex-space recursive least squares," in *2007 IEEE International Symposium on Intelligent Signal Processing*, IEEE, 2007, pp. 1–6.
- [36] B. Wen, D. Boroyevich, R. Burgos, P. Mattavelli, and Z. Shen, "Small-signal stability analysis of three-phase ac systems in the presence of constant power loads based on measured dq frame impedances," *IEEE Transactions on Power Electronics*, vol. 30, no. 10, pp. 5952–5963, 2014.
- [37] Y. Liao, Z. Liu, X. Hu, and B. Wen, "A dq-frame impedance measurement method based on hilbert transform for single-phase vehicle-grid system," in *2017 IEEE Transportation Electrification Conference and Expo, Asia-Pacific (ITEC Asia-Pacific)*, IEEE, 2017, pp. 1–6.
- [38] M. Cespedes and J. Sun, "Three-phase impedance measurement for system stability analysis," in *2013 IEEE 14th Workshop on Control and Modeling for Power Electronics (COMPEL)*, IEEE, 2013, pp. 1–6.
- [39] J. Sun, "Small-signal methods for ac distributed power systems—a review," *IEEE Transactions on Power Electronics*, vol. 24, no. 11, pp. 2545–2554, 2009.
- [40] M. Cespedes and J. Sun, "Adaptive control of grid-connected inverters based on online grid impedance measurements," *IEEE Transactions on sustainable energy*, vol. 5, no. 2, pp. 516–523, 2014.
- [41] A. Rygg, M. Molinas, C. Zhang, and X. Cai, "A modified sequence-domain impedance definition and its equivalence to the dq-domain impedance definition for the stability analysis of ac power electronic systems," *IEEE Journal of Emerging and Selected Topics in Power Electronics*, vol. 4, no. 4, pp. 1383–1396, 2016.
- [42] L. Czarnecki and Z. Staroszczyk, "Dynamic on-line measurement of equivalent parameters of three-phase systems for harmonic frequencies," *European transactions on electrical power*, vol. 6, no. 5, pp. 329–336, 1996.
- [43] Y. Familiant, K. A. Corzine, J. Huang, and M. Belkhat, "Ac impedance measurement techniques," in *IEEE International Conference on Electric Machines and Drives, 2005.*, IEEE, 2005, pp. 1850–1857.
- [44] N. Hoffmann and F. W. Fuchs, "Minimal invasive equivalent grid impedance estimation in inductive–resistive power networks using extended kalman filter," *IEEE Transactions on Power Electronics*, vol. 29, no. 2, pp. 631–641, 2013.
- [45] T. T. Regatron, *Acs-full 4-quadrant grid simulator*.
- [46] Spitzenberger and Spies, *Pas series of 4-quadrant amplifiers*. [Online]. Available: <http://www.spitzenberger.de/download.ashx?weblink=1002..>
- [47] Egston, *Compiso system unit 200 kva/kw*. [Online]. Available: <http://www.egston.com/en/power%20electronics/amplifier200kw.php>.
- [48] Z. Liu, I. Cvetkovic, Z. Shen, D. Boroyevich, R. Burgos, and J. Liu, "Imbalance mechanism and balancing control of dc voltages in a transformerless series injector based on paralleled h-bridge converters for ac impedance measurement," *IEEE Transactions on Power Electronics*, vol. 34, no. 8, pp. 8175–8189, 2018.
- [49] Z.-X. Zou, F. Hahn, G. Buticchi, S. Günter, and M. Liserre, "Interleaved operation of two neutral-point-clamped inverters with reduced circulating current," *IEEE Transactions on Power Electronics*, vol. 33, no. 12, pp. 10 122–10 134, 2018.
- [50] S. Pugliese, S. Flacke, Z. Zou, and M. Liserre, "High-frequency harmonic current control of power converters," in *2019 IEEE Energy Conversion Congress and Exposition (ECCE)*, IEEE, pp. 6915–6921.

- [51] M. Jaksic, D. Boroyevich, R. Burgos, Z. Shen, I. Cvetkovic, and P. Mattavelli, "Modular interleaved single-phase series voltage injection converter used in small-signal dq impedance identification," in *2014 IEEE Energy Conversion Congress and Exposition (ECCE)*, IEEE, 2014, pp. 3036–3045.
- [52] J. A. Suarez Diaz, "Étude et modélisation des interactions électriques entre les engins et les installations fixes de traction électrique 25kv/50hz," Ph.D. dissertation, 2014.
- [53] J. Suarez, P. Ladoux, N. Roux, H. Caron, and E. Guillame, "Measurement of locomotive input admittance to analyse low frequency instability on ac rail networks," in *2014 International Symposium on Power Electronics, Electrical Drives, Automation and Motion*, IEEE, 2014, pp. 790–795.
- [54] P. W. Hammond, "A new approach to enhance power quality for medium voltage ac drives," *IEEE Transactions on Industry Applications*, vol. 33, no. 1, pp. 202–208, 1997.
- [55] N. R. Averous, M. Stieneker, S. Kock, C. Andrei, A. Helmedag, R. W. De Doncker, K. Hameyer, G. Jacobs, and A. Monti, "Development of a 4 mw full-size wind-turbine test bench," *IEEE journal of emerging and selected topics in power electronics*, vol. 5, no. 2, pp. 600–609, 2017.
- [56] C. Saniter and J. Janning, "Test bench for grid code simulations for multi-mw wind turbines, design and control," *IEEE Transactions on Power Electronics*, vol. 23, no. 4, pp. 1707–1715, 2008.
- [57] S. A. Richter, J. von Bloh, C. P. Dick, D. Hirschmann, and R. W. De Doncker, "Control of a medium-voltage test generator," in *2008 IEEE Power Electronics Specialists Conference*, IEEE, 2008, pp. 3787–3793.
- [58] R. Luhtala, T. Roinila, and T. Messo, "Implementation of real-time impedance-based stability assessment of grid-connected systems using mimo-identification techniques," *IEEE Transactions on Industry Applications*, vol. 54, no. 5, pp. 5054–5063, 2018.
- [59] N. Kaminski and O. Hilt, "Sic and gan devices-competition or coexistence?" In *2012 7th International Conference on Integrated Power Electronics Systems (CIPS)*, IEEE, 2012, pp. 1–11.
- [60] H. A. Mantooth, M. D. Glover, and P. Shepherd, "Wide bandgap technologies and their implications on miniaturizing power electronic systems," *IEEE Journal of emerging and selected topics in Power Electronics*, vol. 2, no. 3, pp. 374–385, 2014.
- [61] A. Anthon, Z. Zhang, M. A. Andersen, D. G. Holmes, B. McGrath, and C. A. Teixeira, "Comparative evaluation of the loss and thermal performance of advanced three-level inverter topologies," *IEEE Transactions on Industry Applications*, vol. 53, no. 2, pp. 1381–1389, 2016.
- [62] N. Hildebrandt, **M. Petković**, and D. Dujić, "Evaluation of 1.7 kv sic mosfets for a regenerative cascaded h-bridge multilevel converter cell," in *2018 IEEE International Conference on Industrial Technology (ICIT)*, IEEE, 2018, pp. 718–723.
- [63] Z. Yang, J. Sun, X. Zha, and Y. Tang, "Power decoupling control for capacitance reduction in cascaded-h-bridge-converter-based regenerative motor drive systems," *IEEE Transactions on Power Electronics*, vol. 34, no. 1, pp. 538–549, 2018.
- [64] J. Gong, L. Xiong, F. Liu, and X. Zha, "A regenerative cascaded multilevel converter adopting active front ends only in part of cells," *IEEE Transactions on Industry Applications*, vol. 51, no. 2, pp. 1754–1762, 2014.
- [65] A. Anurag, S. Acharya, Y. Prabowo, G. Gohil, and S. Bhattacharya, "Design considerations and development of an innovative gate driver for medium-voltage power devices with high  $dv/dt$ ," *IEEE Transactions on Power Electronics*, vol. 34, no. 6, pp. 5256–5267, 2018.
- [66] R. Teodorescu, M. Liserre, and P. Rodriguez, "Grid synchronization in singlephase power converters," 2007.
- [67] M. Saitou, N. Matsui, and T. Shimizu, "A control strategy of single-phase active filter using a novel dq transformation," in *38th IAS Annual Meeting on Conference Record of the Industry Applications Conference*, 2003., IEEE, vol. 2, 2003, pp. 1222–1227.
- [68] S. M. Silva, B. M. Lopes, R. P. Campana, W. Bosventura, *et al.*, "Performance evaluation of pll algorithms for single-phase grid-connected systems," in *Conference Record of the 2004 IEEE Industry Applications Conference*, 2004. 39th IAS Annual Meeting., IEEE, vol. 4, 2004, pp. 2259–2263.
- [69] Se-Kyo Chung, "A phase tracking system for three phase utility interface inverters," *IEEE Transactions on Power Electronics*, vol. 15, no. 3, pp. 431–438, May 2000.
- [70] J. Svensson, "Synchronisation methods for grid-connected voltage source converters," *IEE Proceedings - Generation, Transmission and Distribution*, vol. 148, no. 3, pp. 229–235, May 2001.
- [71] A. Timbus, M. Liserre, R. Teodorescu, P. Rodriguez, and F. Blaabjerg, "Evaluation of current controllers for distributed power generation systems," *IEEE Transactions on power electronics*, vol. 24, no. 3, pp. 654–664, 2009.
- [72] A. Yazdani and R. Iravani, "Grid-imposed frequency vsc system: Control in-frame," 2010.
- [73] S. Vukosavic, *Digital Control of Electrical Drives*, ser. Power Electronics and Power Systems. Springer US, 2007. [Online]. Available: <https://books.google.ch/books?id=0HiQI110yUC>.

- [74] T. Suntio, T. Messo, and J. Puukko, *Power Electronic Converters: Dynamics and Control in Conventional and Renewable Energy Applications*. Wiley, 2017.
- [75] Y. Liao, Z. Liu, H. Zhang, and B. Wen, "Low-frequency stability analysis of single-phase system with dq-frame impedance approach—part i: Impedance modeling and verification," *IEEE Transactions on Industry Applications*, vol. 54, no. 5, pp. 4999–5011, 2018.
- [76] R. Luhtala, T. Roinila, and T. Messo, "Implementation of real-time impedance-based stability assessment of grid-connected systems using mimo-identification techniques," *IEEE Transactions on Industry Applications*, vol. 54, no. 5, pp. 5054–5063, Sep. 2018.
- [77] T. Roinila, H. Abdollahi, S. Arrua, and E. Santi, "Real-time stability analysis and control of multiconverter systems by using mimo-identification techniques," *IEEE Transactions on Power Electronics*, vol. 34, no. 4, pp. 3948–3957, Apr. 2019.
- [78] T. Roinila, T. Messo, R. Luhtala, R. Scharrenberg, E. C. W. de Jong, A. Fabian, and Y. Sun, "Hardware-in-the-loop methods for real-time frequency-response measurements of on-board power distribution systems," *IEEE Transactions on Industrial Electronics*, vol. 66, no. 7, pp. 5769–5777, Jul. 2019.
- [79] Y. Liao, Z. Liu, H. Zhang, and B. Wen, "Low-frequency stability analysis of single-phase system with dq-frame impedance approach—part i: Impedance modeling and verification," *IEEE Transactions on Industry Applications*, vol. 54, no. 5, pp. 4999–5011, Sep. 2018.
- [80] M. Luo, D. Dujic, and J. Allmeling, "Leakage flux modeling of medium-voltage phase-shift transformers for system-level simulations," *IEEE Transactions on Power Electronics*, vol. 34, no. 3, pp. 2635–2654, 2018.
- [81] M. Luo, "Dynamic modeling of magnetic components for circuit simulation of power electronic systems," EPFL, Tech. Rep., 2018.
- [82] N. Hildebrandt, M. Luo, and D. Dujic, "Robust and cost effective synchronization scheme for a multicell grid emulator," *IEEE Transactions on Industrial Electronics*, 2020.
- [83] R. Teodorescu, M. Liserre, and P. Rodriguez, *Grid converters for photovoltaic and wind power systems*. John Wiley & Sons, 2011, vol. 29.
- [84] A. Whiteley, "Theory of servo systems, with particular reference to stabilization," *Journal of the Institution of Electrical Engineers-Part II: Power Engineering*, vol. 93, no. 34, pp. 353–367, 1946.
- [85] W. Leonhard, "Regelkreise mit symmetrischer Übertragungsfunktion," *at-Automatisierungstechnik*, vol. 13, no. 1–12, pp. 4–12, 1965.
- [86] C. Kessler, *Das symmetrische Optimum, Teil I, Regelungstechnik* 11, 6, 1958.
- [87] D. G. Holmes, T. A. Lipo, B. P. McGrath, and W. Y. Kong, "Optimized design of stationary frame three phase ac current regulators," *IEEE transactions on power electronics*, vol. 24, no. 11, pp. 2417–2426, 2009.
- [88] E. Lakervi and E. J. Holmes, *Electricity distribution network design*, 21. IET, 1995.
- [89] *SKM150GB17E4G Datasheet*, Rev. 1, SEMIKRON, Nov. 2017.
- [90] L. Harnefors, M. Bongiorno, and S. Lundberg, "Stability analysis of converter-grid interaction using the converter input admittance," in *2007 European Conference on Power Electronics and Applications*, IEEE, 2007, pp. 1–10.
- [91] L. Harnefors, M. Bongiorno, and S. Lundberg, "Input-admittance calculation and shaping for controlled voltage-source converters," *IEEE transactions on industrial electronics*, vol. 54, no. 6, pp. 3323–3334, 2007.
- [92] M. Petković and D. Dujic, "Hardware-in-the-Loop Characterization of Source-Affected Output Characteristics of Cascaded H-Bridge Converter," *IEEE Journal of Emerging and Selected Topics in Power Electronics*, 2020.
- [93] *VS1500B Datasheet*, Rev. 6, ABB, May 2003.
- [94] *LF210-S Datasheet*, Rev. 7, LEM, Oct. 2018.
- [95] *Elsys Tranet 408s Datasheet*, Rev. 1, Elsys, Jan. 2019.
- [96] X. Ge and F. Gao, "Flexible third harmonic voltage control of low capacitance cascaded h-bridge statcom," *IEEE Transactions on Power Electronics*, vol. 33, no. 3, pp. 1884–1889, 2017.
- [97] J.-J. Jung, J.-H. Lee, S.-K. Sul, G. T. Son, and Y.-H. Chung, "Dc capacitor voltage balancing control for delta-connected cascaded h-bridge statcom considering unbalanced grid and load conditions," *IEEE Transactions on Power Electronics*, vol. 33, no. 6, pp. 4726–4735, 2017.
- [98] Y. Li, Y. Zhao, and F. Diao, "High-efficiency model predictive control for star-connected cascaded h-bridge statcom under unbalanced conditions," in *2020 IEEE Applied Power Electronics Conference and Exposition (APEC)*, IEEE, 2020, pp. 982–988.
- [99] H.-S. Kim, H.-S. Jung, and S.-K. Sul, "Discrete-time voltage controller for voltage source converters with Lc filter based on state-space models," *IEEE Transactions on Industry Applications*, vol. 55, no. 1, pp. 529–540, 2018.
- [100] H. Yu, M. Awal, H. Tu, Y. Du, S. Lukic, and I. Husain, "Passivity-oriented discrete-time voltage controller design for grid-forming inverters," in *2019 IEEE Energy Conversion Congress and Exposition (ECCE)*, IEEE, 2019, pp. 469–475.

- 
- [101] A. Lesnicar and R. Marquardt, "An innovative modular multilevel converter topology suitable for a wide power range," in *2003 IEEE Bologna Power Tech Conference Proceedings*, IEEE, vol. 3, 2003, 6–pp.
  - [102] J. Lyu, X. Zhang, X. Cai, and M. Molinas, "Harmonic state-space based small-signal impedance modeling of a modular multilevel converter with consideration of internal harmonic dynamics," *IEEE Transactions on Power Electronics*, vol. 34, no. 3, pp. 2134–2148, 2018.
  - [103] S. N. Vukosavic, *Grid-Side Converters Control and Design*. Springer, 2018.
  - [104] S. Milovanovic, "Mmc-based conversion for mvdc applications," EPFL, Tech. Rep., 2020.
  - [105] A. Korn, M. Winkelkemper, P. Steimer, and J. W. Kolar, "Capacitor voltage balancing in modular multilevel converters," in *6th IET International Conference on Power Electronics, Machines and Drives (PEMD 2012)*, IET, 2012, pp. 1–5.
  - [106] P. Münch, D. Görges, M. Izák, and S. Liu, "Integrated current control, energy control and energy balancing of modular multilevel converters," in *IECON 2010-36th Annual Conference on IEEE Industrial Electronics Society*, IEEE, 2010, pp. 150–155.
  - [107] J. Kolb, F. Kammerer, M. Gommeringer, and M. Braun, "Cascaded control system of the modular multilevel converter for feeding variable-speed drives," *IEEE Transactions on Power Electronics*, vol. 30, no. 1, pp. 349–357, 2014.
  - [108] A. Christe, "Galvanically isolated modular converter," IET, Tech. Rep., 2016.
  - [109] R. W. Erickson and D. Maksimovic, *Fundamentals of power electronics*. Springer Science & Business Media, 2007.
  - [110] P. Krause, O. Wasynczuk, S. D. Sudhoff, and S. Pekarek, *Analysis of electric machinery and drive systems*. John Wiley & Sons, 2013, vol. 75.

